romgreek

FORMATION OF TOPOLOGICAL DEFECTS IN LIQUID CRYSTAL SYSTEMS OF NON-TRIVIAL GEOMETRY

Uroš Jagodič

Doctoral Dissertation
Jožef Stefan International Postgraduate School
Ljubljana, Slovenia

Supervisor: Prof. Dr. Igor Muševič, University of Ljubljana, Ljubljana, Slovenia; Jožef Stefan Institute, Ljubljana, Slovenia

Evaluation Board:
Prof. Dr. Samo Kralj, Chair, University of Maribor, Maribor, Slovenia; Jožef Stefan Institute, Ljubljana, Slovenia
Asst. Prof. Dr. Alenka Mertelj, Member, Jožef Stefan Institute, Ljubljana Slovenia
Prof. Dr. Andriy Nych, Member, Institute of Physics,National Academy of Sciences of Ukraine, Kyev Ukraine

MEDNARODNA PODIPLOMSKA ŠOLA JOŽEFA STEFANA
JOŽEF STEFAN INTERNATIONAL POSTGRADUATE SCHOOL



Uroš Jagodič

FORMATION OF TOPOLOGICAL DEFECTS IN LIQUID CRYSTAL SYSTEMS OF NON-TRIVIAL GEOMETRY

Doctoral Dissertation

NASTANEK TOPOLOŠKIH DEFEKTOV V TEKOČE KRISTALNIH SISTEMIH Z NETRIVIALNO GEOMETRIJO

Doktorska disertacija

Supervisor: Prof. Dr. Igor Muševič

Ljubljana, Slovenia, March 2019

To my grandma

Acknowledgments

Firstly, I would like to thank my wife Ema for supporting me throughout all my life decisions. You make my life worth living.

I would like to thank my supervisor Igor Muševič, who gave me the opportunity to expand my knowledge and develop the little child in me trough experimental work.

Next, I would like to thank all the people of our institute, my friends, who helped me throughout my PhD. I would not be able to make it without you. I would especially like to thank Matjaž Humar, Gregor Posnjak, Jaka Pišljar, Maruša Mur, Miha Škarabot, Janja Milivojevič, Anna V. Ryzhkova and Andriy Nych.

And also to the people from the Faculty of Mathematics and Physics in Ljubljana Žiga Kos, Miha Ravnik, Anja Pusovnik and Simon Čopar, thank you.

My final thank you goes to my friends Tadej Emeršič and Vito Šimonka, you guys are the best.

Abstract

This thesis comprises three parts. In the first part, we study the formation of topological defects surrounding colloidal particles of various geometries immersed in liquid crystals. The impact of extreme geometry, such as a fractal, on the number of topological defects formed around the particles is studied. We print hollow prisms with fractal base of several iterations to study this effect. As we increase the fractal iteration, we observe the creation of additional topological defect pairs whiles conserving the total topological charge. Experimental observations and numerical simulations reveal a geometry-based scaling law connecting the number of topological defects to the geometry of the particles. Next we test the impact of chiral environment on the formation of topological defects on particles with higher genus. We observe the formation of distinct topological states, that become more complicated with increasing chirality compared to the particle size. We use several polarization optical microscopy methods to study the structures.

In the second part, we study the thermal properties of thin nematic layers as they are undergoing rapid phase transition. For this purpose we develop an experimental technique allowing us to measure the time dependency of the temperature inside the liquid crystalline sample cell with the liquid crystal medium acting as a fast thermometer. After laser heating we measure the temperature time dependency to determine the speed of the cooling at the phase transition. By comparing experimental observations and extensive computer simulations of the thermal properties of our system we are able to report cooling rates of up to 40 000 K/s, which allow the sample to cool from the initial temperature of above 100 °C to the nematic phase in approximately 1 ms.

In the third part, we develop and use a nanosecond incoherent illumination system and a stroboscopic imaging technique to study the formation of nematic ordering as the liquid crystal is rapidly cooled. This allows us to study the process with nanosecond resolution, which is at least six orders of magnitude faster than previous observations. Due to the random nature of the isotropic nematic phase transition we study the process by stroboscopic imaging. We take a single image per experiment and delay the exposition in between experiments to stitch the images together forming a movie of the process. We use an sensitive camera equipment to study the emergence of the first nematic ordering from the isotropic melt. Next we develop a custom image processing algorithm to study the emergence of light patches on the images, which are a direct consequence of the formation of nematic ordering from the isotropic melt. We determine the properties and the distributions of the patches as a function of time after the start of the cooling and the radius of the heated area. The resulting data allow us to study the predictions of the Kibble-Zurek mechanism, that describes the formation of nematic domains and its cooling rate dependency. Furthermore, by using light transmission, we are able to study the coarsening dynamics in the samples and determine a sample thickness dependency of the coarsening time. Lastly, we combine the data from the observation of the rapid phase transition with the temperature measurements to determine the supercooling of the isotropic phase for up to 500 µs or in terms of temperature up to 10 °C below the phase transition.

Povzetek

Doktorsko delo je sestavljeno iz treh delov. V prvem delu se osredotočimo na nastanek topoloških defektov okoli koloidnih delcev različnih geometrij v tekočem kristalu. Predvsem preučimo vpliv ekstremnih geometrij, kot je fraktal, na število topoloških defektov. V ta namen izdelamo votle koloidne prizme različnih ponovitev Kochovega fraktala. Preučujemo vpliv fraktalne ponovitve na število topoloških defektov, nastalih ob koloidnem delcu. Z večanjem fraktalne ponovitve opazimo povečanje števila parov defektov, ki pa vedno sledi ohranitvi topološkega naboja. Eksperimentalno in s pomočjo numeričnih simulacij odkrijemo povezavo med geometrijo delca ter skupnim številom parov topoloških defektov. Nadalje opazujemo vpliv kiralnosti na nastanek topoloških defektov okoli koloidnih delcev višjih genusov. Opazimo nastanek različnih topoloških stanj, ki postajajo z večanjem kiralnosti čedalje bolj zapletena. Za analizo teh stanj uporabimo različne optične mikroskopske metode.

V drugem delu preučujemo toplotne lastnosti tankih plasti tekočega kristala med ohlajanjem skozi fazni prehod iz izotropne v nematsko fazo. Uporabimo tekoč kristal sam kot zelo občutljiv termometer, kar nam omogoča meritve temperature tekočega kristala v merilni celici po laserskem gretju. Med ohlajanjem merimo časovno odvisnost temperature ter hitrost ohlajanja ob faznem prehodu. Dodatno primerjamo meritve z numeričnimi simulacijami toplotnih lastnosti. Dosežemo hitrosti ohlajanja do 40 000 K/s pri faznem prehodu, kar omogoča ohlajanje vzorca z začetnih 100 °C do faznega prehoda v manj kot 1 ms.

V tretjem delu razvijemo in uporabimo nano-sekunden nekoherenten osvetljevalni sistem v kombinaciji s stroboskopskim načinom zajemanja slik za opazovanje nenadnega faznega prehoda iz izotropne v nematsko fazo. Tako lahko zajemamo slike z nano-sekundno resolucijo, kar je najmanj šest velikostnih redov hitreje kot v dosedanjih raziskavah. Ker gre pri faznem prehodu za naključen pojav, lahko opazujemo dogajanje, tako da - poskus ponavljamo in vsakič zajamemo posamezno sliko, le da med ponovitvami zakasnimo zajem. Posamezne slike lahko združimo v film nastanka topoloških defektov po faznem prehodu. Z uporabo izredno občutljive sCmos kamere opazujemo nastajanje nematskih domen ob ohlajanju iz izotropne faze. Nadalje razvijemo algoritem, ki nam omogoča spremljanje nastajanja domen ob ohlajanju iz izotropne faze. Pri tem določamo pozicijo ter velikost domen v odvisnosti od časa od začetka ohlajanja ter radija grelnega območja. S pridobljenimi podatki lahko preučujemo napovedi Kibble-Zurkovega mehanizma, ki opisuje nastajanje nematskih domen v odvisnosti od hitrosti ohlajanja. Dodatno s pomočjo preučevanja prepustnosti svetlobe skozi vzorec spremljamo pojav, imenovan coarsening dynamics, ki opisuje združevanje domen in nastajanje nematske faze. Pri tem opazimo odvisnost časa združevanja domen od debeline celice. Nazadnje združimo podatke meritev temperature ter meritev lastnosti domen. Opazimo, da pri hitrem ohlajanju izotropno fazo zaznamo nadaljnjih 500 µs za točko faznega prehoda oziroma 10 °C pod temperaturo faznega prehoda.

Contents

List of Figures **xv**

List of Tables **xix**

Abbreviations **xxi**

1 Introduction **1**

2 Theoretical Background and State of the Art **5**
2.1 Liquid Crystals and Phase Transitions 5
2.1.1 Nematic order and the order parameter 6
2.1.2 Isotropic to nematic phase transition 7
2.1.3 Landau-de Gennes model 9
2.2 Optical Properties of Liquid Crystals 11
2.3 Topological Defects in Nematic Liquid Crystals 15
2.3.1 Formation of topological defects after sudden phase transitions . . . 22
2.3.1.1 Kibble-Zurek mechanism 22
2.3.1.2 Coarsening dynamics 26

3 Methods and Materials **29**
3.1 Liquid Crystals 29
3.2 Dyes 30
3.3 Liquid Crystal Cells 30
3.4 Photo-resists 32
3.5 Two-photon Laser Lithography 32
3.6 Polarization Optical Microscopy 34
3.7 Fluorescent Confocal Polarization Microscopy 35
3.8 Nanosecond Illumination and Stroboscopic Imaging Set-up 36
3.9 Image Processing 38
3.9.1 Image noise - point spread function and deconvolution 38
3.10 Temperature Measurements 38
3.10.1 Static thermal properties of LC sample cells 39
3.10.2 Dynamic thermal properties 39
3.10.3 Light transmission study 41
3.10.4 Modelling of thermal properties 41

4 Formation of Topological Defects Surrounding Colloidal Particles **45**
4.1 Fractal Nematic Colloids 45
4.1.1 Koch colloidal particles 46
4.1.2 Surface smoothness and anchoring of the printed colloids 47
4.2 Polarization Optical Microscopy Study of Koch Colloidal Particles 49
4.3 Toroidal Colloids in Chiral Nematic Liquid Crystals 58

5 Formation of Topological Defects Following Rapid Phase Transitions from the Isotropic to the Nematic Liquid Crystal Phase 65
5.1 Nanosecond Illumination System Characteristics 67
5.2 Thermal Properties of Liquid Crystal Cells While Quenching 68
5.2.1 Stationary thermal properties 69
5.2.2 Dynamic thermal properties 74
5.2.2.1 Thermal characteristics of thick LC layers 80
5.2.2.2 Numerical simulations of thermal properties 82
5.3 Polarization Optical Microscopy Study of Rapid Phase Transition 84
5.3.1 Image processing algorithm 85
5.3.2 Image processing algorithm testing 90
5.3.3 Statistical processing of the image data 92
5.4 Formation of Nematic Ordering 100
5.4.1 Early formation of nematic ordering via the Kibble-Zurek mechanism 102
5.4.2 Late time formation of nematic ordering - coarsening dynamics . . . 109
5.4.3 Supercooling temperature 113

6 Conclusions 117

Appendix A Further Observations 123
A.1 Rapid Phase Transition Surrounding Topological Objects 123
A.2 Rapid Fréedericksz Transition-Induced Defect Jumping 128

References 131

Bibliography 139

Biography 141

List of Figures

Figure 2.1: Schematic representation of the phase ordering in LCs. 6
Figure 2.2: Landau free energy density as a function of temperature. 8
Figure 2.3: Polarization image of first order isotropic nematic phase transition. . . 9
Figure 2.4: Splay bend and twist elastic deformation in LCs. 10
Figure 2.5: Index ellipsoid of a typical liquid crystal molecule. 12
Figure 2.6: Temperature dependence of birefringence for E18. 13
Figure 2.7: Transmittance of light through a birefringent sample 14
Figure 2.8: Schlieren texture of a nematic LC as seen under polarized light. 16
Figure 2.9: Schematic representation of the winding number of topological defects. 17
Figure 2.10: Schematic representation of particles with different genus. 18
Figure 2.11: Typical topological defect configurations surrounding spherical colloids. 20
Figure 2.12: Topological defect states surrounding toroidal colloids. 21
Figure 2.13: Schematic representation of the Kibble-Zurek mechanism. 23
Figure 2.14: First experimental observation of coarsening dynamics in LCs. 26

Figure 3.1: **Absorption and emission spectra of Rhodamine 6G and BTBP.** 30
Figure 3.2: **Schematic representation and characteristics of LC sample cells.** 31
Figure 3.3: **Schematic representation of laser lithography.** 33
Figure 3.4: **JSI toroidal sigma.** 34
Figure 3.5: **Polarization optical microscopy set-up.** 35
Figure 3.6: **Confocal microscope used for FCPM** 36
Figure 3.7: **Stroboscopic imaging set up consisting of a conventional POM microscope set up and a nanosecond illumination system.** . . . 37
Figure 3.8: **Schematic representation of the temperature measurement set-up during fast cooling.** 41
Figure 3.9: **Schematic representation of sample cell used for numerical simulations.** 42

Figure 4.1: SEM image of Koch colloidal particles 47
Figure 4.2: **Close-up SEM image of polymer colloidal particles** 48
Figure 4.3: **Defect structure around colloidal tori in nematic LC.** 49
Figure 4.4: **Experimental observations of Koch fractal colloids.** 51
Figure 4.5: **POM study of 0^{th} iteration Koch fractal colloids** 52
Figure 4.6: **POM study of 1^{st} iteration Koch fractal colloids** 53
Figure 4.7: **POM study of 2^{nd} iteration Koch fractal colloids at $0°$** 54
Figure 4.8: **POM study of 2^{nd} iteration Koch fractal colloids at $30°$** 55
Figure 4.9: **Theoretical study of topological defect structure on Koch fractal particles.** 57
Figure 4.10: **SEM image of a single colloidal torus.** 58
Figure 4.11: **Colloidal tori in chiral nematic LC.** 60
Figure 4.12: **Optical tweezers experiments in chiral nematic LC.** 61

Figure 4.13: **Polarization guiding in twisted nematic LC.** 62
Figure 4.14: **Colloidal tori in chiral nematic LC.** 63
Figure 4.15: **FCPM study of tori in chiral nematic LC.** 64

Figure 5.1: **Isotropic nematic phase transition images by conventional camera equipment.** 66
Figure 5.2: **Spectra and pulse duration of Rhodamine dye cuvette.** 67
Figure 5.3: **Imaging sensor characteristics** 68
Figure 5.4: **Heating laser stability.** 69
Figure 5.5: **Observations of the thermal profile inside LC cells.** 71
Figure 5.6: **Heated area diameter versus heating laser power** 72
Figure 5.7: **Temperature of minimal isotropic islands versus laser power.** . . 73
Figure 5.8: **Gaussian temperature profile.** 74
Figure 5.9: **Temperature dependence of E18 refractive index and birefringence.** 75
Figure 5.10: **Transmittance of LC sample cell while cooling.** 76
Figure 5.11: **Measured of the temperature time dependency inside thin E18 layer.** 77
Figure 5.12: **Fitting error on temperature measurements.** 78
Figure 5.13: **Contour plot of the temperature inside a LC sample cell.** . . . 79
Figure 5.14: **Radial dependence of temperature and quench rates inside 5CB.** 80
Figure 5.15: **Temperature measurements inside thick LC layers.** 81
Figure 5.16: **Comparison of cooling of thick and thin LC layers.** 82
Figure 5.17: **Comsol simulations of thermal characteristics inside LC cells.** . 83
Figure 5.18: **Dynamic temperature measurements using Comsol.** 84
Figure 5.19: **Typical image of a rapid phase transition in a liquid crystal.** . 85
Figure 5.20: **Typical regions of an image of a phase transition.** 87
Figure 5.21: **Deconvolution of experimental images.** 88
Figure 5.22: **Determination of the dimensions of the heated area.** 89
Figure 5.23: **The detection of light patches by algorithm.** 90
Figure 5.24: **Test of the peak detection algorithm.** 91
Figure 5.25: **Zoomed out section of an isotropic nematic phase transition dynamics.** 92
Figure 5.26: **Visualized properties of light patches.** 93
Figure 5.27: **Distribution of light patch widths over the heated area.** 95
Figure 5.28: **Sum of 1000 light patch width distributions.** 96
Figure 5.29: **Light volume distribution over the heated area.** 97
Figure 5.30: **Sum of 1000 light volume distribution.** 98
Figure 5.31: **Light transmission study on images.** 99
Figure 5.32: **Movie of rapid phase transition in nematic LCs.** 101
Figure 5.33: **Zoomed out sections of images of rapid phase transition obtained at selected times.** 103
Figure 5.34: **Distributions of light patch width at different times.** 104
Figure 5.35: **Distributions of light patch light volume at different times.** . . 105
Figure 5.36: **Light transmission study on images.** 106
Figure 5.37: **Comparison of different analytical methods.** 107
Figure 5.38: **Growth of light transmission and light volume.** 108
Figure 5.39: **Growth of nematic order versus radius and quench rate.** 109
Figure 5.40: **Light transmission of a 2.5 µm thick sample cell of 5CB after rapid phase transmission.** 110

Figure 5.41: **Light transmission of a 7.5 µm thick sample cell of 5CB after rapid phase transmission.** . . . 111
Figure 5.42: **Light transmission of a 18 µm thick sample cell of 5CB after rapid phase transmission.** . . . 112
Figure 5.43: **Sample cell thickness dependency of coarsening dynamics.** . . . 113
Figure 5.44: **Measurement of the delay between reaching phase transition and detection of signal.** . . . 114
Figure 5.45: **Time dependency of cooling fir accuracy.** . . . 115
Figure 5.46: **Super cooled isotropic region.** . . . 116

Figure A.1: **Formation of topological defects surrounding a free-standing toroidal colloid.** . . . 124
Figure A.2: **Formation of topological defects surrounding fixed toroidal colloid.** . . . 125
Figure A.3: **Impact of elastic distortions on the formation of topological defects.** . . . 127
Figure A.4: **Fréedericksz transition arround a toroidal particle.** . . . 129
Figure A.5: **Jumping of a disclination line after a sudden Fréedericksz transition.** . . . 130

List of Tables

Table 3.1: **LC material properties.** 29
Table 3.2: **Properties and applications of photo-resists.** 32
Table 3.3: **Thermal properties of materials used.** 43

Abbreviations

LC ... Liquid crystal
5CB ... 4-Cyano-4'-pentylbiphenyl
BTBP... N,N'-bis(2,5-di-tert-butylphenyl)-3,4,9,10-perylenedicarboximide
DMOAP. Dimethyloctadecyl[3-(trimethoxysilyl)propyl]ammonium chloride
NLC ... Nematic liquid crystal
FCPM.. Fluoresence confocal polarization microscopy
Nd:YAG Niodime Yag laser
N* ... Chiral nematic liquid crystal
DPDG.. Digital pulse delay generator
POM ... Polarization optical microscopy
KZ ... Kibble Zurek mechanism
SEM ... Scanning electron microscopy
FEM ... Finite element modelling
NA ... Numerical aperture
FWHM. Full width at half maximum
I-N ... Isotropic to nematic

Chapter 1

Introduction

Common observations of Nature dictate the notion of three distinct states of matter, the solid, the liquid and the gas phase, with strong jumps in properties throughout the phase transitions. Yet, certain materials exhibit one or several distinct phases in between the classical three, hence the name meso-phases. For instance, some elongated organic molecules exhibit a vast number of different stable phases with various degrees of liquid and crystalline-like properties, earning the name liquid crystals (LCs) [1].

The basic properties of phases of matter can be boiled down to the symmetry of the building blocks itself. Highly structured and ordered crystalline phases with well defined orientation and positional order of building blocks have low symmetry. Liquids lose most of the order, exhibiting larger amounts of symmetry. Yet the highly scattered and randomly positioned building blocks of gas phases account to the highest amount of symmetry. Liquid crystals, as for the fact that they can easily flow, a designated liquid-like property, still possess some degree of orientation or translational ordering, typically associated with crystalline phases. Therefore, breaking the symmetry of the phases, [2], [3]. The most simple case of a LC phase is the nematic phase where the typically ellipsoidal building blocks tend to align towards a common direction, called the nematic director n. It is said that the nematic phase possesses orientational ordering. In a more complex LC system, a combination of degrees of orientational or translational ordering can be present, leading to a number of LC phases within the traditional solid and liquid phase [1], [4].

Similar to macroscopic physical systems, the richest and the most interesting properties of materials are the consequence of defects in the system. Typically defects form due to impurities inside the system or the boundary condition imposed by the enclosing surfaces [5]. For example defects inside nematic LCs are areas where the local orientation of the nematic director can not be uniquely defined and there is no smooth transformation of the director field that could get rid of the defects. Those defects are therefore topologically stable entities called topological defects [3]. Analogous to electrostatics each topological defect can be characterized by its interaction with the surrounding field, called its topological charge. Similarly a conservation law applies dictating the total number and charge of the topological defect. Since topological defects increase the local energy, LC systems always seek out the lowest possible number of topological defects that still fulfils the conservation law, to minimize the energy in the system.

The structure and interaction of individual topological defect has been studied in detail in various physical systems, from vortices in Helium, Quantum effects cosmology to LCs [6]–[12]. Yet the formation of topological defects is still lacking experimental observations. One way topological defects can form as a consequence of introduced singularities in the system such as the introduction of colloidal particles of various shapes and topology. The anchoring condition on the surface of the colloidal particles creates singularities in the orientation

field of the LC which forces the system to create its own singularity or topological defect of opposite charge to fulfil the conservation of charge law [2]. The structure of topological defects formed around colloidal particles is strongly dependent on the topology and/or the geometry of the particle, the anchoring condition on the particle and the LC medium itself [13]–[15]. One can therefore expect a whole array different topological defect configurations to emerge after the inclusion of colloidal particles.

Nowadays the introduction of optical tweezers has enabled us to manipulate topological defects and study their interactions. It has been shown that one can use the strong interaction of topological defects for self assembly [16]. For instance one can simply, by stacking colloidal particles in nematics, create photonic crystals which can be used for optical applications [17], [18]. The optical tweezers can be used to move and manipulate the topological defects by means of locally heating, via the opto-thermal effect, the LC medium to create an area of lower elastic energy which acts as an optical trap [19], [20]. By increasing the laser power, one can simply locally heat up the system way beyond its clearing point, and by rapidly shutting down the laser rapidly enforce a phase transition or quench the system back into its ground state. Note that by varying the laser power, one can cross any desired phase boundary, but for the sake of simplicity, we stick to the isotropic to nematic phase transition. Due to the lack of any memory effect in the isotropic phase, this can be used to study multiple stable topological defect configurations by simply quenching the system and resetting the structure of the LC. This can also be used to increase the total amount of topological defects in the system. For instance Nikkhou et al. [21] showed that quenching a localized area of a colloidal fibre creates additional topological defect pairs with opposite charge, which increases the total number of topological defects in the system but still conserves the total topological charge. Similarly, by changing the local environment of the colloidal particles, for instance by introducing chirality into the director field of the LC, one can expect a vast array of topological defect states [13], [15].

The use of optical tweezers for thermal quenching is a well established tool for topological defect research in liquid crystals, yet not much is known about the basic physical processes regarding the process of quenching itself. For instance, since there is no way to measure the temperature locally and at time scales, in which a typical quench occurs, not much is known about the thermal properties of the sample undergoing a quench. Also there is still much to know about the process of formation of topological defects after a quench. Due to experimental limitations only observations at later time scales have been made [22]–[24]. Yet at early times, experimental coverage is sill missing. The quest for the experimental coverage is fired by the recent interest of the study of the formation of topological defects in a whole spectrum of physical systems, from cosmology, superconductivity to various quantum phase transitions over the years [25], [26]. For example in the 70s, Kibble proposed a universal mechanism which describes the formation of matter in the universe after the big bang [27], which later Zurek refined [28], to include the quench rate dependency, into the Kibble-Zurek mechanism (KZ mechanism) [29]. The mechanism can be theoretically proven in any of the stated physical system, yet no experimental observations of the mechanism have been made. The latter is mainly due to the extreme experimental challenges accompanying the systems. Here is where LCs come in as a relatively easy to use experimental system which can be used to study the predictions of the KZ mechanism in the laboratory set-up.

In our work we focus on the formation of topological defects surrounding colloidal particles of various shapes and also on the formation of topological defects after sudden temperature-driven phase transitions. We experimentally study the structure and properties of a defect formed in colloidal particles of known topology with a dramatically different geometry. This is achieved by observing simple hollow prisms with fractal base

with changing fractal order. We observe a simple geometry based scaling law which can be used to describe the number of defects formed based on the fractal geometry. On the other hand, we have experimentally studied the formation of topological defects after a sudden temperature-driven phase transition. We have chosen the simplest possible isotropic to nematic phase transition of a well-known liquid crystal sandwiched into a thin film glass sample cell. We develop an experimental set up consisting of a stroboscopic imaging technique and a nanosecond laser illumination system to study the process in great detail. We developed a custom image processing algorithm to cope with the vast amount of data gained from the experimental observation. We also develop a technique to measure the temperature and thermal properties inside thin LC films while quenching. With the combination of the data obtained from the study of the thermal processes and the data obtained using the imaging set up we gain a novel glimpse in the formation of topological defects and test the predictions of the KZ mechanism.

In the thesis we will focus on the experimental observations of the formation of topological defects in various liquid crystal systems. The structure of the thesis is as follows. Firstly, in Chapter 2, we introduce the basic theoretical background of the phases, the structure and the formation of topological defects in various liquid crystal systems. Additionally, we will take a look at the state of the art in the field of the formation of topological defects after phase transitions and along colloidal particles of various shapes and topologies. Secondly, in Chapter 3, we will introduce the experimental techniques used in the thesis. We show how we use experimental techniques, such as optical microscopy, photolithography and laser illumination systems, to study the formation of topological defects in various LC systems and extensive computer simulations to study the thermal properties of the systems. We also present the algorithm developed to extract and statistically evaluate the experimental data. In Chapter 4, and 5 we present and discuss how the experimental methods, the computer algorithms and the knowledge of the theory combine in the understanding of the formation of topological defects along colloidal particles 4, and after sudden phase transitions 5.

Chapter 2

Theoretical Background and State of the Art

In this Chapter we will introduce the theoretical background and state of the art of the experimental study of the formation of topological defects in various liquid crystal.

2.1 Liquid Crystals and Phase Transitions

As the name implies, liquid crystals posses, properties which link them to ordinary liquids and crystalline solids at the same time. For instance LCs are viscose liquids and can flow just like ordinary liquids, however ordinary liquids do not possess any long- or short-range order like liquid crystals do [1]. The ordering is always orientational and in some cases translational, meaning that the building blocks are orientated in a certain direction or the distance between them is well defined. A combination of the orientation and translational ordering gives rise to several distinct liquid crystal phases [4]. For instance the nematic liquid crystalline phase possesses only orientational ordering whereas smectic phases possesses orientational order and one dimensional periodic ordering into smectic layers. Because the smectic phase is more ordered, it is typically found at lower temperatures compared to the nematic phase. We think of organic molecules as rod like and therefore, we can schematically represent the LC phases as ellipsoids, Fig. 2.1.

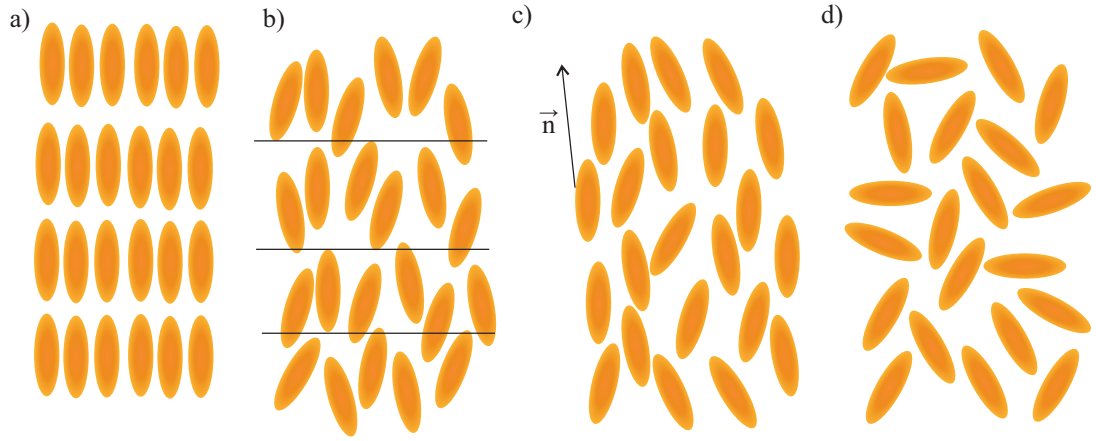


Figure 2.1: Schematic representation of typical phase behaviour of a liquid crystalline material. With increasing temperature thermal fluctuations destroy order in the system and the material goes from crystalline a) to smectic A, b) nematic, c) to the isotropic phase.

The simplest liquid crystalline phase is the nematic phase and only shows the orientational ordering where the building blocks are aligned towards a common direction in space called the nematic director n [1]. This is also reflected in most of the physical properties of the material which are orientation dependent meaning that the property along the direction of n can vastly differ from its value in another direction. Commonly the direction of n is arbitrary in space yet it can be strongly influenced by surface forces and external fields. Due to the rotational invariance of the basic building blocks of nematic, typically rod-like molecules, the direction of n and $-n$ are indistinguishable. The centres of gravity of nematic building blocks are free flowing but still retain long range orientational ordering. When the LC are made of chiral molecules, one obtains the chiral nematic phase, where the molecules are spontaneously twisting in a direction perpendicular to the nematic director. The twist or the so-called pitch can be described as the distance over which the molecules undergo a full 360° twist. This twist is caused by the handedness or chirality of the building blocks, which forces them to pack in a helicoidal fashion [30]. The chirality or the ability to twist can be controlled by the addition of a chiral dopant molecule which enforces a twist in the director.

2.1.1 Nematic order and the order parameter

The nematic director refers to a preferred direction in space in which most of the molecules orient. Due to thermal fluctuations the individual orientations can vastly vary from the director orientation. We express an average ordering of the nematic molecules with respect to the director by means of an order parameter Q which is non-zero in the nematic phase and vanishes in the isotropic phase [31], [32]. This can be done by considering the molecules as rigid cylinders with ϕ and θ as their azimuthal and polar angle. We define an unit vector parallel to the rods in the laboratory reference frame $a_x = \sin\theta\cos\phi$, $a_y = \sin\theta\sin\phi$ and $a_z = \cos\theta$ respectively. Let us define a distribution function $f(\theta, \phi)$ that describes the probability of finding the rods in a small solid angle $d\Omega = \sin\theta d\theta d\phi$ around the direction of the director, which is along the z axis. We describe the average molecular orientation along the nematic director by a tensor parameter Q_{ij}

$$Q_{ij} = S\left(a_i a_j - \frac{1}{3}\delta_{ij}\right). \tag{2.1}$$

As stated, the order parameter is non-zero in the nematic phase and vanishes in the isotropic phase [1]. Since $\langle a_i^2 \rangle = 1/3$ and $\langle a_i a_j \rangle = 0$ we can write a general form of the order parameter

$$[Q_{ij}] = S \begin{bmatrix} -\frac{1}{3} & 0 & 0 \\ 0 & \frac{1}{3} & 0 \\ 0 & 0 & \frac{2}{3} \end{bmatrix}, \tag{2.2}$$

with amplitude

$$S = \frac{1}{2} \cdot \left\langle \left(3\cos^2\theta - 1\right) \right\rangle = \int f(\theta) \frac{1}{2} \left(3\cos^2\theta - 1\right) d\Omega. \tag{2.3}$$

Here $\langle\rangle$ describes a time and spatial average over an ensemble of molecules. Note that for $\theta = 0$ S becomes 1 which indicates parallel alignment and for $\theta = \pi/2$ S becomes -1/2, where all are perpendicular to the nematic director as in the case of dicotic LCs. Typical rod-shaped nematics typically have a positive value of S which is also strongly temperature dependent.

2.1.2 Isotropic to nematic phase transition

Let us use the previously stated rigid rod approximation for nematic phase and the tensor order parameter Q_{ij} Eq. 2.1 to exploit the isotropic to nematic phase transition. Using the Landau-de Gennes approach let us write the free energy density of the system $f(T, S_{ij})$ as a power law series of the order parameter [2], [31], [33]

$$f(T, Qij) = \frac{1}{2}a(T)Q_{ij}Q_{ji} - \frac{1}{3}BQ_{ij}Q_{jk}Q_{ki} + \left(\frac{1}{4}CQ_{ij}^2\right)^2 + \ldots, \tag{2.4}$$

where a, B and C are material constants. For any temperature there is a value of Q_{ij} that minimizes the free energy density of the system.

Let us define a temperature T^* in the nematic phase where Q_{ij} is zero for $T > T^*$ and non zero for $T < T^*$. For temperatures higher than T^* $Q_{ij} = 0$ minimizes the free energy, therefore $\alpha(T)$ must be zero and $a(T)$ must be positive. On the contrary when $T < T^*$ $a(T)$ must be negative since a non-zero S_{ij} minimizes the free energy. Therefore $a(T)$ has to be zero at temperature T^*

$$a(T) = a_0\left(T - T^*\right), \tag{2.5}$$

where a_0 is a positive constant and T^* is the super cooling temperature below which the isotropic phase can not be stable. The other parameters in Eq. 2.4 also have to go to zero at the transition. Also note that the third term cannot be discarded since S and $-S$ are not interchangeable. Combining Eq. 2.4 and Eq. 2.3 the free energy becomes

$$f(T, S) = \frac{3}{4}a_0(T)S^2 - \frac{1}{4}BS^3 + \frac{9}{16}CS^4 + \ldots, \tag{2.6}$$

Again a_0, B and C are material constants. Eq.2.6 depends only on the S. The first term drives the transition, the second term ensures asymmetry of S and the third term bounds the values of S from below. By minimizing the expression one finds an equilibrium value of S_{eq}, [34].

$$S_{eq} = \begin{cases} 0, & T > T_c \\ \frac{1}{2}\left[-B/3C + \sqrt{(B/3C)^2 - 8a(T - T_c^*/3C)}\right] & T < T_c \end{cases} \quad (2.7)$$

We can plot the expression Eg. 2.6 for typical values of $a_0 = 10^5 Jm^{-}3K^{-}1$, $B = -10^6 Jm^{-}3$ and $C = 10^6 Jm^{-}3$ [1] is shown in Fig. 2.2.

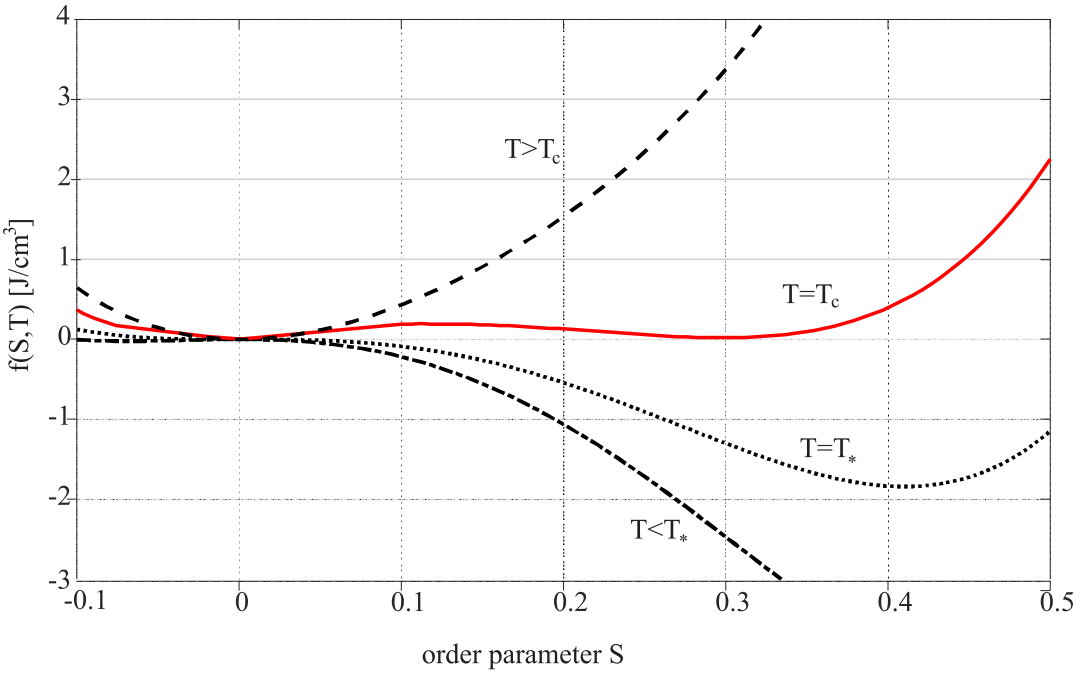


Figure 2.2: Landau free energy density as a function of order parameter S for temperatures above the phase transition temperature $T > T_c$, at the phase transition temperature $T = T_c$, at the supercooling temperature $T = T_*$ and below it $T < T_*$

Here T_c represents a phase transition temperature for which the two phases coexist or in other words have the exact same free energy density. Coexistence of phases is a distinct feature of a first order phase transition which is the consequence of a lack of symmetry of S that is expressed in the third term of Eq. 2.6. Due to the small size of B and the fact that $T - T_*$ is small (app. 1K), we consider the isotropic to nematic phase transition only weakly first order. By setting b to 0 one can rewrite the expansion for second-order phase transitions, such as the case of smectic A to smectic C [33]. A typical experimental image of a coexistence of the isotropic and the nematic phase is shown in 2.3.

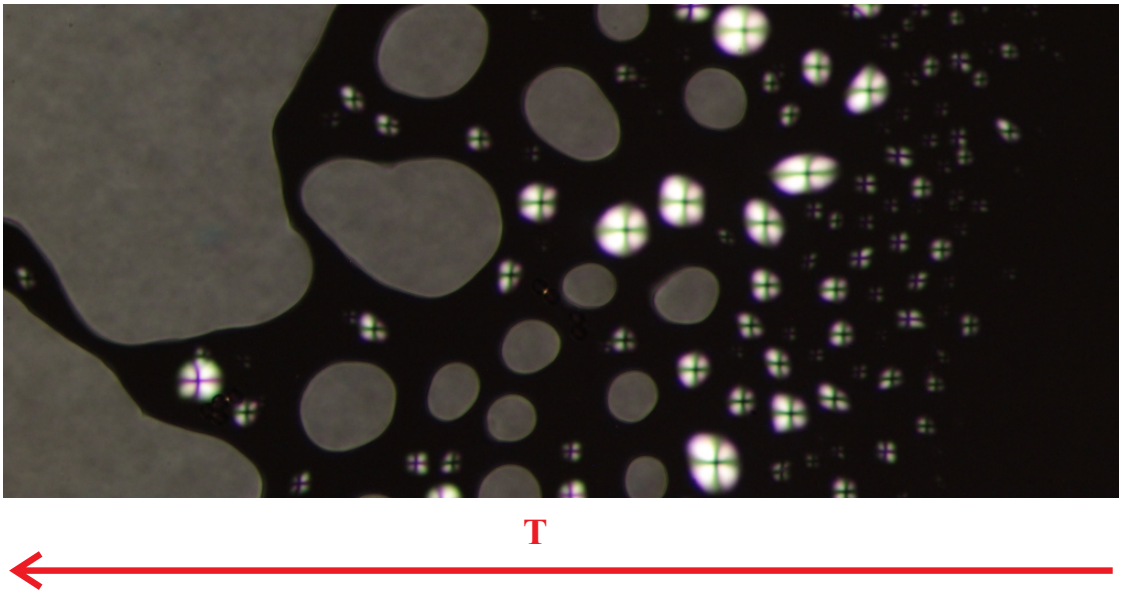


Figure 2.3: Polarization image of first order isotropic nematic phase transition of 5CB. There is a temperature gradient of approximately 1 °C between the far left and the far right side of the image. Before the nematic domains run through the whole volume of the sample, they can be observed as nematic bubbles in the isotropic melt hence the crosses on some patches.

2.1.3 Landau-de Gennes model

The Landau de Gennes model of the free energy of liquid crystal is not only used to describe the isotropic to nematic phase transition, but is a powerful tool, which can be used to calculate the equilibrium nematic ordering including elastic nematic distortions, coupling to external fields and surfaces, and the appearance of topological defects [1], [35], [36]. The basic free energy of the system is

$$F = F_{homogeneous} + F_{distortion} + F_{field} + F_{surface} = \int (F_h + F_d + F_f)\, dV + \int (F_s)\, dA, \tag{2.8}$$

where $F_{homogeneous}$ describes the temperature dependency of the order parameter, which we described in the previous section. $F_{elastic}$ describes the elastic distortions in the system, F_{field} the effects of fields such as electric or magnetic fields and finally the $F_{surface}$ term describes the impact of the anchoring of the LC molecules at the surrounding surfaces.

The free energy density Eq. 2.8 can be rewritten as the Frank-Oseen elastic free energy, where the variations of the order parameter S are neglected and S is considered constant throughout the liquid crystal

$$\begin{aligned} F_{distortion} = {} & \frac{K_1}{2}(\nabla \cdot n)^2 + \frac{K_2}{2}(n \cdot \nabla \times n)^2 + \frac{K_3}{2}(n \times \nabla \times n)^2 \\ & + \frac{K_{24}}{2}\nabla \cdot (n\nabla \cdot n + n \times \nabla \times n) + K_{13}\nabla \cdot (n\nabla \cdot n)\,. \end{aligned} \tag{2.9}$$

The three terms of the expansion represent the basic distortions of the nematic LCs. Here K_1 term presents a pure splay deformation, K_2 term presents a pure twist deformation and K_3 a pure bend deformation. Typical deformations are shown in Fig. 2.4.

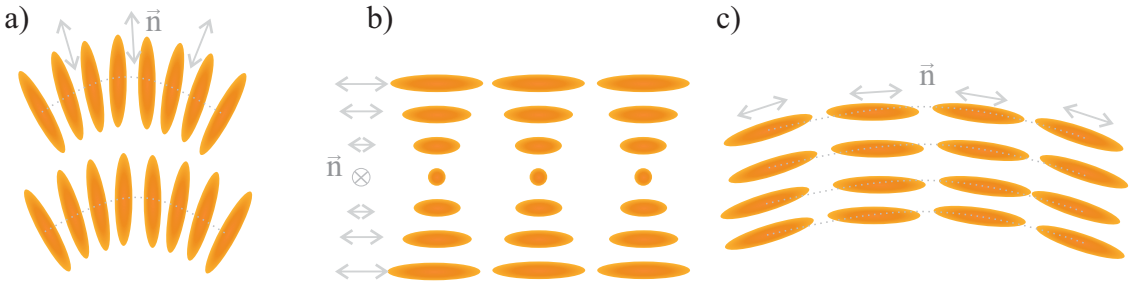


Figure 2.4: Splay **a)** twist **b)** and bend elastic deformations **c)** in liquid crystals.

The expansion also predicts K_{24} which represents a mixed saddle splay conformation term and a K_{13} mixed splay bend, which contain complete divergence terms which can be using the Gauss theorem transformed to surface integrals [37], [38]. And since we typically consider only deviation of the director in the bulk of the LC, those two terms are typically neglected. Typical values for the Francs constant for a typical LC like 5CB are $K = 6 \times 10^{-12} N$ [39] with approximately 40 % difference from the average value across $K_1 - K_3$. Therefore a common approach is to use an one-constant approximation whereby $K_1 = K_2 = K_3 = K$ and we can rewrite the elastic free energy as

$$f_e = \frac{K}{2}\left[(\nabla \cdot n)^2 + (\nabla \times n)^2\right]. \tag{2.10}$$

Distortions of the director can also be caused by applying an external electric or magnetic filed, which couples with the induced electric or magnetic dipoles of the LC molecules. Those dipoles can be either parallel or perpendicular to the nematic director depending on the polarisability of nematic molecules. For instance the interaction of an external electric field with the nematic director can be written as [1], [36], [40]

$$f_{field} = -\frac{1}{2}\varepsilon_0 \left(\bar{\varepsilon}\delta_{ij} + \frac{2}{3}\varepsilon_a^{mol} Q_{ij}\right) E_i E_j, \tag{2.11}$$

where ε_0 is the vacuum dielectric permittivity, ε_a^{mol} the average molecular dielectric anisotropy and $\bar{\varepsilon}$ the average LC permittivity.

Another important factor is the impact of the surrounding surfaces on the LCs. Due to the tendency to minimize the free energy density, LC molecules follow the alignment of the first few layers of building blocks that are strongly bound to the surface through the bulk of the sample [41]. Therefore deviations of the main orientation are penalized by the free energy term in the Frank expansion and written by

$$f_{anchoring} = -\frac{1}{2} W \left(\vec{n} \cdot \vec{n_0}\right)^2. \tag{2.12}$$

$\vec{n_0}$ is the preferred direction of the director on the surface. Molecules on the surface can be aligned in a common direction, such alignment is called unidirectional planar, or randomly, which is called degenerate planar anchoring. If we coat the surface with a surfactant with long apolar chains, the LC molecules can align along the chains that are perpendicular to the substrate and the anchoring is called homeotropic.

2.2 Optical Properties of Liquid Crystals

The anisotropic shape of liquid crystal building blocks which is the cause of the orientational ordering in LC phases also gives rise to interesting optical properties of LCs [42], [43]. Any description of the interaction of matter with light or any other part of the electromagnetic spectrum has to start with the theoretical backbone of the Maxwell equations. The set of four equations describe the relations of the electric and magnetic fields E,B to electric displacement field and magnetic flux densities D and H.

$$\nabla \cdot D = 0, \tag{2.13}$$
$$\nabla \cdot B = 0,$$
$$\nabla \times E = -\frac{\partial B}{\partial t}, \tag{2.14}$$
$$\nabla \times H = \frac{\partial D}{\partial t}.$$

Inside of a medium this becomes

$$D = \varepsilon_0 \underline{\varepsilon} E, \qquad B = \mu_0 \underline{\mu} H, \tag{2.15}$$

where ε_0 and μ_0 represent the permittivity and permeability of the vacuum and $\underline{\varepsilon}$ and $\underline{\mu}$ are the dielectric tensor and the permeability tensor of the material in the field receptively. Since we typically work with non magnetic materials, we can consider $\underline{\mu} = 1$ and for non-absorbing uniaxial LC materials we can rewrite the dielectric tensor as

$$\underline{\varepsilon} = \begin{pmatrix} \varepsilon_{xx} & 0 & 0 \\ 0 & \varepsilon_{yy} & 0 \\ 0 & 0 & \varepsilon_{zz} \end{pmatrix}. \tag{2.16}$$

ε_{zz} is the dielectric permittivity along the long direction of LC molecules. Due to the rotational symmetry the permittivity perpendicular to the long direction of the molecules has no polar dependency, therefore $\varepsilon_{xx} = \varepsilon_{yy}$. The dielectric tensor is directly related to the characteristic optical properties of the material and since it is a three dimensional property, we can represent it by a surface, called a Fresnel or ray ellipsoid [43]. The surface is defined by the locus of the electric fields E that produce the same energy density U as

$$\frac{1}{2} E \cdot D = U = const. \tag{2.17}$$

Considering Eq .2.15, this equation can be rewritten to a parametric equation of an ellipse in the principal coordinate frame as

$$\frac{D_x^2}{\varepsilon_{xx}} + \frac{D_y^2}{\varepsilon_{yy}} + \frac{D_z^2}{\varepsilon_{zz}} = 2\varepsilon_0 U, \tag{2.18}$$

where we know that $\varepsilon_{xx} = \varepsilon_{yy}$. Therefore we only have two distinct values of the dielectric permittivity which influence the speed of the light inside the medium. In other words we have two distinct refractive indices of the medium $n_x = \sqrt{\varepsilon_{xx}}$ and $n_z = \sqrt{\varepsilon_{zz}}$.

In general for any given propagation direction the refractive index can have two values, corresponding to the fast and speed propagations speed with different polarizations of the light beam [43], [44]. There is always a direction of propagation where the two speeds coincide, called the optical axis. In uniaxial media one polarization will always be perpendicular to the optical axis, which is called the ordinary polarization. The other is

orthogonal to the wave vector k of the light beam and also the ordinary polarization, and it is called the extraordinary polarization, shown in Fig. 2.5 a. In liquid crystals as a typical anisotropic uniaxial material we typically find two refractive indices. One can define the long direction of the index ellipsoid as the optical axis of the material. The extraordinary refractive index n_e lies along the long direction of the molecules and perpendicular to it we find the ordinary refractive index n_o.

Light propagating along the long direction of LC molecules therefore experiences only the extraordinary refractive index and perpendicular to the long axis the ordinary. In any other direction of propagation the light effectively sees a combination of both refractive indices n_{eff} shown in Fig. 2.5 b.

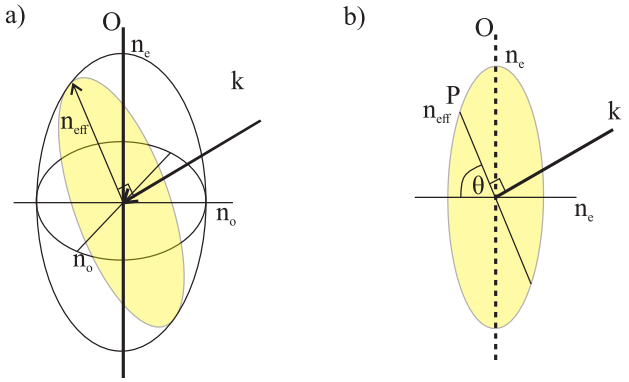


Figure 2.5: Index ellipsoid of a typical liquid crystal molecule. **a)** Light propagating through uniaxial anisotropic media experiences two refractive indices. One can reconstruct the ordinary and extraordinary refractive index by a cross-section of the index ellipsoid perpendicular to the direction of propagation of light, represented by the wave vector k. Light experiences along its long axis an extraordinary refractive index n_e and perpendicular to it the ordinary refractive index n_o. **b)** In any other direction a combination of the refractive indices n_{eff} is observed.

The extraordinary refractive index for a particular direction of propagation can be determined from n_o and n_e as

$$\frac{1}{n_{eff}^2} = \frac{\cos^2 \vartheta}{n_o^2} + \frac{sin^2 \vartheta}{n_e^2}. \tag{2.19}$$

Here θ presents the angle of the propagation direction to the optical axis of the material as shown in Fig. 2.5 b.

The presence of two refractive indices is called birefringence which is measured by the difference between the ordinary and extraordinary indices as $\Delta n = n_e - n_o$. For example a typical nematic LC shows strong temperature dependence of the refractive indices where the extraordinary refractive index decreases drastically as the temperature approaches the phase transition temperature whereas the ordinary refractive index slightly increases. The birefringence also decreases with increasing temperature. Note that the birefringence exhibits a sudden drop at the phase transition temperature from the value $\Delta n >> 0$ to $\Delta n = 0$ which is due to the nature of the first order nematic isotropic phase transition. A typical temperature dependence of the birefringence of a common liquid crystal E18 is shown in Fig. 2.6.

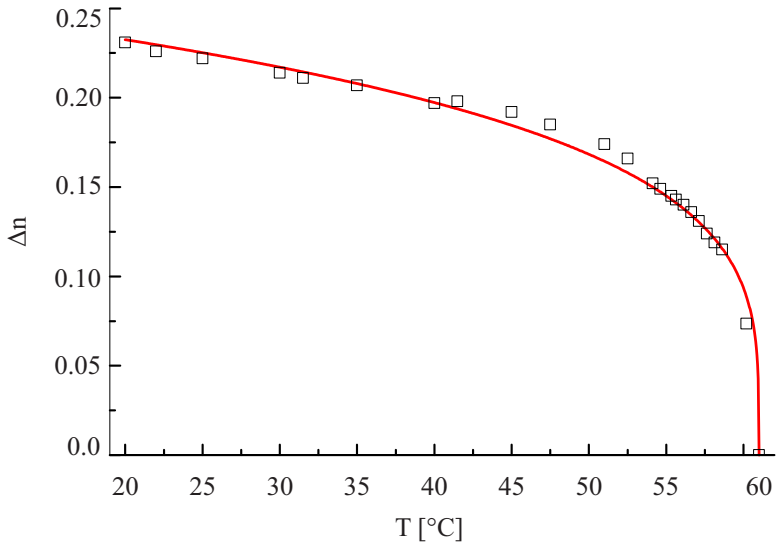


Figure 2.6: Temperature dependence of the birefringence of a nematic liquid crystal E18.

$$\Delta n(T) = \Delta n_o \left(1 - \frac{T}{T_c}\right)^{\beta} \tag{2.20}$$

Here Δn_0 represents the birefringence at zero temperature and T_c the isotropic to nematic phase transition temperature. As for 5CB the typical birefringence at room temperature is $\Delta n = 0.22$ with a phase transition temperature of 35 °C.

The main source of birefringence in the liquid crystals is order, which is in the nematic phase described by the average orientation of the molecules towards the director, summarizers in Eg. 2.3. The typical temperature dependence of the birefringence can be expressed by a temperature fit [45]

$$S = \left(1 - \frac{T}{T_c}\right)^{0.142}. \tag{2.21}$$

One can connect the ordering of the LCs to their optical properties. First we consider the approximation of a single molecule in an isotropic medium. For such a molecule the refractive index (n_{iso}) dispersion in optical frequencies is known as [46]

$$\frac{n_{iso}^2 - 1}{n_{iso}^2 + 2} = \frac{\rho N_a}{3\epsilon_0 M}\alpha_{iso}, \tag{2.22}$$

where N_a represents the Avogadro's number, ϵ_0 the dielectric permeability of vacuum, α_{iso} the mean polarizability of the molecules and M the molar mass. To account for the anisotropy of the LC medium one has to assume two distinct polarizabilities along both common directions of uniaxial molecules α_s, α_p. Using 2.3 as a measure of the average order of nematic molecules in the system, one can describe the average polarizability perpendicular $\alpha_\perp$ and parallel $\alpha_\parallel$ to the director as

$$\alpha_{\perp} = \alpha + \frac{2}{3}\left(\alpha_p - \alpha_s\right) S \tag{2.23}$$

$$\alpha_{\parallel} = \alpha + \frac{2}{3}\left(\alpha_p - \alpha_s\right) S, \tag{2.24}$$

where the average polarizability has the form $\alpha = \frac{1}{3}\alpha_{\parallel} + 2alpha_{\perp}$. Combining 2.2 and 2.2 we obtain

$$\frac{n_e^2 - n_o^2}{n^2 + 2} = \frac{\rho N_a}{3\epsilon_0 M}\left(\alpha_{\parallel} - \alpha_{\perp}\right) S, \tag{2.25}$$

This connects the birefringence of LC to its order. This relation can be experimentally exploited to measure the order of the system by simply measuring the birefringence of the system.

Measurements of birefringence can be done by exploiting the effect of birefringent media on polarized light. By placing a slab of anisotropic medium in between crossed polarizers such that the light first passed through one polarizer then the sample and is detected through a second polarizer oriented perpendicular to the first, as shown in Fig. 2.7, one can measure the birefringence of the sample by measuring the transmission of the composite slab.

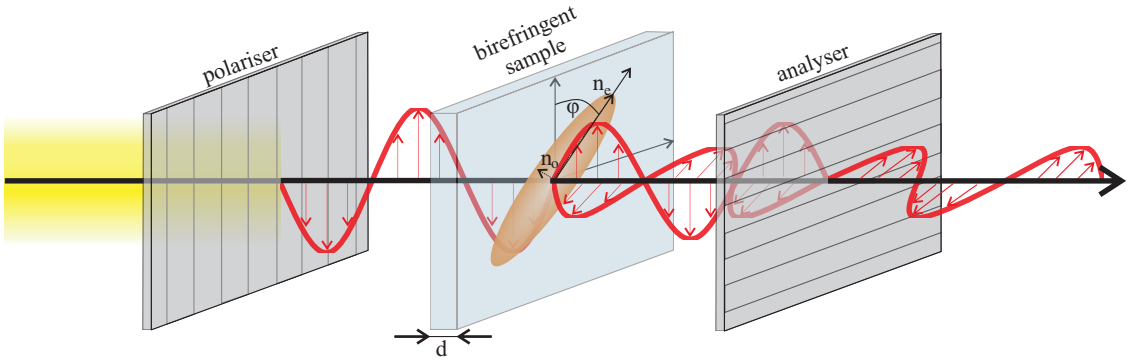


Figure 2.7: Transmittance of light through a birefringent sample between crossed polarizers. From left to right. Light is being polarized by the first polarizer which then passes through the birefringent sample. Depending on the angle of the optical axis towards the polarization axis light is retarded and some light can therefore pass through the second polarizer, called an analyzer.

As mentioned, the birefringence measured by the light is dependent on the orientation of molecules. For instance, a sample with nematic molecules pointing in the direction of light propagation would behave as effectively having only one refractive index and therefore act as an isotropic medium. This position would completely block the transmittance of light, since nothing happens to the polarization of light. On the contrary, if the sample is placed in such a way that nematic molecules point perpendicular to the propagation direction of light, the refractive index observed would be a combination of the ordinary and extraordinary indices depending on the angle between the optical axis and polarization. Using Eq. 2.19, we can calculate the transmittance of an optically uniaxial slab of oriented nematic LC as [43]

$$I_{out} = \frac{I_0}{2} \sin^2(2\Phi) \sin^2\left(\frac{\pi(n_e - n_o)d}{\lambda}\right). \tag{2.26}$$

Here I_0 represents the incoming light intensity, Φ is the angle of the LC molecules towards the polarization axis of the incoming light and the term $\frac{(n_e-n_o)d}{\lambda}$ represents the phase retardation between the ordinary and extraordinary wave. The latter is the measure of how much a certain distance of a birefringent material changes the polarization of light. From Eq. 2.26 we can see that the maximum transmittance will occur at an angle of $\Phi = 45°$. Optical retardation is one of the main tools for experimental observation of LC media. By locally varying transmittance one can simply determine the orientation of LC molecules inside LC samples.

2.3 Topological Defects in Nematic Liquid Crystals

In Section 2.1.3 we considered the energy contribution to the system by smooth variations in the director field considering the order parameter $S = const$. The tensorial field describing the orientation of LC can be well defined in each point of space. However, there are situations, where the orientation of molecules cannot be defined at specific points of the space. These special points are called topological defects. They can be stable for topological reasons, however in many cases they appear in oppositely charged pairs, which are metastable and can annihilate into vacuum [2], [3], [47].

Topological defects are the consequence of spontaneous broken symmetry after a phase transition or simply the consequence of the system trying to reach equilibrium. Since symmetry breaking phase transitions are common in Nature, one can observe topological defects in various physical systems, such as vortices in superconductors [6], Helium three [7], [25] and Bose-Einstein condensates [26]. Also, there are ubiquitous defects in magnetic materials [8]–[10] or even in optics, where they emerge as optical vortices [12], [48], [49].

Defect formation after a symmetry breaking phase transition is well described by the Kibble-Zurek mechanism [27], [50]. The mechanism describes the formation of nucleation sites of the ordered phase or proto-domains after the phase transition. As the speed of crossing the phase transition gets faster, small patches of randomly oriented low temperature phase form, called domains. As the system cools, the domains grow and as they start colliding, topological defects in form of points, loops or walls have to form due to the mismatch of orientation in between the domains. Later domains grow through the process of coarsening dynamics eventually leading to the minimum energy ground state.

Due to the influence of external fields or confinement of the systems, such as the shape of the enclosure, the ground state will sometimes require or even stabilize topological defects. For instance, take a large sphere, of a nematic liquid crystal. If we set perpendicular boundary conditions on the surface of the sphere one sees that the molecules will point to a common point in the middle of the sphere where the orientation cannot be defined and the singularity forms. Similarly, by inverting the problem, such that we place colloidal particles with well defined surface boundary conditions into the LC, the system is forced to form additional topological defects to neutralize the singularity imposed by the presence of the colloidal particle [1], [51], [52].

Let us now continue with the case of the simplest liquid crystal phase, the nematic phase. As the Greek translation of the nematic, strings, imposes a conventional texture or schlieren texture, observed from a nematic LC as string like, as seen in 2.8. Differently colored regions in the polarization image correspond to different orientation of the nematic molecules. And since topological defects have undefined orientation, they can be simply observed as dark regions [1], [53]. The dark brushes like line leading away from

the topological defects are accounted by regions of nematic molecules oriented towards the polarization axis.

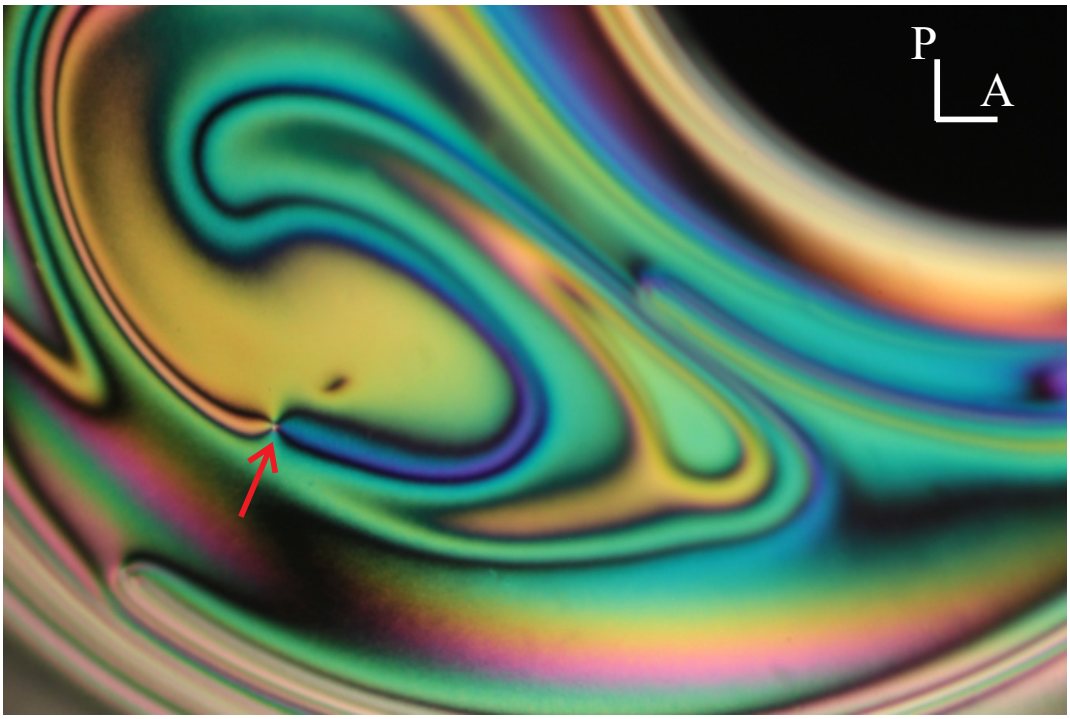


Figure 2.8: Schlieren texture of a nematic LC as seen under polarized light. The red arrow marks a region of undefined orientation of nematic molecules called a topological defect.

Topological defects in nematic liquid crystal are characterized in two dimensions by their winding number or in three dimensions by their topological charge [5], [51], [52], [54], [55]. In the case of a nematic LC confined to two dimensions, or by simply observing a cross-section of a complex three dimensional structure of a nematic, we characterize the effect of the topological defect on the surrounding. This is done by counting the number of turns the director field makes as we encircle the defect core once clock-wise. This number is defined as the winding number, and it can be written as [52]:

$$k = \frac{1}{2\pi} \oint \frac{d\varphi}{dl} dl, \tag{2.27}$$

where φ is the local orientation of the director with respect to the local tangent at a selected point on the closed path. By counting the number of turns we can observe that the number of turns corresponds to half and full integer windings. Also since the director can wind clock and anti-clock wise, there can be + and - winding numbers. Typical examples of topological defects in nematic LC with winding numbers of $+1$, -1, $+1/2$ and $-1/2$ are shown in Fig. 2.9.

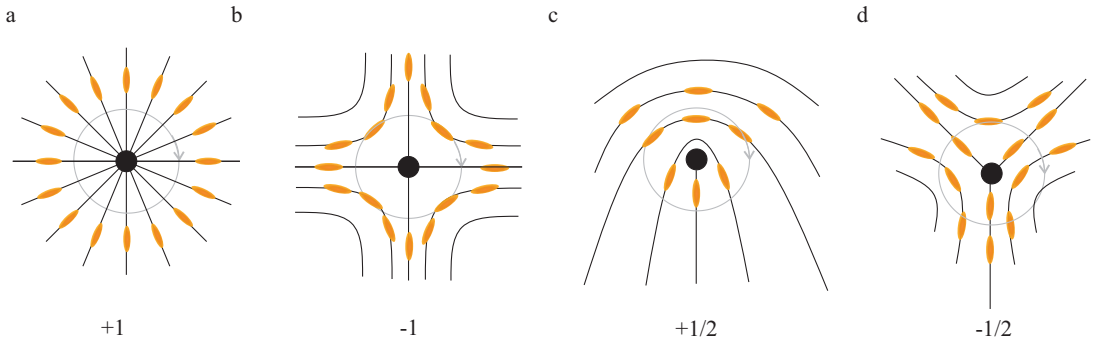


Figure 2.9: Schematic representation of the winding number of topological defects. **a,b** Defects with full integer winding and **c,d** half integer winding.

Here an integer winding number typically represents a cross-section of a 3D point defect, where the director field around the defect core can be radial, circular or hyperbolic hedgehog. On the other hand half integer winding numbers typically correspond to the cross-section of a disclination line in a nematic. Also higher integer winding numbers are possible, yet since the winding number increases the elastic distortions free energy, they are extremely unstable [1]. Recent observation of highly twisted chiral nematic droplets has revealed their existence [56].

Topological defects can also be characterized in 3D. Similar to the characterisation and measurement of electric charges in electrostatics, we measure the topological charge of a defect in 3D by constructing closed Gaussian surface, which embraces the topological defect. The director field plays the role of the "streamlines" and we measure the director flux through the closed Gaussian surface. The topological charge q is then defined as

$$q = \frac{1}{4\pi} \oiint n \cdot (\partial_\theta n \partial_\varphi n)\, d\theta d\varphi, \tag{2.28}$$

Here θ and ϕ represent the spherical coordinates. Contrary to the winding number, a half integer topological charge has no meaning in 3D. For instance, only two possible configurations of point defects have been observed, a radial configuration and a hyperbolic one, corresponding to charge of $+1$ and -1 respectively [52].

Yet, unlike the simple determination of topological charge of a free standing point defect, topological defects surrounding more complicated objects require an understanding of the impact of the shape or topology of the object. Therefore, we rely on the homotopy theory to describe the impact of the topology on the formation of topological defects.

First, we have to classify the object, we include in the field. For each closed surface, such as the surface of a sphere or torus enclosed in the nematic medium, where the nematic field always points perpendicular to the surface, there is a topological invariant called the Euler characteristics that describes the surfaces, fundamental properties regardless of the smooth transformation changing its shape. The Euler characteristics can be determined by counting all the numbers of vertices V_t edges E_d and faces F_c of the surface [57] as

$$\chi = V_t - E_d + F_c. \tag{2.29}$$

The Euler characteristic solely depends on the total curvature of the surface, which can be calculated by measuring the local curvature at each point of the surface and summing the curvature along the closed surface. We define the Gaussian curvature at a given point on the closed surface by multiplying the radii r_1 and r_2 at each point of the surface dS,

thus defining the Gaussian curvature $\kappa = r_1 r_2$. Next we sum the total Gaussian curvature over the enclosed surface by integration as determined by the Gauss-Bonet theorem

$$2\pi\chi = \oint \kappa dS = \oiint \upsilon \cdot (\partial_\theta \upsilon \partial_\varphi \upsilon)\, d\phi d\theta. \tag{2.30}$$

Where υ defines the normal of the surface and φ and θ the spherical coordinates. For instance a simple sphere and all its possible smooth deformations have an Euler characteristics of 2 and for a ring or torus or any comparable shape that possesses one hole the value is 0. Topological properties of closed surfaces are therefore directly related (or described) by the "number of holes" or "handles", or in other words its genus. The genus g of the surface is related to the Euler characteristic of the surface by:

$$\chi = 2\,(1 - g)\,. \tag{2.31}$$

Note that smooth deformations of the surface mean deformation that does not introduce or fill any new holes in the surface. For instance, a sphere is still topologically a sphere, as shown in Fig. 2.10 a, even if we smash it to a discus. Even more extreme is the case of a torus, a handle body with genus 1, that can be deformed into a coffee mug while still be considered a torus, Fig. 2.10 b. However, by tearing another hole into a torus or sticking two together, one creates a surface with two holes, a handle-body with genus 2, shown in Fig. 2.10 c.

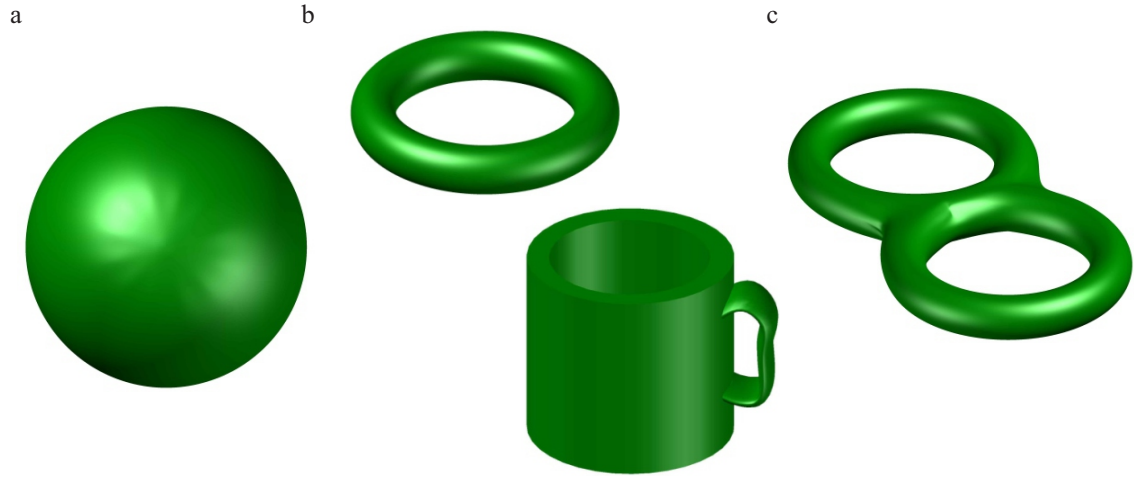


Figure 2.10: Schematic representation of particles with different genus. **I** Sphere of genus 0, **II** Torus and coffee mug of genus 1, **III** Handle-body of genus 2.

Now if we consider a field surrounding the particles, where the field always points normal to the surface, one can determine the topological charge enforced by the surface by first assigning a direction to the field and then counting the total number of times the orientation of the field visits each possible direction in space. This can be done in the case of the director field normal to the surface of the structures by integrating the Jacobian of n(r) over the surface

$$m_c = \frac{1}{4\pi} \oint \cdot n \cdot \left[\frac{\partial n}{\partial \theta} \times \frac{\partial n}{\partial \varphi} \right] d\theta d\varphi. \tag{2.32}$$

Since the director field is always perpendicular to the surface, the integral simplifies to its Gaussian curvature divided by 4 π, due to the 4 π quantization of the Gaussian curvature.

$$m_c = \pm\frac{2\pi\chi}{4\pi} = \pm(1-g). \tag{2.33}$$

Considering that at a point far away from the surface, the field has to be homogeneous, the system has to create additional topological defects close to the surface to compensate the imposed singularity. In mathematical terms this can be expressed as

$$m_c + m_d = 0 \tag{2.34}$$

where m_c is the total charge imposed by the surface and m_d the compensating charge. To sum the previous derivation the Euler characteristics and therefore the genus or total charge of all holes of a particle define the number of the topological defects accompanying the particles as

$$m_d = \mp\frac{\chi}{2} = \mp(1-g) \tag{2.35}$$

Note that the topology of the confinement or inclusion dictates only the total topological charge of topological defects, it does not dictate their type. For instance, the inclusion of small spherical particles into a nematic LC forces the medium to compensate the newly created charge by the creation of any odd number of topological defects with total topological charge of -1. This can be done by a single point hyperbolic point defect (Fig. 2.11 a) or a loop with half integer winding number (Fig. 2.11 b).

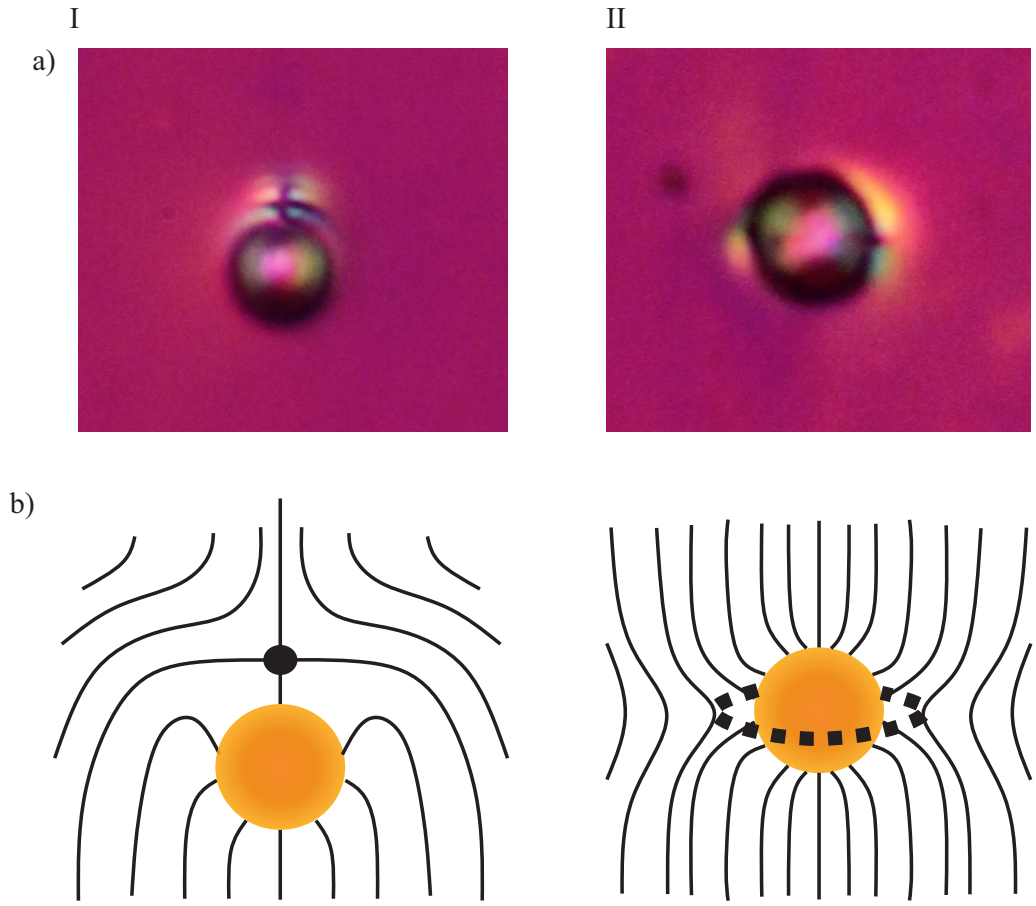


Figure 2.11: Typical topological defect configurations surrounding spherical colloids. **a,b** Experimental images and **c,d** schematic representations of the director field. Point defect left and Saturn ring defect right.

Both configurations are possible, yet the choice of which configuration will appear is strongly influenced by the confinement. In tight confinement, where the thickness of the sample is comparable to the particle size, the loop configuration is preferable and contrary to thick samples the loop can be shrunk down to a point defect, making this configuration preferable [58].

Increasing the complexity of the topology of the confinement [59], [60] or the immersed particles [14], [61] creates a large number of new defect configurations. For instance, a toroidal particle of genus 0 enforces a negatively charged defect inside the hole of the torus and a positive defect on the outside. Yet, the type of the defect strongly depends on the far field orientation of the particles. For instance, in a homeotropic cell where the far field orientation of the director field points normal to the torus a loop defect is always preferred outside with $+1/2$ winding number and charge $+1$, as in the case of Fig. 2.12 a,c.I. On the inside the negative charge can be attributed to a hyperbolic point defect with -1 and winding -1/2 or a loop defect with winding -1/2 and charge -1, Fig. 2.12 a,c.II. On the other side if the same particles, are to be placed into a planar cell with nematic director pointing in plane of the torus, we always observe a hyperbolic point defect inside the torus with charge -1. On the outside, on the opposite side to the point defect,

two distinct configurations can be observed, in the first a loop with winding +1/2 forms Fig. 2.12 a,c.III, and in the other a point defect with charge +1, Fig. 2.12 a,c.IV. Both configurations compensate the total charge to zero.

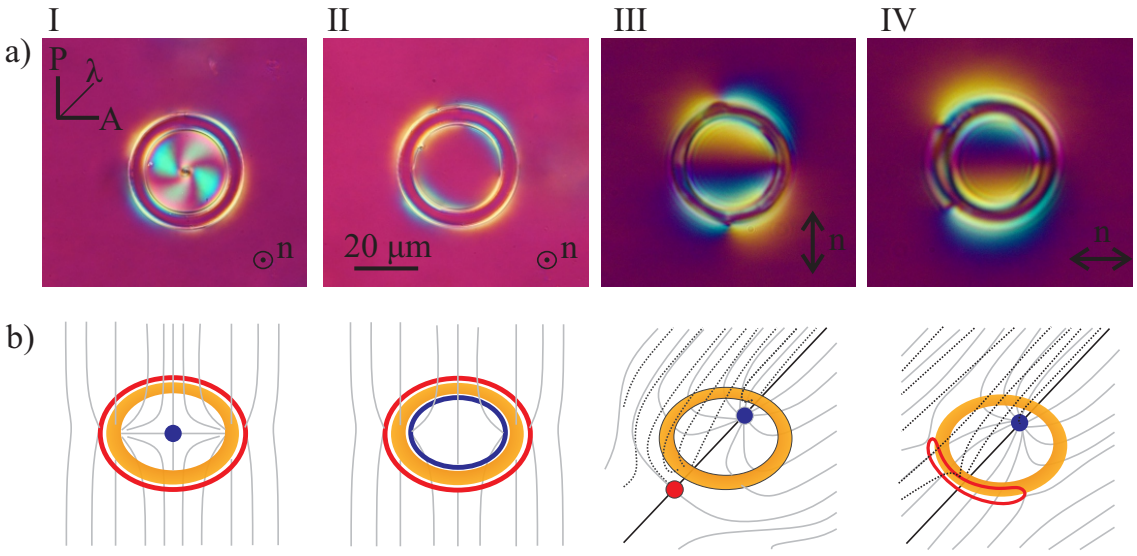


Figure 2.12: Topological defect states surrounding toroidal colloids. **a** Experimental images and **b** schematic representation of the director field of four stable topological defect configurations surrounding toroidal colloids **I-IV**. **b.III-IV** The solid lines depict the director field in the **xy** plane and the dashed line in the **z** plane.

Nowadays optical tweezers have allowed the study not only of stable defect structure but also the mutual interaction of topological defects [16], [19], [62]. For instance, colloidal particles can be tangled to form a crystalline structure that can act as a photonic crystal [17]. Applying an electric field, the crystal can become tunable [18]. By changing the LC medium to a chiral nematic, the defect structure becomes extremely complex. For instance, spherical droplets of a chiral nematic can form highly complex twisted loops and knots sometimes referred to as a zoo of defects [63], or even higher number topological charge defects [56]. Similarly, the inclusion of colloidal particles into a chiral nematic LC forces the defect lines to twist around the particles [15]. Also experimental observation of the entanglement of particles in a chiral nematic shows an extremely complex set of possible configurations, which can be reconfigured using optical tweezers [13].

Recently, the question was asked if the number of topological defects can be increased without breaking the conservation law. This was addressed by the immersion of colloidal fibres into a nematic medium, which act as a spherical particle, in the sense that their charge is compensated by the emergence of a loop surrounding the particle. If now a part of the loop is heated above the phase transition temperature, by optical tweezers, new topological defects can form as a direct consequence of the symmetry breaking phase transition. It was observed that topological defects indeed form, but always in pair of opposite charge, therefore conserving the topological charge of the system [21].

2.3.1 Formation of topological defects after sudden phase transitions

We have already discussed the isotropic to nematic (I-N) phase transition from the field of view of the LdG free energy description. Above the phase transition temperature only the isotropic phase is stable preventing the existence of nematic ordering. As the system cools close to the phase transition temperature, the first-order phase transition nature of the I-N phase transition allows the coexistence of both phases. Sufficiently slow cooling allows the existence of the isotropic phase way below the nematic phase, typically for an additional 1 °C, and below that temperature only the nematic phase is stable. We defined a measure of the degree of ordering, an order parameter in Eq. 2.2, that is zero in the completely disordered isotropic phase and rapidly increases at the phase transition [1], [2], [31]. A non-zero value of the order parameter reveals a certain preferred direction in the system, hence breaking the symmetry.

Yet, this is only true for sufficiently slow cooling rates, where the system has enough time to thermally equilibrate and reach thermodynamic equilibrium. If the cooling rate is sped up, the system reaches a regime, where it can no longer equilibrate fast enough and thermal equilibrium is never reached. If the cooling speed is sufficiently large, the dynamics of the order parameter starts to lag behind the imposed changes and therefore the system stops being adiabatic. Effectively the order parameter dynamics, in the sense that temperature changes are so fast that the out-of-equilibrium dynamics is much slower, the system looks "frozen" in time. Only after a certain time after the phase transition the dynamics can catch up and the system unfreezes. At this point small patches of a few molecules, that were oriented by thermal fluctuation in the isotropic phase, act as nucleation sites for the formation of the low symmetry phase. Additionally, depending on the crossing speed of the transition, the amount of time the dynamics of the order parameter lags behind the imposing changes, called the freezing time, varies. The process is observed in several systems with rapidly symmetry breaking phase transition, and is called the Kibble-Zurek mechanism [27], [50]. After the initial formation of domains coarsening dynamics takes over. It describes the growth of the domains, their merging and finally their annihilation into the stable ground state.

2.3.1.1 Kibble-Zurek mechanism

Topological defects are the direct consequence of symmetry breaking phase transition. When cooling from a highly disordered phase, localized patches of the ordered phase form, therefore breaking the symmetry. In the 1970s Kibble described the formation and structure of topological defects after a sudden symmetry breaking phase transition [27]. He based his idea on the example of the fastest known phase transition, the Big Bang and the creation of the universe. He showed that for a sufficiently rapid phase transition from a disordered to an ordered low symmetry phase, randomly oriented domain structure forms with topological defects occurring as bounding walls. Later Zurek incorporated the idea of strong cooling rate dependency on the formation of the domains [50], thereby coining the term Kibble-Zurek mechanism.

We chose the isotropic to nematic phase transition as an example of a symmetry breaking phase transition. The transition is strictly speaking of first order, i.e. it exhibits latent heat, co-existence of both phases and sudden drops in values of characteristic properties at the phase transition. Yet due to the relatively small value of the latent heat the transition is said to be weakly first order and can be described as continuous phase transitions [64]–[66]. We use the example of the isotropic nematic phase transition to describe the Kibble-Zurek mechanism in detail.

We start of by a nematic LC above its phase transition temperature. The LC is com-

pletely symmetrical and the molecules are completely disordered, thus the order parameter is zero. Whereas the equilibrium order parameter is zero, we have strong fluctuations of the order parameter around the zero value. These fluctuations are rapid, with a typical thermal relaxation rate (i.e. lifetime) of a microsecond. As the system suddenly begins to cool the thermal relaxation time can no longer follow the fast dynamics of the cooling and therefore the system ceases to be adiabatic at a time called the Zurek time t_z before the phase transition temperature. At this point the system crosses into the impulse regime where the dynamics effectively remains frozen [29], [67]–[71]. After the phase transition the system still lags behind the cooling and only after a certain time t_z the system resumes to be adiabatic. This can be seen in the time dependence of the relaxation time of the order parameter, as seen in Fig. 2.13. Additionally, the speed of the transitions is defined by the quench rate τ_q, this is the time the system cools from the phase transition value to zero [65].

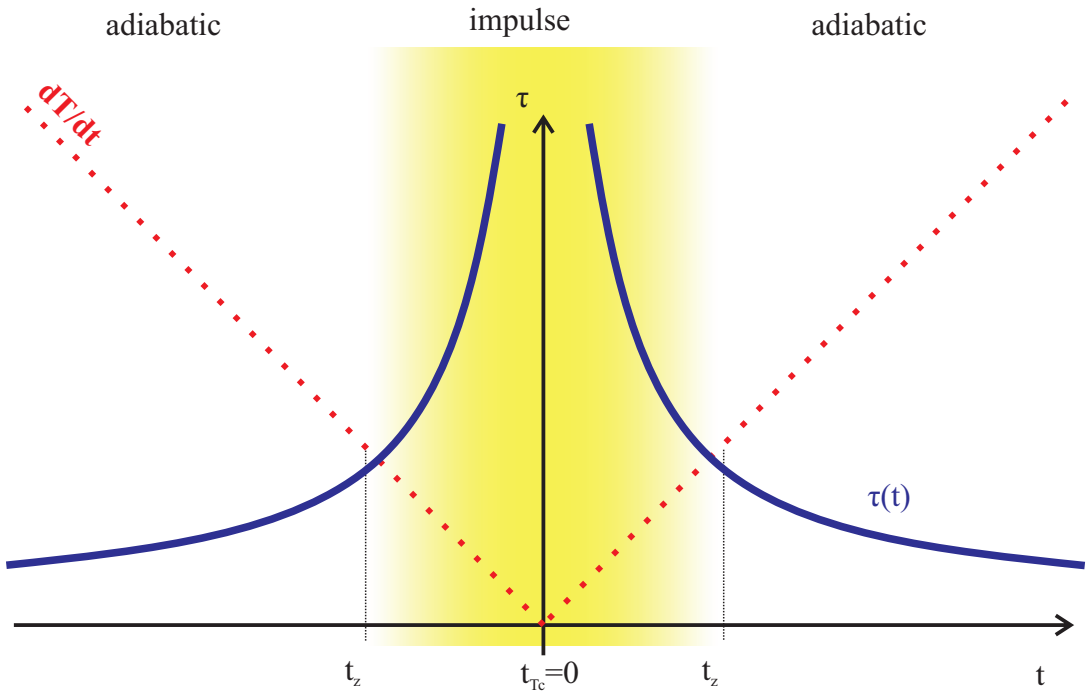


Figure 2.13: Schematic representation the time dependence of the relaxation of the order parameter shows the critical slowing down of the order parameter at the phase transition. The red line represents the linear cooling imposed on the system dT/dt and the blue line the response of the system $\tau(t)$. At point t_z called the Zurek time, the order parameter dynamics starts lagging behind the imposed changes and the system stops being adiabatic and enters the impulse regime. Within the impulse regime the fluctuations are "frozen in time". This is because the thermodynamic restoring force for these fluctuations is very weak, because the free energy landscape is very flat close to the transition.

While the system is effectively frozen, individual thermal fluctuations force a certain random amount of molecules to act as nucleations sites from where order can spread. Inside those patches the order parameter increases from its nucleation value S_f to its equilibrium value reached at t_z as

$$S = S_f e^{t/\tau_q}, \tag{2.36}$$

where τ_q represents the quench rate, calculated as a linear approximation at the cooling speed at phase transition dT/dt. The exponential growth of the order parameter is due to the shape of the free energy landscape in the nematic phase with two local minima at $+ - S_0$. Any fluctuation with a small value of the order parameter will rapidly gain the order and approach local minimum of S. The time scales of the process are determined by the basic characteristics of the material used, its relaxation time τ_0 and the quench rate as

$$t_z = \sqrt{\tau_0 \tau_q}. \tag{2.37}$$

At t_z individual stable proto-domains are formed that possess the equilibrium order parameter. Their size again depends on the material characteristics and the quench rate

$$\xi_p = \xi_0 \left(\tau_q/\tau_0\right)^{\frac{1}{4}}. \tag{2.38}$$

At this point the increase of order parameter is reflected in an increase of birefringence, making the domains observable.

We can look at the Kibble-Zurek also from the view of thermal fluctuations. Any system exhibits thermal fluctuations corresponding to its temperature. For instance, typical thermal fluctuations in the isotropic phase are of order of MHz, or in other words any fluctuation in the orientation of the molecules will annihilate in approximately a micro second. Now, if we cool the system slowly through the phase transition, the thermal fluctuations always have time to annihilate and the system is always in thermal equilibrium. If the speed of the cooling is fast enough in comparison to the thermal fluctuation speed, the orientation of the fluctuation effectively freezes. Additionally, as the fluctuations freezes the temperature drops below the phase transition temperature corresponding to the cooling rate.

Considering the typical time scale of thermal fluctuations in LC we can now predict a limit of cooling rate that allows the observation of the Kibble-Zurek mechanism. For the case of the first-order phase transition like the IN transition we have a coexistence band of approximately 1K. Therefore, the cooling rate has to be sufficiently fast to drop the temperature from the phase transition through the coexistence band in less than 1 micro second, accounting to cooling rates of at least $1\,\mathrm{K}\,\mu\mathrm{s}^{-1}$. In the case of a second-order phase transition no coexistence band exists and therefore the phase transition occurs instantaneously. Yet, a slowing down of the thermal fluctuations as the phase transition is approached is expected. Again slow cooling rates will enable the long wavelength fluctuations to freeze and survive and fast cooling rate the short ones.

We can determine, that the extreme times scales and cooling rates make the Kibble-Zurek mechanism extremely difficult to experimentally study. Only a few experimental observations were performed in all physical systems combined, because cooling rates of up to $1\,000\,000\,\mathrm{K/s}$ are requested, as seen for instance in the review of del Campo and Zurek [70]. Let us mention just the most interesting experimental work in this field.

One of the earliest experimental works was done by Ruuntu et al. where they studied the formation of vortices as liquid ^{3}He is rapidly cooled through the super-fluid transition temperature [7]. Ulm et al. performed Kibble-Zurek experiments and quantum simulations on the scaling on excitation of a single Calcium ion undergoing a quantum phase transition [72]. Lamporesi et al. reported on a power law dependency of the number of solitons

produced with increasing quench rate, therefore obeying the Kibble-Zurek mechanism [73]. The final experimental work in this field is the study of the evolution of crackling noises formed after rock deformation and connecting it to the macroscopic defect structure in the material [74].

Additionally, many works report on so-called experimental simulations. The works rely on extensive computer simulations that use real experimental parameters to test outcomes of experiments, which are in reality numerical simulations. The complex nature of real experiments makes them virtually impossible to recreate using computer simulations, hence the use of several approximations in the works. Some notable cases of simulations experiments are: the study of the KZ scaling law in momentum space using experimental trapping of ions through quantum simulations [75], spontaneous generation of Bose Einstein condensates inside a toroidal confinement [76], quenches in super-fluid phase transitions simulated using the 1D Bose-Hubbard model [77]. And finally simulations base on the Ising model in ferromagnet describing entropy formation in critical systems [78].

Claims of the KZ scaling law observations in various LC system have been made in the past. The typical experimental conditions are set so that the LC sample is heated a slightly above the phase transition temperature, where thermal fluctuations slow down up to the kHz range and then rapidly cool down the system for a small amount. Thereby, the long wavelength fluctuations survive the temperature drop and can form nucleation seeds for nematic domains [79]–[81].

Typical cooling rates reported are below one degree per second, therefore the system never goes out of equilibrium. Hence the system never ceases to be adiabatic and the Kibble-Zurek mechanism can-not be tested. The processes reported are a case of domain formation after equilibrium transition due to the first-order nature of isotropic nematic phase transition.

The only known experiments that achieved rapid phase transition from the isotropic to the nematic phase were reported in the early 90's by Snyder et al. [22], where they used pressure-induced quenches of extremely thick (450 µm) samples to achieve a phase transition in under 8 ms as reported. A pressure difference of 7 MPa was used which roughly correlates to a quench rate of approximately 1 second. An extensive light transmission study and a subsequent microscopy study revealed two distinct regimes of coarsening dynamics in the time scales from 10 ms - 100 ms. For the early regimes up to the first second they observe diffusion of the transmitted light by random walk process, indicating the formation of nematic domains in the sample. At later times, the transmission starts to obey a power law dependence indicating coarsening dynamics as seen in Fig. 2.14.

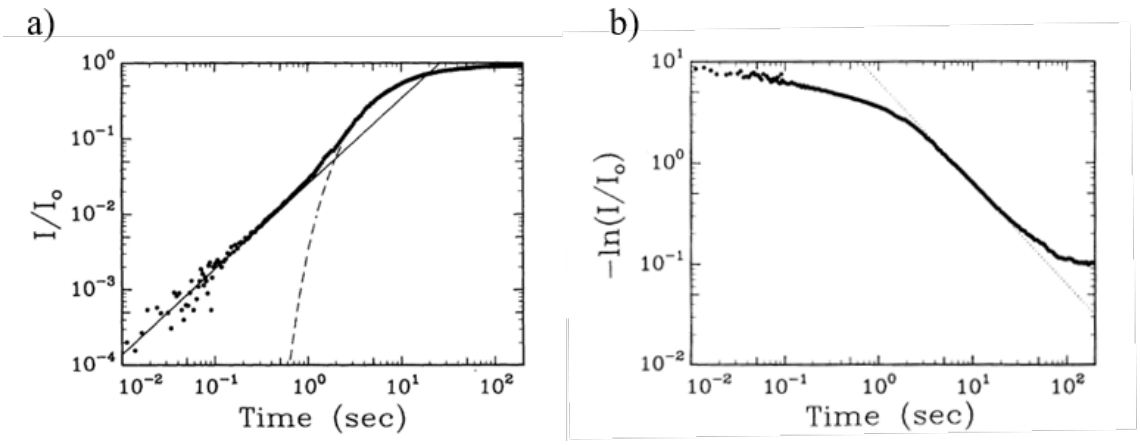


Figure 2.14: First experimental observation of coarsening dynamics in LCs. Performed using light transmission study of thick LC samples. a) Time dependence of the light transmission in the log-log scale (scatter plot) with a solid line fit with a slope of roughly 1. The dashed line corresponds to the late time dependence t^{-1}. b) A significant change in the slope of the transmission signal at time greater than 1 second indicates the late time coarsening dynamics with a corresponding fit slope of -1, dashed line. Reprinted from [22].

2.3.1.2 Coarsening dynamics

In the previous section we described the formation of domains as a result of the rapid passage through the symmetry breaking phase transitions. We saw that as we cool the system rapidly below the phase transition temperature, thermal fluctuations orients small patches of molecules that start to act as nucleation sites. As the temperature drops, the lower symmetry phase starts to form at those nucleations sites forming domains. Due to the waste speed of the cooling, the domains are completely randomly oriented. With further cooling the domains grow forming a dense tangle. As they start touching, they form topological defects, due to the miss-match of their orientations. Therefore, forming a vast array of topological defects that through a process of coarsening dynamics annihilate to form the stable and uniform ground state.

For nematic liquid crystal one can assume the defect formed are disclination lines with a winding of 1/2. We can now describe the coarsening of the defect lines by a handwriting introduction to nematodynamics [1], [82]. The relaxation of the nematic director field can be described by a one-parameter approximation as:

$$\gamma \frac{\partial n^a}{\partial t} = \kappa \left(\nabla^2 n^2 + \left(\nabla n^b \right) \left(\nabla n^b \right) n^a \right), \tag{2.39}$$

where $n^a = n^a(x, y, t)$ represents the director three component field. γ and κ are the rotational and viscoelastic constants. Next we describe disclination lines as simple loops with line tension T and damping Γ and a single length scale ξ. The whole tangle of disclination lines is described by the line density of defect loops as the characteristic length scale per unit volume as $\rho = \xi^{-2}$. We can combine the rate of the loss of energy to the time derivative of the line tensions as [82]

$$\frac{d\rho}{dt} = -c \frac{T}{\Gamma} \rho^2, \tag{2.40}$$

where the time derivative of the density of the disclination lines is correlated to the power of two on the total defect density.

Integrating Eq. 2.3.1.2 we obtain the scaling solution for the line density as:

$$\rho = \left(\frac{\Gamma}{cT}\right) t^{-\nu} \tag{2.41}$$

with ν representing the scaling exponent. This exponent is for the case of a single characteristic length scale equal to one for a nematic liquid crystal. Yet, in real experimental observations it is time dependent due to the changing size distribution of the disclination lines [24].

The light transmission study of Snyder et al. [22] describes the formation of nematic ordering trough a rapid pressure induced phase transition in nematic LC. The distinct change in light transmission behaviour indicates a rapid change in the transmission characteristic and therefore in the ordering of the system. Subsequent microscopy studies [23], [83], [84] confirmed a power law scaling of the coarsening dynamics in nematic liquid crystals.

Chapter 3

Methods and Materials

In this section we explore the materials, experimental set-ups and techniques used in the thesis.

3.1 Liquid Crystals

Liquid crystals can be tuned to interact with light in the optical spectrum that makes them a playground for basic physics research that can be easily studied using various optical microscopy techniques [43]. In this thesis we use several organic compounds which exhibit different LC phases. For instance, one of the simplest and most understood materials used is 5CB (4-cyano-4'-pentylbiphenyl, Nematel) which exhibits the nematic LC phase at room temperature and has a nematic isotropic transition at 35 °C with birefringence of 0.22 in the nematic phase, therefore it enables us to study its interaction with light in a relatively simple laboratory environment. We use a whole range of LC compounds with different clearing points, for instance E18 (Merck), MLC 13300 (Merck) to study the thermal properties of our experimental system. Studying the structure and the properties of topological defects requires the use of LC compounds with lower birefringence which decreases the defocusing of light in the sample. We use two compounds, one is a room temperature nematic 50:50 mixture of CCN-47 and CCN-55 (Nematel GmbH), with negative dielectric anisotropy and the other is MLC 7023 (Merck), also a room temperature nematic but with positive dielectric anisotropy. Basic physical properties of the liquid crystals used are listed in Table 3.1.

Table 3.1: Liquid crystal materials used in the experimental work with typical nematic phase temperature range and birefringence values.

Materials	phase sequence	Δn	$\Delta\varepsilon$
5CB	N $\xrightarrow{35\,^{\circ}\mathrm{C}}$ I	0.18	11
E18	N $\xrightarrow{60\,^{\circ}\mathrm{C}}$ I	0.22	/
CCN-47 & CCN-55	N $\xrightarrow{60\,^{\circ}\mathrm{C}}$ I	0.04	>-1
MLC 13300	N $\xrightarrow{91\,^{\circ}\mathrm{C}}$ I	0.1	6.7
MLC 7023	N $\xrightarrow{35\,^{\circ}\mathrm{C}}$ I	0.06	7.9

3.2 Dyes

For imaging of fast dynamic processes in LC systems we designed a stroboscopic laser illumination system using a concentrated solution of Rhodamine 6G in ethanol to 'convert' coherent laser light into incoherent fluorescent light that can be used for good quality imaging. The mixture has the absorption peak at $\lambda = 532\,\text{nm}$ and emission peak at $\lambda = 550\,\text{nm}$ shown in Fig. 3.1 a. Ethanol is chosen as a solvent, to match the absorption maximum of the solution to the excitation Nd-Yag laser wavelength at $\lambda = 532\,\text{nm}$. The typical concentration used is 11.3 mg of dye per 2.5 ml of ethanol assuring maximum light conversion efficiency.

Fluorescent dyes are also used in contrast enhancing techniques as fluorescence microscopy. We use fluorescence confocal polarization microscopy (FCPM) which uses a combination of low birefringence LC medium and a fluorescence dye that strongly aligns with the LC host such as (N,N'-bis(2,5-di-tert-butylphenyl)-3,4,9,10-perylenedicarboximide) or BTBP [85]. The absorption peak of BTBP inside the LC host is at 486 nm with the emission peak at 550 nm, shown in Fig. 3.1 b. Due to bad mixing of BTBP inside LC we first dissolve the dye into acetone which is then mixed with the LC. Ultrasound is used to mix the LC-dye-acetone mixture, and the mixture is then left overnight to evaporate the solvent at room temperature. Finally, the sample is shortly heated to 90 °C to remove water present in the acetone. The remaining LC-dye mixture is then centrifuged at high speed to remove agglomerates of undissolved dye.

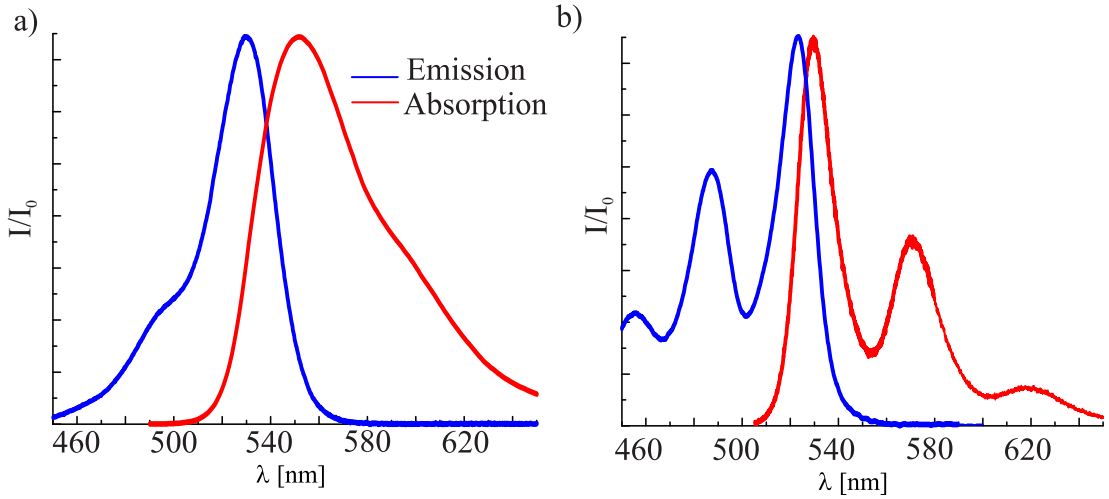


Figure 3.1: The absorption and emission spectra of **a** Rhodamine 6G in ethanol and **b** BTBP in a LC host.

3.3 Liquid Crystal Cells

The properties of LC are mainly dependent on three parameters: the temperature, surface anchoring and external field. We can control all of these parameters by enclosing a small amount of the LC material inside a cell made of two glass plates as shown in Fig. 3.2 a.I-II. We use ITO-coated thin glass substrates with a thickness of 170 µm (DiamondCoatings). The substrates are first thoroughly cleaned and then coated with a thin alignment layer. The ITO layer thickness is usually in the range of 5-50 nm. We test the thickness of the

ITO layer with the help of atomic force microscopy AFM, which measures the height of an etched gap on the ITO itself, shown in Fig. 3.2 b.I-II.

Enclosed LCs tend to align the same way as the first molecular layer touching the surface. This can be exploited by coating the surface of the glass substrates with a thin alignment layer of either a surfactant like dimethyloctadecyl[3-(trimethoxysilyl)propyl]ammonium chloride DMOAP (ABCR Gmbh) or a polymer with long polymeric chains such as Polyimide 2255 (Nissan chemicals) which create either homeotropic or planar alignment of the LC through the volume of the sample [41], [86], [87].

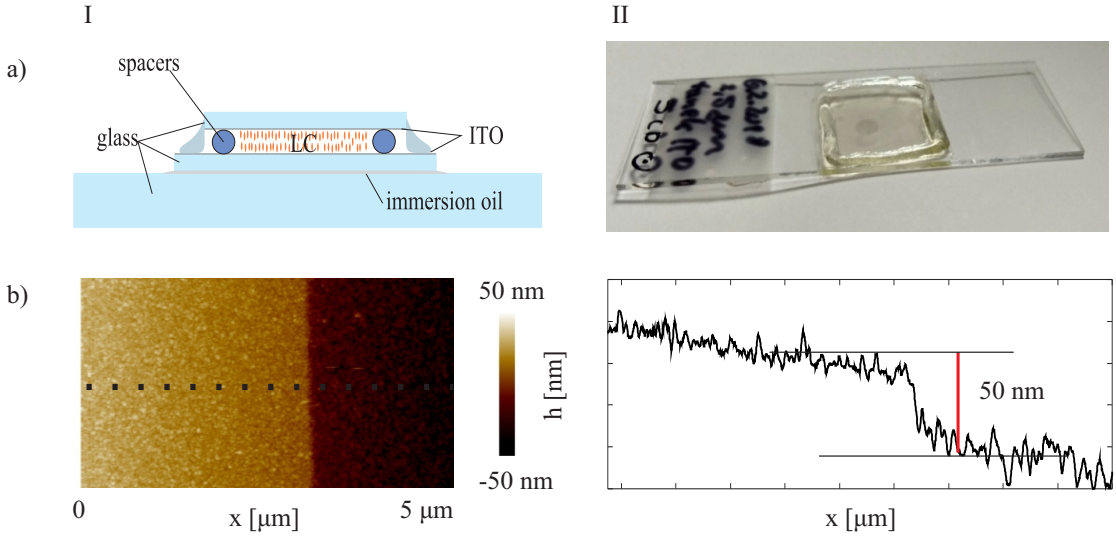


Figure 3.2: **a.I** A schematic representation of a glass cell containing a thin layer of LC. a.II) Photograph of a typical sample cell. **b.I** AFM scan of an etched gap on the ITO surface. **b.II** Measurement of the ITO thickness by image analysis at the marked cross-section.

To achieve a homogeneous alignment of the LC, the substrates are thoroughly cleaned by successive cleaning steps inside ultrasound baths using organic solvents acetone and isopropanol, typically 20 minutes each. The substrates are then placed inside an isopropanol alcohol degreaser and left to cool to room temperature. Before use, they are placed into an UV-O plasma that burns the remaining organic contaminants and also activates the surface of the substrates.

For homeotropic alignment of the LC the substrates are after the cleaning step placed into a 0.5 % aqueous solution of DMOAP where they remain for 5 minutes. Afterwards they are thoroughly washed with deionized water to remove any remaining DMOAP that did not attach to the surface. The surfactant is then polymerized to the surface of the substrates by baking at 110 °C for 1 hour.

If planar alignment is desired, the substrates are, after the cleaning step, spin coated with a thin layer of Polyimide. The spin coating is performed at 2000 *rpm* for one minute which creates a few nm thick layer of polymer on the surface. After spin coating the samples are placed on a heat plate at 90 °C for 1 minute to evaporate any remaining solvent. To harden the polymer, the coated substrates are baked in an oven at 205 °C for 20 minutes and slowly cooled to room temperature. Unidirectional alignment is achieved on the substrates by rubbing them several times using a velvet cloth. The rubbing with velvet creates microscopic groves in the polyimide into which the LC molecules align into.

Eventually sample cells are assembled by placing two prepared ITO cover slips on top of each other with glass beads sprinkled on top of one to act as spacers. The cells are

then filled with the LC sample using capillary force and glued shut with epoxy glue. The sample cell is then adhered to an objective glass plate. An immersion oil is used as the glue to minimize refractive index miss-matching through the sample.

3.4 Photo-resists

Photo lithography is used to obtain colloidal particles of various shapes. This process uses a liquid mixture of monomer, solvent and photo-initiator to produce polymer particles of any desired shape. The mixture is called a photo-resist which in our case are commercially available IP-G, IP-L, IP-Dip (Nanoscribe GmbH, typical use shown in Table 3.4. After the exposure to light the exposed part of the photo-resist becomes completely insoluble inside a chosen solvent. By subsequent washings in the solvent the unexposed resist can be therefore removed. We use a commercially available SU-8 developer (MicroChem) where typically only two short washings steps of 10 minutes are required to remove all of the unexposed resist.

Table 3.2: Basic properties and preparation techniques of negative tone photo resist used.

Materials	Structure	Preparation	Printing technique
IPG	Gel like	drop casting - pre-bake	Oil immersion technique
IPL	Liquid	drop casting	Oil immersion technique
IP-dip	Liquid	drop casting	Dip-in technique
SU8	Liquid	drop casting	Oil immersion technique

3.5 Two-photon Laser Lithography

Photo lithography is performed using our two-photon lithography machine Photonic Professional (Nanoscribe GmbH). The machine is built around an inverted Zeiss Microscope with a 150 mW laser with high frequency pulses with a duration of 100 fs at wavelength $\lambda = 780\,\text{nm}$. The laser light is focused using a 100x 1.4 NA oil immersion objective where the volume, at which the polymerization threshold is reached, called the voxel, can be sub 200 nm in the $x - y$ plane perpendicular to the optical axis of the objective. The effective two-photon wavelength inside the voxel is $\lambda = 395\,\text{nm}$ which triggers the photo-chemical polymerization of the photo-resists.

In contrast to one photon laser lithography Fig. 3.3 a, where all of the illuminated photo-resist is polymerized, two-photon polymerization only occurs above a certain energy threshold in a desired volume in the sample. Depending on the requirements and size of the sample being produced, the machine can be used in two different configurations. Firstly, dip-in laser lithography, or DILL for short, uses the photo-resist itself as the immersion liquid between the objective and the substrate. This enables us to print high resolution structures since the laser light is focused inside the photo-resist itself and it does not need to be passed through the substrates Fig. 3.3 b. This eliminates defocusing due to the refraction of light on the transition between media with different refractive indices and the height of the structures is only limited by the z-plane position of the objective. Therefore, any substrate material can be chosen. The draw-back of DILL is the print of structurally demanding structures, such as hollow objects, which requires the use of either a supporting scaffold or the use of a gel-like material which due to its own stiffness supports the structure while printing. In that case a conventional direct laser writing (DLW) method

is used. This method requires the use of transparent substrates and oil immersion liquid to limit defocusing due to refractive index mismatching Fig. 3.3 c. The height of the object is strongly limited by the working distance of the objective and absorption of laser light on already polymerized resist since the printing process typically starts at the substrate.

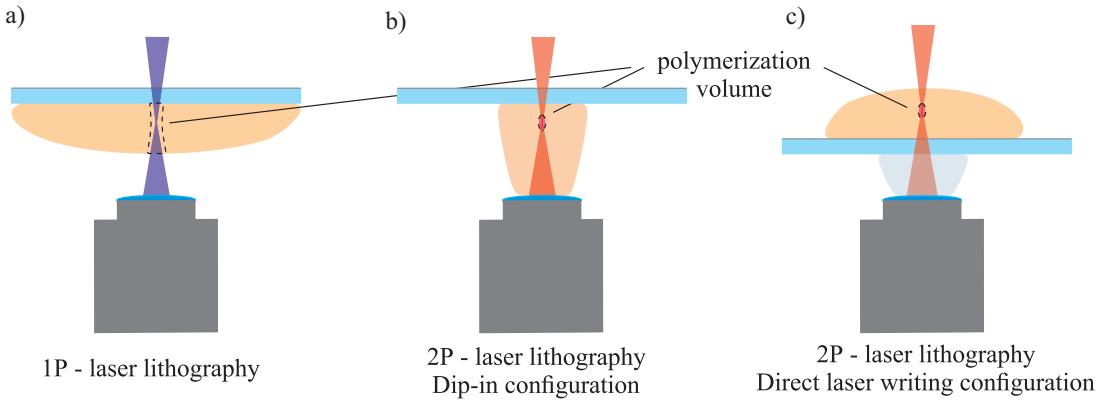


Figure 3.3: Schematic representation of various lithography processes. **a** Conventional laser lithography where all the illuminated photo-resist is polymerized. Two-photon laser lithography is used to expose a small volume of the illuminated photo-resist. The process can be done in the dip in **b** or in the direct laser writing **c** configuration.

To achieve the maximum resolution of the printing process, we use 170 µm thick cover glasses which were thoroughly cleaned by successive cleaning steps with multiple organic solvents and the use of a plasma treatment.

For structures which require structural support during the printing process, we use the DLW method and the gel-like IP-G photo-resist. During the preparation the substrates are covered by the photo-resist and pre-baked at 80 °C to remove most of the containing solvent and then placed onto the machine's sample holder. Immersion oil is used to achieve an optical contact between the oil immersion objective and the substrate glass. The printing process starts at the substrates which makes the particles adhere to the substrate so they do not wash off when developing. To maximize the running time several particles are printed in a predetermined pattern at the same time. A pattern, made form colloidal tori in nematic LC, in the shape of the JSI logo, is shown in Fig. 3.4.

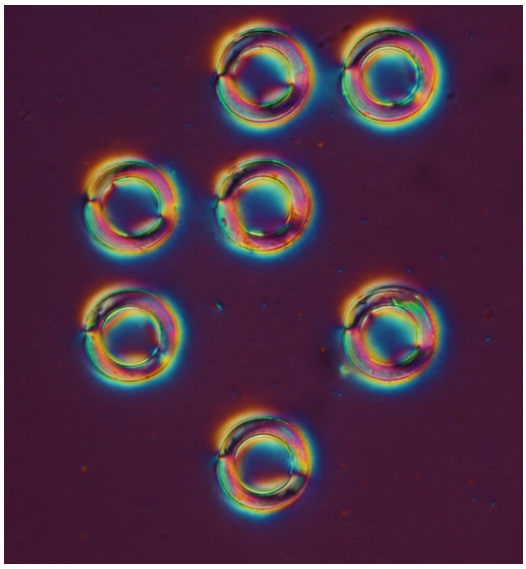


Figure 3.4: Printed colloidal tori in nematic LC in the shape of the JSI logo - the Stefan constant σ.

After printing, the remaining unpolymerized resist can be simply washed off by dipping the whole sample into a commercially available SU-8 developer. The developing step consists of two 10-minute baths in the developer. Additionally, we perform another 5-minute cleaning with isopropanol which removes all traces of the developer.

The colloidal particles prepared by the printing process are then surface-treated by DMOAP to achieve strong homeotropic alignment. The particles are then removed from the surface by detaching them one by one into a LC medium which is then transferred into the desired sample cell.

3.6 Polarization Optical Microscopy

Polarization optical microscopy was extensively used in this thesis. The basic set-up uses a conventional inverted microscope Nikon Eclipse Ti-DH which is equipped with an illumination source, polarisation optics, imaging optics, additional optional laser optics and an imaging camera, shown in Fig. 3.5 a with schematical drawing in Fig. 3.5 b. Firstly, a bright field Kohler illumination system light source is used, which enables the homogeneous illumination of the sample in the imaging plane. The illumination source can be either a LED with a narrow spectrum, a halogen lamp with a wider spectrum or a pulsed fluorescence dye illumination system with extremely narrow spectrum and short bright illumination pulses. In our case we typically use either a 250 W halogen lamp for statical experiments or a nanosecond pulsed illumination system for dynamical experiments. Additional polarization optics is placed just before and after the sample, to determine the change of polarization due to the optical birefringence of the sample [88]–[90]. The imaging optics consists firstly of a 1.4 NA Nikon Plan Apo 100 x oil immersion objective with 130 µm working distance, which collects the light from a desired part of the sample and then magnifies the image by a factor of 100. The light rays leading from the objective are parallel and therefore additional flat optics can be added without distorting the image. We use a custom Nd:Yag laser line mirror (AHF GmBH) to introduce additional laser light into the optical pathway which only reflects Nd:Yag laser light and transmits up to 99.9 %

of the remaining spectrum. The last part is a combination of a condenser lens and an adjustable mirror that focuses all the transmitted light and forms the image of the sample viewed onto an imaging plane into which we place the sensor of the detector. We use several different detectors from a simple photo diode, spectrometer, CCD camera to a high resolution sCMOS camera. The photo detectors will be presented by their appropriate use in experiments later.

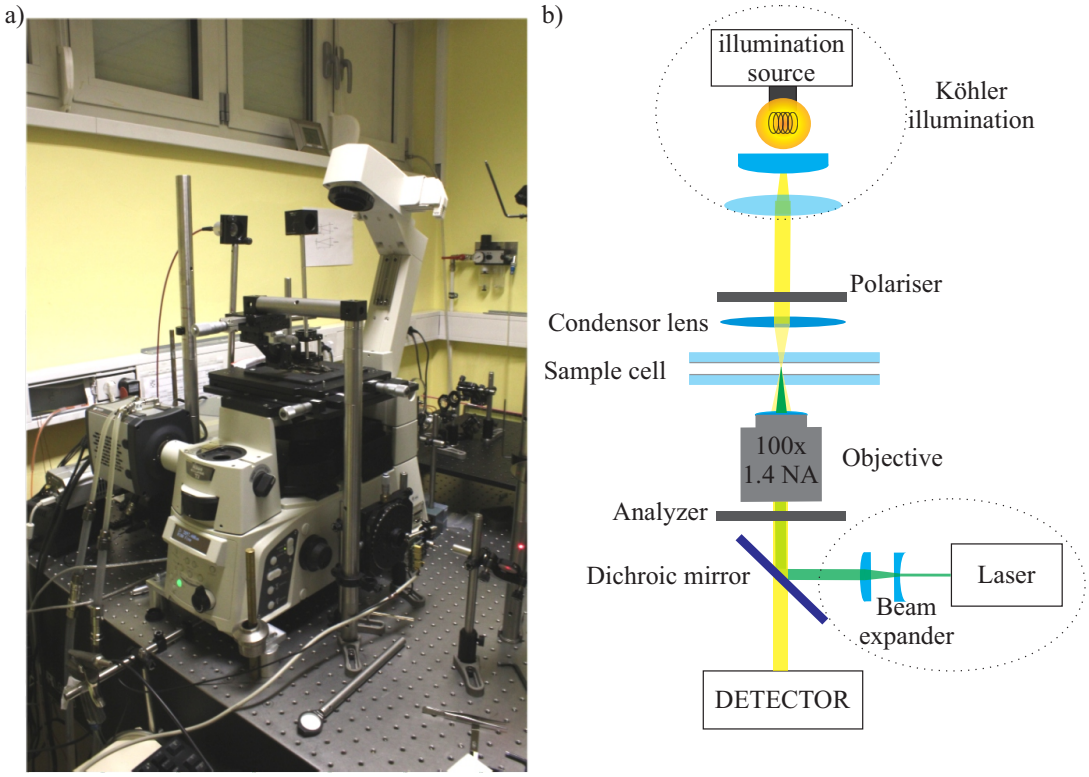


Figure 3.5: Polarization optical microscopy set-up. **a** POM set-up build around a Nikon Eclipse Ti microscope with the corresponding schematic representation of the basic set-up **b**.

3.7 Fluorescent Confocal Polarization Microscopy

In addition to conventional bright-field polarization microscopy, we use fluorescence confocal polarization microscopy FCPM built around an upright confocal microscope Leica TCS SP5 X, shown in Fig. 3.6 a. The system is based on a common confocal set-up using a pinhole in the confocal plane of two sets of lenses, which removes the out-of-focus light from the imaging plane, as shown in Fig. 3.6 b. The system consists of a white light pulsed laser with a continuous visible light spectrum, produced by a photonic fibre. An acousto-optic transmission filter is used to selectively pick a desired narrow spectral range for illumination (1-2 nm). We use the 488 nm spectral line which coincides with the absorption maximum of the solution of LC host and BTBP dye mixture [85], [91]–[93]. Before the sample, we first place a wave plate for 486 nm (Thorlabs) to achieve circular polarization of the initial linearly polarized laser light, and second, a linear polariser allowing us to only illuminate the sample with a desired polarisation of light. The sample is

illuminated using a 63x 1.3 NA oil immersion objective which allows the lateral resolution around 200 nm. A pinhole is used to only excite and detect the light from a small volume of the sample called the voxel. Typical voxel size is 200 nm in the $x-y$ plane and 600 nm in the z direction, e.g. along the optical axis of the objective. A photo multiplier tube was used to detect the light. We scanned the sample at 5 different polarizations and used a custom-developed software to reconstruct the director field [92], [94].

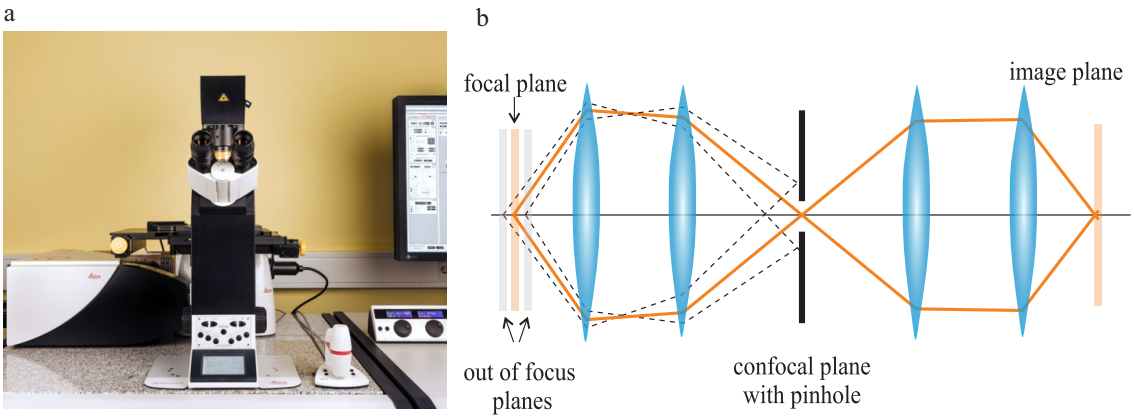


Figure 3.6: Confocal microscope used for FCPM. **a** Microscope set up used for FCPM. **b** Schematic representation of the confocal microscopy, which with the use of a pinhole in the confocal plane of a set of lenses removes the out-of-focus illumination from the imaging plane .

3.8 Nanosecond Illumination and Stroboscopic Imaging Set-up

We build a nanosecond laser illumination system that uses strong 30 ps optical pulses from a Nd:Yag pulsed laser (Ekspla PL2250) and a fluorescent dye solution (Rhodamine 6G in ethanol) to generate light pulses in the nano second range. We use a digital pulse delay generator (DG645 - Standfort Research Systems) to trigger a pulsed Nd:Yag laser. The laser itself is composed of two units: the base unit where 30 ps laser pulses at 1064 nm are generated with maximum 10 Hz repetition rate. The pulses are then guided into the optical harmonic generation unit where using non-linear crystal, the second harmonics at 532 nm is generated.

The light is then guided into a fluorescence dye solution filled cuvette where it is completely absorbed and the dye solution emits high intensity fluorescence light pulses of typical duration 20 ns at peak wavelength 550 nm. Using a 10 mm focal distance lens the light is collected into the fibre coupler (PAFSMA7A-Thorlabs) and guided through an optical fibre to the microscope. Here a 15 mm condenser lens is used to homogeneously illuminate the LC sample cell placed onto the microscope imaging plane.

Additionally a conventional POM system is set up surrounding an inverted Nikon Eclipse TiD microscope. A schematic representation of the whole set-up is shown in Fig. 3.7. To minimize the losses of image quality and intensity, an oil immersion 100x Nikon Plan Apo objective is used. The objective has NA 1.4 and the working distance of 130 µm. Additionally, the set-up consist, of two polarisers and a laser line dichroic mirror (AHF) which only reflects Nd:Yag harmonics 532 nm and 1064 nm and transmits the remaining

spectrum. The mirror is used to introduce additional external laser light into the main optical axis of the microscope allowing us to locally control the temperature of the LC cell with the help of the opto-thermal effect. The transmitted light through the LC sample is then focused on an imaging plane in which we place a highly sensitive externally triggerable camera. We use a sCmos Andor Neo camera with dual pixel amplifiers which allow the high sensitivity and high dynamic range of the image acquisition. The camera can be run in two acquisition modes, a rolling and a global shutter which refers to the way in which data is being read from the sensor. In the rolling shutter mode the data is read line by line in a continuous manner from mid to top/bottom where each line has a delay of a fer microseconds to the previous. The other option is the use of the global shutter where all of the pixel rows are read at once and the whole image is acquired at the same time. The speed of the rolling shutter is too slow for the short illumination pulse of 20 ns, which would only illuminate part of the imaging sensor, therefore, only the global shutter mode can be used. Typically, the camera exposure is set to 25 µs, whereas only the 20 ns pulse exposes the image.

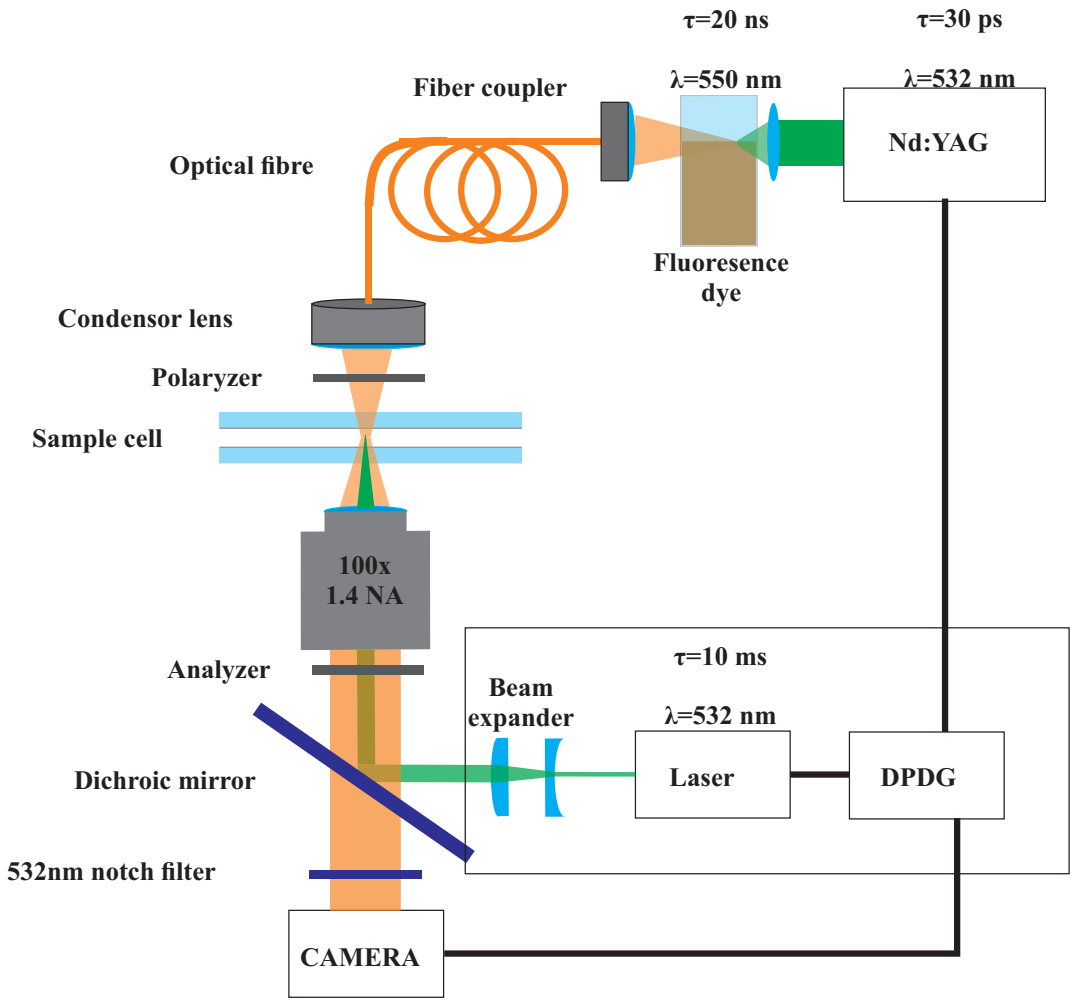


Figure 3.7: Schematic representation of the POM microscopy set up with custom nanosecond laser illumination system.

3.9 Image Processing

A commercially available numerical computing environment Matlab is used to create a custom algorithm to cope with the large amount of data extracted from the images obtained during the imaging of the rapid phase transition experiments [89], [95], [96]. The algorithm comprises four parts. Firstly, we import the experimental images. Secondly we improve their quality by deconvolution, thirdly we extract the data and finally process the data to visualize the growth of nematic ordering after sudden phase transitions. A typical experimental run consists of 1000 images taken at a desired delay where single images are acquired by a 2180 x 2560 pixel array with sensor pixel size of 6.5 µm which, due to the magnification used, corresponds to image pixel size of 65 nm. The images are stored in a 16 bit .tiff format adding up to approximately 20 gigabytes per scan. An implementation of matrix-based algorithms and parallel computing of the gigabytes of image data, are used to reduce the computation time down to hours per image stack. Further details on the algorithm with extensive quality testing are presented in the result section.

3.9.1 Image noise - point spread function and deconvolution

Images, obtained by the camera, are a combination of the actual object and distortions caused by imaging optics with the addition of some random noise due to thermal effects and read out noise. The distortions of the system can be described by a physical function that describes how the image of the point source is transmitted trough the imaging system. The function is called the point spread function PSF and is a measurable property of the imaging system [88], [89], [93]. We impose a theoretical approximation of a bright field PSF of our system which takes into account the typical wavelength of our illumination source $\lambda = 550\,\text{nm}$ and the characteristics of the optics used, especially the numerical aperture of the objective (NA 1.4). We use a simple Wiener type deconvolution algorithm which uses the theoretical PSF that at the first approximation is a Gaussian type function with FWHM of approximately the diffraction limit of light to obtain the distortion free original image [97].

To limit the noise of the camera equipment we use a highly sensitive sCmos type imaging sensor which is cooled down to $-40\,^{\circ}\text{C}$ to minimize the thermal noise. Another step is to use low exposure times, which minimizes the external light, the dark current, which can also expose the camera. Furthermore, a camera-integrated spurious noise filter is used to illuminate shot noise caused non-functioning pixels in the imaging sensor.

3.10 Temperature Measurements

In addition to imaging rapid phenomena, we build an experimental set-up that allows us to measure dynamic thermal properties inside thin LC samples. We use the strong temperature dependence of the LC birefringence as our thermometer. The temperature measurement system is built around a POM and consists of two parts. We determine the static thermal properties by heating the LC sample at different laser powers and imaging the resulting isotropic island sizes. Due to the nature of the first-order phase transition the edge of the heated area has to be exactly at phase transition temperature, which allows us to map the maximum temperature at any given laser power.

The cooling rates are determined by a slight modification in the POM set-up. We substitute the sample cell with a similar sample cell with planar anchoring conditions. The sample placed in the imaging plane of the microscope under crossed polarizers acts as a retarder with strong temperature dependence of the birefringence and therefore the

transmittance. By measuring the transmittance of the sample, one can simply measure the temperature at any given time in the sample cell.

3.10.1 Static thermal properties of LC sample cells

The static thermal properties of thin LC layers are determined by the use of glass cells filled with LCs with different phase transition temperatures and a variable pulsed heating laser. We use 5CB, E18 and MLC-13300 with phase transition temperatures 35 °C, 60 °C and 91 °C, respectively. We place the LC materials in sample glass cells of 2.5 µm thickness, where the glass walls of the cell are coated with 50 nm of a conductive transparent ITO layer. This layer absorbs 12 % of the laser light which, due to the opto-thermal effect, locally heats up the LC inside the cell. The laser is a diode laser (MGL-III-200mW - Chanchung New Industries Optoelectronics Technology Co., Ltd.) with laser emission at 532 nm which is externally triggered by the digital pulse delay generator to produce 10 ms light pulses. In this time the LC medium inside the cell is heated well above its phase transition temperature and an isotropic island is formed during the light pulse, where the temperature is equal to the phase transition temperature at the edge of the isotropic island. The size of the island remains static well before the laser is turned off indicating the thermal equilibrium is reached in just 10 ms. We measure the size of the island at exactly the time the laser is shut down as a function of laser power to determine the stationary temperature profile for the three LC samples. The measurements of the laser power dependence are used to determine the initial temperature profile when quenching a 5CB homeotropic cell of the same thickness at laser power of 90 mW.

3.10.2 Dynamic thermal properties

Dynamical thermal properties of thin LC cells are measured using a custom experimental set-up built around an inverted microscope Nikon eclipse Ti-D, Fig. 3.8. The system consists of a HeNe laser where the laser light is passed through a wave plate and a beam expander to create a 3 mm wide circularly polarised beam. The beam is then guided using mirrors to the microscope where it is passed first through a polariser and then through a condenser lens with focal length of 15 mm to focus it onto the imaging plane of the microscope with a beam spot size of 6 µm. The light passes the sample and is collected by a Nikon Plan Apo oil immersion 100x 1.4 objective with 130 µm working distance. The light then passes through a dichroic mirror that also allows the introduction of another laser. This diode laser which can be externally triggered using a DPDG is used as a heating source. After the dichroic mirror we place a polariser before the light is collected onto a photo diode with 1 µs sampling interval (Siemens). The signal from the photo diode is then acquired by a GHz oscilloscope (Infiniium MSO9404A, Agilent Technologies, Inc.) and collected. A schematic representation of the system is shown in Fig. 3.8.

We measure the time dependence of the temperature within thin LC layers, while cooling from a quench. To measure the temperature inside the cell we have to measure a physical characteristic of the cell which strongly depends on the temperature. One such is birefringence, the value of which is zero in the isotropic phase and it strongly increases in the cooler nematic phase. To measure the temperature via the measurement of the birefringence above the clearing point we exchange the LC with one with a higher clearing point. We take E18 and MLC 13300 which have a high phase transition temperature and measure the temperature dependence of their birefringence. For E18 we use an Abby type refractometer with custom heating stage that consists of a heated water bath and a small pump that circulates the water and heats the sample holder of the refractometer to the desired temperature. We heat the water slowly and measure both the ordinary

and the extraordinary refractive indices and calculate the birefringence. For MLC 13300 the refractometer with a safe working limit of 60 °C cannot be used. Therefore, we use a planar cell of MLC 13300 with known thickness between two crossed polarisers such that the rubbing direction is at 45° to the polarization axis. In this set-up the LC cell behaves as an optical retarder and the transmitted intensity strongly depends on the birefringence. We vary the temperature of the cell using a heating stage (Instec) and measure the transmitted light intensity from which we calculate the corresponding birefringence.

We then measure the time dependence of the temperature within LC cells whilst cooling. We prepare two cells of E18 and MLC 13300 which were identical in the thickness of ITO and thickness of the LC layer. The only difference is that we coat the glass plates with polyimide and rub them with a velvet cloth to achieve homogeneous unidirectional planar anchoring of the LC inside the cell. We place the LC filled cells inside the microscope holder in such a way that the rubbing direction lies at 45° to the polarization axis. Since the polarisers are crossed, no light should pass if we place an isotropic medium in between but due to their birefringence, the cell basically behaves as an optical retarder and some light can pass through the polarisers. Then we heat up the cell to close to the phase transition temperature using the externally triggered diode laser and measure the time dependent transmitted intensity. And since the time dependent intensity is strongly dependant on the birefringence, for which the temperature dependency is known, we can calculate the time dependency of the temperature inside the cell.

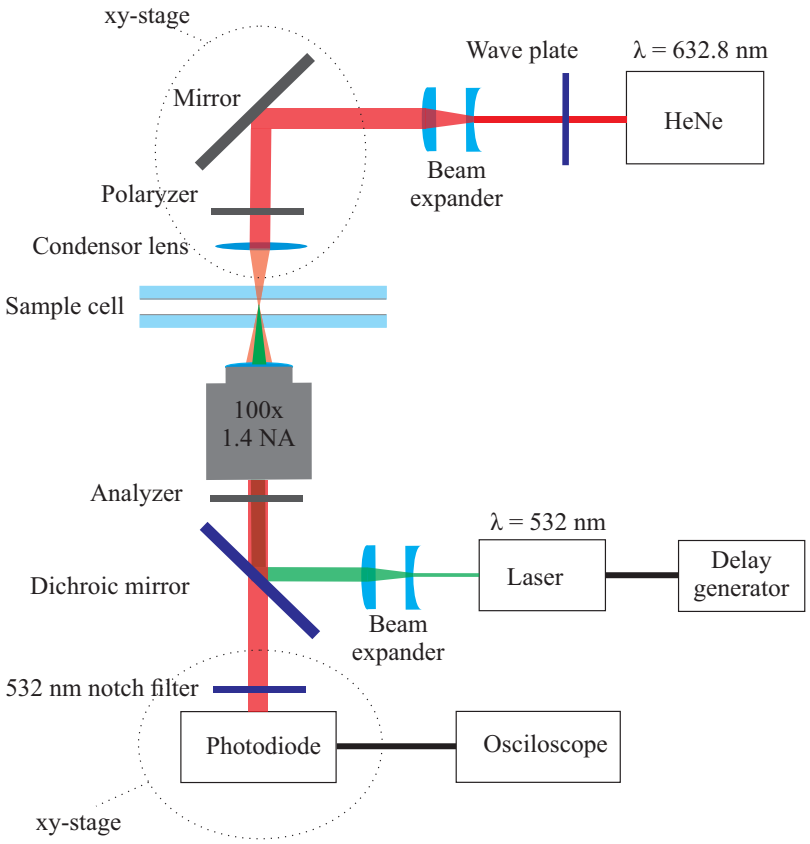


Figure 3.8: Schematic representation of the temperature measurement set-up during fast cooling. The system consists of a measuring laser that is guided onto the cell through polarization optics while the LC cell is cooled. The intensity variations due to the temperature-dependent birefringence are measured using a photo-diode.

3.10.3 Light transmission study

In addition to measuring the thermal properties inside the sample cell, the temperature measurement set-up can be used for light transmission experiments. In these experiments time dependence of light transmission through the LC sample is measured, which gives valuable information on the creation of defects, which are strong scatterers of light. Due to the relative small measuring spot of approximately 6 µm and the ability to use photo diodes with fast sampling time, one can gather information about the sample transmittance that could be missed by camera equipment. Stroboscopic imaging only allows us to image snapshots of the process yet the complete time evolutions cannot be imaged. Combination of the light transmission study with the stroboscopic imaging technique provides an insight into the processes over several time scales with the ability to image snap shots at any desired time.

3.10.4 Modelling of thermal properties

Computer simulations based on the experimental measurements are used to study the thermal properties inside the LC sample cells. The aim was to predict the time dependence of the temperature of the LC layer after the heating light was switched off and the LC

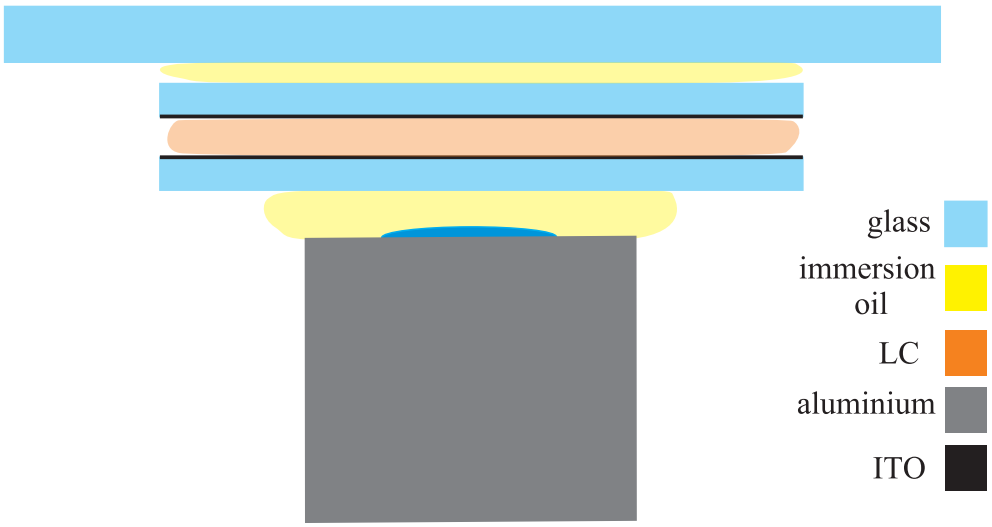


Figure 3.9: Schematic representation of sample cell used for numerical simulations. From top to bottom the sample cell consists of a glass plate, immersion oil, another glass plate coated with a thin ITO layer, a thin LC layer, another ITO coated glass plate where the ITO layer faces the LC, and finally a layer of immersion oil, a glass plate and an aluminium layer representing the oil immersion objective. Note that the layer thicknesses are exaggerated to visualize all materials despite the orders of magnitude difference in thickens.

started cooling by heat diffusion into the cell and environment. We use a finite element simulation software COMSOL to study the thermal properties of LC cells. The software uses a graphical interface and several physics modules allowing finite element numerical modelling of physic processes. In our case we use mainly two moduli: first the electromagnetic module to simulate laser absorption on the sample cell and second the heat transfer module to simulate the internal heat flows in the sample cell. We build our simulation around blocks of various thicknesses and physical properties representing our LC sample cell. The base geometry of the sample cell 3.3 is reproduced as follows. First a 300 µm glass layer that represents the objective glass attached to the microscope, followed by a 30 µm layer of immersion oil used to adhere the glass cell to the objective glass. Next the actual LC cell consists of two 170 µm glass layers, two 50 nm conductive ITO layers and the 2.5 µm LC layer itself. Beyond the cell there is another 30 µm immersion oil layer, a 100 µm glass layer and a 300 µm aluminium layer representing the oil immersion objective. A schematic representation of the basic geometry of the sample cell is shown in Fig. 3.9.

The basic thickness and thermal properties of materials are chosen to fit the real experimental parameters and shown in Table 3.10.4.

Table 3.3: Thermal properties of materials used.

Material	thickness	thermal conductivity W/(mK)	heat capacity kJ/(kgK)
5CB	2.5 µm	0.15	2
Objective glass	300 µm	2.2	0.84
Cover glass	170 µm	2.2	0.84
Aluminium	300 µm	200	0.91
Immersion oil	30 µm	0.2	2
ITO	50 nm	70	0.21

Chapter 4

Formation of Topological Defects Surrounding Colloidal Particles

The introduction of colloidal particles into a uniformly aligned LC system changes the local free energy of the system by introducing singularities in the director field. Due to the conservation of topological charge, the system forms topological defects to compensate for the singularity created by the particle. The type of the topological defect which is formed by the system strongly depends on the topology of the particle and the LC medium surrounding it. For instance, the introduction of particles with genus zero (in other words they have no holes) typically introduce a single virtual point defect into the system that the system accounts for by forming a single defect around the particle with opposite topological charge [14], [16]–[19], [21], [52]. The local environment of the particle can have an effect on the type of the topological defect which can become a simple point of line defect in a nematic and a complex twisted loop in chiral nematic system [13], [15].

Novel particle fabrication methods, such as 3D lithography, enable the study of the colloidal particles of arbitrary genus inside LC systems [14], [61], [98], [99]. For instance, it has been shown that toroidal particles which are of genus 1 inside nematic LCs form two topological defects to neutralize the singularity imposed by the particle [14] and that the total number of topological defects can be increased by means of laser tweezers as long as the charge conservation law is conserved [21].

In this chapter we will present our work on the formation of topological defects surrounding colloidal particles of various shapes. Firstly, we will take a look at the impact of local geometry on the formation of topological defects. Our work shows how an extreme geometry, such as a fractal, can impact the total number of topological defects surrounding colloidal particles, without changing the topology of the particles. In the second part we will investigate the impact of chirality on the formation of topological defects surrounding particles of genus one - tori.

4.1 Fractal Nematic Colloids

Recently, questions arose on how one can influence the number and characteristics of topological defects [14], [21]. Since topological defects are residues of symmetry breaking phase transition, one can for instance use localized heating to introduce new topological defects into the otherwise ordered nematic surrounding a colloidal particle [21]. We want to go one step further with the question, by asking what impact does local geometry have on the structure and number of topological defects.

To answer this question we chose particles of simple topology, like tori of genus type 1, where we drastically modify their geometry. We set the basic shape of the particles

as hollow prisms, where we can modify the base to any desired geometry. An extreme example of drastic geometry is fractal self similarity, which describes a repeating pattern in the structure of over several length scales. Fractality is broadly seen in various soft matter systems where random motion is present. Examples range from Brownian motion, polymer networks, porous media and also brain networks [100]–[107]. Purely geometrical fractals are characterized by self-similarity of the system to itself over several length scales [108], [109]. One well known fractal shape is the Koch fractal [110], where all the properties of the structure are purely based on the fractal iteration and described by a geometrical scaling law. Due to their extreme change of geometrical characteristics over the fractal iterations, fractals are the ideal testing ground for the impact of geometry on the formation of additional topological defects surrounding particles.

We design and print particles with genus one with different iterations Koch fractals as base. The particles are immersed in nematic LC, and using polarization optical microscopy we are able to determine the number of topological defects formed and compare it to theoretical results obtained using finite element modelling (FEM) simulations.

4.1.1 Koch colloidal particles

Using the DLW method and the gel-like IP-G photo-resist we produce hollow prisms with various iterations of the Koch fractal as base. The height of the particles is 8 µm and the wall thickness is 600 nm, whereas the whole particle size in the $x-y$ plane of the particles is 20 µm, as seen from the SEM images in Fig. 4.1. With the typical polymerization volume width of ∼150 nm and height of ∼700 nm a total of four layers in the $x-y$ plane and 12 layers in the z directions are required to produce a single particle.

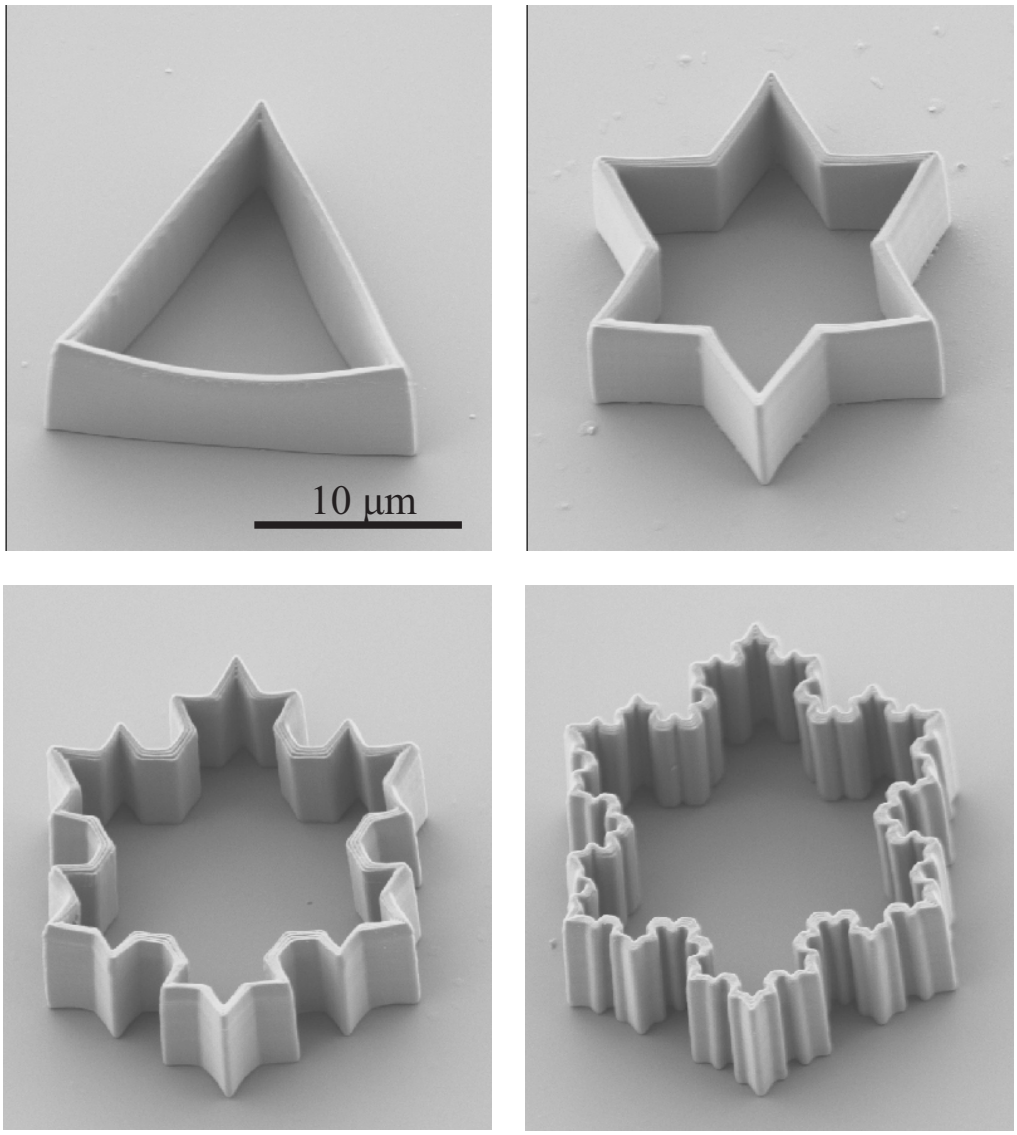


Figure 4.1: SEM images of the first four iteration Koch colloidal particles.

4.1.2 Surface smoothness and anchoring of the printed colloids

The interaction of colloidal particles and the surrounding medium is strongly dependent on the surface anchoring of the LC molecules on the colloidal particles. Typically LC molecules tend to align parallel to the solid surfaces without any preferred orientation, this is called planar degenerate anchoring [41], [86]. With the use of surfactants with long apolar chains we can force the LC molecules to align perpendicular to the surface. Typical, we use silanes, such as dimethyloctadecyl[3-(trimethoxysilyl)propyl]ammonium chloride (DMOAP) to achieve a homogeneous alignment of the LC on the surfaces [87].

Without the use of surfactants the degeneracy of the molecules can also be broken by means of surface texturing which is typically achieved using a small layer of polymer that is rubbed to create surface grooves into which the molecules can align.

The particle smoothness is best seen on the surface of toroidal particles Fig. 4.2 a where the main 'pore' size observed on the surface is a few tens of nm which does not

influence the surface anchoring. We can observe the printing process on the Koch-shaped particles Fig. 4.2 b, which is a consequence of the layer by layer printing process of the particle wall.

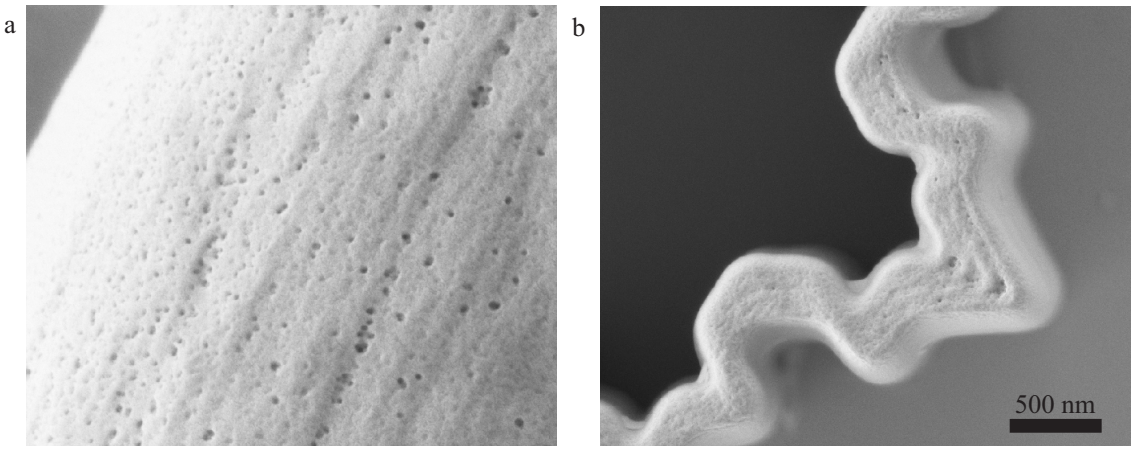


Figure 4.2: SEM image of the surface of colloidal particles obtained by the DWL printing process. **a** A close-up on the surface of toroidal particles shows the main 'pore' size on the surface of a few tens of nm. **b** A close-up of the Koch-shaped particles showcases the line by line printing process.

To achieve homogeneous homeotropic anchoring on printed polymer particles, surfactants have to be used. Typically surfactants bond onto free hydroxyl groups which are present on the surfaces. We observe that our polymers do not have enough free hydroxyl groups and consequently the surfaces have to be activated before the adhesion of the surfactant. We achieve this by placing the particles right after printing under a corona discharge plasma (BD-20AC Laboratory Corona Treater, Electro-Technic products), where the produced ozone activates the surface. The particles are then placed in a 0.5 % water solution of DMOAP to assure strong homeotropic anchoring on the particle surfaces.

To test the surface anchoring quality we place colloidal tori with major radius 25 µm and minor radius 3 µm inside a homeotropic Fig. 4.3 a and a planar Fig. 4.3 b cell of thickness 20 µm where distinct topological defect patterns can be observed using a POM set up.

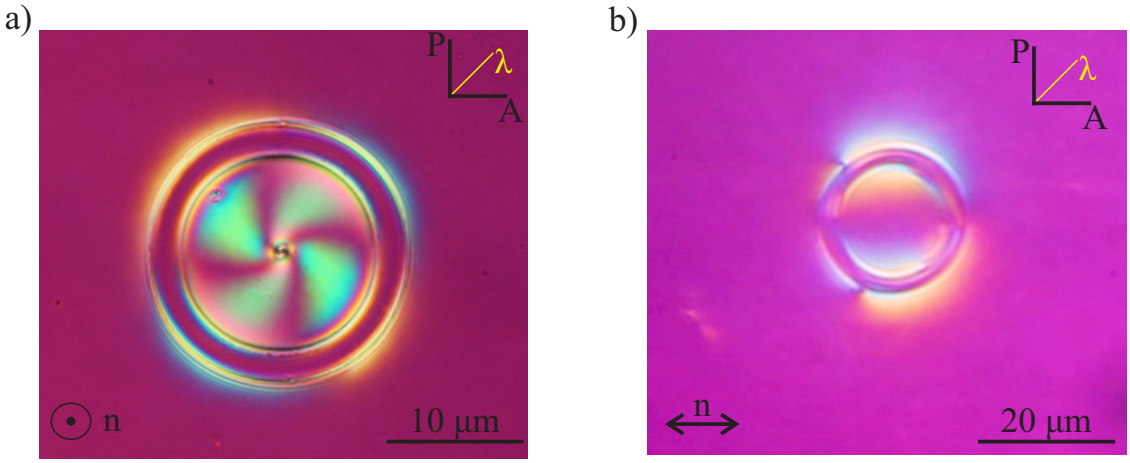


Figure 4.3: Defect structure around colloidal tori in nematic LC. Colloidal tori treated with DMOAP in **(a)** homeotropic and **(b)** planar cell. The topological defects structure is observed using crossed polarizers and a retardation plate.

The strong similarity of the topological defect pattern observed in our work compared to the reported results from Senyukh et al. [14] indicates a good quality surface alignment of the surface of the colloidal particles.

4.2 Polarization Optical Microscopy Study of Koch Colloidal Particles

Colloidal particles in the shape of hollow prisms with a Koch fractal base, are surface treated to achieve strong homeotropic surface alignment of LC molecules and placed in a 30 µm thick LC cell which is composed of two ITO-covered cover glasses treated with polyimide to achieve strong unidirectional planar alignment inside the cell. The cell is filled with a low birefringent ($\Delta n = 0.04$) nematic mixture of CCN-47 and CCN-55 (50:50 by weight). A low birefringent LC mixture is used to improve the resolution that would otherwise suffer from the strong scattering of light on the topological defects. The cell is first heated above the isotropic clearing point of approximately 63 °C which removes effects of the filling process on the LC structure. The cell is then placed on the imaging plane of an inverted polarization optical microscope which is equipped with a 100 x oil immersion objective and a bright field illumination system. For additional observations, a retardation plate is used which allows the distinction of the in-plane orientation of the director field. We use the first three iterations of Koch fractals and different combinations of the polarizations to determine the structure of the topological defects surrounding the particles. The experimental images are presented in Fig. 4.4 a-f, with columns I-III representing experimental images and column IV simulation results.

In column I of Fig. 4.4 a-f the particles are freely floating in the isotropic phase at 70 °C allowing us to determine the optical artefacts that occur due to the refractive index mismatch between the polymeric particles (1.50) and the surrounding nematic liquid (1.52). Note that the particles are free to float in the middle of the cell and their motion is solely Brownian.

In column II of Fig. 4.4 a-f the particles are left to cool to the room temperature of 21 °C and observed using crossed polarizers. Here the rubbing direction and the polariza-

tion axis of the input light coincide, therefore any orientation of the director field parallel or perpendicular to the rubbing direction results in no transmitted light, for a homogeneous LC, which coincides with dark regions on the image. Otherwise any deviation in the orientation from the polarization axis results in retardation of light which results in transmission of light with light intensity roughly corresponding to the in-plane angle of the direction. Due to a mismatch of the orientation of the LC molecules on the glass substrate and the particles an elastic repulsion is present and the particles levitate inside the mid point of the LC cell and do not sediment. Since the particles are free to rotate in any direction, we expect the particles will orient themselves in such a way that the total elastic energy will be minimized. We observe that in all the iterations of Koch fractals two stable configurations occur. For instance, for the 0^{th} iteration in Fig. 4.4 a, a site of the particle is parallel to the rubbing direction whereas in Fig. 4.4 b the site is perpendicular to the rubbing direction. In other words in one case a particle edge is parallel to the rubbing direction and in the other the edge is at 30°. Both orientations are roughly energetically similar since the probability of each configurations is roughly 50 %. Similarly we observe for the 1^{st} and 2^{nd} iteration two stable configurations where in Fig. 4.4 c,e one point of the shape points parallel to the rubbing direction, whereas in Fig. 4.4 d,f it points perpendicular to the rubbing direction. We observe several dark areas with rapidly varying intensity and color of the surrounding that we can correlate to topological defects. Due to the strong pinning of the topological defects to the walls of the colloidal particles, probed by laser tweezers, it is hard to discus the 3D character of the defects. For this reason we will only determine the 2D projections of the topological defects on the focal plane and determine their characteristic winding number.

In column III of Fig. 4.4 a-f an additional retardation plate at 45° towards the optical axis of the polarizers is used enabling the detection of the in-plane orientation of the nematic molecules. Here, regions with orientations in the optical axis correspond to areas of pink color, orientation at 45° from left to right correspond to a blue color, and otherwise at 45° from right to left the orientation results in a yellow color.

Finally in column IV of Fig. 4.4 a-f corresponding snapshots of the finite element modelling (FEM) computer simulations are shown. Here a Landau-de Gennes numerical model is used, which is based on the free energy expansion of the nematic LC. We present a cross-section of a 3D simulation box corresponding to the mid-plane of the real particles.

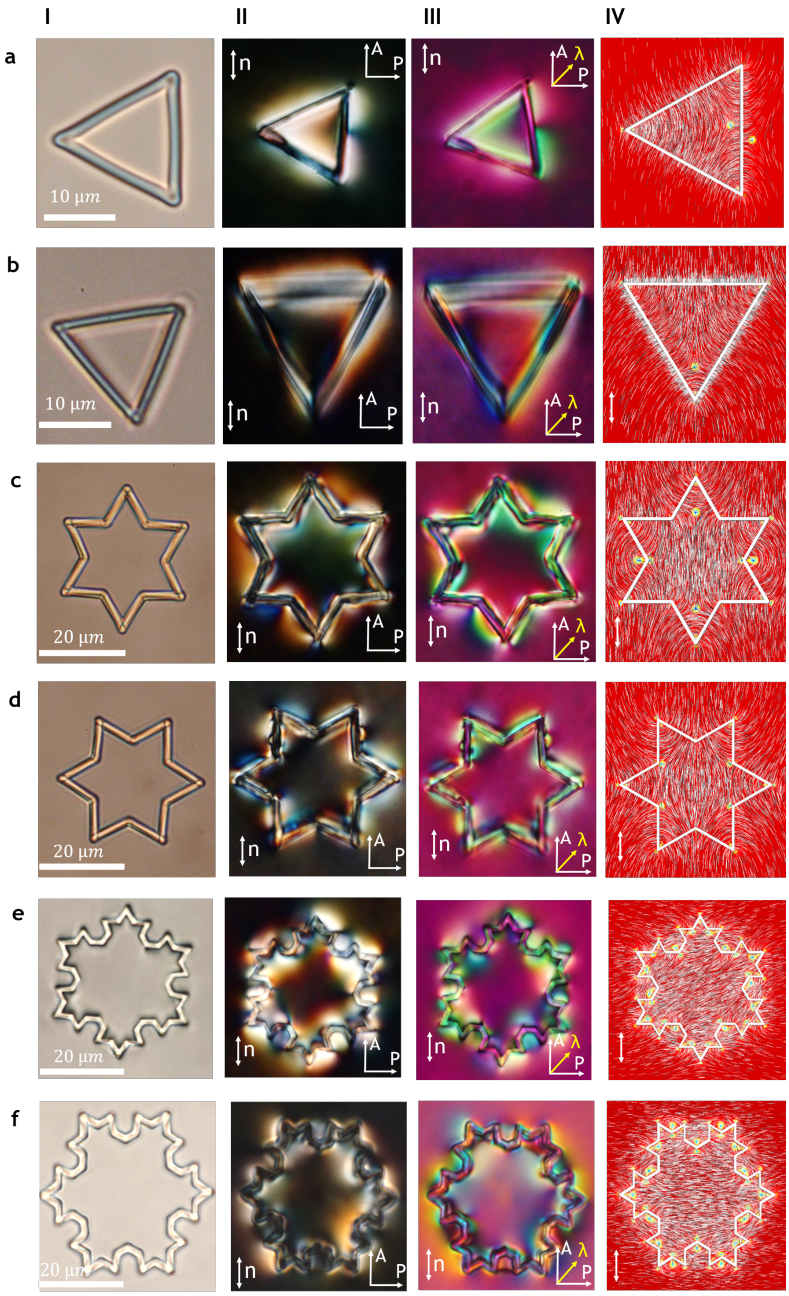


Figure 4.4: **a-f)** Experimental observations of Koch fractal colloids. Column **I** Koch-star particles in the isotropic phase of the CCN mixture at 70 °C in unpolarized light. Column **II** The same particles as in column **I**, now observed between crossed polarizers at room temperature. Defects are recognized as point regions in the optical image, surrounded by rapidly varying intensity of the transmitted light, indicating strong distortion of the director field. Column **III** The same particles as in column **II** now viewed between crossed polarizers and red plate added at 45°. Different colours are due to different in-plane orientations of the nematic molecules. Column **IV** FEM numerical modelling illustrating contour plots of the scalar order parameter in the midplane of the particles. The calculated director field in the x–y plane of the contour plots is also superposed. Reprinted from [111] under the terms of the Creative Commons Attribution 4.0 International license (http://creativecommons.org/licenses/by/4.0/)

The number of topological defects, surrounding various iterations of Koch fractal colloidal particles, is determined using a simple procedure in the POM optical set up. By rotating the analyzer with respect to the fixed polarizer, the contrast of the regions with rapidly changing optical retardations is highlighted corresponding to the position of the topological defects that can be simply counted.

As seen in Fig. 4.5 we can clearly resolve a disclination line winding along the upper edge of the particle simply by comparing the images taken at different positions of the analyzer, panels Fig. 4.5 a-c. Additional test were performed using optical tweezers where the disclination line can be pulled of the particles all around the colloidal particle. In panel Fig. 4.5 d a 3D representation of the FEM modelling is presented where the red line corresponds to an iso-surface of low order parameter which corresponds to the defect core.

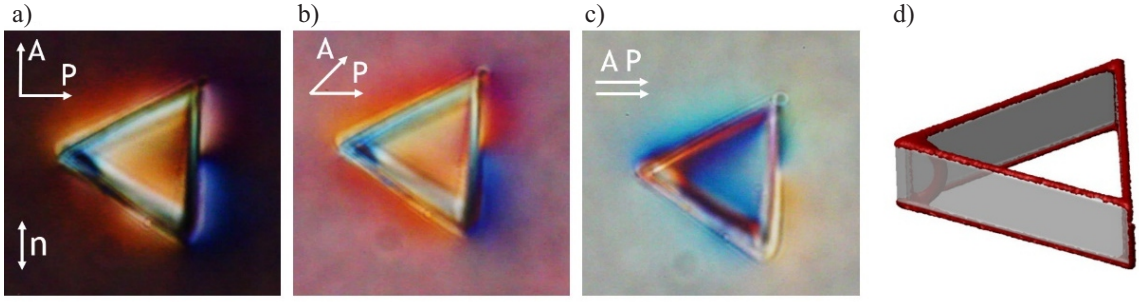


Figure 4.5: POM study of 0th iteration Koch fractal colloids. **a-c** POM images of the 0^{th} iteration Koch fractal colloids with different angles between the polarizer and the analyzer. **d** The 3D representation of the FEM numerical simulation reveals clearly a disclination line running trough the edges of the particle. Reprinted from [111] under the terms of the Creative Commons Attribution 4.0 International license (http://creativecommons.org/licenses/by/4.0/).

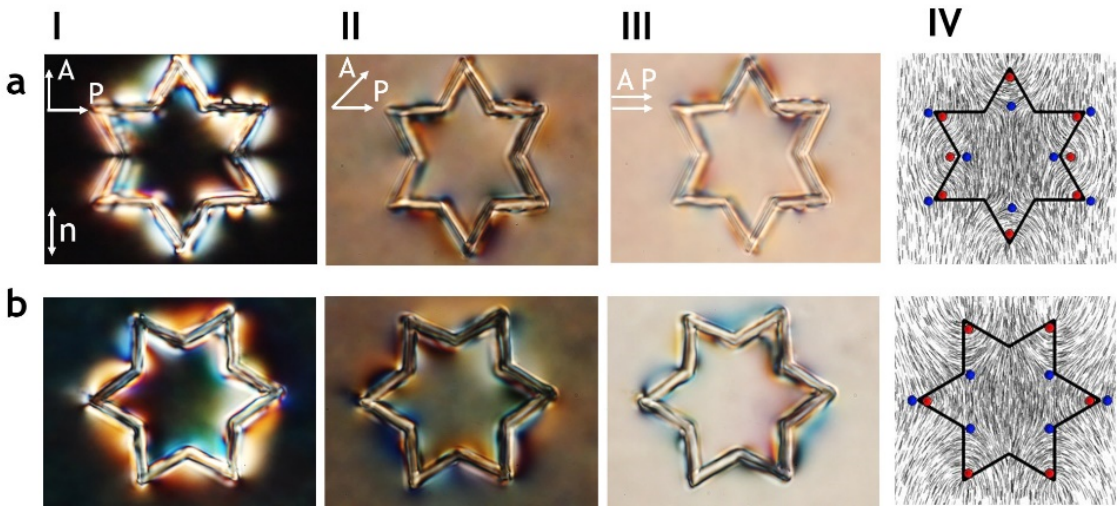


Figure 4.6: Koch particles at **(a)** 0° and **(b)** 30° towards the rubbing direction. Experimental images **I-III** showcase the positions of the topological defects as dark central regions surrounded by a rapidly varying intensity and color. The total number of topological defects is also backed by the numerical simulation IV where +1/2 defects are marked as red and −1/2 as blue. POM of LC samples. Reprinted from [111] under the terms of the Creative Commons Attribution 4.0 International license (http://creativecommons.org/licenses/by/4.0/).

By observing the particle cross-section under the POM set-up, one can observe the projections of the disclination line onto the 2D imaging plane. By counting the total number of topological defects inside and outside of the 0^{th} iteration Koch particles and observing the local orientation of the director field from Fig. 4.4 III, we observe three topological defect pairs. On the inside there are three +1/2 defects pinned on to each corner of the particle with a single −1/2 defect in the middle of the particle which makes the total inner winding equal to +1. Similarly on the outside of the particle we observe two topological defects with winding −1/2 accounting for a total outer winding of −1. Combining the total winding on the inside with the total winding on the outside of the particles, accounts to a total winding of 0. This fits exactly the Gauss-Bonnet theorem, that states that particles of genus g carry a total topological charge equal to $\pm(1-g)$ that for tori with genus $g = 1$ equates to a total charge of 0. The occurrence of 3 pairs of topological defects coincides with the recent result of Nikkhou et al. [21] where they used optical tweezers to create additional pairs of topological defects along a colloidal fibre inside a nematic. The number of topological defects is the same with the particle oriented with one side at 0° or 30° towards the rubbing direction. This situation changes in the case of the 1^{st} iteration Koch particle where with the help of the rotating analyzer we detect 8 pairs of topological defects for the 0° case and only 6 for the 30° case, Fig. 4.6 a,b. I-III. The result is further backed by the numerical simulation which is shown in Fig. 4.6 a,b. IV.

Here we also perform additional tests, using optical tweezers, but contrary to the 0^{th} iteration particles we are not able to pull the disclination line from the particle, only two −1/2 defect on the adjacent corners inside the particle Fig. 4.4 c. II can be pulled and freely moved.

The case of the 2^{nd} iteration Koch fractal particles gets a little more complicated since the edges of the particle get smaller and smaller and almost approach the diffraction limit of

light. This is also the limiting factor for the experimental observation from only the 0^{th} to the 2^{nd} iteration Koch fractal, since already in the 3^{rd} iteration, the edges are too small for optical microscopy. We use a high numerical aperture oil immersion objective to increase the resolution especially at the edges of the particles. To showcase the position of the topological defects, we divided each image obtained at different positions of the analyzer into quarters and analysed them separately, as shown in Fig. 4.7 I-III, and compared them to the numerical simulations in Fig. 4.7 IV. The same process was again done on the 30° position particles in Fig. 4.8.

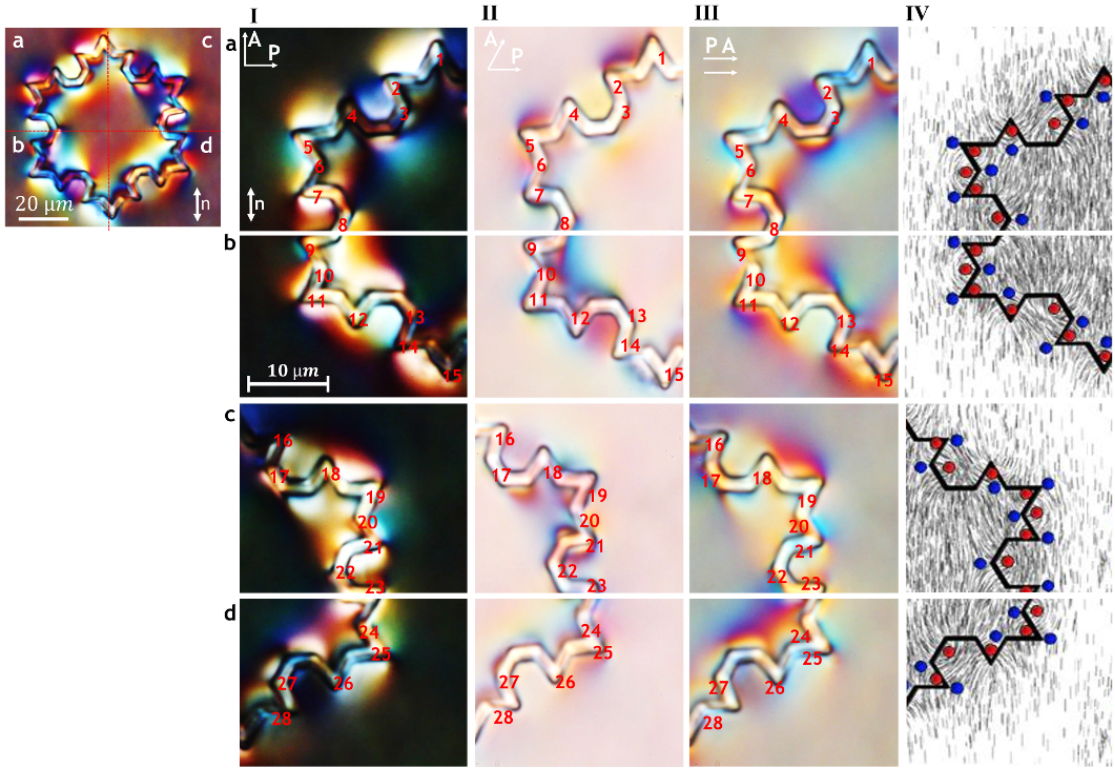


Figure 4.7: Individual images obtained at different positions of the analyzer towards the fixed polarizer of the 0° position of the Koch fractal colloid were divided into quarters **a-d**. We compared them with the numerical simulations where a cross-section result IV shows 28 pairs of TD with +1/2 defects marked as red dots and −1/2 as blue ones. POM of LC samples. Reprinted from [111] under the terms of the Creative Commons Attribution 4.0 International license (http://creativecommons.org/licenses/by/4.0/).

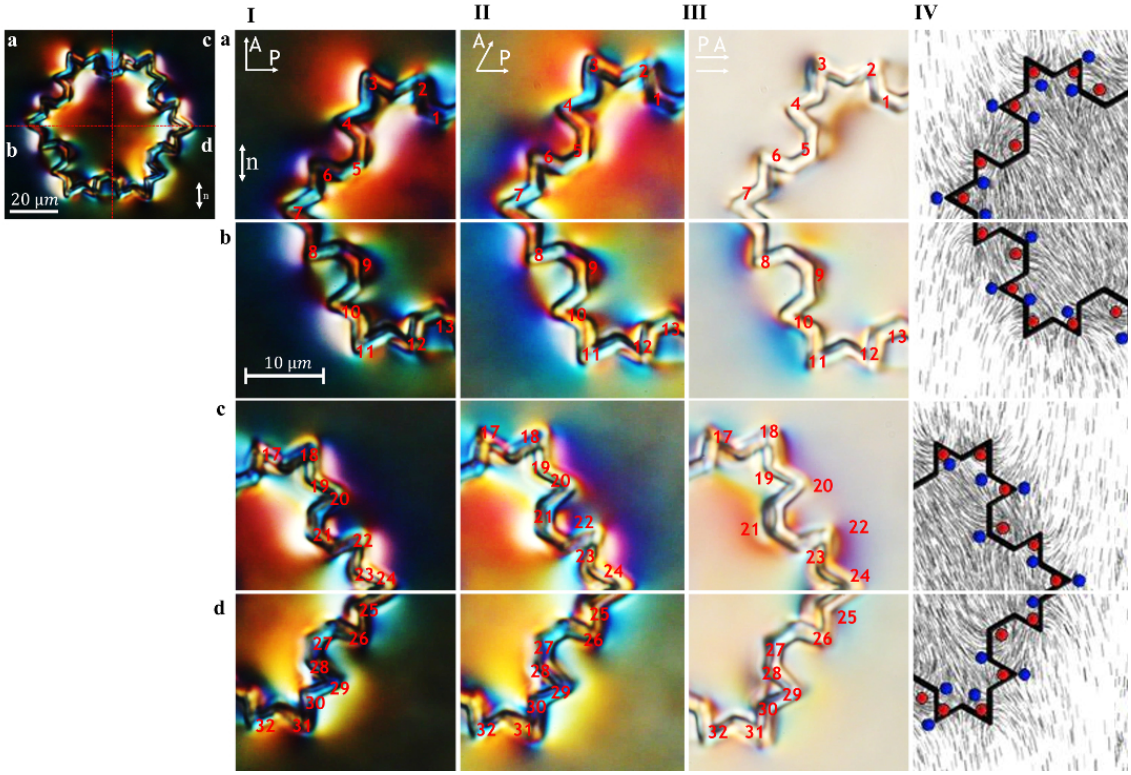


Figure 4.8: Individual images obtained at different positions of the analyzer towards the fixed polarizer of the 30° position of the Koch fractal colloid were divided into quarters **a-d**. We compared them with the numerical simulations where a cross-section result IV shows 26 pairs of TD with +1/2 defects marked as red dots and −1/2 as blue ones. Reprinted from [111] under the terms of the Creative Commons Attribution 4.0 International license (http://creativecommons.org/licenses/by/4.0/).

For the 2^{nd} iteration we observe a total of 28 topological defect pairs in the 0° case and 26 in the 30° one. Using optical tweezers, neither a disclination line can be pulled of the particles nor the defects themselves can be moved. It is important to note that we are able to rotate and move the particles freely using optical tweezers regardless of the large particle size. We are also able to locally quench the system from the isotropic to the nematic phase which resulted in the formation of meta-stable defect states which were extremely hard to investigate, therefore a slow cooling from the isotropic melt is preferred to promote the occurrence of stable low energy defect states.

Combining the results, we observe that, due to the change of the geometry of the particles, we can create a number of topological defect pairs that can be significantly greater than in the minimum case of a torus [14]. Also any additional defects occur in pairs following the principle of the Gauss - Bonet theorem, which for particles of genus 1 dictates a total topological charge of 0 [1], [47]. We study the 0^{th} to 2^{nd} iteration Koch fractal colloids experimentally and we study up to the 4th iteration in numerical simulations. Counting the total number of topological defect pairs in all of the investigation leads us to a simple geometry base scaling law which connects the iteration of the fractal to the number of topological defect pairs. For the 0° case $n = 3 + 5\sum_{i=1}^{N} 4^{i-1}$ where n is the number of topological defects pairs and N the fractal iteration and for the 30° case $n = 6 + \frac{9}{2}\sum_{i=1}^{N} 4^{i-1}$, note that $N > 0$ and for $N = 0$ $n = 3$.

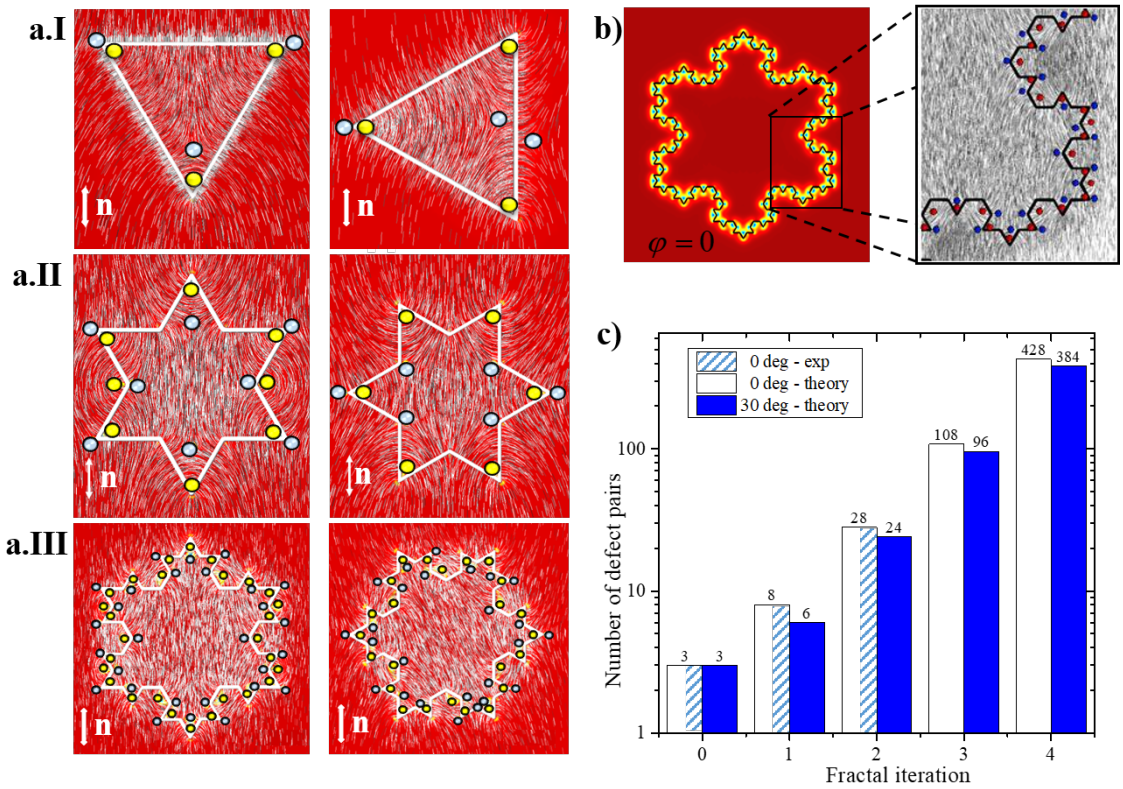


Figure 4.9: Numerical simulations of the Koch fractal colloids showcase the position and the winding number observed in our experiments **a. I-III** and computer simulations for higher iterations of fractals **b**. The total number of defects pairs plotted as a bar plot in **c**. POM of LC samples. Panels b,c are reprinted from [111] under the terms of the Creative Commons Attribution 4.0 International license (http://creativecommons.org/licenses/by/4.0/).

4.3 Toroidal Colloids in Chiral Nematic Liquid Crystals

In the previous section we investigated the impact of the particle geometry on the formation of topological defects surrounding colloidal particles with genus 1. We observe a number of topological defect pairs formed due to the strong geometrical impact of the fractal shape of the particles. Here we want to test the impact of the LC surrounding on the formation of topological defect along colloidal particles. By keeping the geometry as simple as possible and immersing them into a nematic LC doped with various amounts of chiral dopant, we are able to test the impact of twisting nematic director field on the topological defect structure.

Our work was inspired by the observations of the topological defects surrounding colloidal spheres inside the chiral nematic environment [13], [15], [17]. Especially in the work of Jampani et al. [15] the authors observed that the spheres in a planar nematic with no twist form a simple defect loop along the equatorial plane of the particle, which, with the increase of twist in the system, begins to twist around the particle.

In our case we use two-photon lithography to produce toroidal particles with the major radius of $R = 20\,\mu\text{m}$ and minor radius $r = 3\,\mu\text{m}$, as shown on the SEM image of one particle Fig. 4.10 a. The particles were printed, developed and then silanized with DMOAP to achieve strong homeotropic alignment. We then place the particles inside a glass cell made from two cover glasses coated with a thin polyimide layer, which is rubbed with velvet to achieve unidirectional planar alignment. The particles are then immersed into a low birefringence mixture of CCN-47 and CCN-55, with $\Delta n = 0.04$, and the mixture is using capillary action filled into the glass cell.

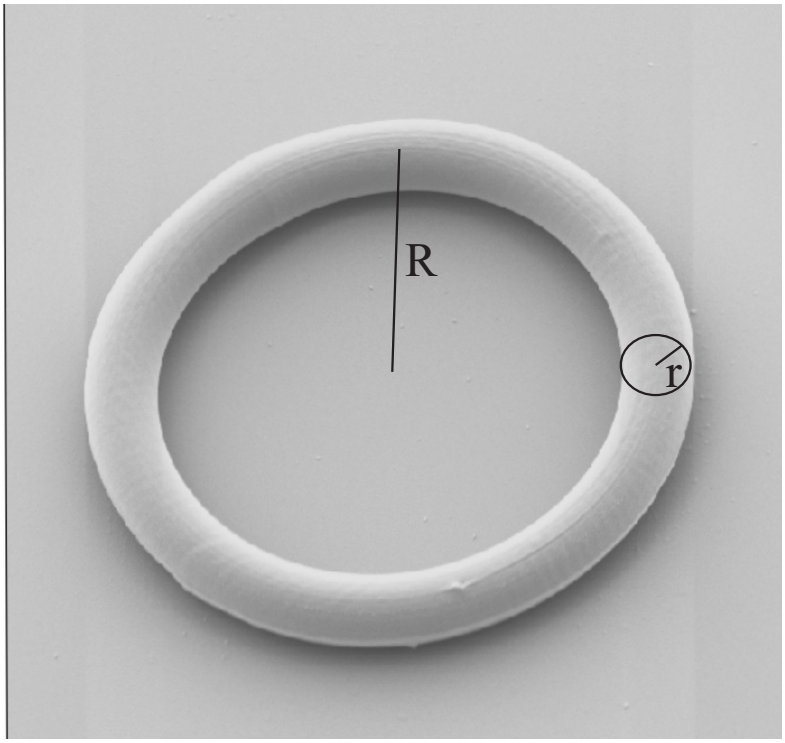


Figure 4.10: SEM image of one toroidal particle showcasing the printing quality and the major and minor radius. Typical major radius **R** is 20 µm and minor radius **r** is 3 µm.

For the first experiment we assembled the glass cell in such a way that the rubbing direction on one glass is perpendicular to the other. This forces the LC molecules to smoothly rotate for 90° from one surface to another. The cell thickness was kept to four times the small radius of the toroidal particles (12 µm), to keep the particles from rotating out of the $x - y$ plane. To achieve a homogeneous mono domain sample, a small amount of a chiral dopant CB-15 is added. This gives us a pitch of the LC molecules four times greater than the cell thickness.

After filling the cells are heated to the isotropic melt $T > 70\,°\mathrm{C}$ and slowly left to cool to room temperature. This allows the formation of stable low energy configurations of the topological defects states. We use a POM set up where the polarizer and the analyzer are placed parallel and a retardation plate is added at 45° towards the polarization axis. This allows us to observe the positions and characteristics of the topological defects formed around the particles. From Fig. 4.11 a-c. I we observe three distinct states of topological defects. One can simply imagine the behaviour of the director field inside the LC cell by dividing the cell into thin xy planes which act as regular planar LC layers which rotate as we move in the z direction. We use this to schematically draw the disclination lines position on the right panels of Fig. 4.11 a-c. II.

In panel Fig. 4.11 a. I we observe a single disclination line running around the particles inner top side, which then, at the positions of highest orientation miss-match wind around the particle to emerge at the outer top part. If we now take a 2D cross-section of the director field in the middle plane of the particle, Fig. 4.11 a. II, we can observe that as the disclination line crosses the plane on the inside the winding number of the line is $+1/2$ and on the outside $-1/2$ and since it crossed the plane two times on each side, the total winding outside is -1 and on the inside $+1$ corresponding to a total winding of 0 which again confirms the Gauss-Bonnet theorem.

In panel Fig. 4.11 b. I a similar case is observed, yet here the winding around the particle does not occur symmetrically. Here the disclination line winds once from the outside of the particle inwards and in the opposite direction on the other side. Areas, where the disclination line crossed the mid plane, are marked by red lines. Again, by mapping a cross-section, Fig. 4.11 b. II, one can observe the presence of two pairs of defects with opposite winding number, obeying the conservation law. A more detailed experimental investigation of this case with the use of optical tweezers is discussed further on.

For the case of Fig. 4.11 c. I, instead of one we observe two disclination lines winding around the particle at opposite sides. The crossing points through the middle plane are again at the areas of highest miss-match of the orientation. In addition, we observe a slight color change inside the particle which indicates a slight rotation of the inner director field due to the pulling of the disclination line inside. Areas of highest distortions, marked with red arrows indicate areas where a soliton could be positioned. Further investigation is required to determine the validity of this statement. Here also by mapping the cross-section in the mid plane of the particle one determines the sum of the total winding to be zero, Fig. 4.11 c. II.

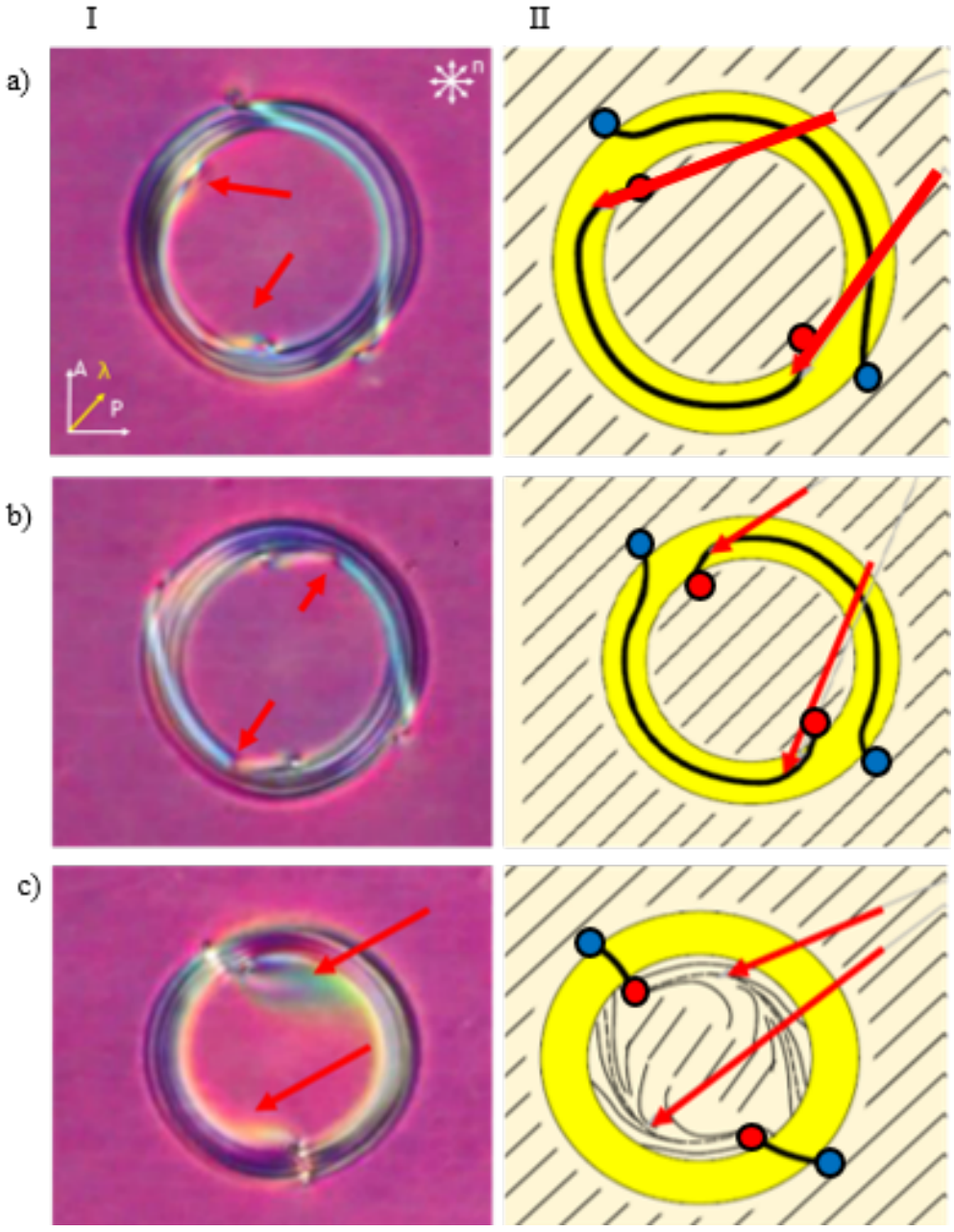


Figure 4.11: Experimental images using POM with parallel polarizers and a retardation plate **I** and schematic drawings of the director field at the cross-section in the middle of the particle **II**. Three distinct configuration forms **a-c**. One observes one **a**,**b** or two **c** disclination line running along the particle. In all cases the mid-plane is crossed four times. By mapping the director field at this point **a-c.II**, one can confirm that the total winding always equals zero.

Next with the use of optical tweezers we study the position and the properties of the disclination lines winding around the particles. Especially in the configurations shown in Fig. 4.11 b, we observe a interesting change in the color of the optical distortions as shown by the red arrows. We use optical tweezers and pull away a disclination line, confirming indeed a single solid disclination line is winding around the particle, shown in Fig. 4.12 a. Next we pull the disclinaiton line on the inside where we observe a distinct color change in the director field behind the line, indicating a change in the winding of the disclinaiton line, which then causes a change in the orientation of the director field as the line is pulled away, shown in Fig. 4.12 b. Next we also repeat the same experiment on the upper part of the particle to confirm the symmetrical nature of the disclination line, shown in Fig. 4.12 c. Note that all images were obtained using parallel polarizers and are dark due to polarization guiding of the sample.

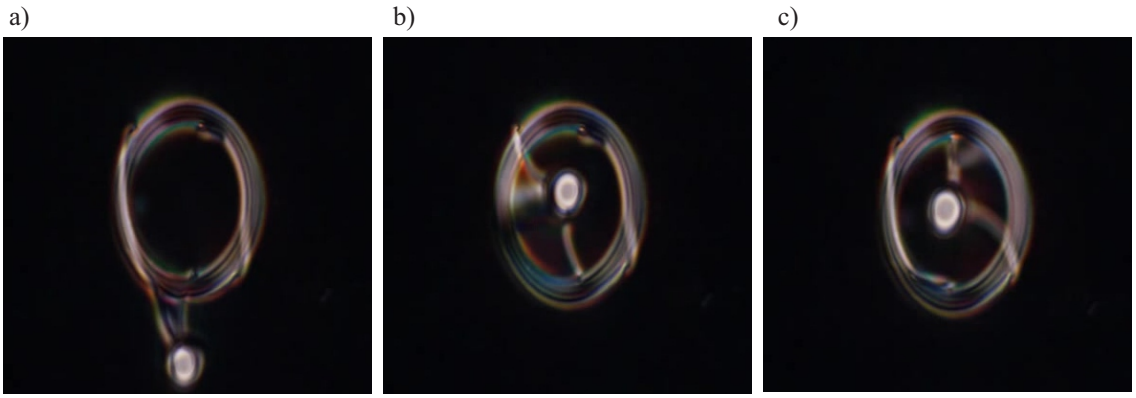


Figure 4.12: Optical tweezers experiments in chiral nematic LC. **a)** A disclination line can be pulled of the particle indicating a continuous line winding around the particle. **b)** Detaching the disclination line inside the particle causes change in the orientation of the director field behind the line indicating a change in the winding of the disclination line. **c)** The same effect on the upper part of the particle.

Next we try to use another polarization optical microscopy technique to study the structure of the disclination lines winding around the particles. We use fluorescence polarization confocal microscopy, where we add a fluorescence dye into the liquid crystal that aligns along the director field and using polarization optics in the excitation and fluorescence we are able to using a custom computer algorithm reconstruct the director field [85], [92], [94], [112]. We first try to use this method on the cells with pitch much longer than the sample thickness. Due to the relative long pitch of the molecules inside the sample cell we encounter an effect called polarization guiding. Here the transmitted intensity trough crossed polarizers not only depends on the birefringence of the medium but also on the polarization of the incoming light. This effects depends on the length of the pitch of the sample and also on the sample thickness and is called the Mauguin limit $Ma = p\delta n/2\lambda$. For long pitches this limit is close to one and polarization guiding occurs. And for shorter pitches the value drops towards zero where a isotropic medium can be approximated that does not change the polarization at all. In our case for instance we are at the Mauguin limit number of 0.98 indicating polarization guiding. Typical scans show completely dark images at all polarizations expect the one which is being guided trough the sample. Therefore the FCPM method can only be used in small Mauguin numbers where the sample can be treated as isotorpic.

By placing toroidal particles with minor radius of 3 µm into a LC medium with pitch

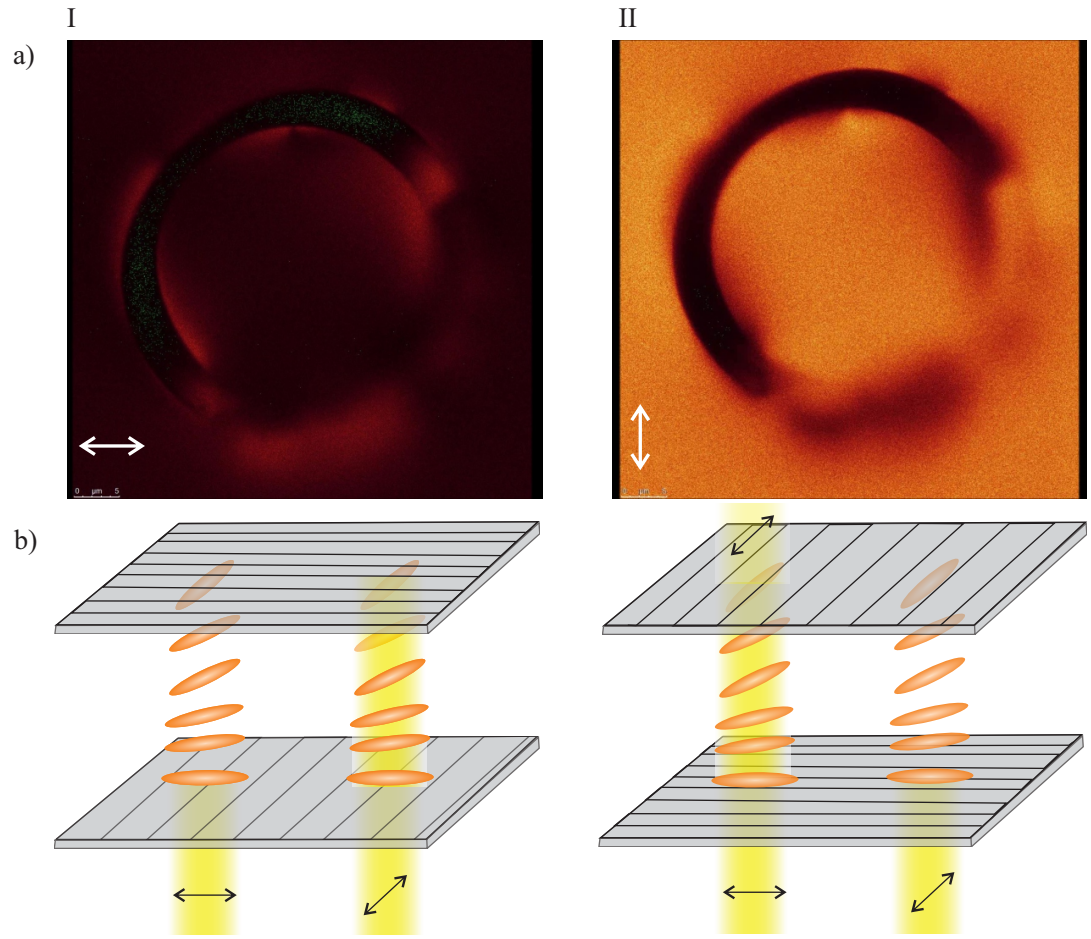


Figure 4.13: Polarization guiding in twisted nematic LC. **a)** Confocal image with polarization parallel to the sample. No light is transmitted trough the sample in **b) with perpendicular polarization to the sample all light is being transmitted due to polarization guiding.**

48 µm the particle only 'observe' approximately one eight of the rotation of the director field. Therefore, only small twist deformations on the surface are present. If one now increases the chirality of the LC medium soon the pitch becomes comparable to the particle size increasing the local twist deformations. As the local twist deformations increase in size we expect an ever more complex toplogical defect structure. We showcase the complexity by comparing a simple case of a toroidal particle in the $\pi/2$ sample cell in Fig. 4.14 a.I, with a structure obtained by placing the same size particles into a cell with half shorter pitch π Fig. 4.14 a.II. Pitches are schematically represented with Fig. 4.14 b.I-II, where a cross-section of a toroidal particle is added for size comparison.

Immediately, one observes a dramatical increase of complexity of the structure. One can no longer just by simple observations determine the underlying structure. As the chirality increases, disclination lines around the particles, start to wind and twist around each other. By simple observations, one can no longer determine the underlying defect structure. We introduce two new experimental techniques. Firstly, we use optical tweezers to grab individual defect lines. By stretching and unwinding the defect line lines we are able to study the structure. Secondly, we take advantage of the method for director reconstruction from fluorescent confocal polarization microscopy data FCPM.

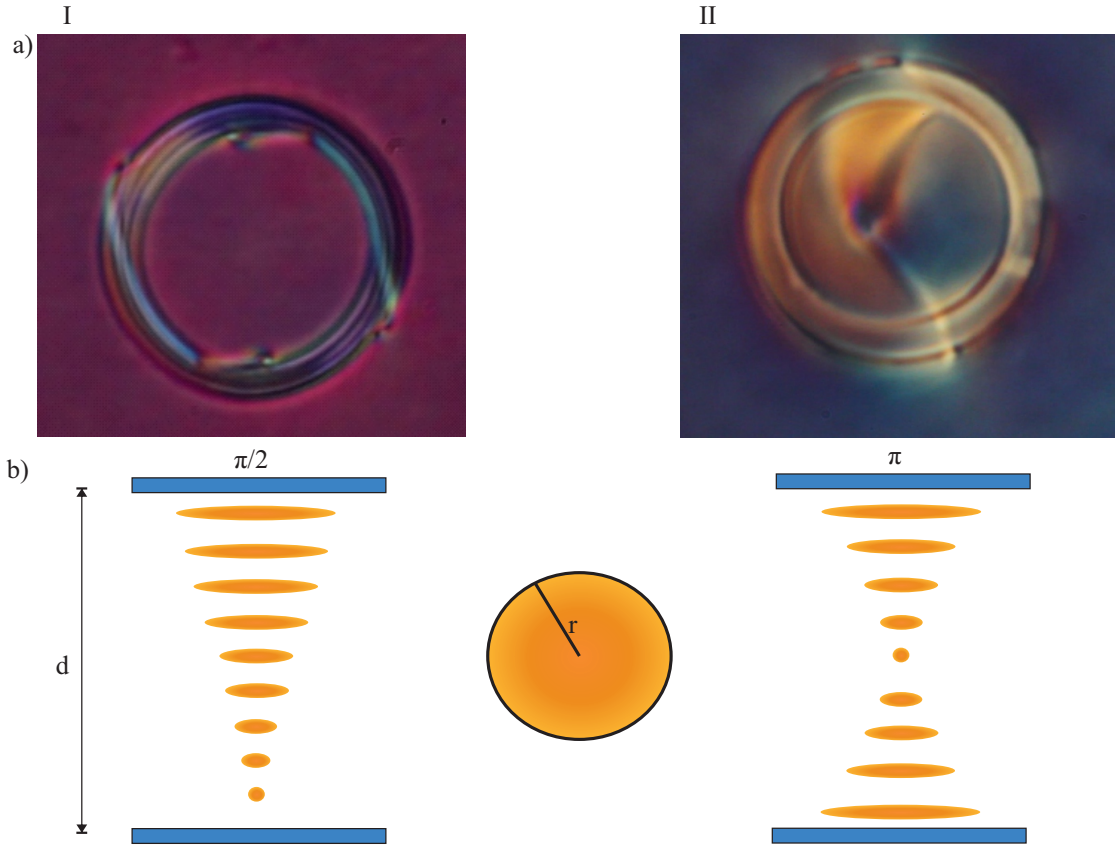


Figure 4.14: Experimental images using POM with parallel polarizers and a retardation plate **I** and schematic drawings of the director field at the cross-section in the middle of the particle **II**. Three distinct configuration form **a-c**. One observes one **a,b** or two **c** disclination line running along the particle. In all cases the mid-plane is crossed four times. By mapping the director field at this point **a-c.II** one can confirm that the total winding always equals to zero.

Let us describe the use of the FCPM director reconstruction on a case of a homeotropic toroidal particle in a highly twisted LC sample cell. We use a LC medium with a small amount of chiral dopant added, setting the pitch equal to the sample thickness of 12 µm, Fig. 4.15 IV. The particle size is $R = 20\,\mu\text{m}$, $r = 3\,\mu\text{m}$. The sample also contains a small amount of BTBP dye required for the fluorescence study.

First, we observe the complex structure of the topological defects surrounding the particle using POM in Fig. 4.15 I. Here the polarizer and analyzer are crossed yet a blue tinted background is clearly observed with darker and lighter patches close to the surface of the particle. The changes in the intensity could indicate a change in director orientation yet further numerical simulations are needed to understand the propagation of light trough samples with high chirality.

Next the particle is placed into imaging plane of a confocal microscope 3.7. We excite the sample using laser light at 488 nm. The excitation and the collection of the emitted light is done at five different polarizations. Scanning is done with a voxel, a 3D pixel, with 200 nm lateral size and double height. Depending on the angle between the excitation and the dye molecule dipole a significant amount of signal intensity is observed. For instance, in Fig. 4.15 II bright regions correspond to the director field parallel to the polarization axis

and dark regions to perpendicular. Contrary, the same image obtained at perpendicular polarization Fig. 4.15 III shows the inverse intensity profile. We repeat the scans also at 45° and 135°. Next we use a director field restoration algorithm that assigns a corresponding orientation to each part of the 3D image from the experimental scans. The algorithm used two extrema in the orientation of the molecules as reference points. Completely dark regions typically indicate regions where the molecules point perpendicular to the substrate surface and completely bright regions indicate in plane orientation. Since our samples do not contain any well defined out of plane orientation of the molecules we can only roughly reconstruct the director field inside the sample cell. A sample cross-section of the reconstructed director field in **xy** is shown in Fig. 4.15 V and **xz** in Fig. 4.15 VI. One is now able to pass trough the sample cell and observe the orientation of the director field and observe the structure of the topological defects close to the particles.

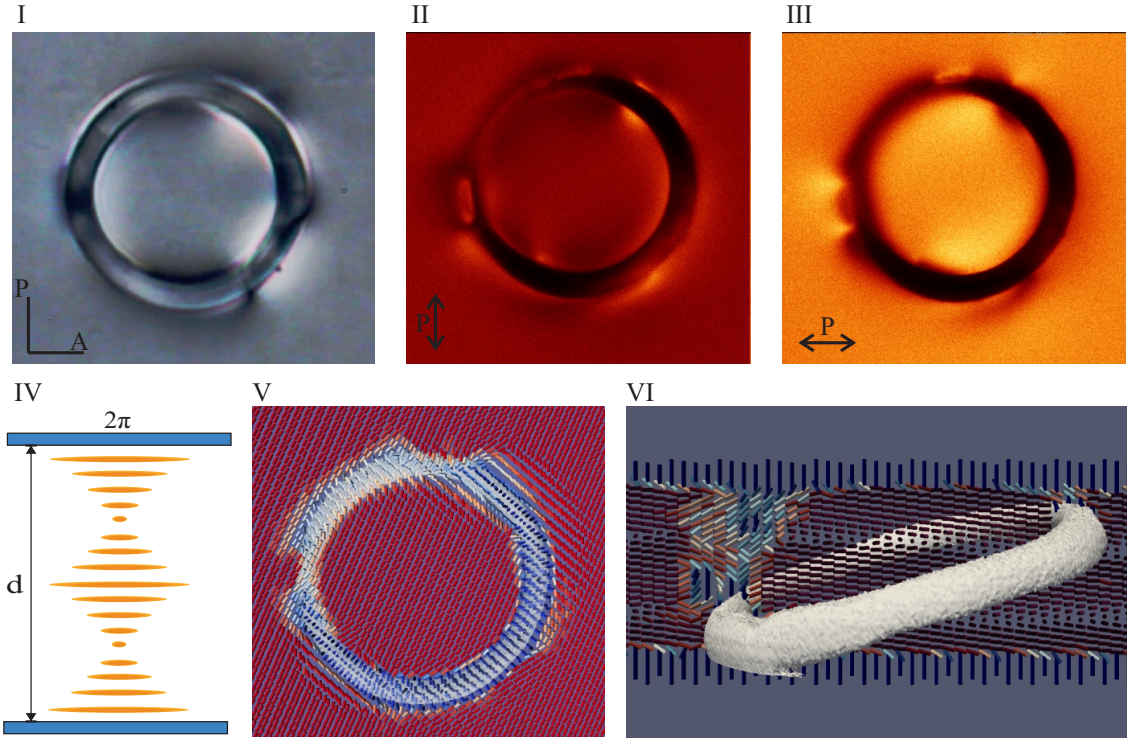


Figure 4.15: FCPM study of colloidal tori in chiral nematic LC. **I** Toroidal particle in a 2 π nematic cell under crossed polarizers. **II-III** FCPM scans of the toroidal particles. **IV** schematic representation of the twist structure. **V xy** cross-section of a reconstructed director field. **VI xz** cross-section of the calculated director field.

In figure Fig. 4.15 VI we observe a complex disorder patch above the colloidal particle. This indicated another draw back of the method that is the screening of the particles itself. Since the particles are not completely transparent the region is basically in the shadow of the particle and therefore the reconstruction could lead us to false conclusions. Further work in this field is needed to understand the complex structure of the director field and topological defects around colloidal particles in highly twisted chiral nematic LC samples.

Chapter 5

Formation of Topological Defects Following Rapid Phase Transitions from the Isotropic to the Nematic Liquid Crystal Phase

In the previous chapter we investigated the formation of topological defects surrounding colloidal particles immersed in nematic LC. The imposed anchoring conditions on the surfaces of the particles create a mismatch of orientation in the nematic director field, creating a singularity. The LC responds by forming its own singularity, that is counteracting the one imposed by the colloidal particle, called a topological defect. In terms of a conservation law the singularities or topological defects, are of opposite topological charge, therefore conserving the total charge of the ground state without a particle.

Topological defects are the direct consequence of symmetry breaking phase transition. When cooling from a disordered phase, localized patches of the ordered phase form, therefore breaking the symmetry. In mathematical terms we define an order parameter that is set to zero in the disordered phase and suddenly increasing to a certain value in the low symmetry phase. If the cooling speed is increased the dynamics of the order parameter can start to lag behind the dynamics of the cooling and the system becomes frozen in time. This process is well described in various physical systems from the formation of cosmological strings, the formation of vortices in superfluids or even the formation of solitons in Bose-Einstein condensates.

Despite the universality of the process experimental observation of the process is still missing due to the sheer experimental difficulties. Therefore the relatively easily observable rapid phase transition form the isotropic to the nematic LC phase is a good candidate to study dynamical process of defect creation. In our experiments we measure the temperature inside the LC and also image the process in detail.

A custom laser illumination system is built and used surrounding a stroboscopic imaging set-up. With exposure times down to 20 ns and a combination of polarization optical microscopy set-up and a stroboscopic imaging technique, we are able to image the phase transition dynamics in detail. First localized laser heating of the LC is used to heat the sample above its clearing point and then as the laser shuts down and the LC starts cooling down. A thick metallic deposit on the sample cell serves as a heat sink, allowing cooling rates of up to $10\,\mathrm{K\,ms^{-1}}$. Conventional camera equipment completely misses the dynamics of the process due to the long exposure times. A typical set of images acquired at a regular frame rate of one hundred frames per second and exposure times of 10 ms is seen in Fig.

5.19.

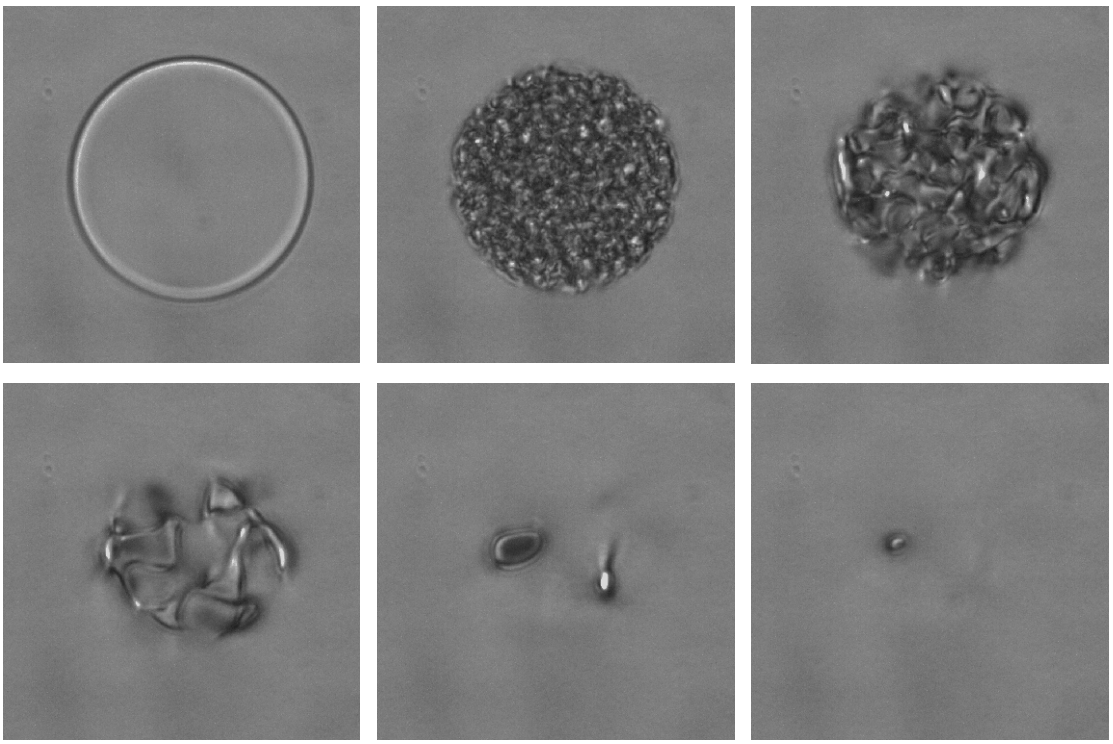


Figure 5.1: Isotropic nematic phase transition images by conventional camera equipment. Exposure times of images are 10 ms. Illuminated by a LED.

The dynamics of the process is extremely rapid and is virtually illusive for camera equipment. The main limiting factors are the amount of light available and the speed of the camera processing the image data. The amount of light from conventional bright field illumination sources, such as halogen or LED lamps, is sufficient enough for exposure times of up to a few tens of microseconds. Therefore the use of our laser illumination system and the stroboscopic imaging technique provides a solution to capture fast dynamics of cooling of the nematic.

Additionally we measure the temperature and the thermal properties of the sample cells used. This allows us to determine the exact temperature inside the cells at the time after the system reaches the phase transition temperature. Combining the imaging data and the temperature measurements, we test one of the most illusive predictions of the Kibble-Zurek mechanism of a freezing time caused in the phase transition dynamics dependence on the cooling rates.

In this chapter we will present the results following an extensive experimental investigation of the formation of topological defects after rapid phase transition. First we take a look at the physical characteristics of the laser illuminations system we developed. Secondly we present the thermal properties of the experimental cell containing the nematic sample. Furthermore we present the POM study of the formation of topological defects and the extensive computer analysis of the experimental data obtained. Finally we combine the data obtained to test the predictions of the Kibble-Zurek mechanism.

5.1 Nanosecond Illumination System Characteristics

The dynamics of the nematic LC passing rapidly across the phase transition typically occurs in the time scales of a few milliseconds and requires the use of extremely rapid imaging techniques. We use a stroboscopic imaging method with a nanosecond laser illumination system [113]. The illumination system is build around a pico second Nd:Yag pulsed laser that is used to illuminate a fluorescent dye sample, Rhodamine 6G in ethanol ($c = 0.01\,\mathrm{mol\,l^{-1}}$). The emitted light is then, using an optical fibre, led to the microscope imaging plane. Details of the experimental set-up are presented in Section section 3.8.

Here we focus on the physical characteristics of the illumination system such as pulse duration and coherence. By observing the emission spectra of the dye solution, presented in Fig. 5.2 a, one can clearly observe two regimes of operation. In Fig. 5.2 a,b.I, without any specific alignment of the dye, we observe a regular fluorescent emission spectrum of the Rhodamine 6G in ethanol with pulse duration of 50 ns Fig. 5.2 b.I. With alignment of the dye cuvette one exceeded, the lasing threshold of the cuvette. The resulting emission spectrum, Fig. 5.2 a.II shows distinct narrow line corresponding to the laser modes of the cuvette. Also the pulse duration falls below the measuring capabilities of our sensor Fig. 5.2 b.II.

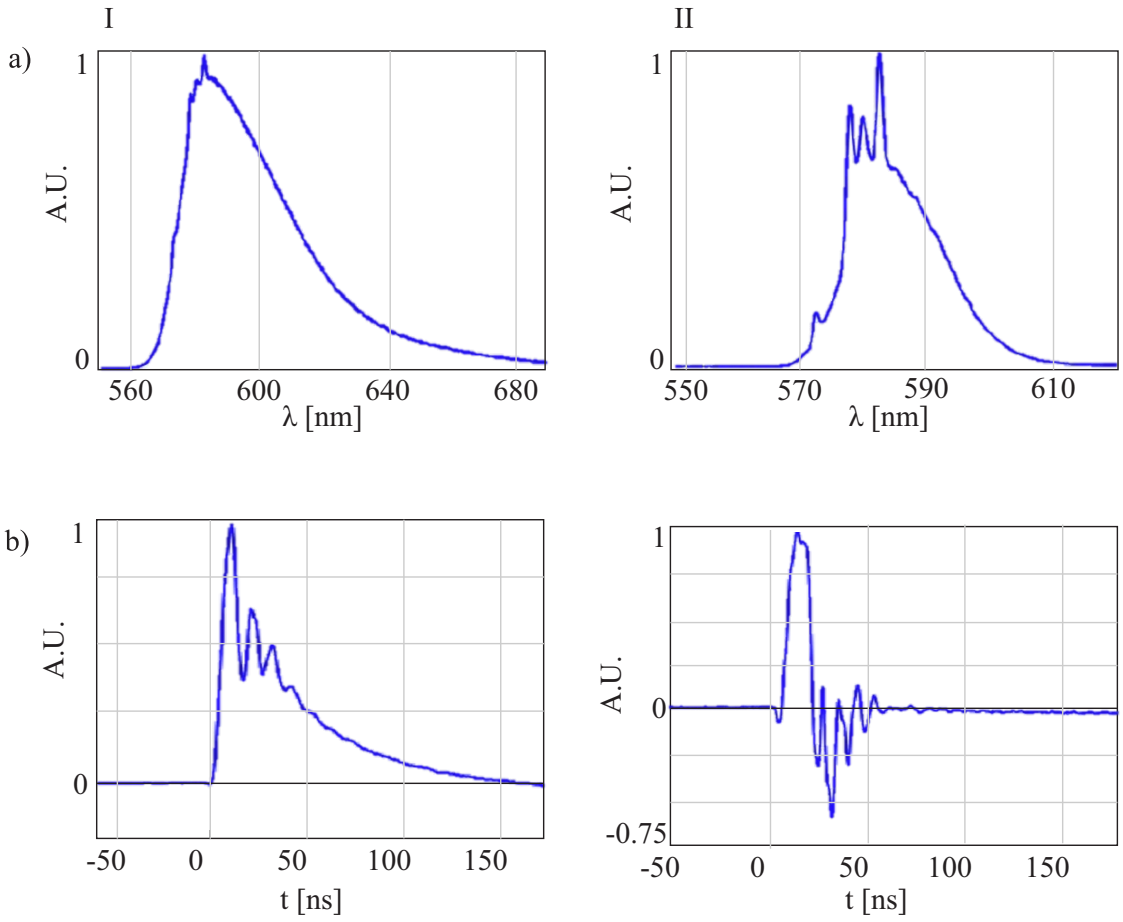


Figure 5.2: Emission spectra and pulse duration of Rhodamine 6G in ethanol inside a cuvette. Spectrum **a)** and pulse duration **b)** of the dye cuvette below **I** and above the lasing threshold **II**. The dye is excited using a pico second laser pulse at 532 nm.

We further test the illumination system using a sCmos camera equipment. The camera

used is designed for low noise imaging, using a combination of imaging sensor design and cooling of the camera sensor to reduce electronic noise. Since we observe the cooling of the nematic LC using POM and crossed polarizers, we first take a reference image of a sample of a isotropic medium, in this case immersion oil, placed in the imaging plane without any kind of illumination source, shown in Fig. 5.3 a.I, and we calculate the average pixel value with standard deviation on every column of the out-take, shown in Fig. 5.3 a.II. Using the 16 bit dynamic range of the imaging sensor the typical sensor saturation of the reference image is $(2.5 \pm 0.3)\,\%$. Next, we move the polarizers in a parallel position and image the same sample with the laser illumination system, Fig. 5.3 b.I where the imaging sensor saturation can reach up to $(86 \pm 1)\,\%$, Fig. 5.3 b.II.

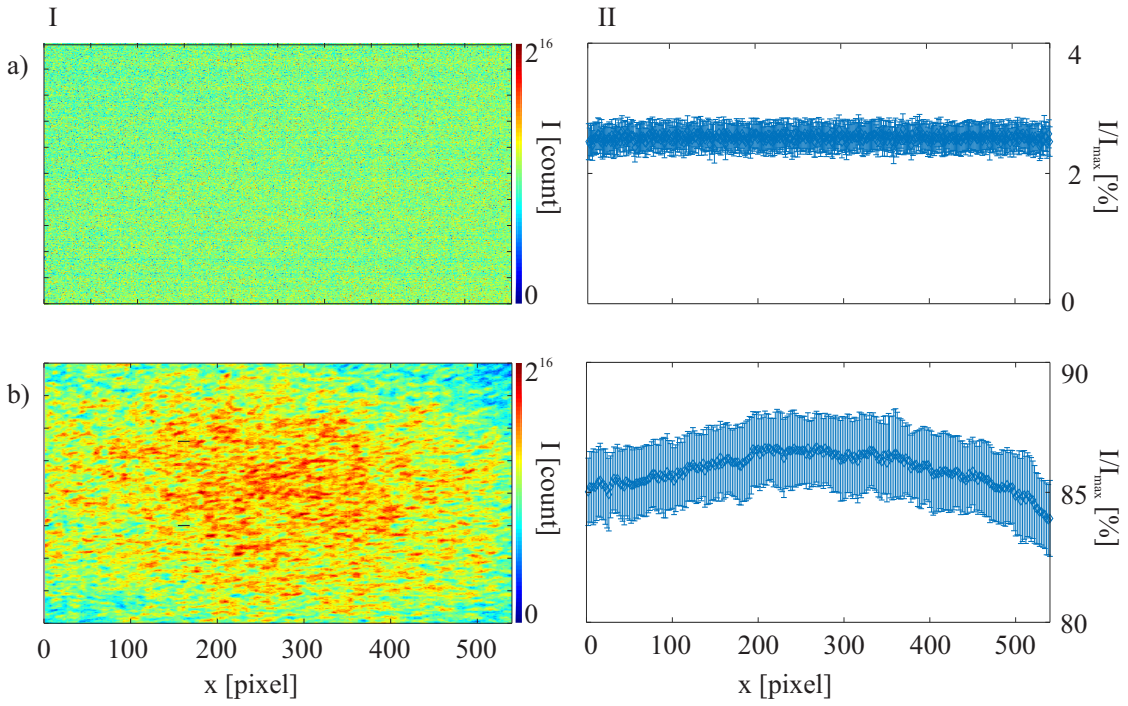


Figure 5.3: Image sensor characteristics. **a.I** 500 by 500 pixel out-take of a reference image of an isotropic immersion oil in the imaging plane under crossed polarizers. **a.II** Saturation values of the imaging sensor averaged over columns with average value of $(2.5 \pm 0.3)\,\%$. **b.I** 500 by 500 pixel out-take of an illumination beam inside an isotropic sample in the imaging plane under parallel polarizers. **b.II** Saturation values of the imaging sensor averaged over columns, with average value of $(86 \pm 1)\,\%$.

Note the presence of speckles, Fig. 5.3, inside the illumination source as the direct consequence of the lasing of the dye solution cuvette. The slight coherence of the illumination source produces interference effects inside the optical fibre used to guide the illumination light onto the imaging plane. One has to keep in mind that optical signal equal or below the speckle intensity can not be observed.

5.2 Thermal Properties of Liquid Crystal Cells While Quenching

To study the formation of topological defects during rapidly crossing the phase transition phase transition we typically use a 2.5 µm thin layer of 5CB sandwiched in between two

glass cover plates of 170 µm thickness. The glass plates are coated with a 50 nm layer of ITO that serves as a heating source and a heat sink at the same time. ITO is used since it allows high absorption of laser light, due to the opto-thermal effect. The laser heats up the LC and after the laser light is shut down the ITO layer allows fast dissipation of the heat due to its high thermal conductivity.

In our experimental investigation we heat up the 5CB layer well above its 35 °C phase transition temperature with a 10 ms laser pulse of a diode laser at 90 mW which creates an isotropic island with a radius of the order of 50 µm. When the heating laser is applied, we first observe a formation of an isotropic island growing in time until at approximately 5 ms the island stops growing, indicating a thermal equilibrium inside the cell. The typical profile of the diode laser pulse is shown in Fig. 5.4, measured over 1000 repetitions. One observes a rise time of approximately 4 ms and a fall time of below 20 µs.

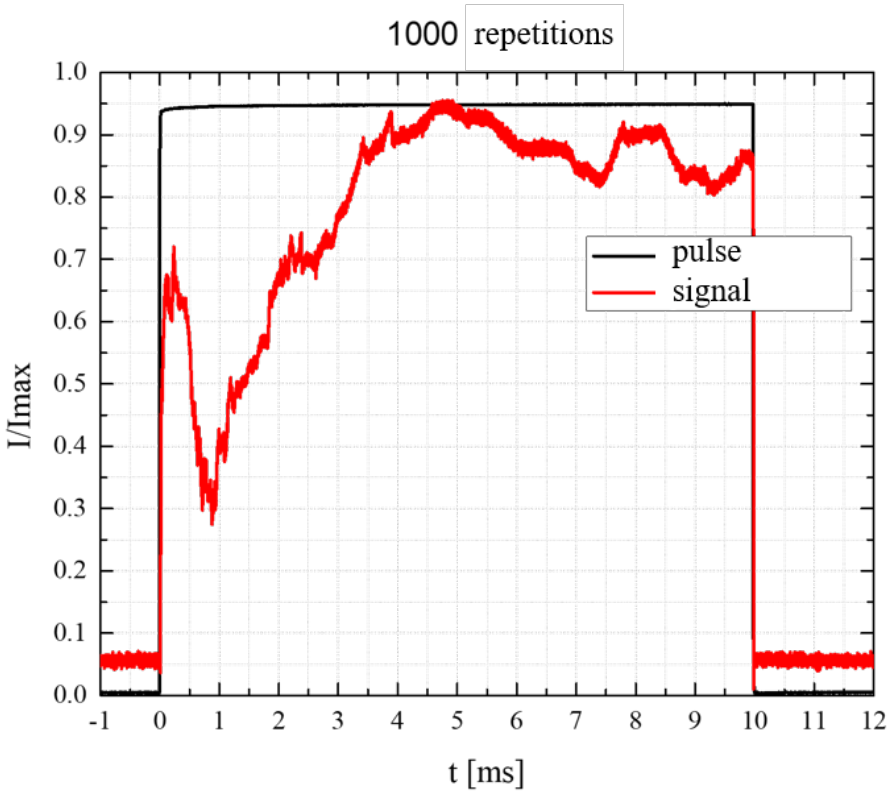


Figure 5.4: The black line indicates the 10 ms signal the delay generator used to externally trigger the heating diode laser. The red line shows a 1000 repetitions average of the heating laser intensity profile, measured using a megahertz photo-diode. Typical rise time of 4 ms and fall time of 20 µs are observed.

The signal width also indicated a high stability of the laser pulses, therefore enabling us to neglect any deviations in thermal properties due to laser instability.

5.2.1 Stationary thermal properties

To study the initial temperature profile, we take three liquid crystals with different nematic to isotropic phase transition temperatures and make glass cells with equal thickness of the

ITO coating (50 nm) and the LC layer (2.5 µm). Three different cells are filled with three different LCs and placed onto the microscope imaging plane and we use the nanosecond illumination set-up to image the maximum size of the isotropic island achieved by laser heating at various laser powers. Since the edge of the isotropic island has to be at the phase transition temperature, the maximum radius of the island can be used to map the temperature inside the cell at various laser powers.

The timing of the experiment is as follows. The experiment is repeated every two seconds allowing thermal stabilization of the system after every run. We repeat the experiment for 10 runs in order to improve the statistical accuracy of the data. The heating laser is triggered first and is run for 10 ms, afterwards at a desired time after the laser heating we trigger the illumination laser and the camera equipment, thereby allowing the 20 ns illumination pulse to expose the imaging sensor and take the instantaneous picture of the sample. We observe the image taken 1 ms after the heating laser shuts down, where the heated area already exhibits signs of nematic order that can be easily distinguished from the surrounding ordered nematic by polarization optics. Due to the first-order phase transition we can connect the border of the heating area directly to the phase transition temperature. We additionally observe the process in cells of the same thickness filled with LCs with a higher phase transition temperature, as shown in Fig. 5.5 a-c. Thus enabling us to determine the temperature profile inside the cell at various laser powers.

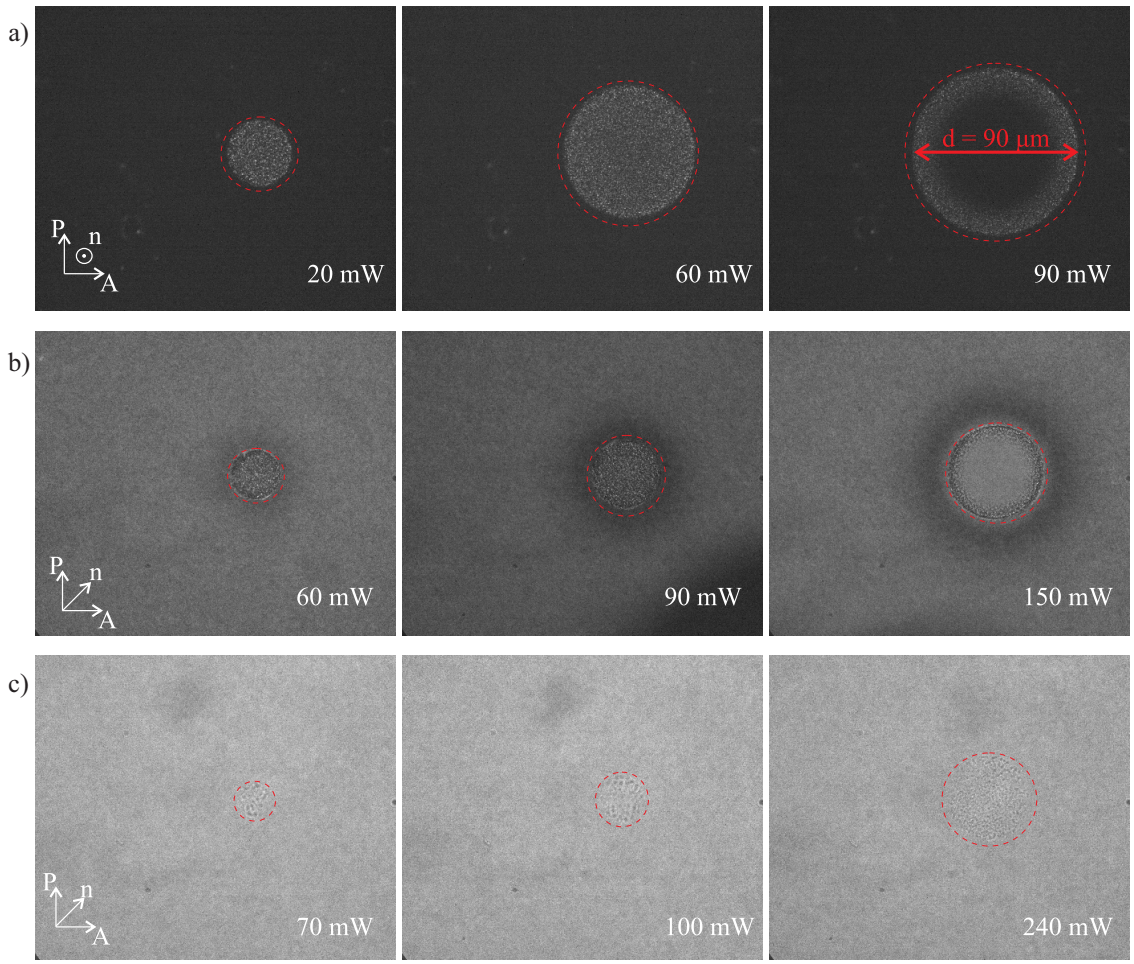


Figure 5.5: **a-c** Experimental images of 2.5 µm thick cells filled with: **a** 5CB, **b** E18 and **c** MLC13300 at different heating laser powers. Images were taken 1 µs after the heating laser was shut down using polarization microscopy. The red dotted line shows the perimeter of the heated area and the red arrow points out the size of the isotropic island of 5CB at 90 mW. Reprinted under thesis dissertation reuse request from Taylor and Francis from [114].

We measure the diameter of the heated areas in all three samples to achieve a diameter versus laser power plot, shown in Fig. 5.6.

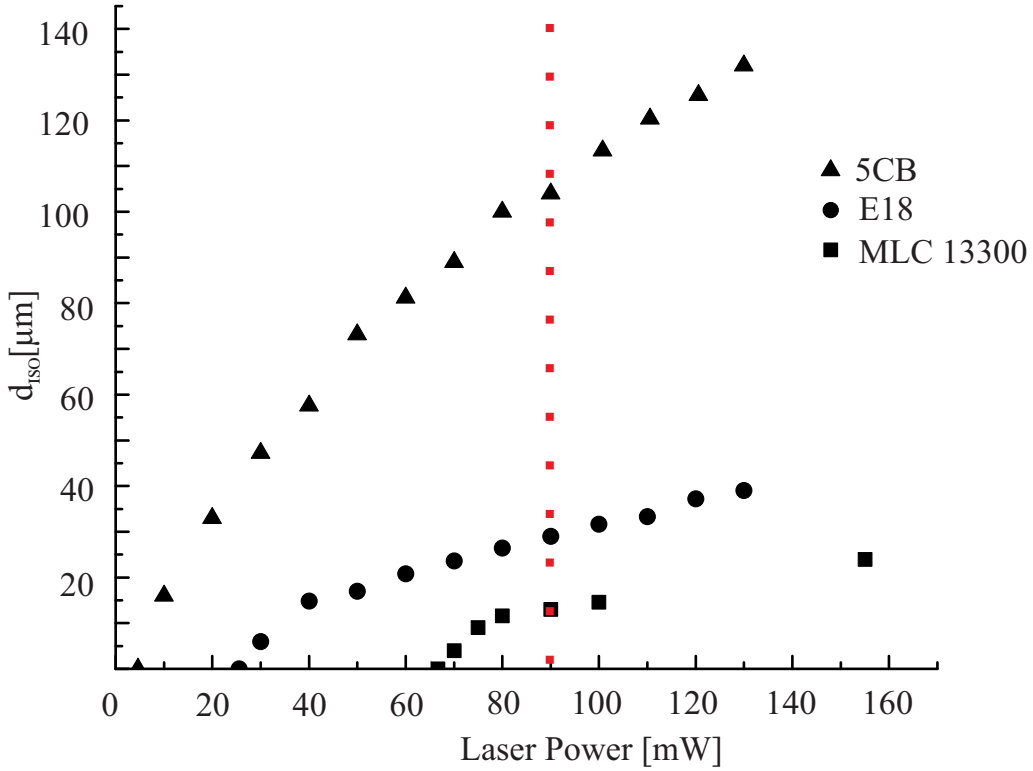


Figure 5.6: Diameter of the heated area at different heating laser powers for 5CB, E18 and MLC13300. The vertical red dotted line indicates the 90 mW line, typically used to perform the imaging experiments. Reprinted under thesis dissertation reuse request from Taylor and Francis from [114].

The nematic isotropic phase transition temperatures of the crystals used are: for 35 °C for 5CB, 60 °C for E18 and 91 °C for MLC-13300. Since all the cells prepared were of practically the same thickness and made from glass slides with the same thickness of ITO coating, we can use the measurements of the maximum diameter of the isotropic island as a temperature scale.

The scale can be read in two ways. First, we look at what minimum laser power we see the formation of an isotropic island in the middle of the heated area. Since the formation of the isotropic phase requires the heating to at least the phase transition temperature, we can have tree points in the temperature versus laser power scale. By fitting a power law dependency, we can create a temperature scale over the whole laser power range, as shown in Fig. 5.7.

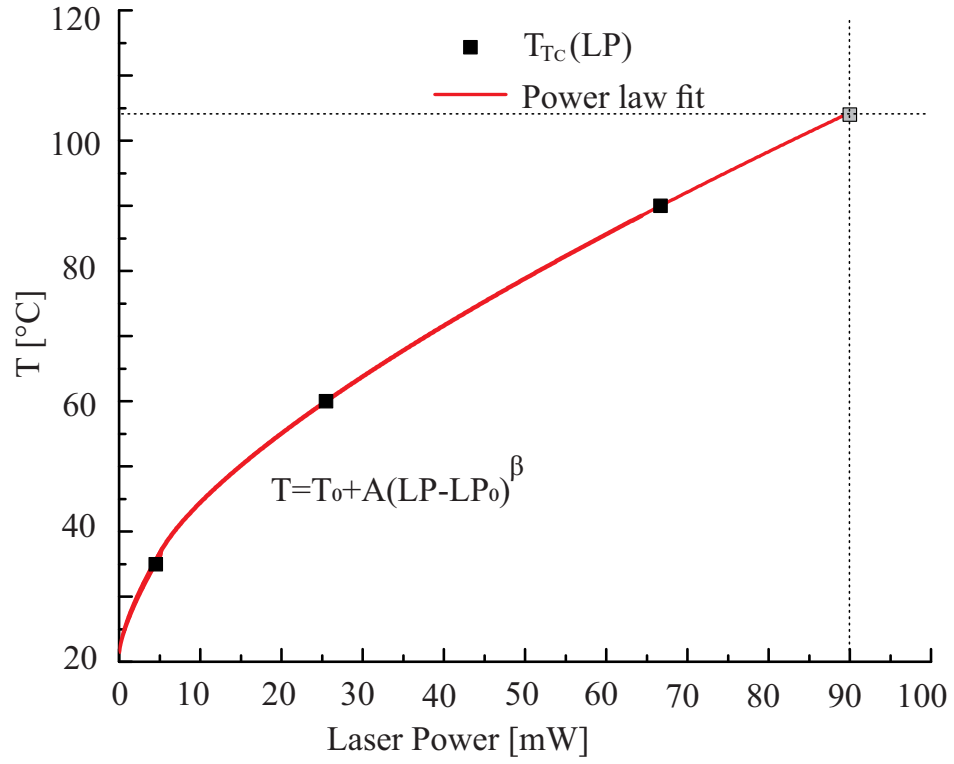


Figure 5.7: Temperature in the centre of the heating spot as a function of laser power. Data is obtained from the minimal size of isotropic island detected on the images of isotropic islands at various laser powers. The gray square indicates the temperature at 90 mW, which is the typical laser power used to perform experiments with 5CB. The red line is a power-law fit of the form $T = t_0 + A\left(LP - LP_0\right)^P$ with parameters $T_0 = 21.8$ $A = 5.3$, $LP_0 = 0.006$ and $\beta = 0.61$. Reprinted under thesis dissertation reuse request from Taylor and Francis from [114].

Using the power law fit $T = t_0 + A\left(LP - LP_0\right)^P$, we can calculate the temperature in the middle of the heated area at 90 mW, a typical laser power used in the experiments, to be 104 °C within 2 °C error. The second deduction from the measurement of the isotropic island size can be done by looking at the size of the isotropic islands at the same laser power. By fitting the basic shape of the heating laser we can determine the peak temperature. The basic shape of the heating laser is determined by imaging the heating laser inside a thin glass cell filled with an ethanol Rhodamine 6G solution, as shown in Fig. 5.8 a. The fit of the Gaussian function onto the data obtained by measuring the radius of the heated area at 90 mW is shown in Fig. 5.8 b.

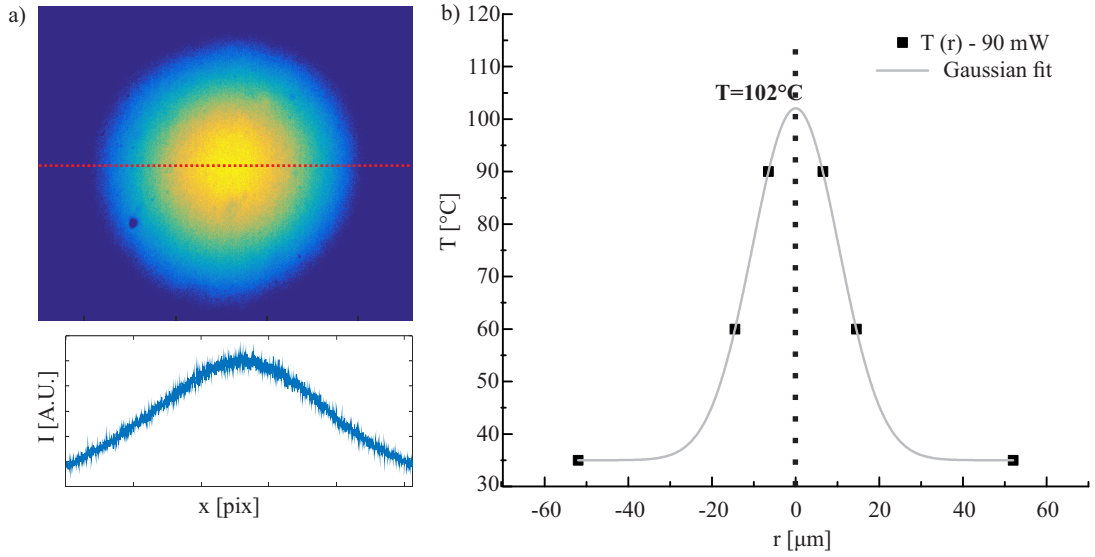


Figure 5.8: The intensity profile of the heating laser **a** is determined to be a Gaussian shape, which is then used to fit to the data of the radii of the heated area at 90 mW. Reprinted under thesis dissertation reuse request from Taylor and Francis from [114].

The maximum of the fitted Gaussian function gives us the temperature in the middle of the heated area, which is determined to be 102 °C with 2 °C error that confirmed the predictions made by fitting a power law dependency onto the point of minimum laser power of the three cells used. Using this fit, we can determine any initial temperature profile inside thin 5CB layer simply by measuring the diameter of the isotropic island created.

5.2.2 Dynamic thermal properties

Typical experiment of rapid cooling of the nematic LC across the isotropic-nematic phase transitions is made with thin layers of LC sandwiched in between two ITO coated glass plates where the ITO serves as the heating source as well as the heat sink. We use 5CB which has an isotropic-nematic phase transition temperature at 35 °C and heat it up using a pulsed diode laser. We determined the initial temperature just after the laser is shut down to be approximately 102 °C in the center of the heated area. We observe the formation of the nematic phase first at the edge of the heated area and in the middle after approximately 1.6 ms depending on the thickness of the cell used. Immediately two questions arise: firstly at what time a certain region of the heated area is cooled below the phase transition temperature and secondly at what temperature we do observe the formation of nematic ordering.

To answer this questions we measured the time evolution of the temperature inside the LC cell using a custom experimental set-up based on thin planar LC cells and POM. We prepare three identical cells of 5CB, E18 and MLC13300 made from ITO covered glass plates that are covered with a thin layer of Polyimid, which is rubbed with a velvet cloth, to assure strong uni-directional planar alignment inside the LC cell. We equip the microscope with polarisers before and after the glass cell and cross them to detect only changes in the retardation of light. We place the thin glass cells inside the microscope imaging plane in such a way that the rubbing direction and the polarization axis of the polarisers are at 45°, respectively. Therefore, the transmitted intensity only depends on

the optical retardation of the sample as shown in Eq. 2.26. The optical retardation of a sample in this configuration depends on the thickness of the sample and the birefringence. The transmitted intensity gives an exact measurement of the birefringence of the LC inside the cell. Since the birefringence of the LC is strongly temperature dependent we can use the LC-filled cells as very fast thermometers.

First, we measure the thickness of the cells used by means of optical interference. We illuminate the cells before filling them with a white light source and we measure the distance of the maxima inside the interference spectrum which are caused by the thin layer interference. The measurements give us the values 2.5 µm for the 5CB cell, 2.3 µm for the E18 cell and 2.4 µm for the MLC13300 cell.

Second, we measure the temperature dependency of the birefringence for E18 using an Abbe type refractometer equipped with a custom heating stage. We measure the ordinary and extraordinary refractive index up to the phase transition temperature 60 °C, as shown in Fig. 5.9 a. The difference of the the values of the indices represents the birefringence shown in Fig. 5.9 b.

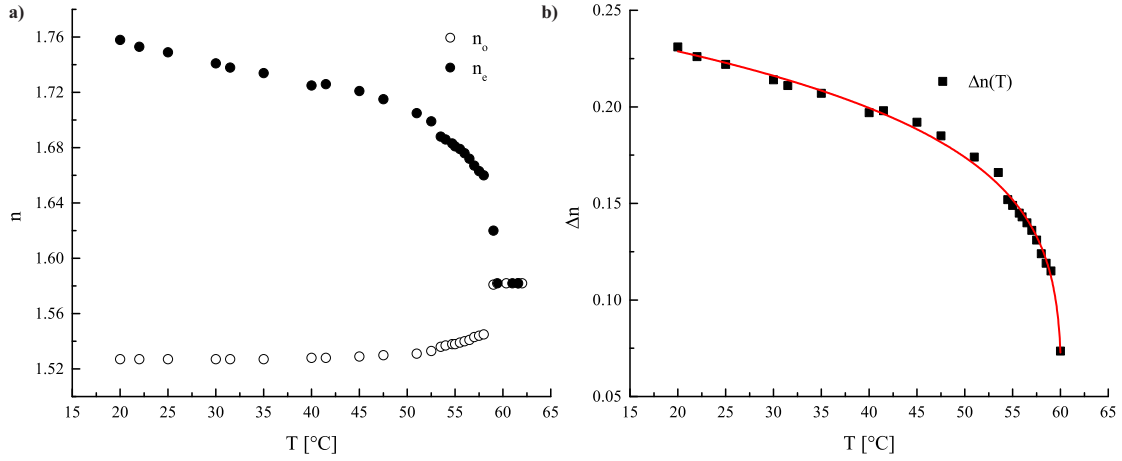


Figure 5.9: **a** Measured temperature dependence of the ordinary and extraordinary refractive index of E18. **b** Calculated temperature dependence of the birefringence, the red line indicates a power law fit. Reprinted under thesis dissertation reuse request from Taylor and Francis from [114].

From Fig. 5.9 b one observes a typical power law dependence $(T/T_c)^{\beta}$ of the birefringence. T_c denotes the phase transition temperature and β is a fitting parameter.

Next, we use a HeNe laser focused onto the imaging plane of the LC sample to a beam spot of 6 µm, to locally measure the transmitted light intensity in the mentioned configuration Section subsection 3.10.2. The intensity is measured by a photo diode with a microsecond response time. The sample is heated up close to the phase transition temperature and left to cool down to room temperature. Note that the phase transition temperature should not be exceeded, since it would cause the emergence of defects that would drastically interfere with the transmittance of the sample cell.

During the fast cooling experiments we assured that the temperature of the experimental room and the microscope was always kept to the room temperature of 21 °C±1 °C. This is important, as it determines the baseline temperature of our experiments. This is the temperature to which the cell approaches at very long times. Next we measure the trans-

mittance of the sample cell at known temperatures to calibrate our thermometer. First we measure the transmittance of the sample cell at temperature above the phase transmission temperature. Here the LC is in the isotropic phase and does not change the polarization of the light and therefore we do not detect any transmittance. Next we measure the transmittance of the same sample cell at room temperature. Here the non zero value of the birefringence of the LC allows some light to be transmitted through the sample. Next we measure the time dependence of the transmittance of the cell that is heated close to the phase transition temperature and left to cool. Transmittance measurements are shown in Fig. 5.10.

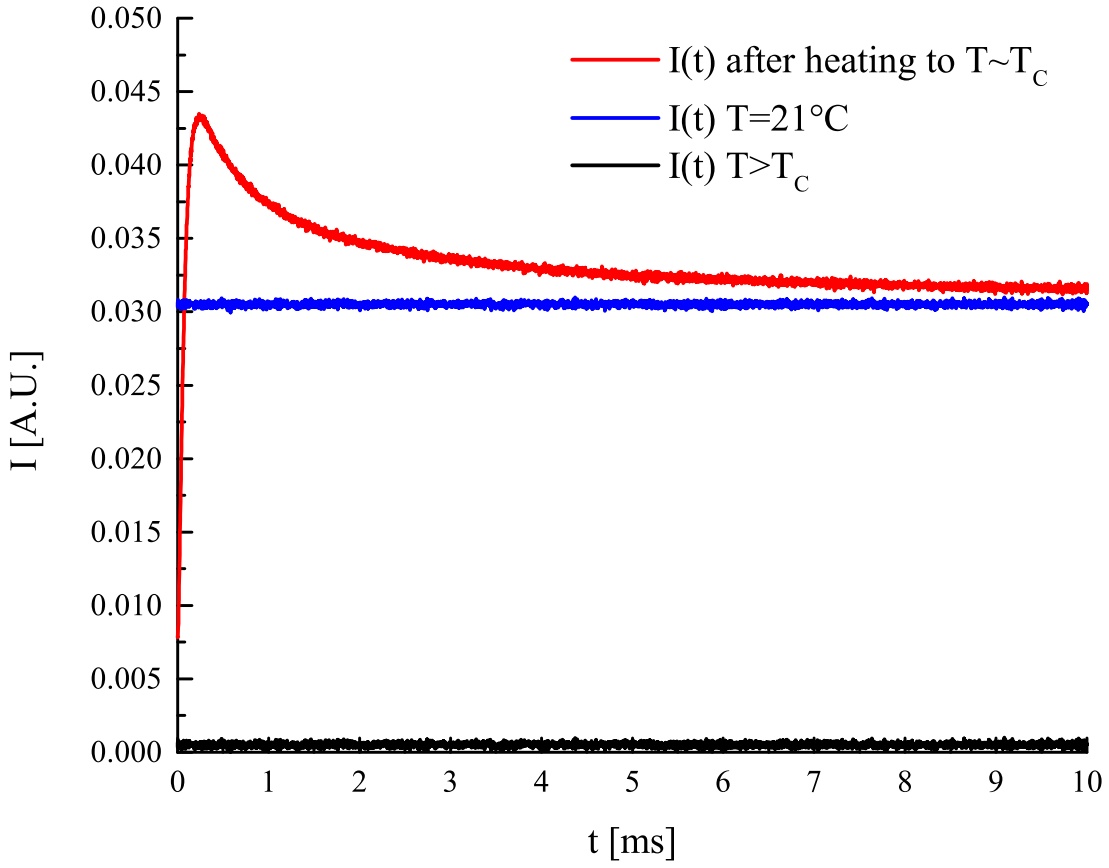


Figure 5.10: Signal of transmitted light intensity on the photo-diode. Here the black line indicates the transmittance of the sample cell heated to the isotropic phase and the blue line the transmittance of the cell at room temperature. The red line in the measured time dependence of the transmittance of the sample cell cooled from the isotropic phase. Reprinted under thesis dissertation reuse request from Taylor and Francis from [114].

We now combine the data from the thickness measurement, the measurement of the time dependence of the birefringence and the time dependence of the transmission of the cell to calculate the time dependence of the temperature inside the cell. Using the known temperature dependence of the birefringence Eq. 2.20 and the transmittance of a LC cell that acts as an optical retarder Eq. 2.26 one can determine the time dependence of the temperature as

$$T(t) = T_c \cdot \left(1 - \left(\left(k\pi - \arcsin\sqrt{\frac{2I}{I_\circ}}\right) \cdot \frac{\lambda}{d\pi}\right)^{\frac{1}{\alpha}} \frac{1}{A}\right) \tag{5.1}$$

where k stands for the retardation order and I_0 for the incoming non-polarized light. We use the measured temperature dependence of the birefringence of E18, shown in Fig. 5.9 in Eq. 5.1 to fit the measured time-dependent transmittance of the thin layer of E18 to obtain the time dependence of temperature inside the thin LC layer. Calculated values are shown in Fig. 5.11.

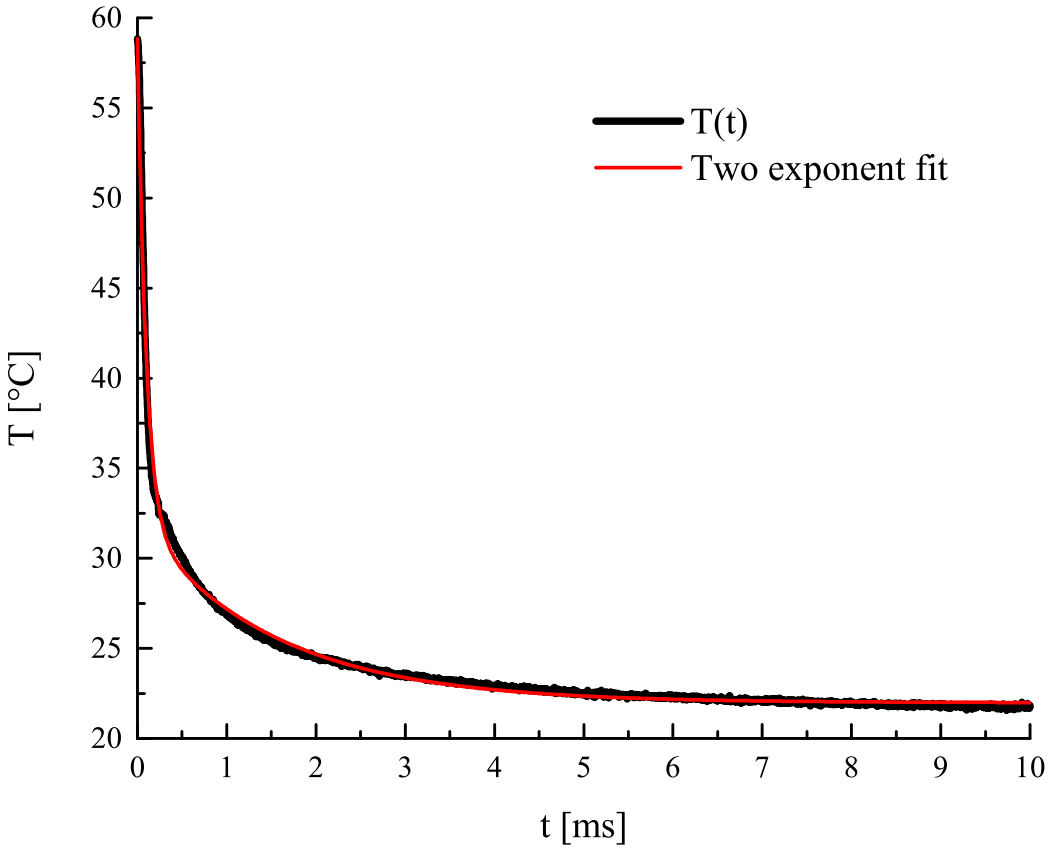


Figure 5.11: Measurement of the time dependence of the temperature of the E18 layer during rapid cooling, starting from 59 °C. The phase transition of E18 is 60 °C. Calculated value of the time dependence of temperature inside the middle of heated area of an E18 layer. The red line shows the best two exponent fit. Reprinted under thesis dissertation reuse request from Taylor and Francis from [114].

A fit to the measured data points provides a two exponent fit

$$T(t) = T_0 + A_1 \cdot \left(1 - e^{\left(\frac{t}{\tau_1}\right)}\right) + A_2 \cdot \left(1 - e^{\left(\frac{t}{\tau_2}\right)}\right) \tag{5.2}$$

here τ denotes the two time constants $\tau_1 = 0.7\,\text{ms}$ and $\tau_2 = 4\,\text{ms}$ and amplitudes $A_1 = 60\,°\text{C}$ and $A_2 = 20\,°\text{C}$, respectively. The equation 5.2 also uses a hidden constant, the room temperature, from combines A_1 and A_2 and deducting from T_0. Typically two exponent fits require a combination of two uncoupled physical processes the system, yet this is highly unlikely since we measure the integral quantity of the total transmission through

the whole sample. A possible reason are the different thermal properties surrounding the two ITO-covered glass plates which are separated by a thin LC thermal isolation layer of LC material.

Next we estimate the error of the two exponent fit shown in figure Fig. 5.11. We measure the temperature difference from the measured value to the fitted value for the first 10 ms after the start of the cooling, shown in Fig. 5.12 a. Also we measure the difference of the

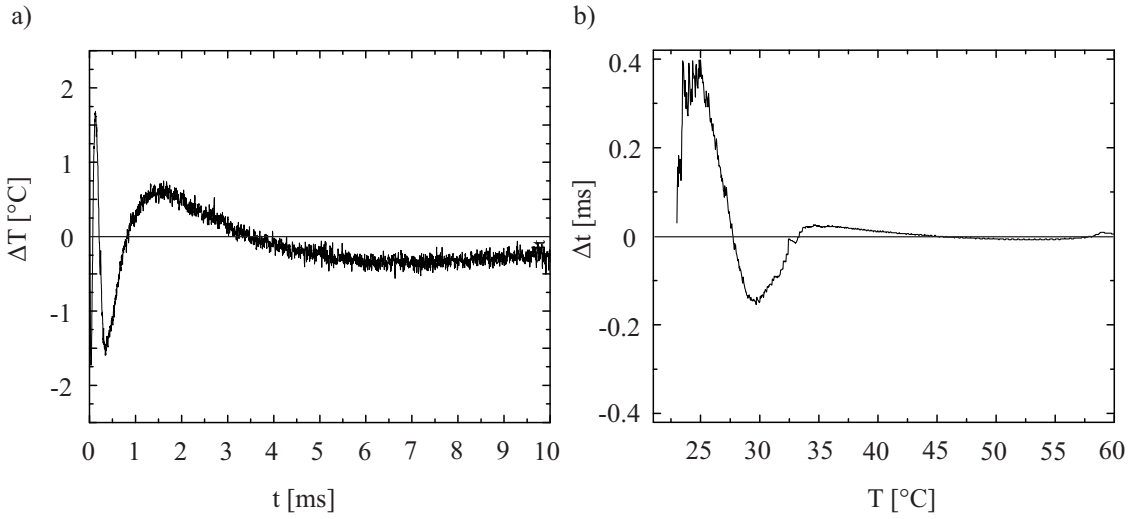


Figure 5.12: Fitting error on temperature measurements.

The basic thermal properties of 5CB and E18 can be treated as equal, since E18 is a mixture mostly containing 5CB with additional LCs, added to widen the nematic temperature range of the material. Therefore, the LC materials can be interchanged without changing the typical thermal properties of the glass cell containing the material. To determine the temperature of the cell containing 5CB, typically used for the imaging experiments, we combine the experimental fit of the initial temperature inside the cell with the experimentally measured cooling function determined inside of the E18 cell. We plot a contour plot of $T(r,t)$, shown in Fig. **??** and use the data to determine the typical cooling rates of the cell in the region of the IN phase transition temperature of 5CB $T_c = 35\,^{\circ}\mathrm{C}$.

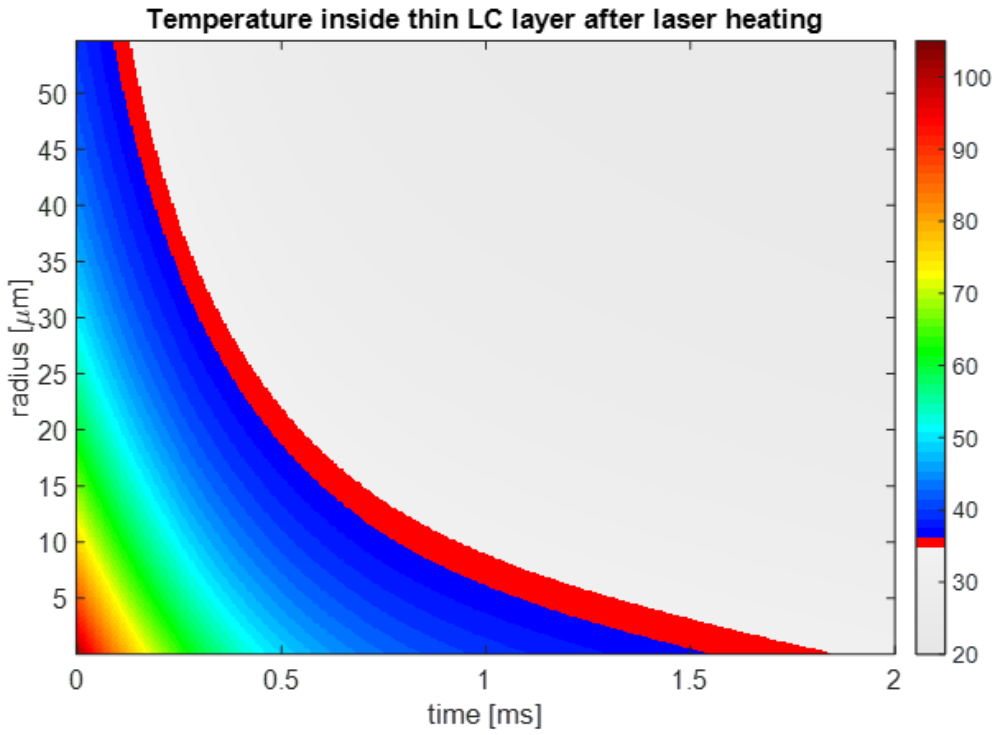


Figure 5.13: Contour plot of the radial and time-dependent temperature inside a 2.5 µm glass cell filled with 5CB and heated by a 10 ms laser pulse at 90 mW. The gray area indicates temperatures below the phase transition temperature of 5CB.

The cooling rates close to the IN phase transition temperature should influence the typical time and size dynamics of the lower symmetry phase formed by the phase transition according to the KZ mechanism [50], [65], [68]. Further implications will be discussed later. We see, that cooling rate at a certain temperature $dT(t)/dt$, for small temperature drops from the initial temperature to the IN phase transition temperature, are only depended on the short time exponent τ_1 and for large drops on τ_2 of the fit Eq. 5.2. We plot the initial spatial dependent temperature $T(r)$ for the cell after laser heating and overlay the plot with the correspondent radial dependency of the cooling rates in Fig. 5.14.

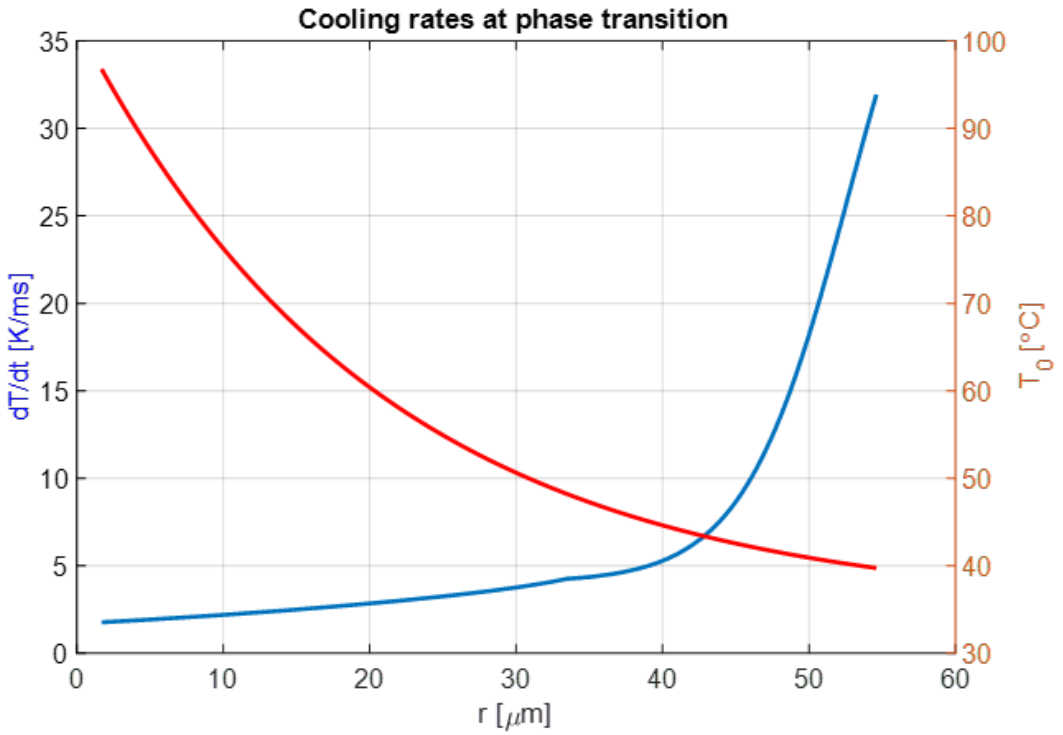


Figure 5.14: Radial dependence of the initial temperature of the 2.5 µm thick cell of 5CB after laser heating indicated by the red line and right scale bar. The blue line indicates the radial dependence of the cooling rates at phase transition temperature with scale bar on the left. The fastest cooling rates across Tc are obtained at large radii, however, the initial T is close to Tc at those points.

5.2.2.1 Thermal characteristics of thick LC layers

We typically use thin layers of LC inside a glass cell to assure a homogeneous initial temperature profile normal to the glass plates i.e. throughout the 2.5 micrometer thickness of the nematic LC. Nevertheless, we measure the thermal profile in a much thicker, 17.5 µm thick layer of E18. We expect that due to the greater thickness the sample would go through several retardation maxima whilst cooling. We observe the sample under the microscope and heat it up using diode laser pulses with step by step increasing laser power. We observe that when the mid point is heated close to the isotopic phase the regions of LC which are closer to the ITO are heated well above phase transition temperature. This hinders the light transmission measurements since it gives us the total change in transmission through the whole sample. In this case two effects would affect the transmission, the change of birefringence due to cooling and the formation of topological defects due to the cooling through the isotropic to nematic phase transition. We use our nanosecond illumination source to image a small focal volume in the middle of the glass cell as it is cooled. We observe a radial interference pattern caused by the radial difference of the optical different optical retardation of the sample, as shown in Fig. 5.15 a. A cross-section of the pattern is taken and observed over time, shown in Fig. 5.15 b.

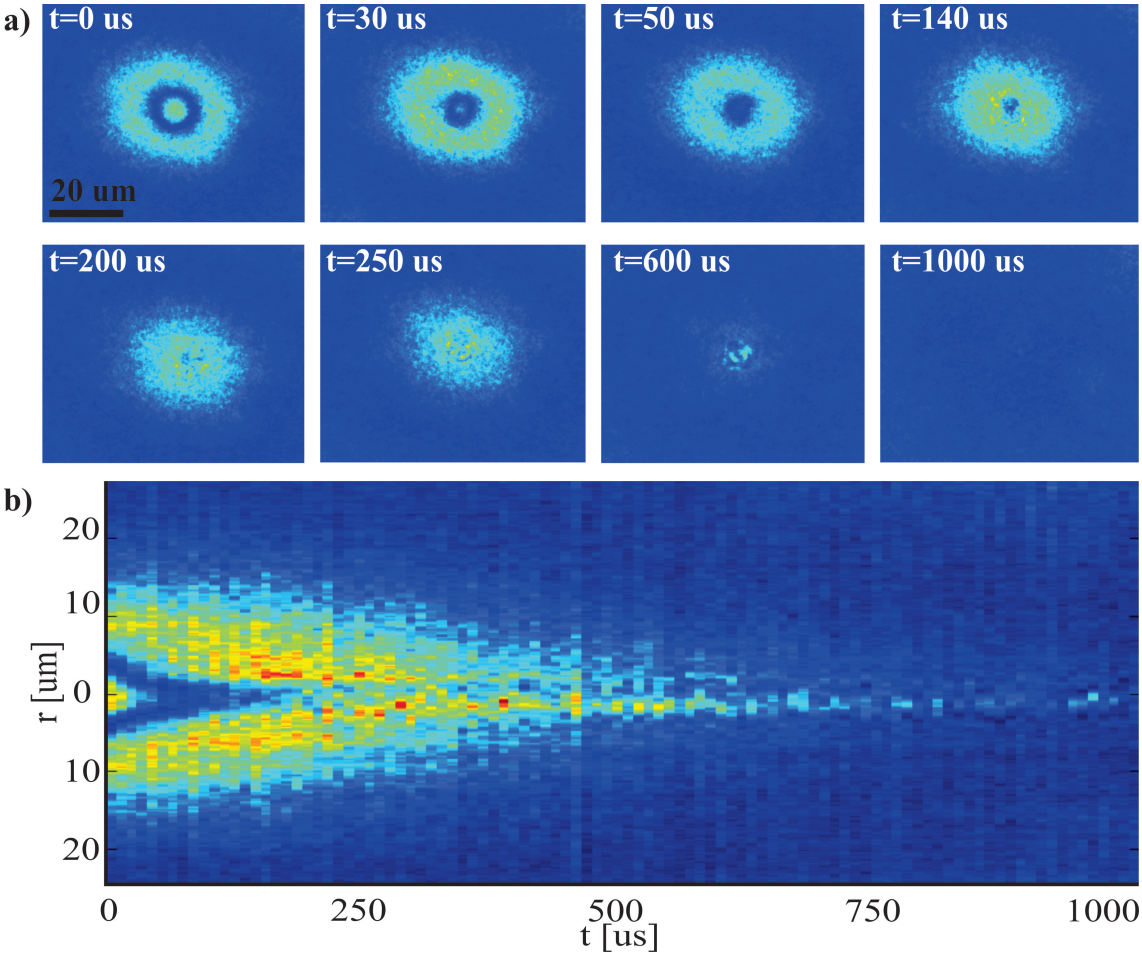


Figure 5.15: Sequence of stroboscopic images of a 17.5 µm thick planar cell of E18 taken between crossed polarisers set at 45° at different times after switching-off the heating laser. The light intensity pattern is caused by local temperature variations and therefore different birefringence of the E18 LC. **(b)** The set of light intensity cross sections taken for the frames shown in **(a)** and also other frames at different delay times. The cross sections are taken through the centre of the heated region as illustrated in the first frame taken at zero delay. Note that images are gray-scale and only for visualization purposes presented in false color. Reprinted under thesis dissertation reuse request from Taylor and Francis from [114].

Using Eq. 2.26, we determine the temperature profile at every given time step for every time steps given in Fig. 5.15 b. Note that the sample is heated to approximately 52 °C to assure the out-of-focus part of the LC is not heated to the isotropic phase, which would cause a phase transition and drastically change the optical properties of the sample while cooling due to generation of defects. Next we use the reconstructed temperature time dependences from the 17.5 µm thick sample cell, as shown in Fig. 5.15, and compare it to the thin 2.5 µm, as shown in Fig. 5.11, both filled with E18 for the first 250 µs, as shown in Fig. 5.16.

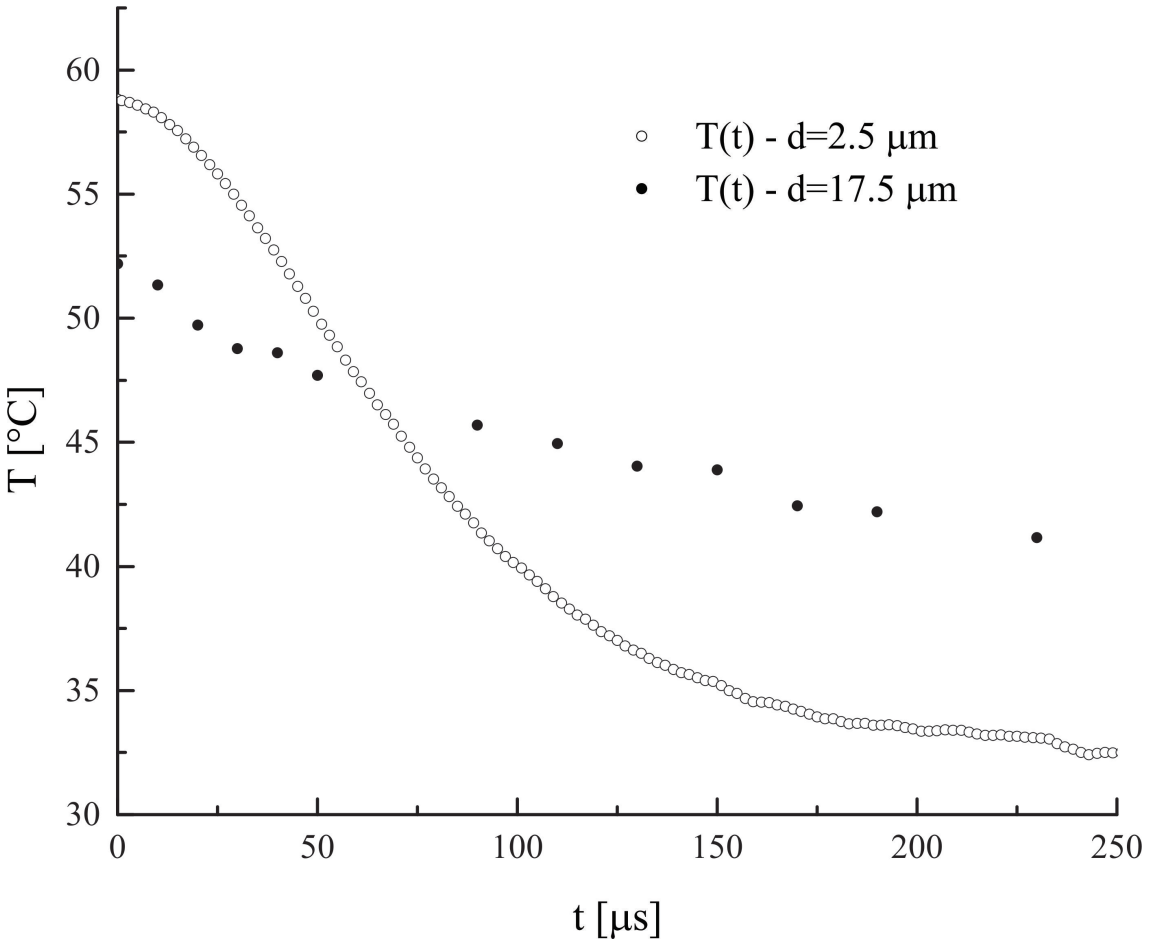


Figure 5.16: A comparison of the cooling inside thick and thin layers of LC while cooling. Open circles are data reconstructed from the measurements of transmitted light intensity between crossed polarisers for the 2.5 µm thick sample cell. Full circles are values of temperature, as reconstructed for the 17.5 µm thick sample cell filled with E18. Reprinted under thesis dissertation reuse request from Taylor and Francis from [114].

We can observe that the thin layer of LC material cools for approximately 25 °C in 250 µs while the thick layer cools only for 10 °C. We attribute this huge difference of cooling rates to more efficient heat conduction from the thin 2.5 µm liquid crystal layer to the metalic ITO layer on the substrates which which acts as a heat sink. On the other side, in the thick LC layer the heat has to pass first through a thick layer of LC, which is an thermal insulator, to reach the heat sink. This isolation of the liquid crystal by the liquid crystal is one of the reasons, we use thin sample cells to study rapid phase transitions.

5.2.2.2 Numerical simulations of thermal properties

We use a commercially available finite element numerical simulation software COMSOL to study the thermal properties of thin LC layers inside the glass cells. The software allows us to test out the effects of various combinations of parameters which would require extensive experimental work in the laboratory setting. We build the simulation around a 1 mm long composite block where the layers represent the materials found in the layers of the glass cells used. This size was chosen since it is by a factor of 5 bigger than the field of view of the microscope set-up. When creating the basic geometry of the cell we take into account

the basic layout of the experimental sample cell placed on the microscope. The basic thermal characteristics of the cell are presented in Section subsection 3.10.4. We simulate the characteristics of the hating laser, as seen in Fig. 5.4 by implementing a 4 ms rise time on the simulated heating laser. The laser is allowed to heat up the sample via absorption through the ITO for 10 ms. As the laser is turned off, in the measured fall time of 20 µs the heat is allowed to dissipate through the ITO layer into the glass substrate and eventually into the surrounding through the microscope. A typical simulation cross-section at the laser shut-down time is shown in the **xy** projection Fig. 5.17 I and as a **xz** projection Fig. 5.17 II. Not that the LC layer is approximately 100 times smaller than the simulation box, we therefore highlight the temperature profile through the sample cell. As the plane depicts the temperature distribution in the mid point of the LC layer, Fig. 5.17 I, one clearly sees a spherically symmetrical temperature distribution. In Fig. 5.17 II one also clearly observe a temperature difference in the top and bottom region of the cell, caused by the absorption of the heating light firstly on the bottom ITO layer and secondly on the top layer. By highlight the heat fluxes inside the cell, one can determine that the main heat dissipation occurs through the ITO layer and almost no lateral heat fluxes are present. This confirms the notion that as the heated isotropic islands cool their diameter does not change, what would be an indication of lateral heating of the LC by the LC itself.

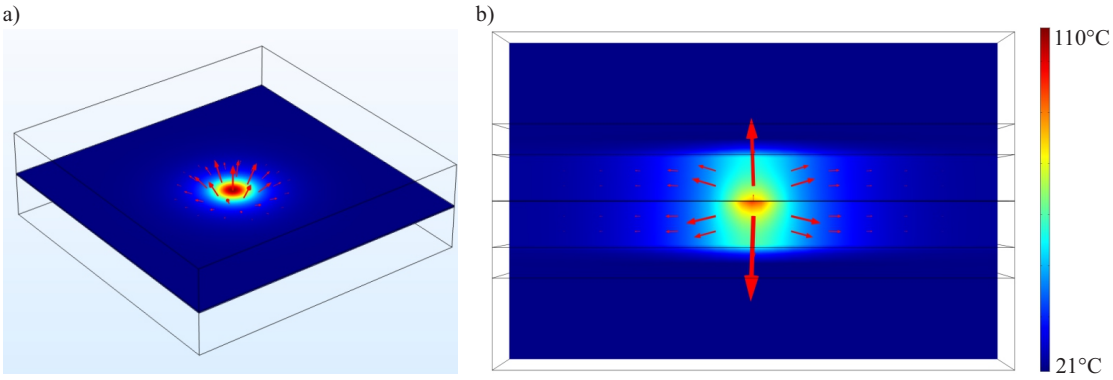


Figure 5.17: *I* xy cross-section of the simulation box indicates a spherical initial temperature profile inside the LC layer. **II** The xz cross-section indicates the difference in the temperature through the z directions. Red arrows indicate the heat flux direction and amplitude.

After the system is heated for 10 ms, the laser is shut down and the LC rapidly cools to room temperature. We measure the temperature inside the 5CB layer in the center close to both ITO layers, shown for the first 20 ms in 5.18I. After the two step heating, caused by the rise time of the laser, one can observe a difference in temperature of approximately 20 °C at the end of heating. As the system cools to room temperature we can measure the cooling speed at the phase transition.

We also want to study the interesting two-exponent fit observed in Fig. 5.11. We change the laser power in the simulation to the laser power used to heat up the sample of E18 close to the phase transition temperature, and observe the cooling of the sample, shown as a lin-log plot in Fig. 5.18 II. One can observe a significant two exponent behaviour of the cooling, with fast cooling for the first 0.5 ms and a much slower cooling at later times.

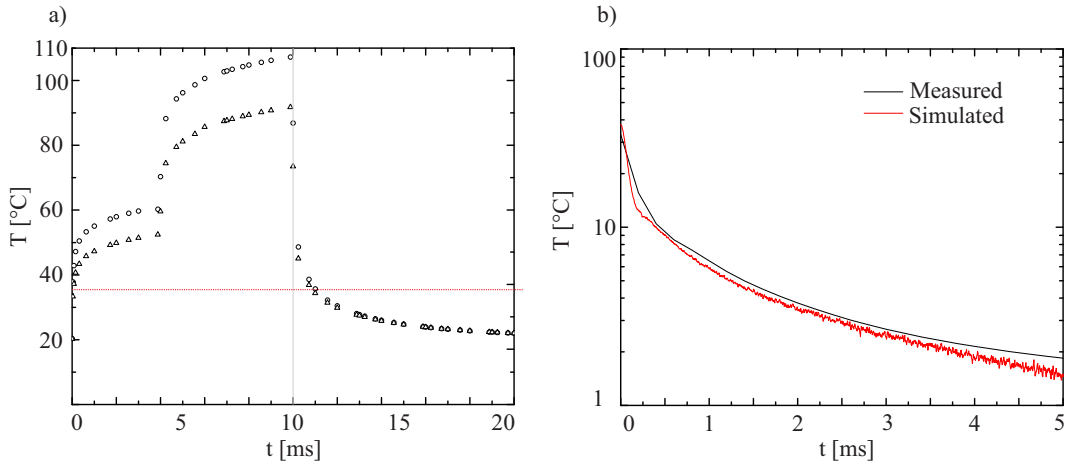


Figure 5.18: **I** Dynamic temperature measurement of the 5CB layer close to the two bounding ITO layers. **II** Comparison of the measured and simulated cooling inside a thin E18 layer.

5.3 Polarization Optical Microscopy Study of Rapid Phase Transition

We study the formation of topological defects after a sudden temperature driven phase transition from the isotropic to the nematic liquid crystalline phase. Due to the first-order phase transition characteristics of the phase transition, we expect a coexistence of the two phases right at the phase transition. The high difference of the optical properties of the two phases makes them rather easily distinguishable using conventional polarization optical microscopy techniques. Our experimental sample, that is presented in detail in Section section 3.3, is typically a thin film of nematic LC sandwiched in between two ITO-coated glass plates. To induce a phase transition we use a laser light pulse to locally heat up the LC way above its clearing point and observe the sample as the laser shuts down.

Using conventional camera equipment we are only able to image the coarsening dynamics and the annihilation of topological defects occurring long time after the phase transition. The limitations are mainly caused by slow read out times of camera equipment and low imaging sensor sensitivity. The formation of ordered domains and topological defects remains hidden due to time scales in the micro second range.

We use a combination of stroboscopic imaging and a laser illumination system, to take a glance at the processes at time scales, only limited by the illumination pulse duration. The completely random nature of the phase transition dynamics enables us to use stroboscopic imaging, i.e. taking of individual snap shots in each experiment and than repeating the experiment at different delays. Individual snap shots can then be combined into a movie of the whole process, with any desired sampling rate. Also, due to the random nature several thousand images can be taken at any given time-step, therefore increasing the statistics of the investigation. The second part of the imaging equipment is our custom illumination system that enables us to produce a 20 ns light pulse with 50 nm bandwidth. Using this system and a POM set-up with crossed polarizers we are able to neglect the imaging sensor acquisition time since the sole exposition of the sensor occurs in 20 ns of the illumination pulse. A typical image of a rapid phase transition observed using crossed polarizers is presented in Fig. 5.19.

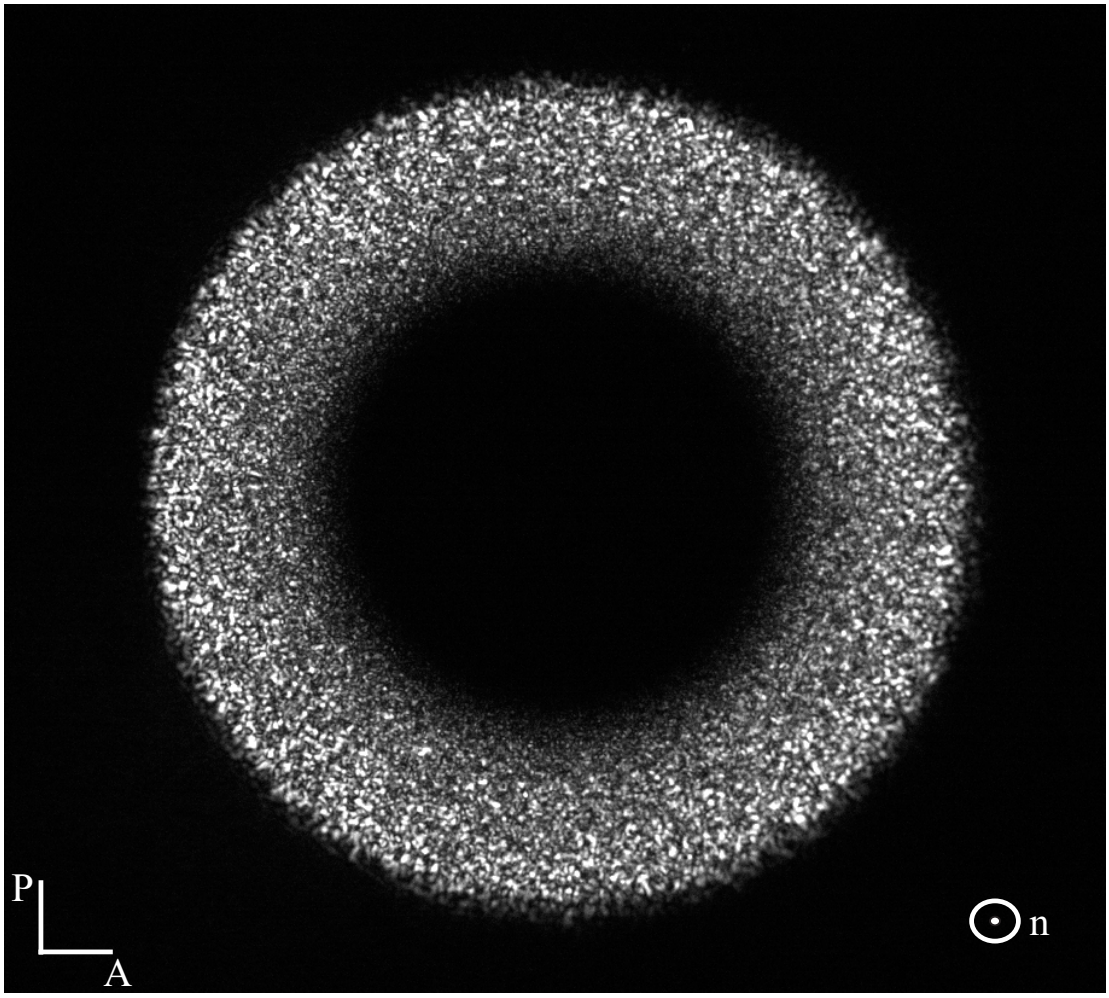


Figure 5.19: A typical image obtained using POM with crossed polarizers, a sensitive sCmos camera and a nanosecond laser illumination system. The image shows the formation of topological defects 1 ms after the start of the cooling. Exposure time of the image is 20 ns.

A digital pulse delay generator with accuracy in the pico second range is used to assure accurate timing of the experiment. The time scales of the experiment are as follows. First, the thin layer of LC is heated for 10 ms. As it is left to cool to room temperature we set the camera equipment to expose the imaging sensor. Since no light is hitting the sensor yet, the sensor can be left in this open position for a long amount of time. At a desired time we use another trigger signal from the delay generator to trigger the illuminations system, illuminating the imaging sensor. The system is left to thermally stabilize for two seconds and then the experiment is repeated. By simply adjusting the delay from the start of cooling to the trigger of the illumination, one can observe the process at any desired time.

5.3.1 Image processing algorithm

Using our nanosecond illuminations system and POM set up we are able to create several thousand images of the formation of topological detects. Processing such an amount of images requires development of a custom image processing algorithm, that can cope with

this amount of data whilst extracting the physical data contained in the images.

The algorithm is written in the software environment Matlab and the main results are plotted in Origin lab. The image acquisition settings of the Andor Neo camera are set inside the Andor Solis software package and the timing and delay of the systems are set using a pico second digital delay generator also triggered using Matlab. We chose full image resolution of 2180x2560 pixels with 12-bit gain allowing low noise acquisition whiles still providing a large dynamic acquisition range of the imaging sensor. The delay between the heating laser and the camera exposition is freely adjustable using the delay generator.

Due to the random nature of the phase transition dynamics, we are able to take up to 1000 images to obtain a statistical significant amount of data, at any given time step. The images are then stored using a 16 bit interpolation as .tif formats. The images are obtained using a POM set-up where the polarizer and analyzer are crossed, producing images with extremely high dynamic range. For visualization we are relying on the use of false-color color maps. For instance, we mainly use the color map "jet" that interpolates a typical dynamic range of 255 gray scale values to there times 255 values of red, green and blue.

The algorithm can be simply explained using a typical image obtained in the experiment. For instance, in Fig. 5.20 a an typical image obtained during the quenching experiments shows the process 1.2 ms after the laser heating. It is apparent, that due to the Gaussian nature of the heating laser beam a spherical region will form. We notice three distinct regions on the image. If we move from the inside of the image outwards, we first observe a region of LC still heated above the phase transition temperature inside a circle of highly unordered region full of domains and defects - called the defect phase. Surrounding those two regions of unordered LC there is a highly ordered nematic region. The strong alignment is caused by the homeotropic anchoring conditions imposed by the surrounding surfaces. A typical intensity cross-section, as shown in Fig. 5.20 b, in the middle of the heated area, also highlights there regions. We observe the lowest intensity in the isotropic phase, a slightly larger intensity in the ordered nematic phase, caused by increased thermal fluctuations, and finally a significant increase of intensity in the defect phase caused by optical retardation.

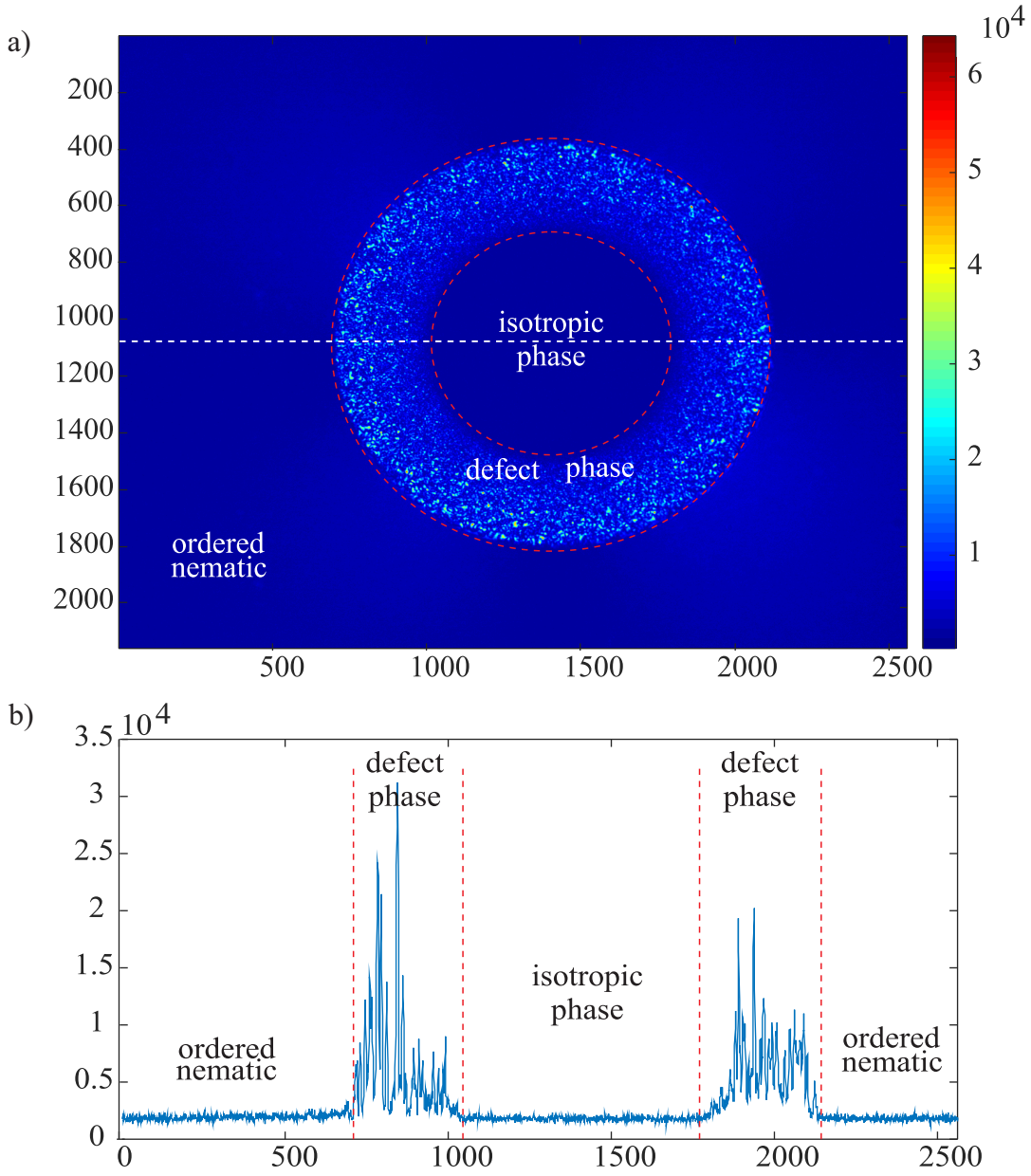


Figure 5.20: **a** A typical image and **b** intensity cross-section highlight three regions in the image. A highly disordered isotropic phase, an ordered nematic phase and a defect phase where nematic order only starts to form.

Observing the image we see that individual patches of light form right at the edge of the isotropic region, indicating the presence of the first domains of ordered nematic after the phase transition. Since we want to study the formation of those patches, we need to extract the position and other physical characteristics of the light patches using our algorithm.

We start by importing the experimental images into the Matlab environment where they are presented as a data array, such as M(x,y,I). We first use an integrated deconvolution routine to minimize the distortions on the image due to the optical characteristics of the experimental set-up [95]–[97]. Next, a theoretical point spread function (PSF) is used to deconvolve the images. An approximation of the point spread function is a simple Gaussian

function with FWHM set to the diffraction limit of our system. The diffraction limit is calculated as $\lambda_{diff} = \lambda_o / (2 \cdot NA)$ where λ_o denotes the illumination wavelength and NA the numerical aperture of the imaging objective.

A zoomed out section of a raw experimental image, Fig. 5.21 I is a convolution of the raw experimental data and the distortions of the imaging system. By using a theoretical PSF Fig. 5.21 III one is able to remove the distortion from the image and expose raw experimental data Fig. 5.21 II.

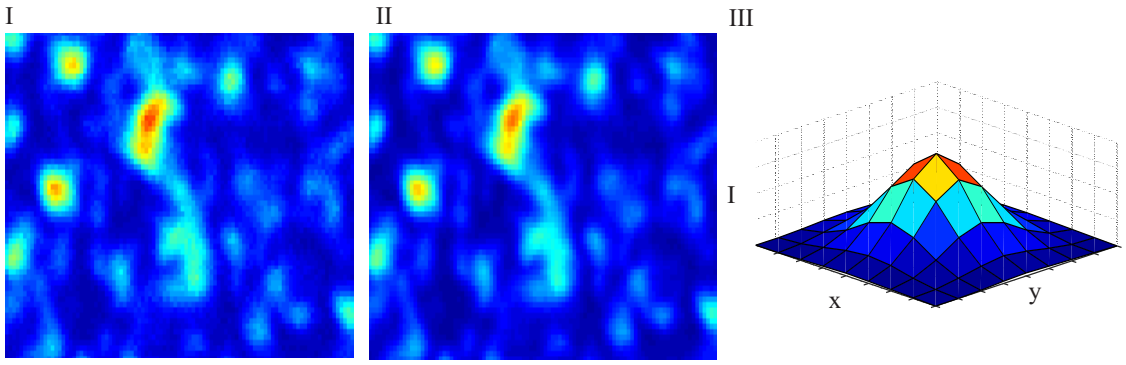


Figure 5.21: **I** Section of a raw experimental image. **II** The same section after the deconvolution procedure. **III** The theoretical approximation of the PSF.

We determine the exact central point of the heated area in each image, to eliminate any jitter in the position of the heated area due to heating laser instability. An automatic routine is used, which thresholds the image above an intensity value slightly higher than the typical intensity in the ordered nematic phase. All further work refers to the center of the determined area, as shown in 5.22. To also investigate the processes at the edge of the heated area we extend the investigation radius to 5 % larger than the determined radius r_{ISO}.

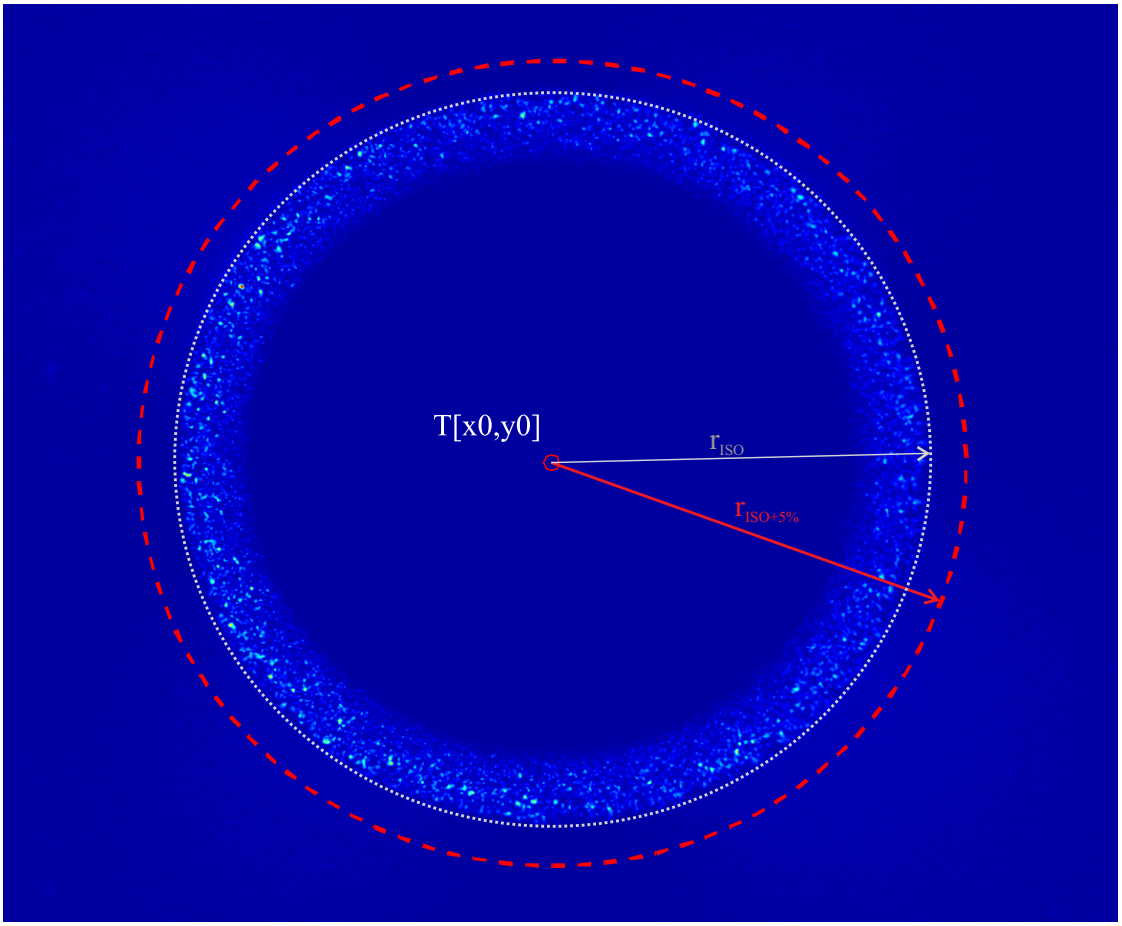


Figure 5.22: Properties of the heated area. By thresholding the image above the typical intensity of the ordered nematic phase, we determine the central point $T[x_0, y_0]$ and the radius of the heated area r_{ISO} (gray vector). We use a slightly 5 % larger radius to also include the edge in the investigation (red vector).

Next, we determine the positions and the properties of the light patches observed in the image. We can imagine the light patches on the image, as regions of the sample where the local orientation of the nematic ordering allows retardation of light to change and therefore, some light is passed by the analyzer.

To determine the position of the light patches we want to determine the location of their maxima in intensity. This is done by determining the intensity local maxima row by row and column by column by means of simple derivation, where the intersections of the determined local maxima are determined as true global maxima. Local maxima created by shot noise or random noise not removed by the deconvolution routine, are eliminated by the use of a simple threshold condition in the algorithm. We eliminate any maxima with a width of less than 3 pixels in any direction. This value is chosen since it roughly matches the diffraction limit of light or 180 nm on the imaging plane. This can be justified by the fact that due to the nature of light propagating through any optical system, even a point source is spread out and is detected at least as the size of the diffraction limit of roughly 200 nm.

Finally, to remove random patches of noise, we set a condition where the intensity of the maximum detected has to be greater than the average value of the intensity in the

isotropic phase. Thus enabling us to extract the light patches when they just start to appear from the isotropic melt. A typical images with marked intensity maxima found by the algorithm is presented in Fig. 5.23.

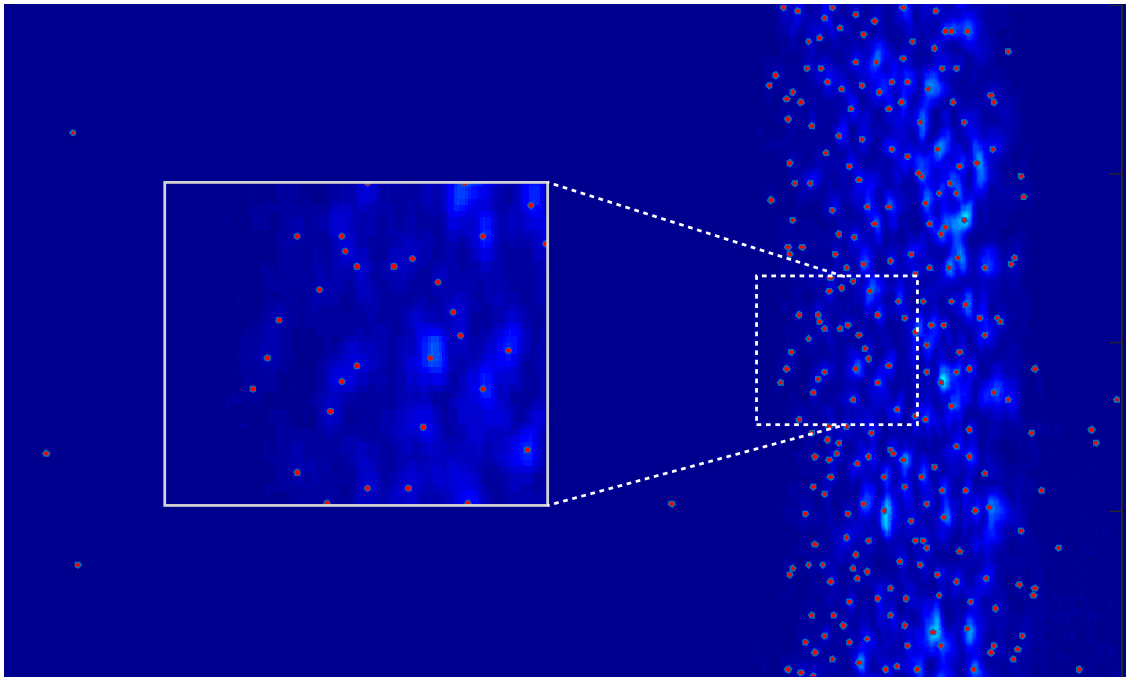


Figure 5.23: The detection of light patches by algorithm. By using a derivation routine and a sequence of tresholding procedures we are able to detect the light patches as they emerge from the isotropic melt.

Now that we have located the light patches we have to determine their basic properties. We determine their position relative to the central point of the heated area, their width, maximum intensity, area, etc. Later we combine this data and compare the distribution of the properties of the light patches over the radius of the heated area and over time.

5.3.2 Image processing algorithm testing

The quality of the imaging algorithm has to be tested to assure we only detect real light patches from the start of their appearance out of the isotropic melt to the formation of huge clusters of merging patches.

We start by creating a purely theoretical image of perfectly shaped Gaussian light patches scattered within the image. We compare the known size distribution and positions of the Gaussian with the ones determined by the algorithm. The test picture are of size 2180x2560 pixels in which we randomly scatter from 600, 3000 to 12000 Gaussian light patches. A zoomed out section of approximately 20 % by width is shown in Fig. 5.24 a-c.I, with marked position of the patches. We run our algorithm on the images and mark the found positions of the Gaussians in Fig. 5.24 a-c.II. Finally, we compare the distribution of widths of the detected patches with the known width distribution in Fig. 5.24 a-c.III.

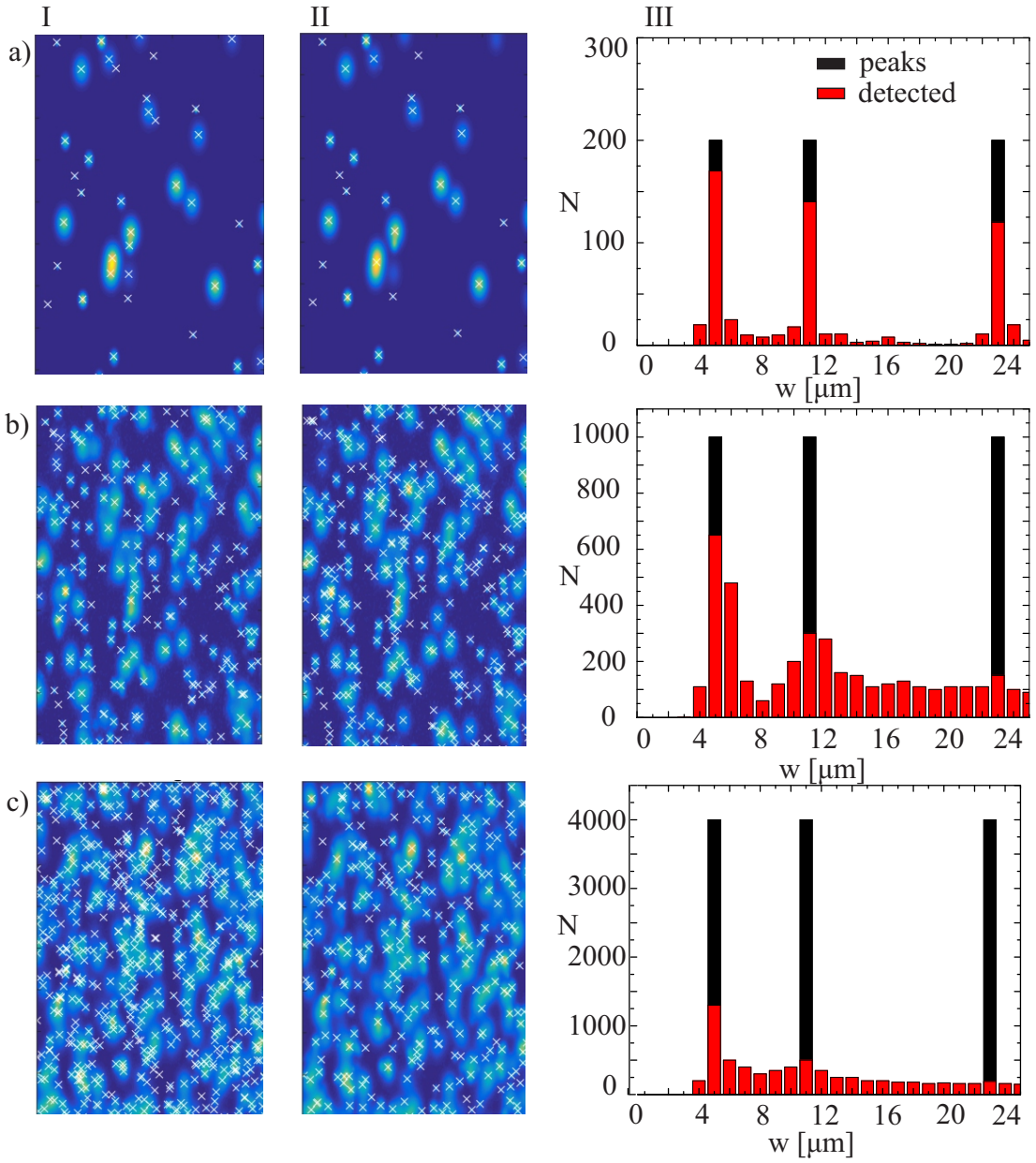


Figure 5.24: Test of the peak detection algorithm. **a-c.I** 600, 3000 and 12000 Gaussian light patches scattered on the image with marked central positions. **a-c.II** The detected algorithm positions of the peaks. **a-c.III** A comparison of the determined patch width distribution with the known distribution, red bar plot denotes the detected widths.

We notice a really good detection rate on the image containing 600 Gaussian light patches with a detection of up to 87 %. This is due to the high possibility that the patches do not overlap. When the number of patches increases though, the possibility of overlap increases as well. This leads to a drop of the detection rate to 52 %, as seen in the image containing 3000 light patches. In the extreme case of 12000 light patches scattered on the image the detection rate further plummets to approximately 25 %. The number of light patches was chosen to roughly replicate the distribution of the light patches detected on the experimental images 5.20. Moving from the inside isotropic phase, we first observe

small isolated islands and as we move further they come closer together and eventually merge. Therefore, we can state that using our algorithm we can observe up to 87 % of the isolated light patches, whereas the detection of the patches as they start to merge drops to 52 %. On the parts of the image closest to the ordered nematic the LC cools for the longest amount of time and also some alignment effects from the ordered nematic are expected. Thus, the patches are usually clustering and overlapping, dropping the detection rate to 25 %.

5.3.3 Statistical processing of the image data

We can exploit the spherical symmetry of the heating laser by assuming thermal properties at any given radius do not have any azimuthal dependency. Therefore, we divide the heated region into concentric bands with band width of $l = 200\,\text{nm}$, as shown in Fig. 5.25. This width corresponds to the smallest possible width of a light patch. For a typical heating area of radius 50 µm the area is divided into $50\,\mu\text{m}/200\,\text{nm} = 250$ individual concentric bands. Next, all light patches with the central region inside a determined band are collected and their properties compared.

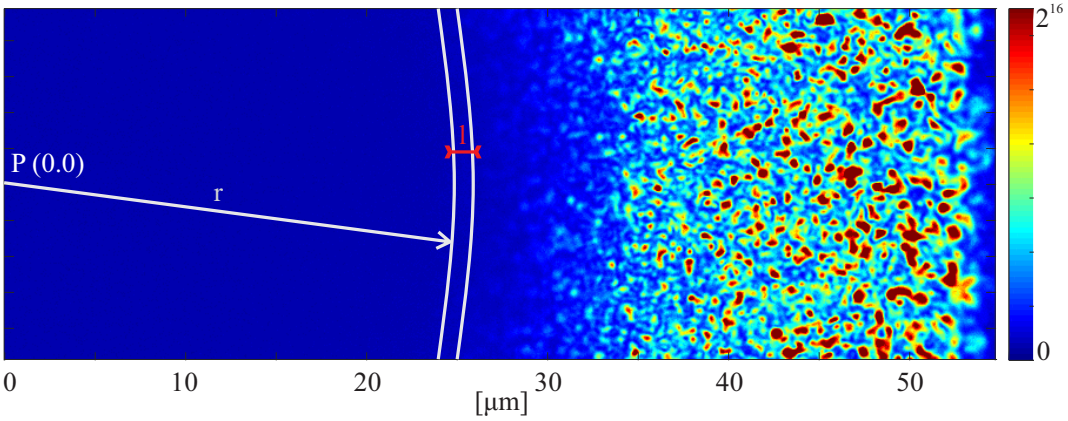


Figure 5.25: Zoomed out section of an isotropic nematic phase transition dynamics. Spherical symmetry allows the division of data into bands with equal properties.

The main properties determined by the algorithm, describing the basic properties of the light patches, are their size and their apparent light volume. The size of the light patch is determined as the width of the cross-section at FWHM. Here the baseline is set to the background value corresponding to the signal of the isotropic phase.

The next property is the so-called light volume. It combines the area of the light patch with its maximum intensity. In other words, it is considered a cylinder with a width equal to the patch diameter and height corresponding to the maximum intensity in the patch.

A combination of the two base properties provides information of the local retardation of the LC. Small patches indicate a small amount of retardants which furthermore indicates a small amount of order in the system. Moreover, the light volume is used to distinguish small domains as they form from the isotropic melt.

For every light patch we therefore determine the central point $P(x, y, I)$ and measure the width of the ellipsoid cross-section at FWHM, as shown in Fig. 5.26 a. The position of a cross-section is highlighted my mapping it in a surface plot in Fig. 5.26 b.

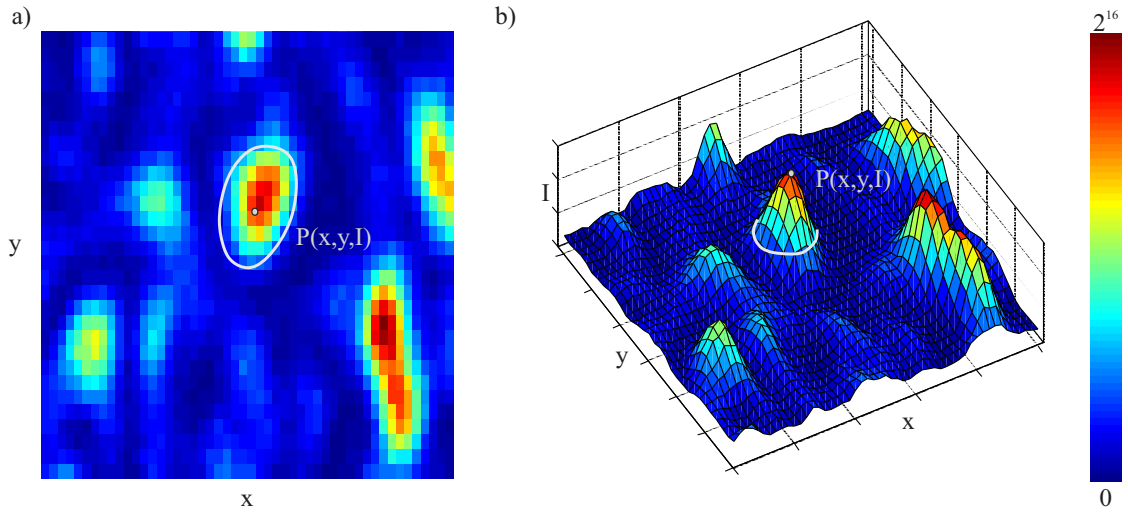


Figure 5.26: Visualized properties of light patches. **a** A section of the image Fig. 5.25 highlights the shape and the relative size of domains. Note that the pixel size corresponds to 65 nm. **b** A surface plot of the same area of the light patch highlights the cross-section position and maximum intensity.

We compare the properties over the whole heating area and over several time steps. This is done by comparing the distributions of light patch widths within different bands on the heated area. For instance, let us consider the case of a thin layer of 5CB imaged at 1.1 ms after the heating laser turns off. A close up using POM and nanosecond illuminations is shown in Fig. 5.27 a. We observe, from left to right, a central region of LC still unordered and therefore no light passes through the polarizers. This region can be seen as isotropic, Fig. 5.27 a.I. Further on we observe small light patches forming from the isotropic melt, Fig. 5.27 a.II, indicating an increase of the nematic order. Those light patches grow and collide, Fig. 5.27 a.III, until the edge of the heated area when the relatively sharp interface separates the area from the surrounding highly ordered nematic, Fig. 5.27 a.IV.

To calculate the size distributions of the light patches we have to define a range of widths and bins into which we sort the patches. The minimum width is defined by the pixel size of 65 nm. We set a range of 300 bins, each representing a pixel to a maximum width of 19.5 µm. Similarly, the bins of the light volume of the patches are set from 1 to 3.14×10^{16} counts per pixel, covering the whole range from a basically dark image to a domain of radius of 1 µm with intensity equal to the whole sensor dynamic range. Since this value is not so strictly defined as the width, we divide the bin range into 5000 equal parts for the analysis.

To compare the distributions over all bands we combine individual distributions by placing them back to back into a 2D color map plot with y axis defining the property bins of the patches, the **x** axis, the radius of the bands and the number of patches within a certain bin is marked using a RGB color map, an example shown in Fig. 5.27 b.

Individual cross-sections at different significant radii are marked and their distributions are shown side by side, such as in Fig. 5.27 c.I-IV. The position of the diffraction limit of light ($d_\lambda = 200$ nm) is also marked. Note that we can not say anything about the patches below this limit, since we can not physically observe them.

From Fig. 5.8 we know that the central region is at the highest temperature and the

edge is much cooler. Therefore, we predict the crossing of the phase transition temperature at the edge first and later at the middle. As seen in Fig. 5.27 a, we observe three distinct regions indicating that thee regions are at different stages of the phase transition dynamics.

The inner region, with higher initial temperature, Fig. 5.27 a-c.I, behaves as an isotropic region, with no transmission under crossed-polarizers and therefore no detection of light patches.

In region Fig. 5.27 a.II, we are right at the edge of the isotropic melt. We observe the start of the formation of small light patches as nematic order forms from the isotropic melt. Also a small amount of light patches is detected, as seen by the distribution Fig. 5.27 b-c.II.

As we move to further to Fig. 5.27 a.III we observe clearly formed and individual light patches, indicating a growth of nematic order. Yet the patches are still separated by dark regions - the isotropic melt. A clear distribution of patch widths formed with a clear peak at 300 nm can be seen in Fig. 5.27 b-c.III.

The last section of the defect phase Fig. 5.27 a.IV, is close to the edge of the heated area. This region has has the longest time to cool from the initial temperature, therefore we expect the greatest nematic ordering to be present. This is indicated by the distributions of patch widths with clear peak at 500 nm in Fig. 5.27 b-c.IV.

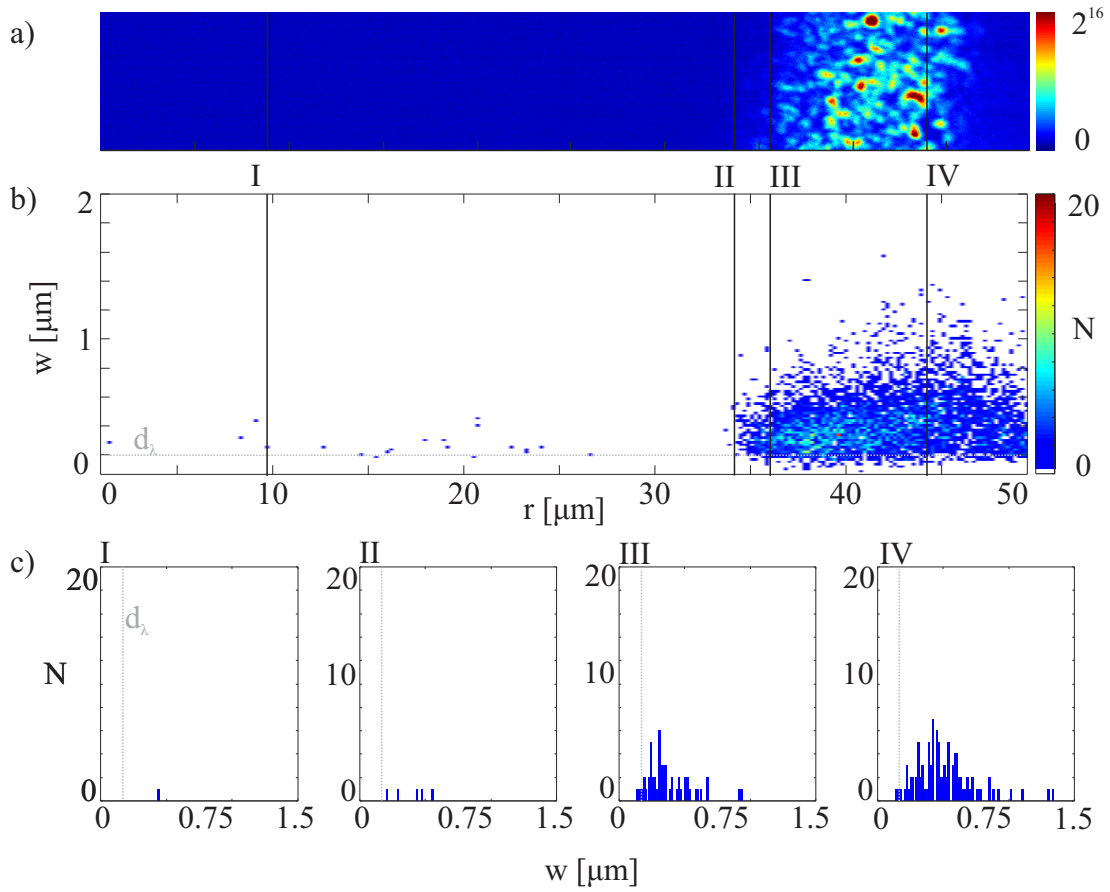


Figure 5.27: Distribution of light patch widths over the heated area. **a** Zoomed out section of the heated area at 1.1 ms after start of the cooling. **b** Stacked distributions of patch widths. The y-axis corresponds to the width of the patches and x-axis to the radius of the band. The number of patches is indicated by the color map on the right. **c.I-IV** Four individual cross-sections at different radii are highlighted and their distributions are shown. (d_λ) denotes the diffraction limit of light. Moving outwards, we observe **I** the isotropic phase, **II** the formation of nematic ordering, **III** growth of individual light patches and finally **IV** the size merging of bigger patches.

As seen in the Fig. 5.27 a, we observe the growth of the nematic ordering as we move from the inner most heated part of the heated area to the outer cooler parts. Monitoring the distributions one can also observe an increase of patches detected and a shift in the maximum patch size, Fig. 5.27 b-c.I-IV. From the data in Fig. 5.27 a-c.II one can not clearly determine the presence or absence of nematic ordering, since the number of light patches is simply to small. This problem can be simple solved due to the random nature of the process. If we repeat the experiment for, lets say, 1000 times with the same parameters of the heating, the amount of data will gather up and we will be able to determine the evolution of the process in greater detail.

We take the same sample cell, of a 2.5 µm layer of 5CB and observe the cooling at 1.1 ms after the start of the cooling, as seen in Fig. 5.28 a. Again we mark the same position as in Fig. 5.27 a.I-IV. We repeat the experiments 1000 times with 2 s delay steps to assure thermal relaxation in between experiments and study the size distribution for the whole 1000 images.

In Fig. 5.28 b-c.I one still can not observe any significant amount of light patches,

confirming the region is still in the isotropic phase. Next in Fig. 5.28 b-c.II one clearly sees a distribution of patch widths indicating the early formation of nematic ordering. The distribution shows a clear peak at 300 nm. In Fig. 5.28 b-c.III one sees a distinct sharp distribution of patch widths indicating the presence of individual separated light patches with peak width of 400 nm. Cloaser to the edge, Fig. 5.28 b-c.IV, on sees a wider distribution indicating the merging of ever bigger patches. The average patch size is 500 nm.

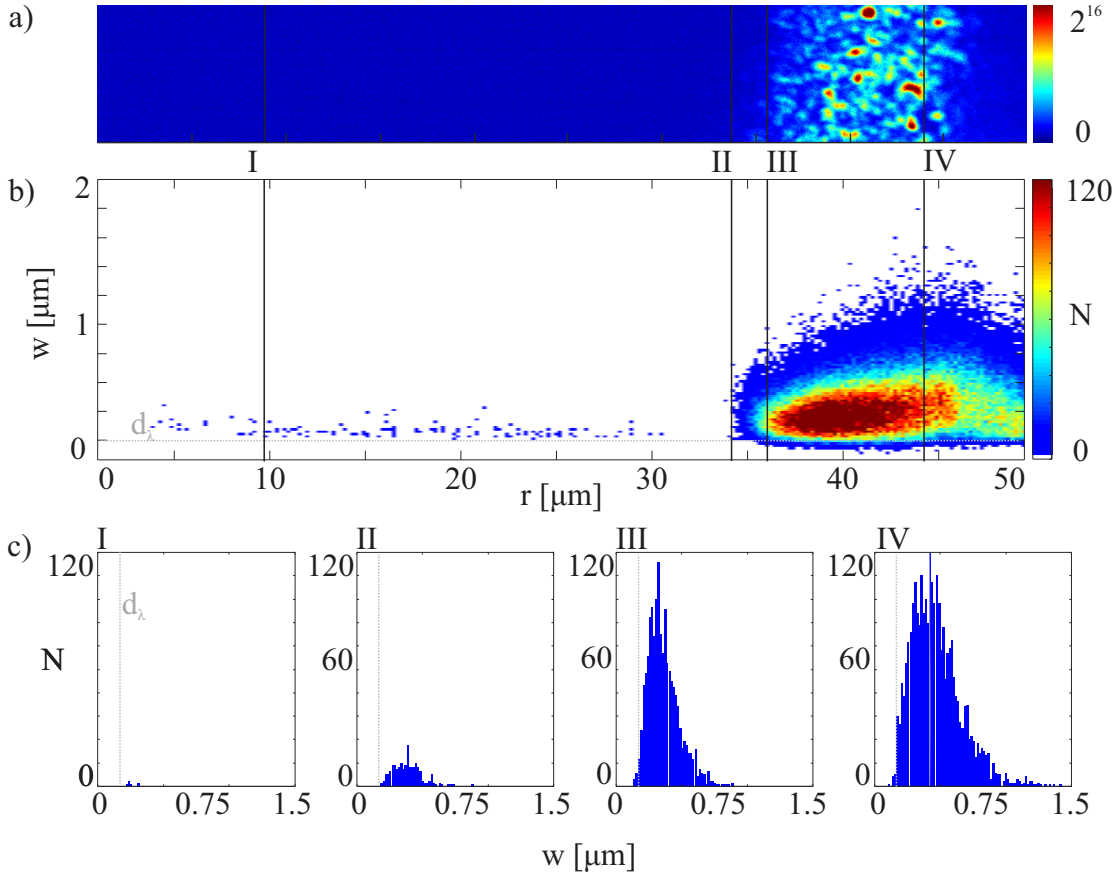


Figure 5.28: Sum of 1000 light patch width distributions. **a** A zoomed out section of the heated area at 1.1 ms after start of the cooling. **b** Stacked distributions of patch widths. The y-axis corresponds to the width of the patches and x-axis to the radius of the band. The number of patches is indicated by color map right. **c.I-IV** Four individual cross-sections at different radii are highlighted and their distributions are shown. (d_λ) denotes the diffraction limit of light. Moving outwards, we observe **I** the isotropic phase, **II** the formation of nematic ordering, **III** growth of individual light patches and finally **IV** the size merging of bigger patches.

Next we consider the distributions of light patch light volume. The combination of the information about the widths of the patches with their intensity can provide a clearer image of the formation of nematic ordering. The width of the patches that would be detected below the diffraction limit, due to the optical properties of the microscopy system spreads out and is detected as the limit itself. Thus, introducing the intensity of the patches into the picture, one can hope to distinguish in between the signal of sub-diffraction limited light patches.

The results are showcased on the same images as in Fig. 5.27 a. We again compare

the distribution of light patches at four significant position of the heated area Fig. 5.29 a-c.I-IV.

The combination of light patch width and intensity again shown the presence of an isotropic phase at position Fig. 5.29 b-c.I. At position Fig. 5.29 b-c.II, where light patches were detected in Fig. 5.28 b.II one can not detect any signal, indicating that the detected light patches correspond to nematic ordering below the diffraction limit. Further on at position Fig. 5.29 b-c.III, one can again observe a significant amount of light patches detected with a coresponding narrow distribution of light volume. At the edge of the defect phase Fig. 5.29 b-c.IV the distributions widen indicating again the merging of individual patches into bigger patches.

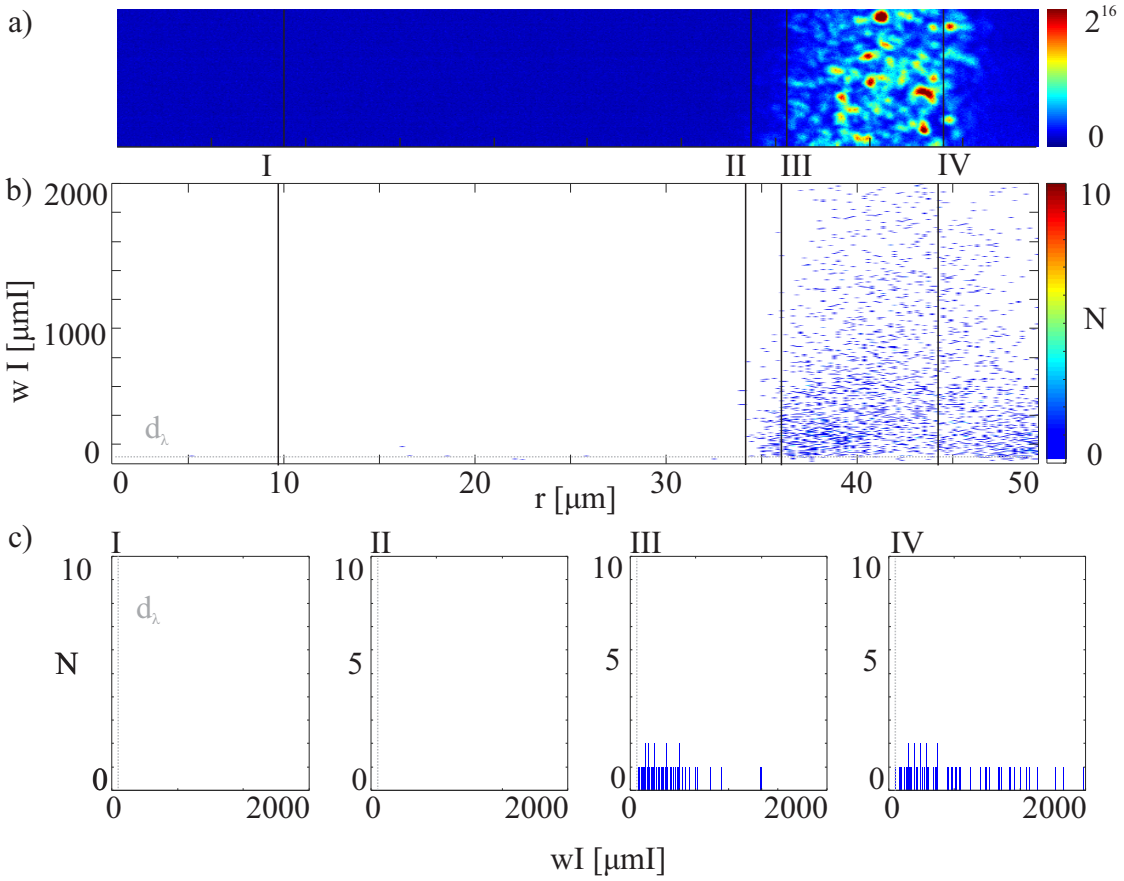


Figure 5.29: Light volume distribution over the heated area. **a** Zoomed out section of the heated area at 1.1 ms after start of the cooling. **b** Stacked distributions of patch light volume. **c** individual distributions of patch light volume at significant radii **I-IV**.

Again, we use 1000 repetitions of the experiment to increase the statistical accuracy of the experimental data. A zoomed out section of the image at 1.1 ms is shown in Fig. 5.30 a. Individual distribution are stacked into a colormap plot in Fig. 5.30 b. Individual distributions at significant radii Fig. 5.30 a.I-V are compared in Fig. 5.30 c.I-IV.

In Fig. 5.30 b-c.I one observes a small amount of detected patches yet their light volume is comparable or below the diffraction limit of light. Therefore, the area can be considered in the isotropic phase.

In Fig. 5.30 b-c.II one clearly sees an increase of detected light patches with ditribution maximum clearly above the diffraction limit, indicating the emergence of nematic ordering.

Ye,t some patches are detected below the diffraction limit indicating a presence of sub-200 nm light patches.

In Fig. 5.30 b-c.III one observes a clear increase in the number of detected patches. The relatively sharp shape of the distribution indicates individual separated light patches. At the edge of the heated area in Fig. 5.30 b-c.IV we observe a widening of the distribution indicating the merging of light patches.

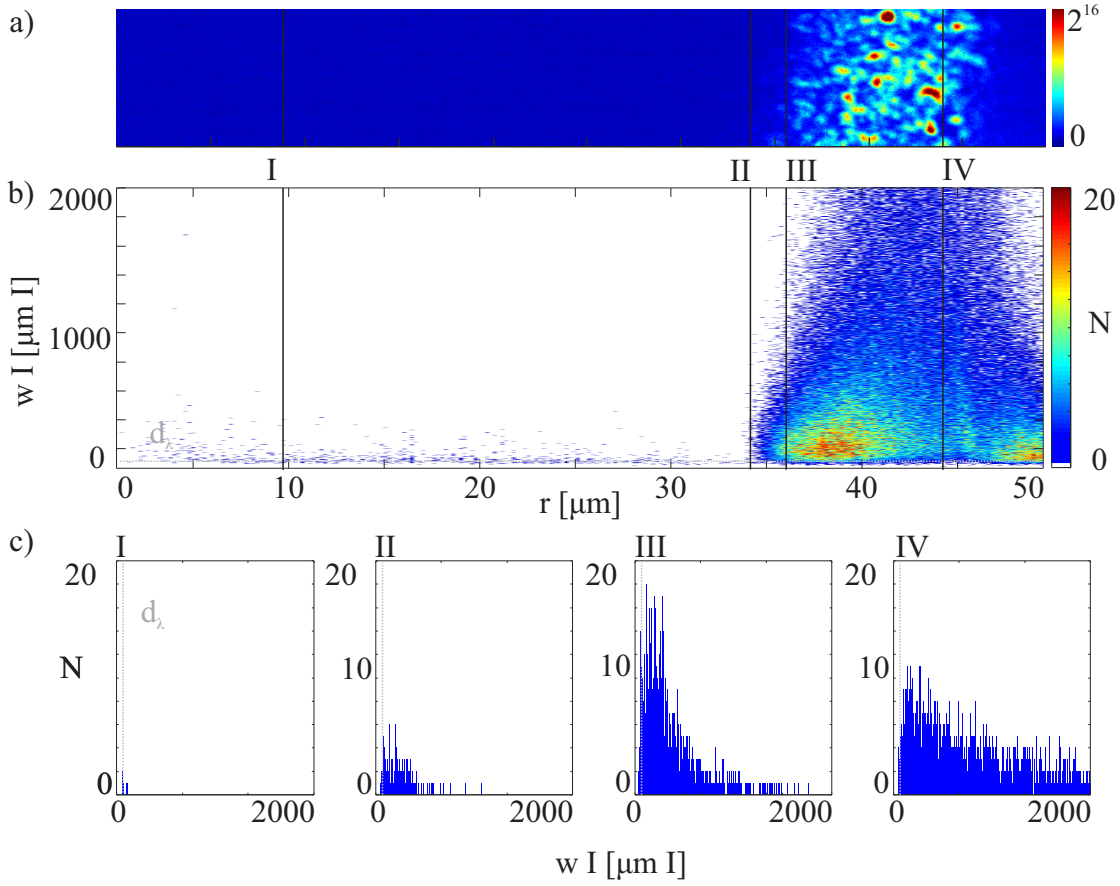


Figure 5.30: **a** Zoomed out section of the heated area at 1.1 ms after start of the cooling. **b** Stacked distributions of patch light volume. **c** Individual distributions of patch light volume at significant radii **I-IV**.

The algorithm data allows us to study the formation of nematic ordering by observing the distribution of light patch properties over the heated area. Yet it is not completely clear how the light patches directly relate to the nematic order in the system. The average nematic domains as it forms from the isotropic melt should be of the size of a few tens of nano meters, and considering they are spherical a few ten could fit in the imaging plane we typically observe. Since individual domains orient in random direction, the cumulative effect of light passing that produces the light patches we observe, does not tell much about the structure and the properties of individual domains.

We draw inspiration of light transmission experiments in the past where simple laser transmission through thick LC samples was used, to show how topological defects form after rapid phase transitions [22]. We can use the data contained in our experimental images to basically perform light transmission experiments on them. Due to the spherical symmetry of the heating area we are able to combine pixels at the same radius from center of the heating area together and use them as digital ring photo-diode with width of a single

pixel 65 nm.

For instance, if we study an experimental image obtained at 1.1 ms after the start of cooling, as seen in Fig. 5.31 a, one can observe again the presence an isotropic island surrounded by light patches that form due to the formation of nematic order in the system. Now we sum the pixel values for all radii over the azimuthal angle, from the center of the heated area to the edge of the ordered nematic region. Additionally, we normalize the sum by dividing it with the circumference of the ring. Again, we combine 1000 images and compare the intensity on a given circumference or the intensity density at different radii. For instance, at Fig. 5.31 b.I, we clearly observe again no significant signal, confirming the presence of the isotropic phase. Next at Fig. 5.31 b.II, in contrary to previous distributions, as seen in Fig. 5.30 b-c.II, one already observes a significant amount of signal, confirming a presence of nematic ordering that allows transmission of light through the sample before it can be detected by our algorithm. Also at Fig. 5.31 b.III one observes an increase of signal corresponding to the growth of the light patches, until just before Fig. 5.31 b.IV one observes the presence of a peak of the signal. The presence of the peak just before the edge of the signal, indicates a slightly different behaviour at the edge of the heating area probably influenced by the surrounding ordered nematic. Finally, we take a section of the image from 21 µm to 34 µm where the first signal is detected and still no light patches can be observed and determine the characteristics of the signal, in Fig. 5.31 c. At approximately 30 µm from the centre, the signal starts to grow from the background value and at 32 µm the slope of the signal changes dramatically. We determine the slope k to be 8.7. The units are percent per micro metre indicating how much the signal grows towards the maximum value every micro metre.

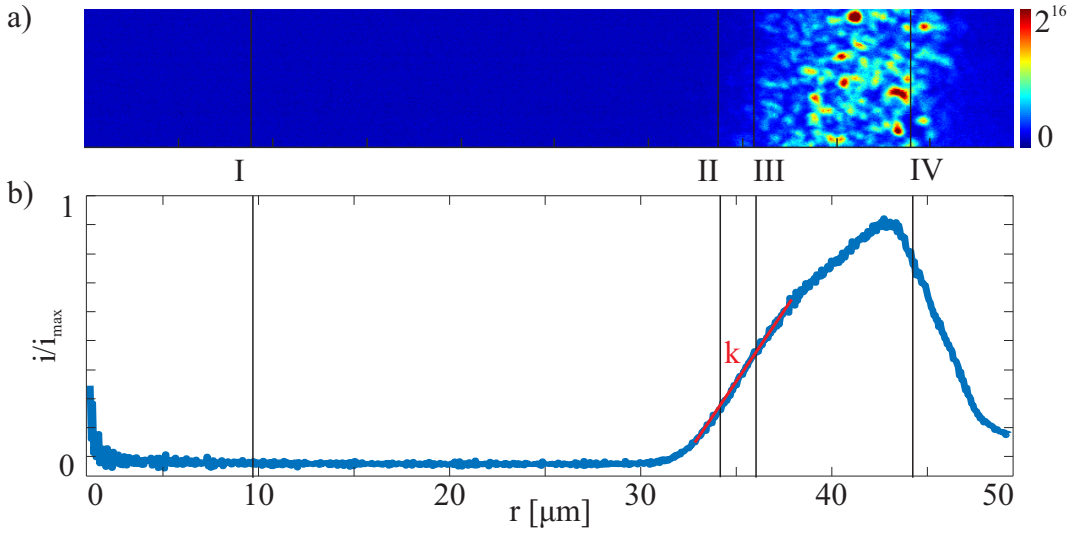


Figure 5.31: Light transmission study on images. **a** A zoomed out section of an experimental image obtained at time 1.1 ms after start of the cooling. **b** Counting the pixel values at different radii over the azimuthal angle at different times after the start of cooling, can be used to study the formation of nematic ordering at different cooling rates. Red line indicated the distinct increase of the signal growth from the isotropic melt with slope $k2 = 8.7\%/\mu m$.

5.4 Formation of Nematic Ordering

In the previous section we presented the basic techniques used to extract the data obtained by studying rapid phase transition in nematic LCs. Here we want to use the data to test theoretical predictions of the formation of order in the system. We start by taking a look at the whole picture of the phase transition in thin layers of nematic LC.

We use a thin layer of 5CB placed into a sample cell made of ITO coated glass substrates. By covering the substrates in a surfactant, strong homeotropic anchoring is enforced. Next, using the opto-thermal effect, a localized section of the sample is heated above its phase transition temperature and as the heating laser is turned of the system undergoes a rapid phase transition. We observe the process by imaging using a stroboscopic imaging technique and nanosecond the nanosecond illumination system. In a typical experiment a total of 1000 images are taken at desired time steps after the start of cooling. We are interested in the early times, when nematic ordering starts to form from the isotropic melt. Therefore, we image the process from the start of the cooling at time 0 ms until 2 ms in 100 µs intervals, thus producing a 'movie' containing 20 frames of the process, as seen in Fig. 5.32.

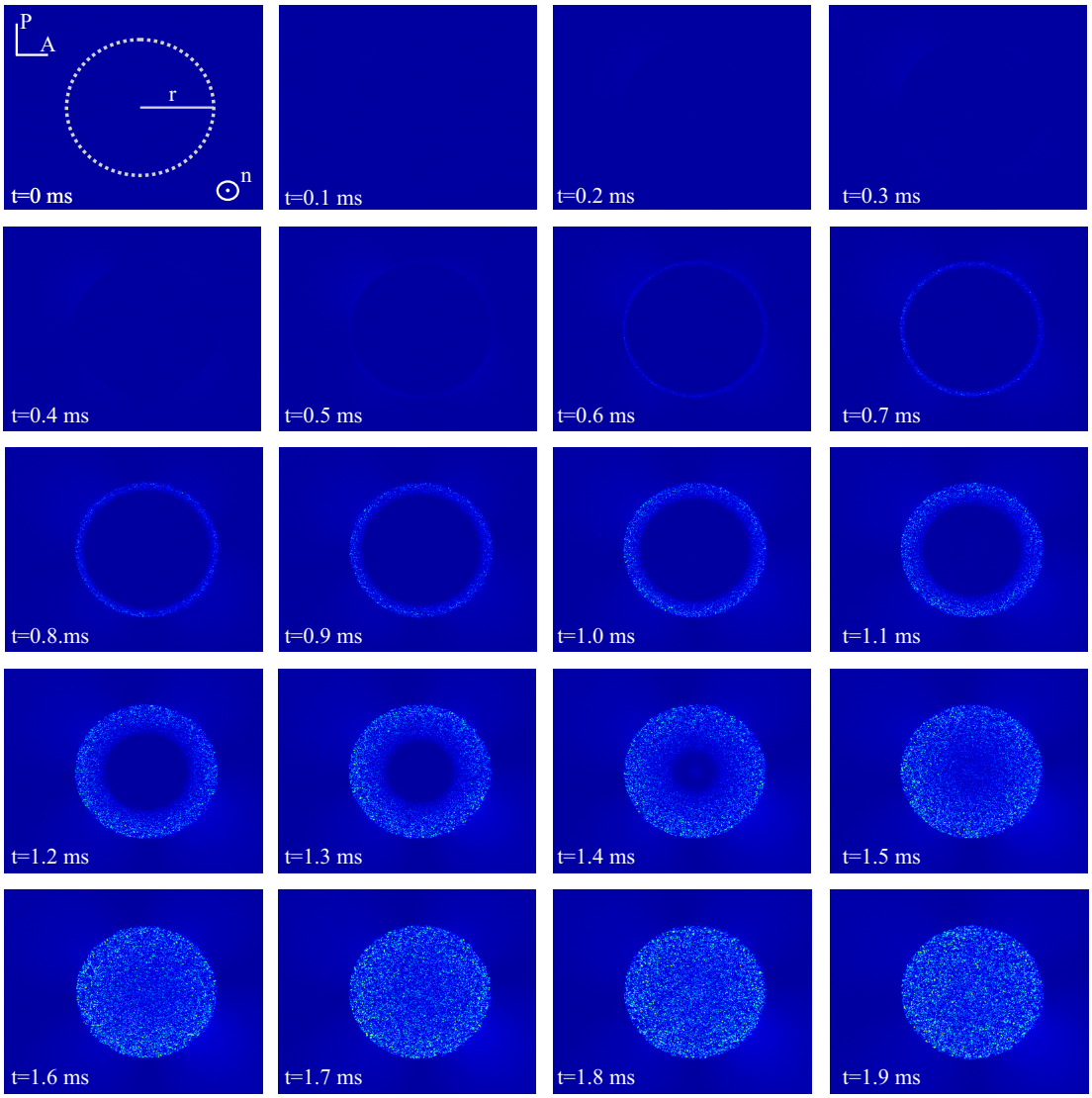


Figure 5.32: Movie of rapid phase transition in nematic LCs. Images taken every 100 µs after the start of cooling, capture the processes surrounding rapid phase transition in detail. The exposure time of the images is 20 ns.

From the images in Fig. 5.32, one can clearly observe that at first the whole heated area is in the isotropic phase and as the system cools small light patches start to form at the edges of the heated are indicating the formation of nematic ordering. Therefore, the predictions of the initial temperature profile seem to be correct 5.8. As the system cools further we observe light patches starting to aper ever so closer to the center uncovering a moving front of nematic ordering. This process is described in various other system, where topological defects form as a consequence of symmetry breaking phase transitions, by the so called Kibble-Zurek mechanism. At later times when nematic order is well establish the process of coarsening take over where nematic domains grow with the expense of smaller domains to eventually form the ground state of the system.

5.4.1 Early formation of nematic ordering via the Kibble-Zurek mechanism

Cooling of a nematic LC heated to the isotropic phase causes the system to form nematic domains from nucleation sites formed by thermal fluctuations. As the speed of the cooling increases, one expects that the cooling rate will reach a point in which the dynamics of the order parameter will start to lag and the system will eventually freeze. After a certain amount of time after the phase transition the system will catch up with the changes and start forming nematic domains. The size of the domains formed and the freezing time will be influenced by the cooling rate. The process was described in theory in the formation of mater in the early universe, by Kibble and Zurek[27], [50], hence the name the Kibble-Zurek mechanism. Calculations determine the freezing times to be in the order of a few tens of micro seconds and the size of the domains formed right after the freezing from thermal fluctuation sites is predicted to be in the area of a few tens of nano meters [65]. The small size of the domains makes them hard to detect using optical microscopy. The only possibility is the detection of scattered light on the small slightly birefringent domains, that can be picked up at the edges of the isotropic melt. Also by calculating the exact times when the phase transition is reached we should observe a delay between the detection of transmitted light and the point the phase transition temperature is reached. Lastly, the KZ mechanism predicts all of the predictions above to have a strong cooling rate dependency.

We start of by repeating the steps described in 5.3.3 on images obtained at the first 2 ms after start of the cooling. For simplicity we only visualize the data obtained at significant time steps, Fig. 5.33. For reference, the first image is obtained exactly as the heating laser is shut down marking the start of our time. At this point the whole heated area is in the isotropic phase. Next time step is 0.6 ms, where the first light patches start to form at the edge. We continue at every 100 ms until the whole sample is covered with light patches indicating the start of coarsening dynamics.

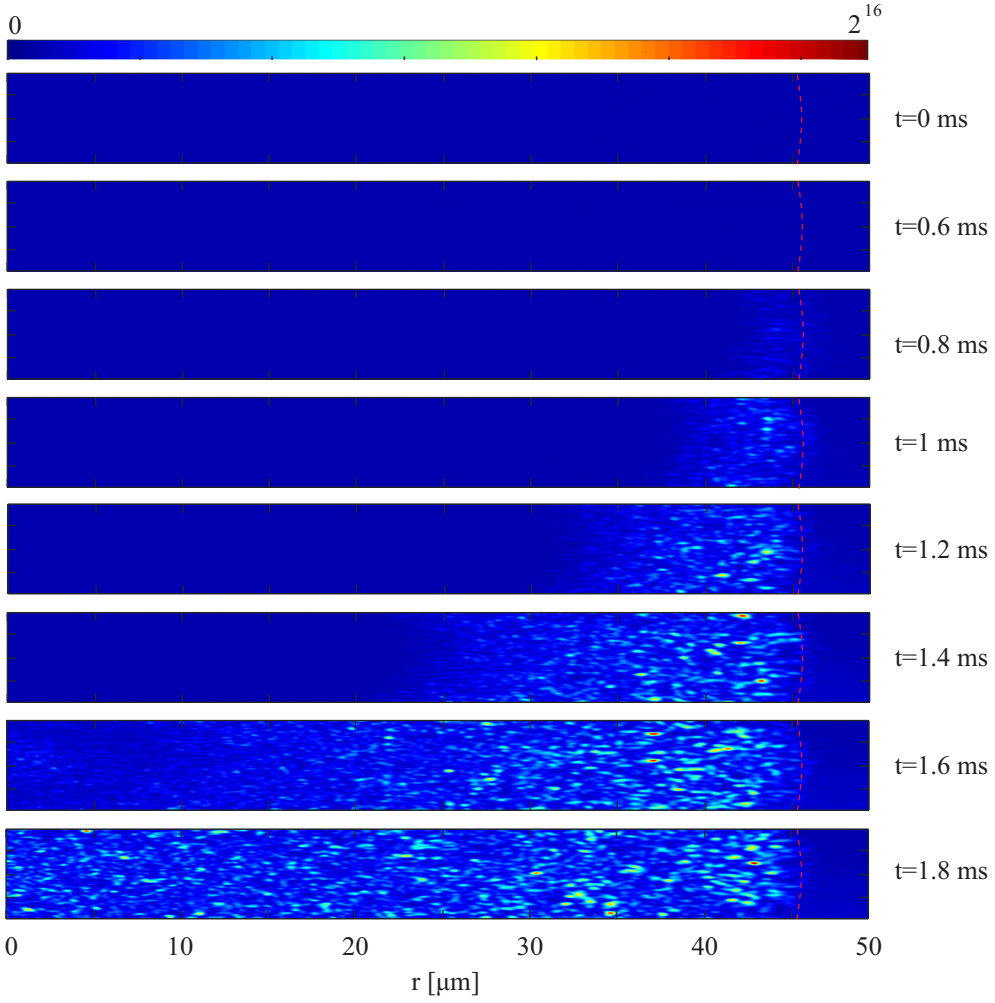


Figure 5.33: Zoomed out sections of images of rapid phase transition obtained at selected times. Images are obtained from start of the cooling until the whole sample shows light patches, at 2 ms at every 100 µs. The color map "jet" is used with range $0 - 2^{16}$.

The experiment at each time step is run 1000 times, assuring statistical relevance of the data. Next, the algorithm 5.3.1 is used on each of the images. We determine the properties of the emerging light patches and visualize the sum of the distribution of the properties for 1000 experiments, Fig. 5.34 and Fig. 5.35. First we observe the distributions of light patch width different time steps, shown in Fig. 5.34. At time 0 ms we observe the signal typical of the isotropic phase. Later at 0.6 ms we observe the first emergence of light patches at the edge of the heated area indicating the presence of nematic ordering. The front of the light patches moves towards the center of the heated area until at time 1.6 ms all the area is covered.

In addition to the distributions of patch width, we want to include the intensity of the light patches into the analysis. We compare the distributions of light volumes at different significant times, Fig. 5.35. Again we observe a signal reminiscent of the isotropic phase at time 0 ms and the emergence of signal at the edges at 0.6 ms. The algorithm detects the presence of light patches as they move towards the middle of the heated area until at time 1.6 ms the whole areas is covered.

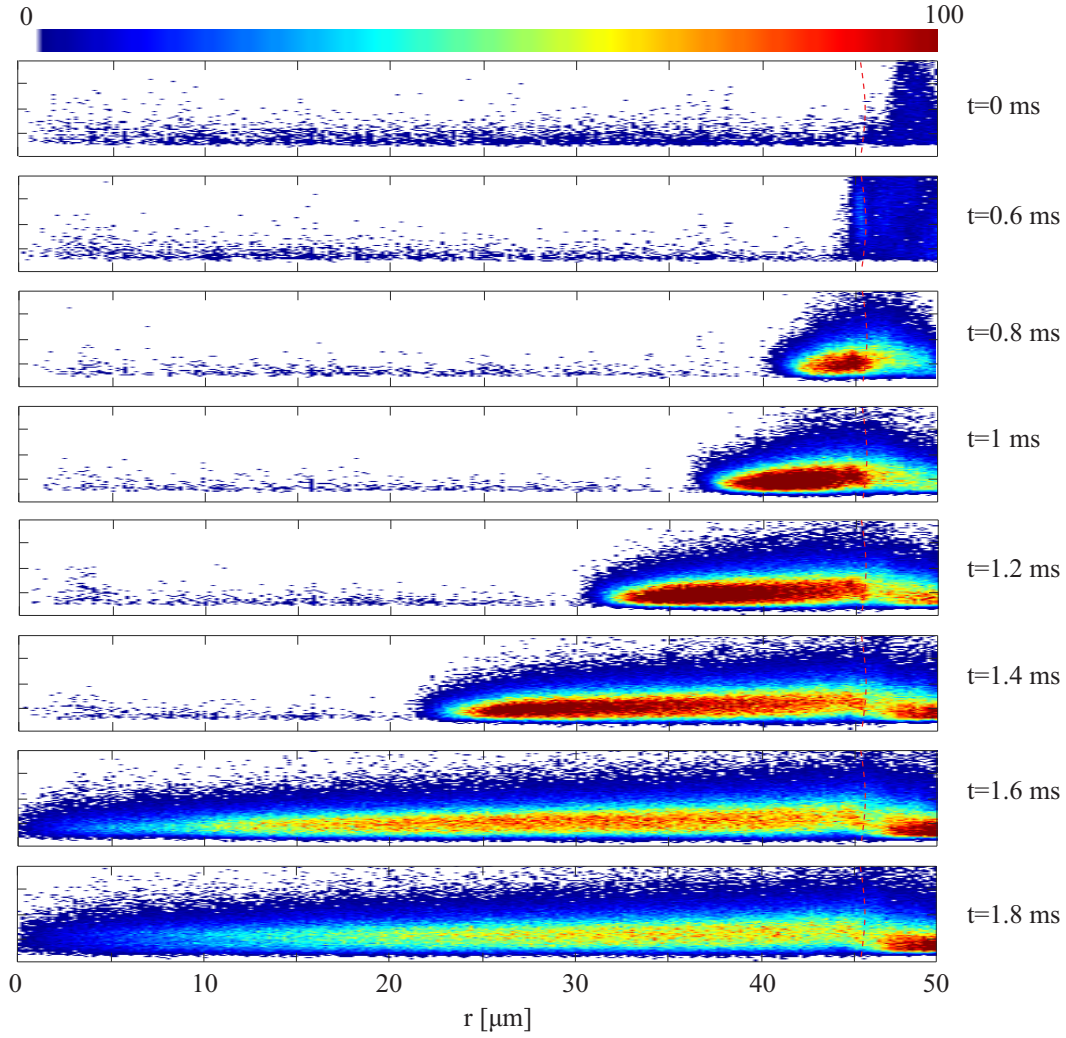


Figure 5.34: Distributions of light patch width at different times. At time 0 ms the whole area is in the isotropic phase, at later times light patches form at the edge and by further cooling they move towards the middle of the area. The distributions are averaged over 1000 repetitions. Color map "jet" range $0 - 100$.

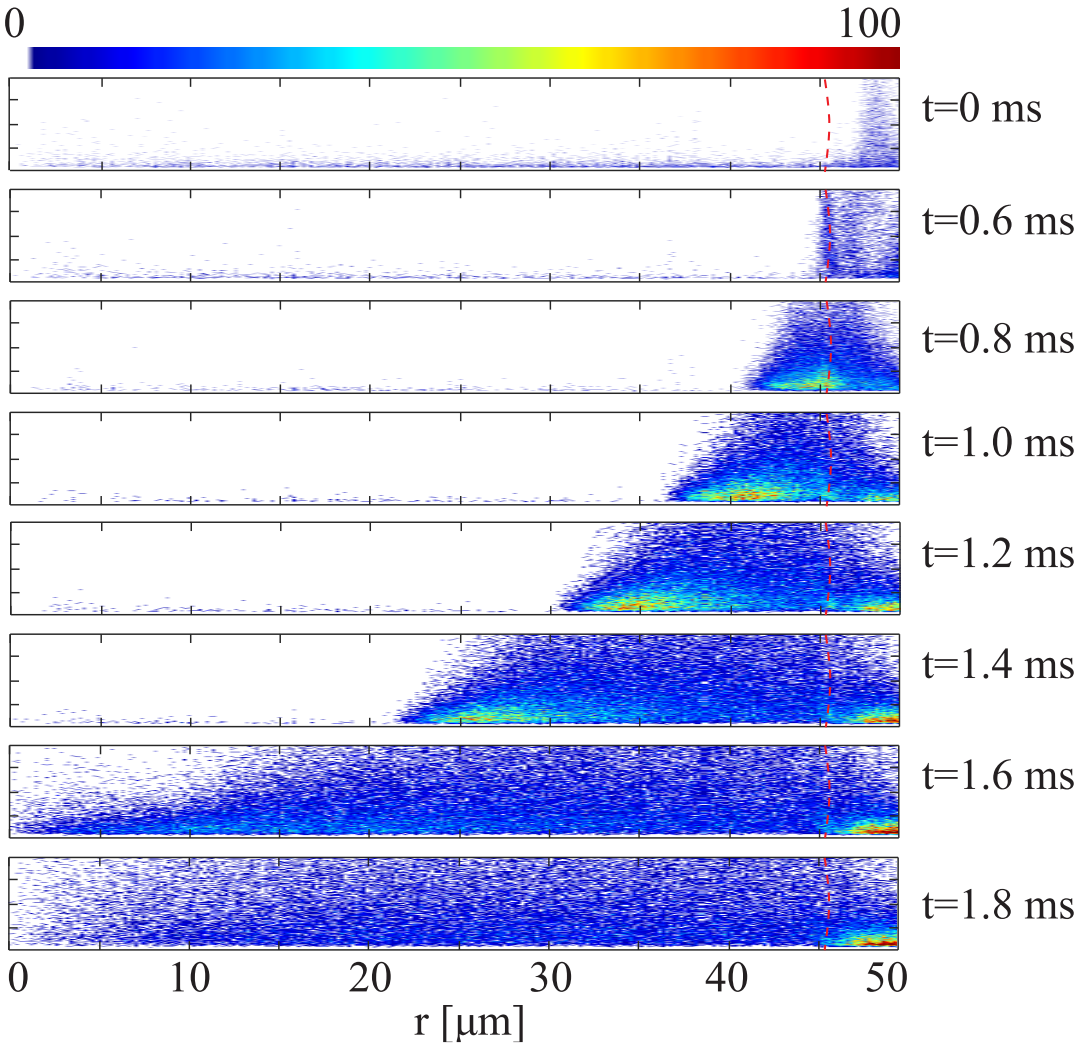


Figure 5.35: Distributions of light patch light volume at different times. At time 0 ms the whole area is in the isotropic phase, at later times light patches form at the edge and by further cooling they move towards the middle of the area. The distributions are averaged over 1000 repetitions. Color map "jet" range $0 - 100$.

The combination of light volume and the patch width provides us with the information of the light patch growth as the system cools from the nematic phase. We also compare the light transmission data obtained by summing all the pixel values at a certain radius over the azimuthal angle. For reference we compare them with a typical image taken at 1.1 ms after the start of the cooling, as seen in Fig. 5.36 a. We plot the intensity as a function of radius in Fig. 5.36 b, for early times and for later times in Fig. 5.36 c. At 0 ms we observe an almost completely flat line, indicating an isotropic phase. As time goes on and the temperature drops we observe a formation of order at Fig. 5.36 b.IV. Further on the with time we observe the intensity front to move towards the middle indicating the moving front of the nematic ordering. At time 1.7 ms we already observe the complete area covered with light patches.

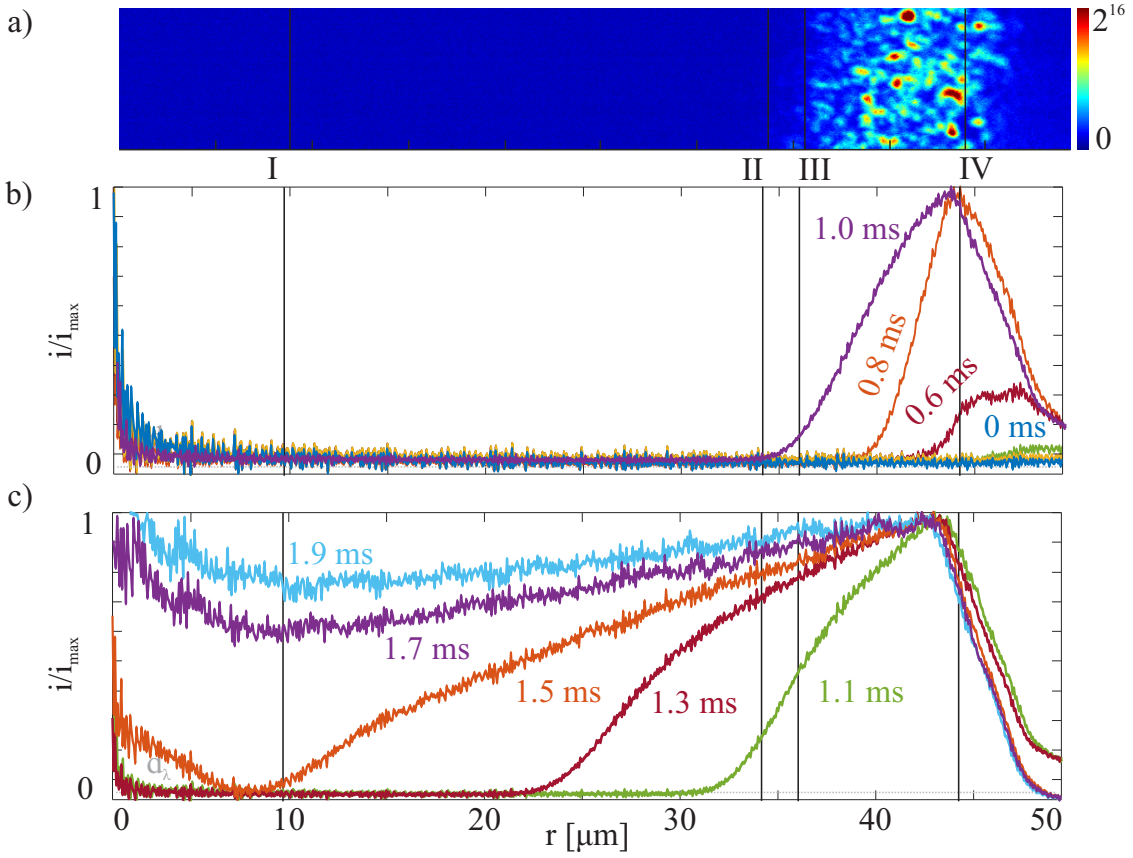


Figure 5.36: Light transmission study on images. **a** A zoomed out section of an experimental image obtained at time 1.1 ms after start of the cooling. **b** The plots for the first 1 ms after start of the cooling, indicate that the formation of nematic ordering starts at the edge. **c** At later times one observes that the ordered nematic front moves towards the middle increasing the transmittance.

We observed the formation of nematic ordering by imaging, observing the distribution of widths and their light volumes and also we analyzed the light transmission over the images. Now it is the time to compare the obtained data. This is done by picking a set time after the cooling starts and comparing the distributions and th elight transmission, Fig. 5.37 a-d. We pick the time 1.1 ms since it provides a compromise between the width of the isotropic phase and the defect phase size, allowing us to analyze both. A typical image at that time is shown in Fig. 5.37 a. Again we mark four radii of significance Fig.

5.37 a.I-IV. At positions I and II, one can by eye not spot any light patches as they start to appear at position III and grow to the maximum size at IV.

Fig. 5.37 b.I-IV, contains the distribution of width for 1000 repetitions imaged at 1.1 ms. We observe the detection of light patches already at position Fig. 5.37 b.II making the algorithm much more sensitive than the naked eye.

Fig. 5.37 c.I-IV we visualize the distributions of light volume for the light patches. Additionally to the information about the size of the light patches one can compare the intensity. Clearly the detection is similar to the detection of widths. In Fig. 5.37 c.I we observe the isotropic phase, in Fig. 5.37 c.II the start of the light patch detection, which rise to a maximum size at position Fig. 5.37 c.IV.

Furthermore in Fig. 5.37 d.I-IV we calculate the sum of the intensity for a certain radius over the azimuthal angle. Interestingly one can observe an increase of signal way before position Fig. 5.37 d.II indicating the presence of small nematic domains that scatter light. The domains are not detected using the algorithm due to the proximity to the noisy isotropic melt.

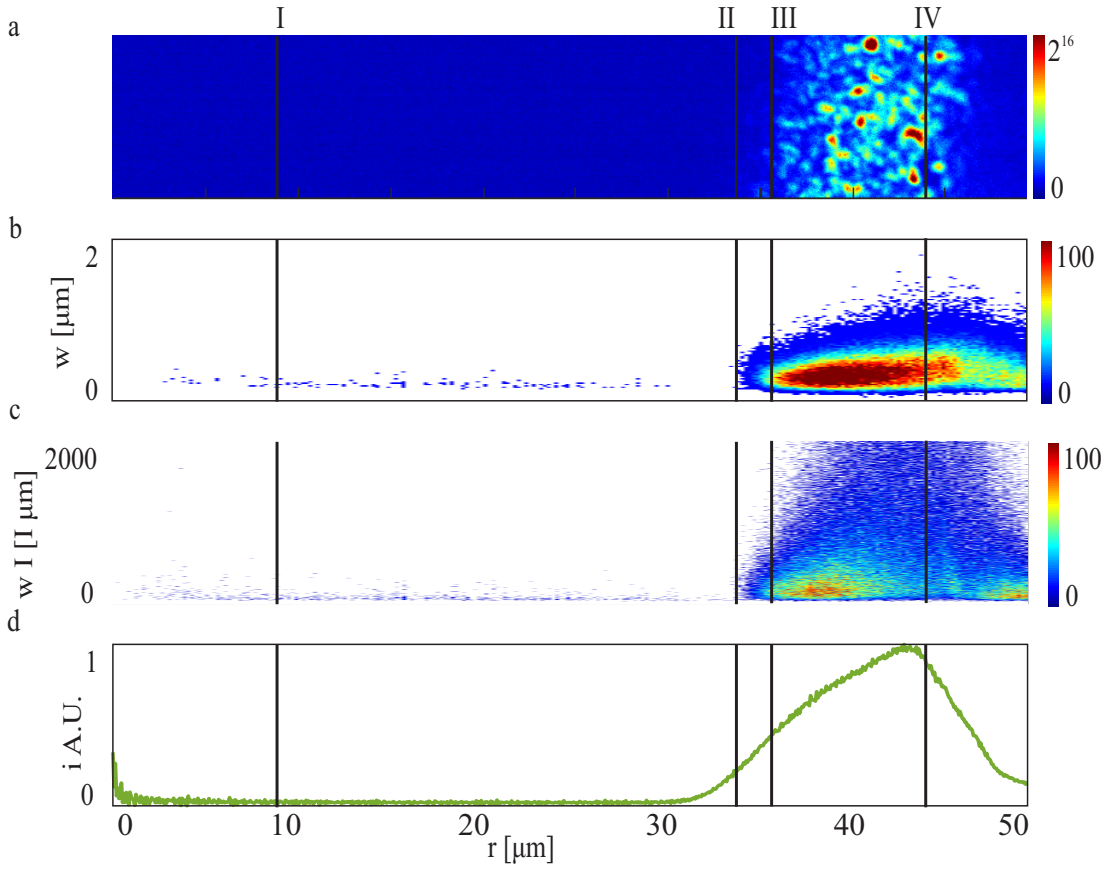


Figure 5.37: Comparison of different analytical methods. **a** A typical image at 1.1 ms. **b** The distribution of light patch widths at the same time averaged over 1000 experiments. **c**. The distribution of light patch light volume at the same time averaged over 1000 experiments. **d** Light transmission study on the experimental images. The positions I-IV mark interesting radii. One can observe that at position II the algorithm fails to detect the smallest domains found by the transmission study.

Considering the image Fig. 5.37 we can determine that using our experimental approach we are able to detect the presence of nematic ordering right after sudden phase

transition. Sadly we are not able to determine the size of the nematic domains formed, due to experimental draw backs. We are only able to detect the scattering of light on the slightly birefringent domains.

Next we want to test the predictions of the Kibble-Zurek mechanism, that predicts a strong dependency of the formation of nematic ordering on the cooling rates. We start by taking the information of the initial temperature in the sample cell and the thermal properties determined in Fig. 5.8 and Fig. 5.11 combined in Fig. 5.14. Those information provide us with a simple translator toll that can prescribe each radius at each time its temperature and the cooling rate at the phase transition temperature.

First we determine a measure the growth of the nematic ordering. We use the mean values of the distribution of light patch light volumes and the light transmission study data, to determine the significant increases of signal close to the isotropic melt. Since the absolute values of the data do not provide any physical meaning we normalize both data sets. We determine the slopes values for both signal as seen for times 1.1 ms and 1.5 ms in Fig. 5.38.

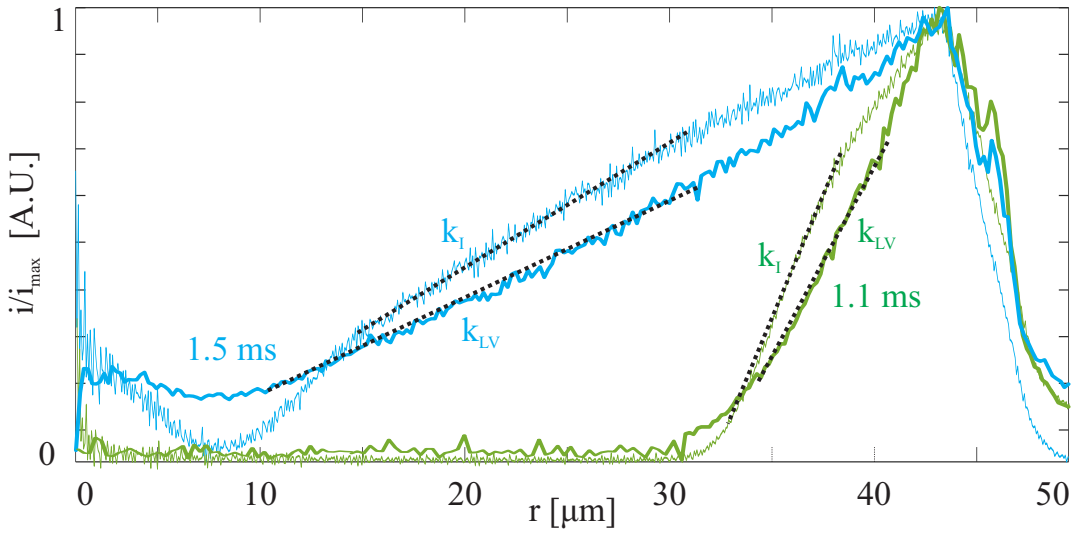


Figure 5.38: Growth of light transmission and light volume. The blue line denote the data obtained at 1.5 ms and the green at 1.1 ms. We determine the slopes of the mean light patch data for the bold lines k_{LV} and for the light transmission data k_I

Next, we plot the measured slopes again the radius of the start of the slope in Fig. 5.39 I and also for the cooling rates calculated at those radii Fig. 5.39 II.

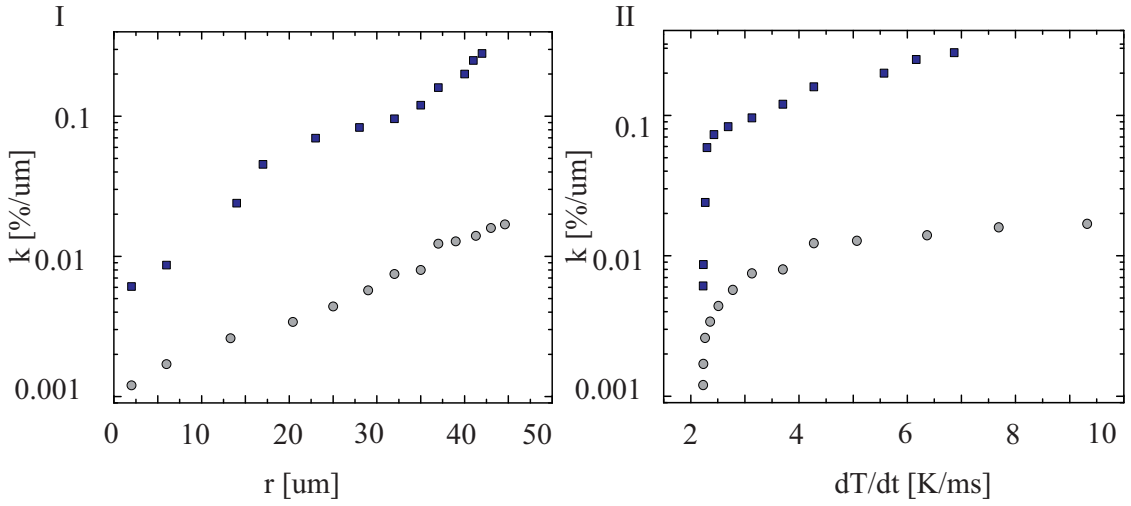


Figure 5.39: Growth of nematic order versus radius and quench rate. **I** The slope of the growth of signal for the transmitted intensity and for the mean light volume right at the edge of the isotropic phase, measured at different radii. **II** The same data plotted in a log-lin plot again the cooling rates at the phase transition temperature. Squares denote the data from transmission data and circles the mean light volume data.

Comparing the data plots in Fig. 5.39, we can certainly say that light transmission and the light volumes of the light patches grow faster at the edges compared to the middle. Also, one can observe an interesting behaviour as we plot the same slops against the cooling rates calculated at the phase transition temperature. We observe that initially as the cooling rate increases from a few degrees per milli second to $4\,\mathrm{K\,ms^{-1}}$ a small increase of the cooling rate significantly increases the signal growth. Above $4\,\mathrm{K\,ms^{-1}}$ the increase becomes much slower.

5.4.2 Late time formation of nematic ordering - coarsening dynamics

After a rapid phase transition from the isotropic to the nematic LC phase small isolated patches of nematic order form, called domains. Globally, the whole system tends to orient in the same direction, typically predefined by the surface boundary condition. In our case most of the system is already aligned homeotropically. Only a small isolated area is heated to the isotropic phase by laser heating. As domains grow from the isotropic melt they start to touch while they are only separated by the domains walls that can be described as 2D topological defects. After there is no more isotropic LC left, the domains inevitably start to merge into bigger domains. Whiles merging the domain walls tend to get smaller and smaller until they form only line defects. The main distance between the defect lines corresponds to the domains size. Since the domains tend to be roughly spherical, the domain size limit is the sample cell thickness and as this size is reached the defect lines start to unwind to form free standing loops that in time annihilate and the system takes over the surrounding LCs orientation..

We test the sample cell thickness dependency on the coarsening dynamics by placing 5CB into tree cells with thickness 2.5 µm, 7.5 µm and 18 µm. All cells are created equally from the ITO coating to the surfactant used. After assembly we place the samples onto the imaging plane of our microscope and observe, using our light transmission set up, the transmission of the cells after laser heating again for 10 ms at 90 mW. We also image the

process at significant times using our stroboscopic imaging technique.

First, we test the 2.5 µm sample cell that is also used for the topological defect formation study. The radius of the heating area is approximately 50 µm and the measuring spot radius is 3 µm located in the center of the heated area. A lin-log plot averaged over 256 acquisitions is shown in Fig. 5.40 a. As the system cools and forms nematic order we also image the processes at significant times Fig. 5.40 b. From start at 0 ms (Fig. 5.40 a.b.I) where the heated area is completely in the isotropic phase, it takes a few hundred micro seconds for the system to reach a point where ordered domains can form. We observe the first-ordering as individual light patches at the edges at 1.5 ms (Fig. 5.40 a.b.II) and as the ordered front moves towards the centre, we start to see at 1.7 ms (Fig. 5.40 a.b.III), the increase of transmittance of the sample cell in the measured area. The transmittance roughly peaks at the moment the light patch size matches the sample cell thickness at 3 ms (Fig. 5.40 a.b.IV). Furthermore, at that time light patches rapidly start to merge and annihilate seeking the ordered ground state. Some individual defect lines remain at 5 ms (Fig. 5.40 a.b.V) until at some point they also annihilate and the whole heated area resumes the order imposed by the surface anchoring conditions at 10 ms (Fig. 5.40 a.b.VI).

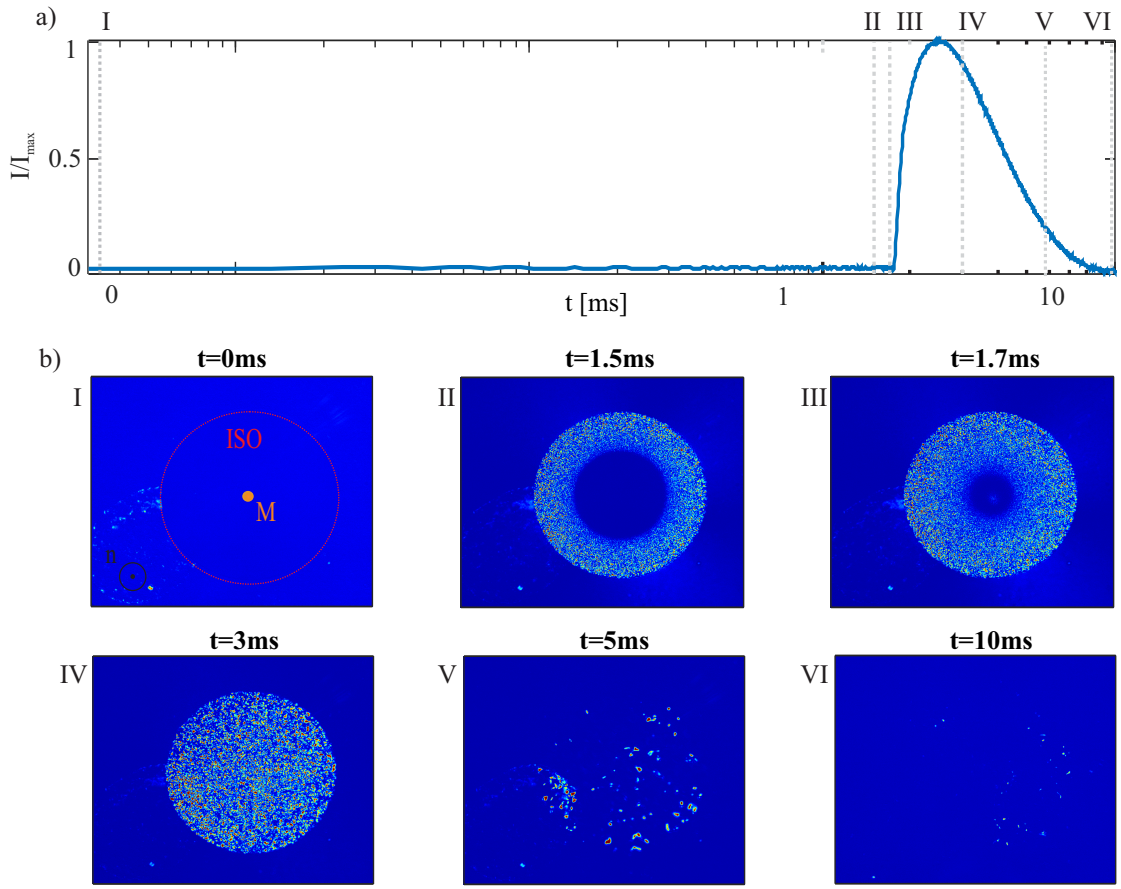


Figure 5.40: **a** Light transmission of a 2.5 µm thick sample cell of 5CB after rapid phase transmission. **b** Individual POM snapshots at significant times are marked from 0 ms **I** when the whole heated area is heated high above the phase transition temperature to 10 ms **VI** when the system cools to room temperature and restores the ordering imposed by the boundary conditions. The edge of the heated area is marked by a red circle and the measuring spot is marked by an orange dot (M).

Next, we increase the sample cell thickness to 7.5 µm and again observe the light trans-

mission after laser heating in Fig. 5.41 a, and show typical snap shot in Fig. 5.41 b. At time 0 ms, Fig. ??a.b.I. the whole heated area is in the isotropic phase. At time 1 ms, Fig. 5.41 a.b.II we observe the first light patches forming at the edges of the heated area and at 1.5 ms, Fig. 5.41 a.b.III the patches move towards the center of the heated area. The area is completely filled at 1.7 ms, Fig. 5.41 a.b.IV. Light patches grow, 2 ms, Fig. 5.41 a.b.V, for significantly longer times since at time 10 ms, Fig. 5.41 a.b.VI we still observe significant light patches and no defect lines.

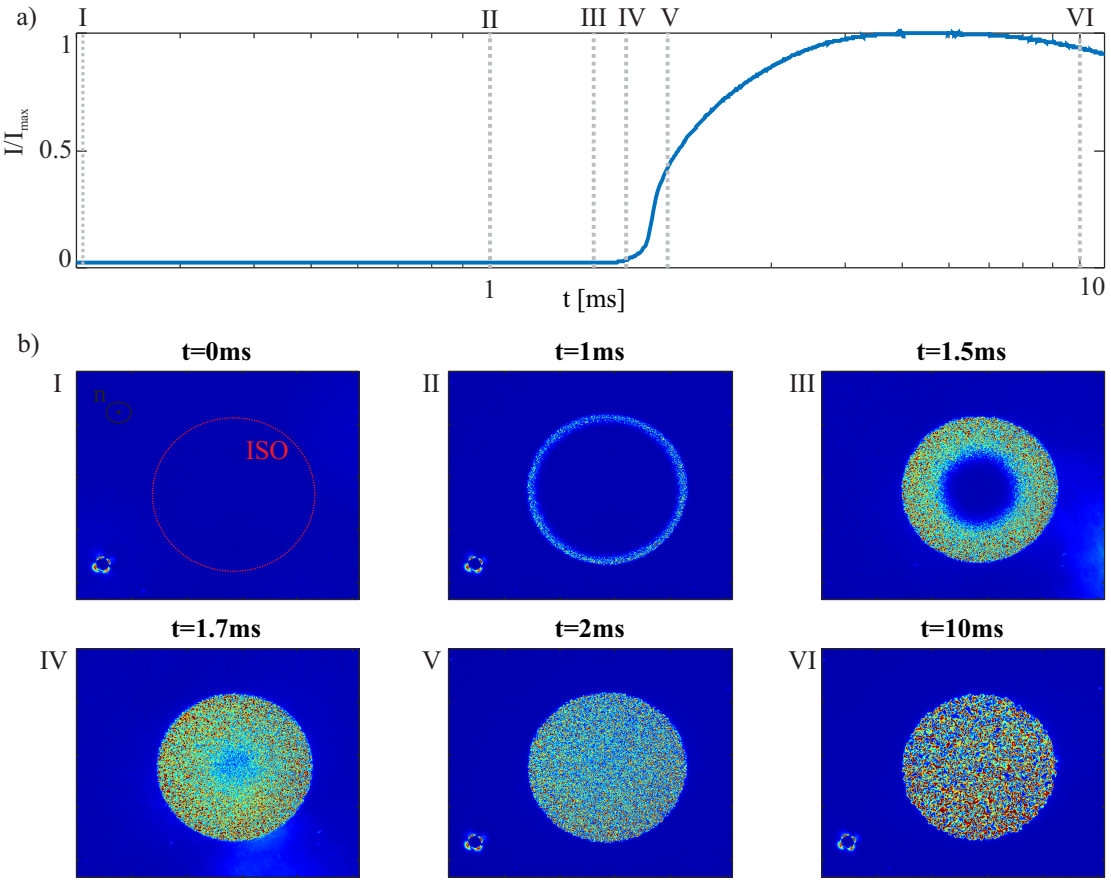


Figure 5.41: **a** Light transmission of a 7.5 µm thick sample cell of 5CB after rapid phase transmission. **b** Individual POM snapshots at significant times are marked from 0 ms **I** when the whole heated area is heated high above the phase transition temperature to 10 ms **VI**, where due to the greater thickness the system did not jet restore order. The edge of the heated area is marked by a red circle and the measuring spot is marked by a green dot.

Finally, we increase the sample cell thickness to 18 µm and again observe the light transmission after laser heating Fig. 5.42 a and show typical snap shot in Fig. 5.42 b. At time 0 ms, Fig. 5.42 a.b.I. the whole heated area is in the isotropic phase. At time 1 ms , Fig. 5.42 a.b.II we still do not observe any signs of ordering inside the heated area. Eventually light patches start forming at the edges of the heated area at 1.5 ms, Fig. 5.42 a.b.III. The patches move towards the center of the heated area until at times 2 ms, Fig. 5.42 a.b.IV and 2.1 ms, Fig. 5.42 a.b.V. The light patches need significantly longer to reach the mid point and are approximately the biggest size at 10 ms, Fig. 5.42 a.b.VI, yet the coarsening dynamics is still ongoing for more than 100 ms.

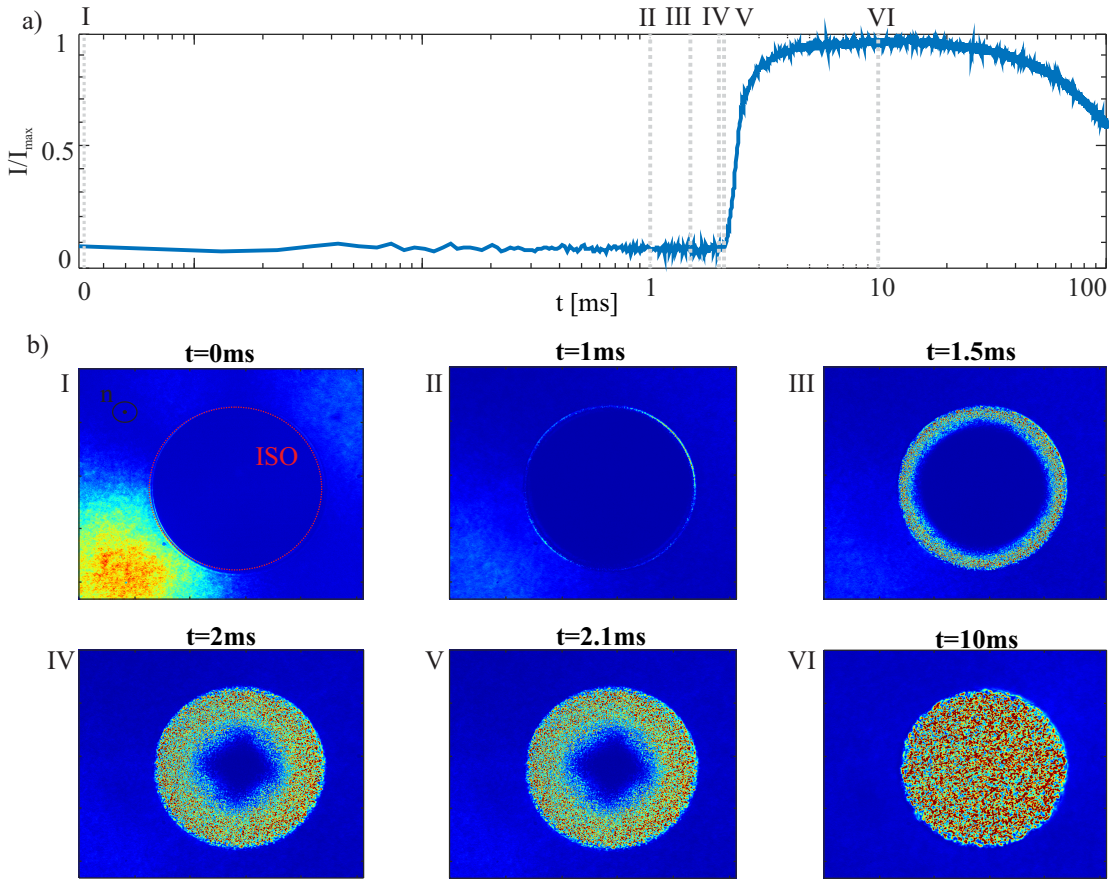


Figure 5.42: **a** Light transmission of a 18 µm thick sample cell of 5CB after rapid phase transmission. **b** Individual POM snapshots at significant times are marked from 0 ms **I** when the whole heated area is heated high above the phase transition temperature to 10 ms **VI** where the system still shown large light patches. The edge of the heated area is marked by a red circle and the measuring spot is marked by a green dot.

Also if we look at the snap shots in Fig. 5.42, we can observe a strange pattern emerging in the isotropic regions of the heated area as is cools to room temperature. This is due to currents being produced inside the isotropic island by to the huge temperature difference in the z direction of the sample cell, due to mutual insulation of individual liquid crystal layers.

Combining the data from the light transmission studies shown in Fig. 5.40, Fig. 5.41, and Fig. 5.42 into a lin-log plot shown in Fig. 5.43 a, we can clearly observe the impact of the sample thickens on coarsening dynamics after rapid phase transitions. We compare the widths of the transmission curves at half maximum to get a rough approximation of the scaling law of coarsening time vs sample cell thickens. By plotting the data onto a log-log plot, we observe a linear behaviour with slope of 1.85 ± 0.05, indicating an almost square dependency of the sample cell thickness on the coarsening dynamics.

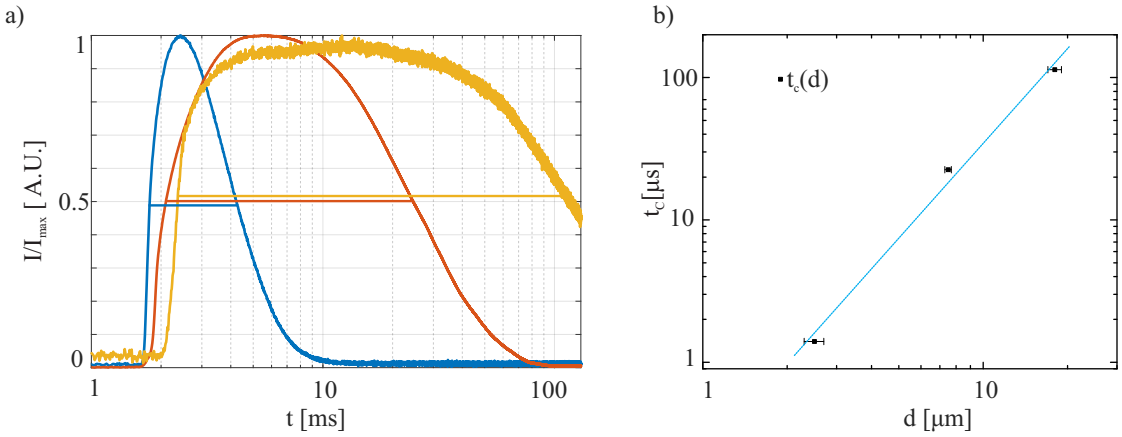


Figure 5.43: Sample cell thickness dependency of coarsening dynamics. **a** Light transmission study on 2.5 µm (blue), 7.5 µm (red) and 18 µm thick cell under crossed polarizers. **b** The time measured at FWHM indicated an almost square dependency of the impact of the sample cell thickness on the coarsening dynamics.

5.4.3 Supercooling temperature

In previous sections, we used the light transmission of LC sample cells to determine the time a the LC sample needs from start of the phase transition to he stabilization into the ground state, through the process of coarsening dynamics. In previous sections we also measured the dynamic thermal properties of the cells, thus enabling us to connect the time of the detection of signal to the time the system cools to the phase transition temperature. We use the light transmission set up and measure the transmission of two sample cells filled with 5CB or E18, respectively. Both cells are 2.5 µm thick and, therefore, the cooling rate of botch cells should be the same. We put the cells onto the imaging plane of the microscope and measure the transmittance in the middle of the sample cell as the cell is locally heated to various temperatures above the phase transition temperature of the LC inside. A typical measurements, from initial temperature of 100 °C, is plotted in Fig. 5.44. For comparison we also add the calculated time evolution of the temperature inside the cell.

Comparing the times the system needs to cool to the room temperature and the time we detect a signal, we observe a delay, indicating the presence of a supercooled isotropic phase. For the E18 sample cell we detect a delay of 130 µs and for the 5CB cell a total of 500 µs. Those delays are significantly larger than any predicted delay due to the Kibble-Zurek mechanism. One option is that, since the transition is weakly first-order a delay occurs due to the presence of latent heat, yet this argument can hardly explain more than a few 100 µs. Further theoretical predictions are required to determine the physical background of the delay.

To be certain about the calculated values of the temperature inside the samples, we perform test starting on the accuracy of the two exponent fit in Fig. 5.11. We test the plausible variations on the free parameters of the fit, those being the initial temperature, the amplitudes and the time exponents. Variations in those three parameters show a 10 % error at 60 °C and a total of 35 % error at 35 °C, seen in Fig. 5.45. Such an increase of the error can be explained by the two exponent nature of the fit, since one time exponent is significantly larger than the other.

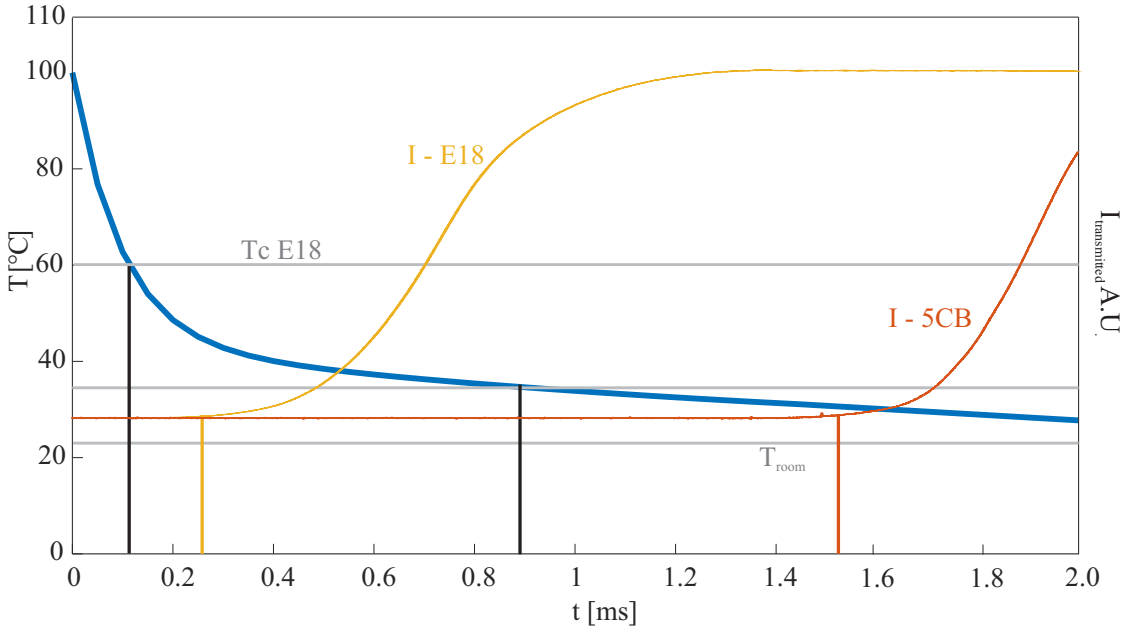


Figure 5.44: Measurement of the delay between reaching phase transition and detection of signal. A delay of 130 µs for E18 and 500 µs is detected.

To determine the presence of a supercooled isotropic phase, we perform the light transmission study of the two sample cells of 5CB and E18 at various initial temperature. Considering the error determined in Fig. 5.45, we plot the resulting data in Fig. 5.46 I for 5CB and Fig. 5.46 II for E18.

Considering the time delay measured in between the phase transition temperature and the observance of the signal we can calculate the temperature difference. For the maximum time of the 5CB sample cell we observe a 500 µs delay, corresponding to a temperature drop of 5 °C and for the case of the E18 sample cell we obseve a delay of 130 µs accounting to a temperature drop of 24 °C. By calculating the cooling rate at the phase transition we can further on calculate the temperature drop during the Zurek time. We first have to calculate the quench rate considering the cooling rates at phase transition temperature of $10\,\mathrm{K\,ms^{-1}}$ for 5CB and $135\,\mathrm{K\,ms^{-1}}$ for E18. We rely on the definition of [65] where they define the quench rate as the time needed to reach zero temperature at this cooling rate. We calculate a value of 30 ms for 5CB and 2.5 ms for the case of E18. Those values provide us with a ruff estimate of the Zurek times in both cases. We calculate the value as $\tau_z = \sqrt{\tau_q \tau_o}$, where we take $\tau_o = 10^-6s$the value for the relaxation time on a typical nematic LC. We find a value of 170 µs for the 5CB and 50 µs for the case of E18 with a corresponding temperature drop of 1.7 °C for 5CB and 6.7 °C for E18 indicating that we have successfully cooled the system for more than the coexistence band of 1K in the time the thermal fluctuations have been frozen, the Zurek time.

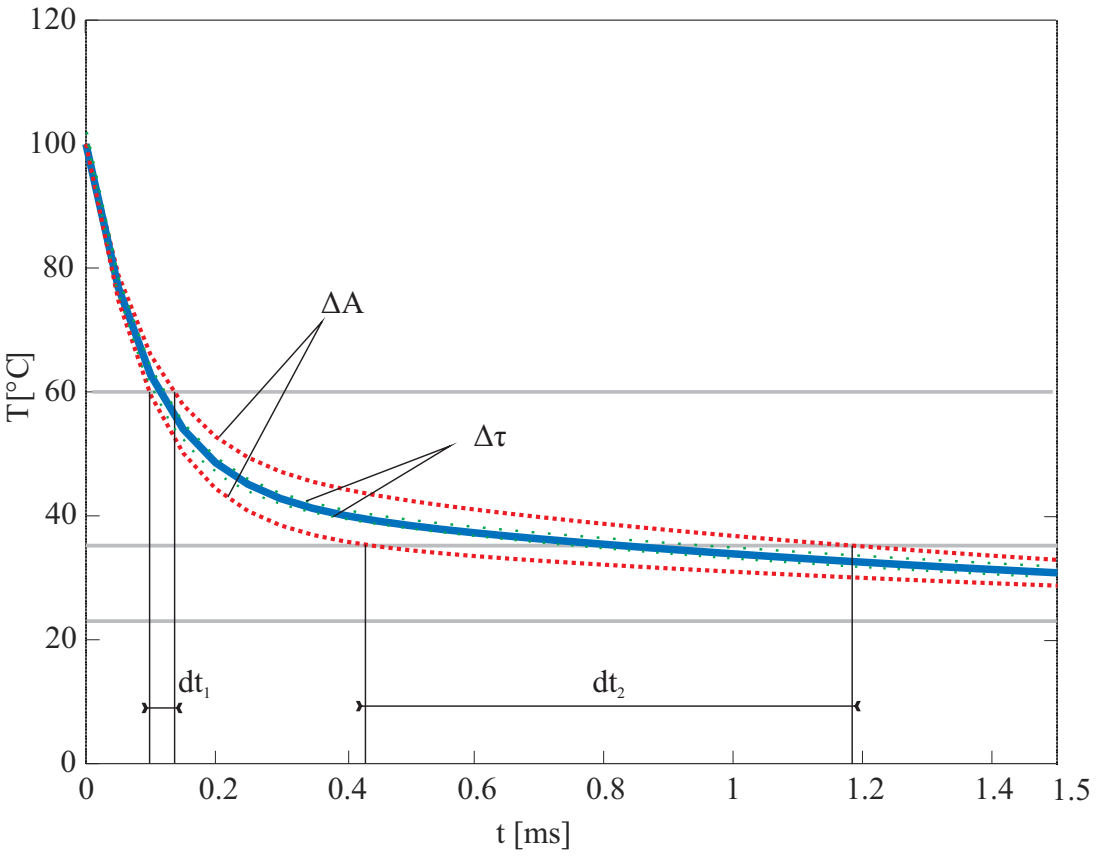


Figure 5.45: Time dependency of cooling fir accuracy. A rigours testing of fitting parameters of the two exponent cooling fit provide a total of 10 % error at 60 °C and 35 % at 35°.

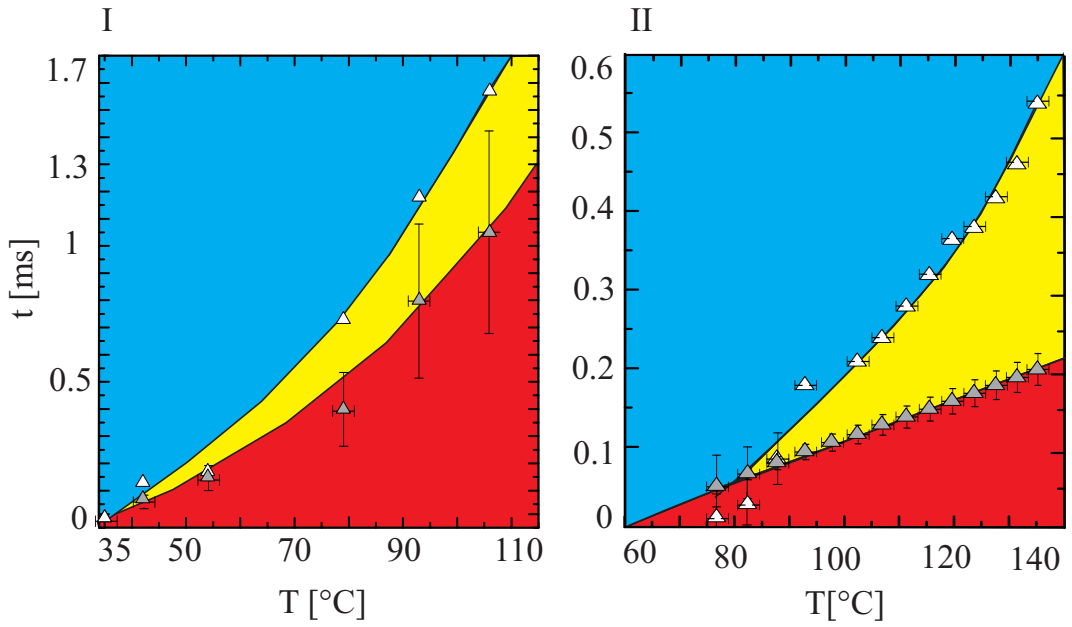


Figure 5.46: Super cooled isotropic region. **I** Data points for 5CB and **II** for E18. The red area marks the time the system is above the phase transition temperature. The blue area indicates the system cooled below the phase transition temperature and also we detect the formation of nematic order. The yellow area marks the region where the system is below the phase transition temperature, yet still no ordering is detected.

Chapter 6

Conclusions

The study of topological defects has gained a wide spread interest in various physical systems. It started with the study of the formation of cosmic strings after the big bang and continued to the study of the formation of vortices in super fluids and recently to the study of solitons in quantum Hall effects and the Bose-Einsten condensates. Although the amount of theoretical studies increases almost exponentially, experimental coverage is still lagging behind. Especially in the formation of topological defects, where due to the extreme experimental conditions almost no experimental coverage has been done so far.

In our work we first study the formation of topological defects surrounding colloidal particles of various shapes and in the second part we study the formation of topological defects as they form from rapid symmetry breaking phase transitions.

To study the formation of topological defects surrounding colloidal particles, shown in Chapter 4, we produce particles of various shapes, enforce the surface anchoring conditions and immerse them in various LC samples. We start by fabricating the particles using a two-photon polymerization technique, where we produce two types of particles. We aim to study the impact of local geometry on the formation of topological defects. Therefore, we produce particles of the same genus type where we drastically change the geometrical properties in between the particles. We pick the genus one, or in other words the particles we produce only have one hole, as for instance a torus, a coffee mug etc. To study the impact of geometry we pick the extreme geometry of a fractal, where the basic characteristic of the particles is described by self-similarity over several length scales. We produce hollow prisms with the first four Koch fractal iterations as base and immerse them in nematic LC. The resulting mixture is then placed into a planar glass cell and observed using POM. Due to the miss-match of surface orientation of molecules on the particles and on the substrates, the particles levitate in the mid-plane of the cell and also after long times do not sediment.

Using a high amplification oil immersion objective and a trick in the POM set-up, where we rotate the polarizer towards the analyzer to enhance the contrast of the disclination lines, we are able to determine the positions and structure of topological defects for the first three iterations of kick particles. Due to the 60° symmetry of the particles two orientation towards the nematic director are possible. A disclination line is running all around the particles, yet due to strong pinning we are only able to detect the crossing point of the disclination line through the mid-plane of the particle. By observing the positions of and structure of the crossing points, we are able to detect an increasing number of topological defect pairs as we increase the fractal iterations. Also by observing the impact of the defects on the surrounding director field cross-section, we are able to determine the winding number of the defects. All iterations obey the Gauss-Bone theorem that connects the total winding number of topological defect to the genus of the particles. Due to the genus of our particles of one, the total winding has to be zero, as is seen in the experimental

observations. By additional FEM numerical simulations we are able to continue the study beyond the experimental limitations even to the 5^{th} iteration Koch fractal. By combining the data we are able to detect a purely geometry-based scaling law connecting the total number of topological defects to the fractal iteration.

Using fractal shapes allowed us to determine the impact of the colloidal shape on the formation of topological defects. Next we want to study the impact of the surrounding LC on the formation of defects. Therefore, we continue with printing the simplest possible particles of genus type one, colloidal tori, and immerse them in LC with various amounts of chiral dopant. The addition of a chiral dopant causes a twist in the director field of the molecules as we move from the substrates. The amount of twist is solely dependent on the amount and structure of the chiral dopant. We start off by a simple planar sample cell where the surrounding substrates are placed perpendicular towards each other. This configurations allows a twist in the director field of $\pi/2$. We include toroidal particles, that we treated with a surfactant to assure homeotropic anchoring condition on the surfaces. The structure of the disclination lines is observed using optical tweezers and the a POM set-up. We are able to detect three distinct configurations of the positions of the disclination lines. We notice that in all cases the crossing point of the disclination lines through the mid-plane of the particles occurs at the point of maximal miss-match of orientation on the particle surfaces and the director field.

The structures are relatively easily observed and understood, yet with the increase of the chirality of the system the structure becomes extremely hard to understand. We test this by placing the same kind of particles into planar cells filled with nematic LC with various additions of chiral dopant. Already by observing a cell with a twist equal to π we observe highly twisted structures with a structure that is hard to determine using conventional POM. Therefore, we seek the help of an experimental technique that allows us to determine the exact position of the dislination lines and also the orientation of the director field. The method is based of FCPM with a computer algorithm that allows direct reconstruction of the orientation of the director field. Using the method we are able to detect a vast array of different topological defect configurations surrounding toroidal particles. Yet due to the extreme complexity of the configurations further experimental and theoretical work is required to classify the structure and study the impact of chirality on the structure.

Several topological defect configurations can be studied on a single particles by simple heating the particle into the isotropic phase and letting it cool back to the ground state. Due to the complete random nature of the isotropic phase there is no memory effect of the previous configuration in the isotropic phase. The topological defects form through the process of rapid symmetry breaking phase traditions. As the system cools, thermal fluctuations in the orientation of the building blocks act as nucleation sites that grow to form isolated patches of nematic ordering below the phase transition point. The process is extremely universal and was first observed in the formation of cosmic strings after the Big Band [27], later the impact of the cooling speed was studied in the process coining the so called Kibble-Zurek mechanism. It can be used to describe all symmetry breaking phase transitions, where an order parameter can be defined which increases its value from zero in the symmetrical phase to non-zero in the phase with broken symmetry. The basic prediction of the KZ mechanism predicts that as we increase the speed of the cooling, we reach a point where the dynamics of the order parameter starts to lag behind the imposed dynamics, effectively freezing the system. Only after a certain time after the transition, the dynamics catches up and the system forms patches of low symmetry phase, called domains. The orientation of the domains is determined by seeds, caused by thermal fluctuations in the isotropic phase. As the system further cools, domains grow with the expense of

smaller domains to eventually annihilate to the stable ground structure defined by the orientations imposed by the confinement. The process is called coarsening. The process of coarsening dynamics has been experimentally observed down to a few milli seconds after the transition through light transmission study experiments. Yet experimental coverage of processes leading up to coarsening is still missing.

We develop a novel experimental technique, enabling us to study the formation of topological defects right to the start of cooling. The technique consists of two parts the first is a laser illumination system that uses shot pico second laser pulses and a dye solution, to create an almost incoherent extremely bright light source with pulse duration of approximately 20 ns. Thus enabling us to freeze the dynamics within the time of the illuminations. Although we can expose images in this short amount of time, the read-out time of a camera forbids us to capture images less than 10 ms apart without the loss in quality. Therefore, we chose a stroboscopic imaging technique, where the camera sensor is open for a long period of time and only the illumination pulse exposes the image. By running the experiment repeatably and adjusting the delay when the illumination pulse exposes the image, we are able to combine the images into a movie of the whole process.

A rapid phase transition is induced by localized laser heating of a thin metallic layer of ITO, coated on the substrate. We use a pulse of a diode laser to heat up an area in the sample cell way above its phase transition temperature. As the heating laser is turned off, the metallic layer acts as a heat sink dissipating the heat with up to $10\,\mathrm{K\,ms^{-1}}$. Through cooling we image the process in detail, using crossed polarizers. We observe the formation of nematic ordering, by detecting small light patches on the images as the small nematic domains form from the isotropic melt, start to scatter and retard the light. As the system cools, we observe the light patches growing and later merging into ever larger ones. At this point coarsening dynamics take over and the patches annihilate to the stable director configuration.

As the process of rapid phase transition is extremely temperature and cooling rate dependent, we want to measure the thermal properties of the sample cells used. First we want to measure the initial temperature of the LC just before the heating laser turns off. By exploiting the first order phase transition nature of the transition we can simply observe the position of the edge of the isotropic island formed by the heating and attribute it the phase transition value. By repeating the experiment for several LCs with different phase transition temperatures we are able to determine the exact initial temperature profile inside the sample cell. Since most properties of the LC are strongly temperature-dependent, we can measure the time evolution of the temperature using the LC itself as the thermometer. The most notable temperature dependent property we exploit is the birefringence, which is completely zero in the isotropic phase and grows obeying a square root dependency in the nematic phase. In a certain geometry configuration, the sample cell acts as an optical retarder. And since the retardation is birefringence dependent, we can measure the temperature of the sample cell by measuring its transmittance. This is done by focusing a laser beam onto a small spot of the heated area and measuring the transmittance. Since the birefringence is zero in the isotropic phase where we want to determine the time dependency, we use a LC with a higher phase transition temperature for the measurement. We locally heat up the sample close to the phase transition temperature and measure the transmittance. From this information and the measured temperature dependency of the birefringence we are able to determine the time evolution of the sample cell for any initial temperature.

Next, we focus on the imaging data acquired using the laser illumination system and the stroboscopic imaging technique. A typical experimental run produces an abundance of data that simply can-not be processed by a human. Therefore, we develop an image

processing algorithm that extracts the data from thousands of images and statistically processes them. The basic properties, provided by the images, are the location of the light patches relative to the center of the heated area, their relative size and their relative intensity. By comparing the data at different time steps after the start of the cooling and also combining the data acquired from thousands of images taken at the same time, we are able to follow the phase transition dynamics in unprecedented detail. By analyzing the data we are able to determine the occurrence of the nematic ordering right as it forms from the isotropic melt to where coarsening dynamics takes over. The whole process takes less than 2 ms and we are able to follow it with nano second accuracy. Additionally to the image acquisition algorithm we measure the transmittance over the radius of the image and detect additional signal, probably caused by scattering on small nematic domains, where the resulting light is not picked up by the algorithm. The information gathered by the experiments provides enough data to predict the presence of nematic domains way below the diffraction limit, yet additional testing is required. Furthermore, since the light patches are a direct cause of the formation of nematic domains through the sample, we are not sure how the two are connected, and if there is a way we can determine one from another.

Coarsening dynamics describes the merging and annihilation of domains to form stable ground configurations. Using our experimental images we observe, that light patches form at the edge of the isotropic melt and grow to a finite size at the edge of the heated area. And due to surface tension we expect the nematic domains to be roughly spherical. A direct consequence is that the maximum domains size can only be the cell thickness. We test the impact of cell thickness on the coarsening dynamics by performing light transmission studies on cells of various thicknesses. We detect a novel sample thickness dependency of the process, which connects the cell thickness with the square of the time of coarsening.

Finally we set out to test the predictions of the Kibble-Zurek mechanism. The first being the impact of the cooling rates on the formation of nematic order. Therefore, we measure the typical growth rates of the light volume and the pixel intensity, at different times. And since at different times the growth starts at different radii, which correspond to different cooling rates, we are able to determine the effect of the cooling rate. Interestingly, we are able to detect two regimes. For small cooling rates of up to $4\,\mathrm{K\,ms^{-1}}$, we detect a slow growth and for larger cooling rates a much greater growth. This contradicts the notion of the KZ mechanism, where faster cooling rates produce smaller domains and short freezing times. The probable cause is that the small domains require a larger amount of time to grow from the proto-domain size to the size experimentally detectable. Further theoretical investigation is still required.

The second prediction is the freezing of the system after rapid phase transition. Therefore, we combine the thermal measurements to determine the exact time at which each and every spot of the heated area reached the phase transition temperature. Next, using the light transmission set-up we measure the local transmittance of the sample cell under crossed polarizers, thus enabling us to determine the exact timing the light starts being transmitted due to the presence of nematic ordering. Combining the timing for two separate LC samples, we are able to detect a significant delay of up to half a milli second. This implies that the isotropic phase is stable for an additional half a milli second in the nematic phase. We can calculate that this time translated to a 5 °C temperature drop for the slower 5CB phase transition and 24 °C for the E18 transition. Also by calculating the appropriate quench rates we are able to observe a significant drop of temperature in the freeze out time called the Zurek time implying that we have successfully "transferred" the isotropic phase beyond the coexistence band of 1 °C between the two phases.

We conclude that we have observed the formation of topological defects in the regime

of $\tau_q/\tau_o < 2^3$ that is significantly faster than observed by the only known experimental observation following pressure quenches by a factor of 400. By modifying the experimental set-up we could be able to increase the speeds close to the speed of thermal fluctuations, which are in the area of µs. This could be done by the use of a sample cell that would be a better heat sink than the current one. For instance, with the use of sapphire substrates one could increase the thermal conductivity of the sample cell by a factor of 30.

This work opened a whole new path for experimental exploration of rapid phase transition dynamics. The developed experimental techniques provide a testing ground for a whole array of phase transition dynamics to be studied. One interesting phase transition is the formation of topological defects after a second-order phase transition, such as the smectic C to smectic A phase transition. Here, since no phase co-existence should exist, domains formation in an isotropic melt would directly prove the KZ mechanism. Additionally the method can be used to study the formation of topological defects surrounding colloidal particles, providing the connection of the phase transition dynamics to the topology of the system.

Although the current experimental set-up provides a proving ground for experimental observations, small modifications to the set-up would provide a new picture of the process. For instance, if we were able to capture two images in rapid succession, we could study the actual dynamics of individual domains. Furthermore, since the system allows nanosecond exposure times, we could potentially capture the dynamics of thermal fluctuations.

To conclude, this work provides a starting ground in the experimental observation of rapid phase transition phenomena that could not be observed so far due to a lack of experimental techniques. By increasing experimental coverage we also raise a whole array of questions that have to be addressed by the theory. In order to fulfil this gap, further investigation is required. Therefore, this research field is still wide open.

Appendix A

Further Observations

In this section we will provide additional preliminary results that still lack proper explanations and were therefore not included in the main part of the work.

A.1 Rapid Phase Transition Surrounding Topological Objects

We studied the formation of topological defects following rapid symmetry breaking phase transition in nematic LCs. We developed an experimental set-up consisting of a rapid laser illumination system and a stroboscopic imaging technique. We studied the impact of cooling rate on the formation of nematic order as it emerges from the isotropic melt. All experiments had in common a ground state containing zero topological charge or in other words a vacuum. Next, we set out to test the impact of cooling rates on the formation of topological defects surrounding colloidal particles of various topologies. We set up two experiments. First, we print toroidal colloids with the major radius of 12 µm and the minor radius of 3 µm treated with DMOAP to assure strong homeotrpic anchoring on the surfaces of the colloids. Next, we place the particles into a nematic LC, in our case 5CB. The resulting mixture is then due to the capillary force filled into a sample glass cell we prepared. The cell is made of two ITO-covered glass plates and 10 µm spacers are added to assure adequate spacing. We chose glass with a thick ITO layer, which acts as a heating source and also as the heat sink of our experiments. The sample cell is placed onto the imaging plane of the microscope and using a diode laser pulse we locally heat up the surrounding of the particle above the phase transition temperature. As the heating laser shuts down we use the nanosecond illumination system and stroboscopic imaging technique to image the formation of topological defects as the LC cools to the nematic phase. Additionally, we use crossed polarizers to enhance contrast between the birefringent nematic phase and the isotropic phase.

By repeating the experiments we soon observe that the particles move every time the LC is heated into the isotropic phase, as seen in Fig. A.1.

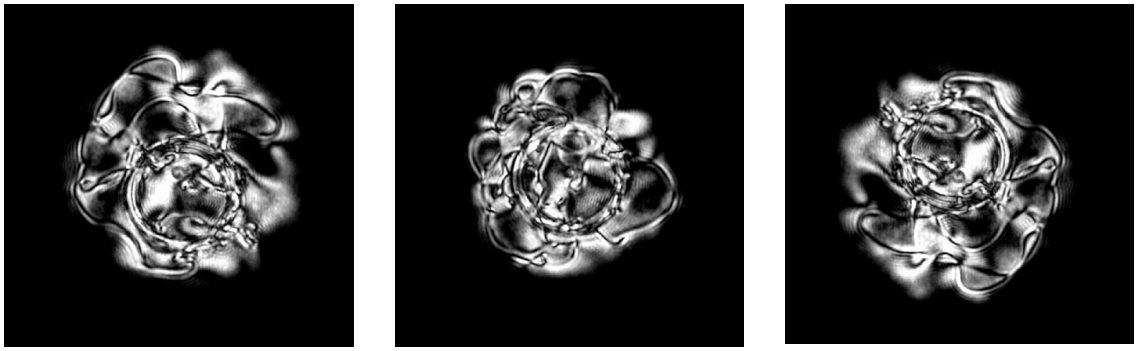


Figure A.1: Formation of topological defects surrounding a free-standing toroidal colloid. Images are obtained at different experiments indicating moving of the particles. Due to the presence of uncontrollable flows in the isotropic phase the torus moves in between experiments.

As seen in Fig. A.1, the positions of the particle move quite dramatically. This makes the images incomparable since due to the extreme movement of the particles the thermal conditions surrounding the particles vary and the defect structure forms at different conditions. We try to solve this problem by fixing the particles to the surface. Although this eliminates the singularity from the system and we can no longer talk about topological defects. Still defects lines form due to the strong mismatch of orientation on part of the torus where the orientation of the molecules on the surface is perpendicular to the orientation imposed by the anchoring conditions. We test this idea by printing a handle body made of two tori with the same dimensions as mentioned. Yet, here we print the particles directly onto the ITO-coated substrates. Again, we surface treat the particles and also the substrates and assemble a sample cell with thickness of 10 µm. Experimental observations of the process of the formation of topological defects in this case is shown snap shot in Fig. A.2. We observe the formation of nematic ordering first at the edge of the heated area, indicting a Gaussian temperature profile. As the area further cools the nematic ordering starts to appear ever closer inwards. The dense light patch structure completely masks the colloidal particles underneath. Only as, due to coarsening dynamics, disclination lines form and start to annihilate we observe the structure again.

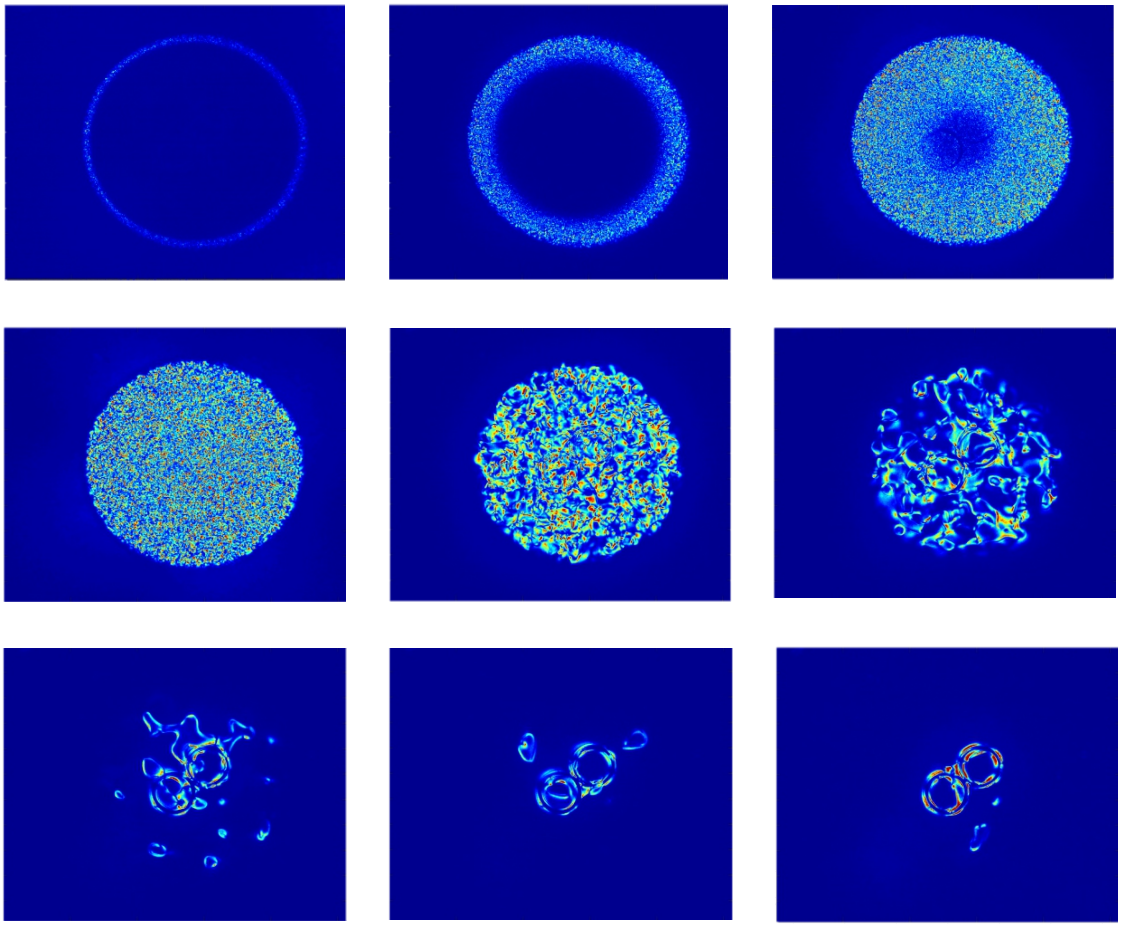


Figure A.2: Formation of topological defects surrounding a toroidal colloid. Images have a 20 ns exposure time. First row represents the first 2 ms after the cooling. We observe the appearance of nematic ordering at the edge. Second row shows the process at times from 5 ms to 10 ms covering most of the coarsening dynamics. The final row shows the winding of individual disclination lines around the handle-body at times of up to 100 ms.

The topological structure of colloidal tori is well studied [14], yet we still do not know at what point in time or at what stage of the coarsening dynamics the system "decides" in what configuration it will go. Further testing is required to address this question. For instance, the addition of a second camera into the system, which would capture the end configuration, would help to systematically study the formation of defect structures.

As mentioned, the defect structure of toroidal particles attached to the surfaces is not caused by singularities in the system, it is a consequence of an extreme miss-match of orientation on the surface compared to the surrounding, causing an area of extreme elastic deformations. We expand the idea by excluding miss-matches of orientations from the picture, to test only the impact of elastic deformations on the formation of topological defects. We chose a structure, that can be in simplest terms described as an egg-carton. In mathematical terms the height of the structure varies as a harmonic function of the **xy** coordinates. The valleys and the peaks of the structure present areas of higher splay in the system. Additionally, with the a phase shift of 90° between the **x** and **y** coordinates, the lips between neighbouring peaks and valleys form areas of high saddle splay. The structure is schematically shown in the first panel of Fig. A.3. The structures are printed onto the glass substrates with a gradual slope on the glass-structure interface, eliminating the pinning of individual defects. The maximum height of the structure is 5 µm and the diameter 20 µm. We repeat the assembly of the cells as mentioned, by coating ITO cover slips in a homeotropic surfactant and assemble the cells with 10 µm spacers. As we heat the sample into the isotropic phase we observe the formation of nematic ordering using polarization microscopy. We set the polarizer and analyzer to parallel this time to distinguish between the structure and the defects. The surrounding of the structure is heated up to the isotropic phase and then rapidly cooled to the nematic phase. At first the story repeats. The nematic order starts to form at the edges of the heated area and an ordered front forms that encloses the structure, as seen in the first row of Fig. A.3. Yet in the second row of Fig. A.3 we can clearly observe a much faster coarsening dynamics resulting in a far lesser defect density. Further on the trend continues, as seen by the fact that the bulk of the defect structure annihilates around the structure in last row of Fig. A.3.

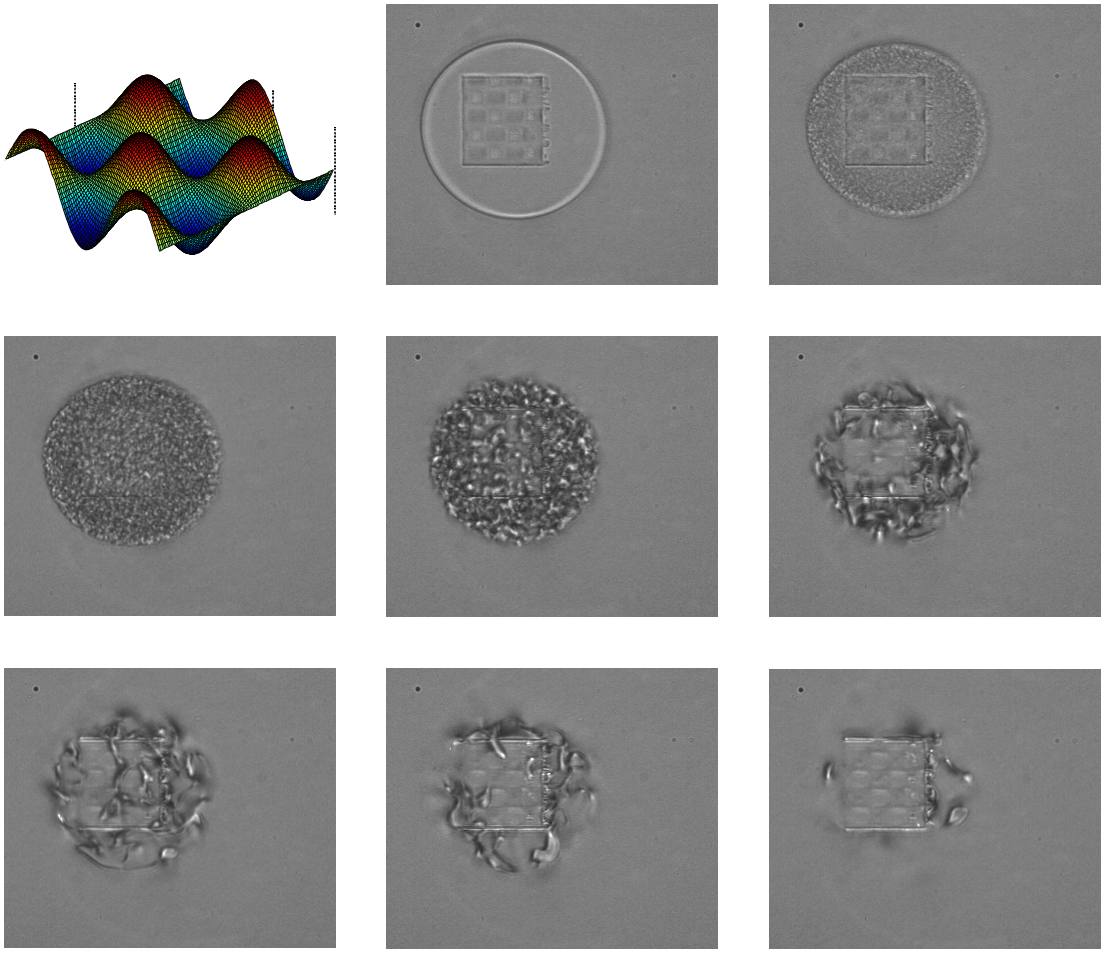


Figure A.3: Impact of elastic distortions on the formation of topological defects. A schematic drawing of the structure is shown in the first panel. Images obtained using parallel polarizers are shown next. As the system cools, a faster coarsening dynamics is observed above the structure compared to the surrounding.

The speed-up of the coarsening dynamics is mainly due to the smaller volume of LC above the structure and therefore the system can reach the ground state of energy. A similar observation was made in Section 5.4.2, where we study the impact of the cell thickness on the coarsening dynamics. Interestingly, we do not observe any significant impact of the elastic deformations on the formation of nematic ordering. This is probably due to the relatively shallow structure that probably exerts too little elastic deformation to have an impact on the process. Yet, thicker structures will unevenly distribute the polymer structure, resulting in extremely uneven thermal properties of the system. Addition of metallic particles into the polymer structure, which would equalize the thermal properties of the structure, would help distinguish between the impact of thermal characteristics or elastic deformations.

A.2 Rapid Fréedericksz Transition-Induced Defect Jumping

In Section 4.3, we studied the formation of topological defects surrounding particles immersed in chiral nematic LC. As we were testing the stable configurations, we had an idea to test if a change in the orientation of the sample would cause a restructuring of the topological defect structure. One method of reorientating molecules is the Fréedericksz transition [115], where a large electric field is applied inside the sample cell and the resulting torque extorted on the molecules causes them to reorient to a homeotropic configuration. We test this method on several sample cells filled with MLC 7023 that has a positive dielectric anisotropy, required to reorient the molecules to a homeotropic configuration. We dope the LC with CB-15, a chiral dopant, to assure a chiral structure of the director field. Next, we create sample cells of 10 µm thickness made of two ITO-coated cover glasses. Additionally, wires were soldered to the ITO side of the glasses to assure a strong homogeneous electric field in the sample. We use a function generator to create the field by passing an AC current with 10 V amplitude and 1 Hz frequency onto the ITO. Homeotropically treated toroidal particles are placed into the LC mixture and placed into two sample cells. The first sample cell is made of two substrates with strong homeotropic anchoring condition, as evidenced by the resulting finger print pattern structure [116]. As we apply the electric field, we observe the Fréedericksz transition as the system starts to aper black under crossed polarizers. Interestingly, we observe one of the fingerprint pattern to split and wrap around the toroidal particle, as seen in Fig. A.4. The particle seems to stabilize the structure as the formation is stable for hours.

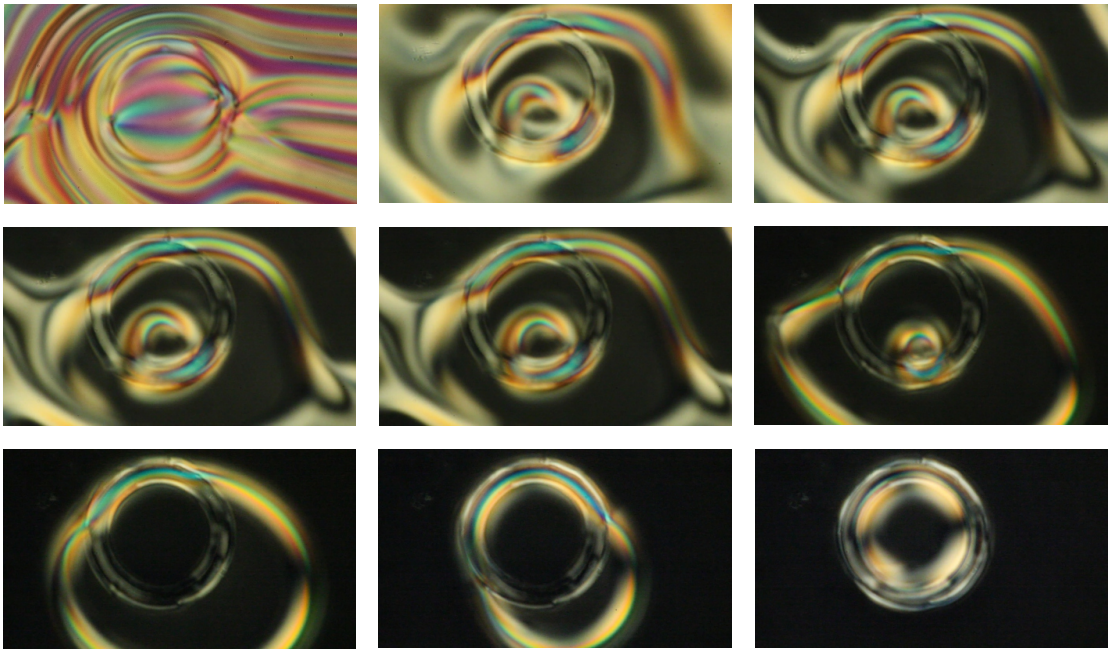


Figure A.4: Fréedericksz transition around a toroidal particle. A fingerprint appears to wind around the torus. As we slowly increase the voltage of an applied electric field on the sample cell to induce a Fréedericksz transition, we observe the unwinding of the fingerprint structure. Yet one fingerprint seems to wrap around the included torus, that appears to stabilize the structure.

Furthermore, we repeat the experiments in a planar cell, where the chirality in the system results in a $2pi$ winding of the director field. If the electric field is applied suddenly, we observe an extremely interesting phenomenon, where the complex defect structure surrounding the toroidal colloid has to unwind rapidly, therefore causing jumping of a defect loop out of the structure into the surrounding.

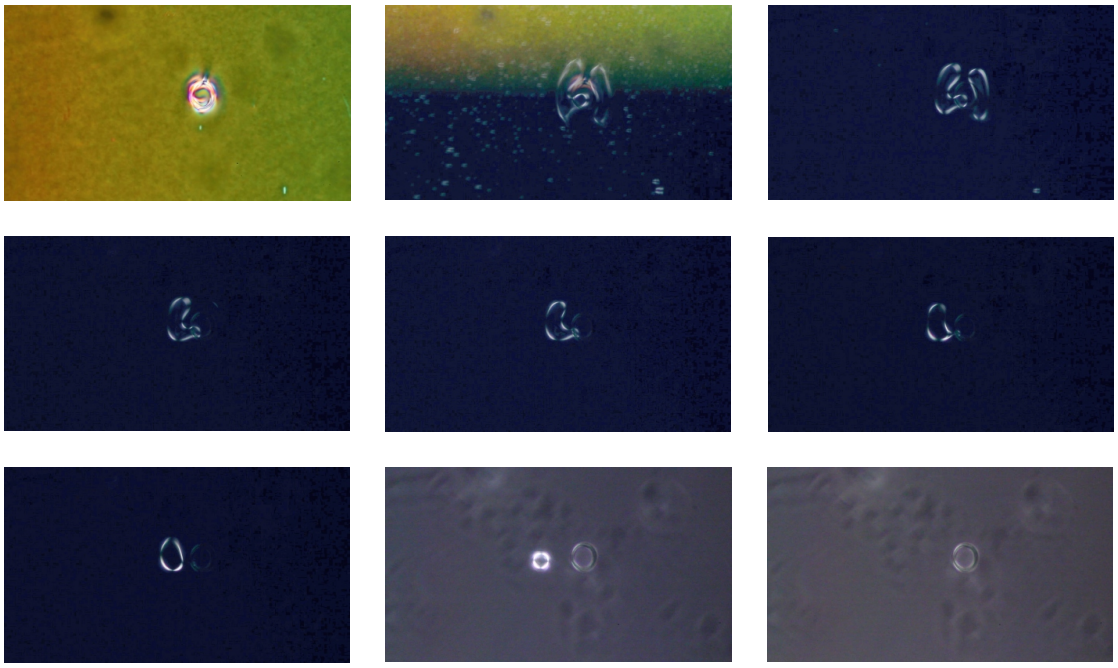


Figure A.5: Jumping of a disclination line after a sudden Fréedericksz transition. As we apply an electric field rapidly to induce a Fréedericksz transition, the highly twisted topological defect structure surrounding the torus in a twisted nematic rapidly unwinds, causing a detachment of a single disclination line, that jumps off the torus and annihilates off the side.

Both processes are repeatable and were observed on several particles. Yet we do not understand the phenomenon in detail. Therefore, additional testing is required. For instance, in the case of the defect jumping we plan to use the nanosecond illumination system to study the process in detail with higher resolution in time. For the case of the winding of the fingerprint structure we plan to use FCPM, since the process can be slowed down enough to enable the use of the method.

References

[1] J. Prost, *The physics of liquid crystals*. Oxford university press, 1995, vol. 83.

[2] M. Kleman and O. D. Laverntovich, *Soft matter physics: an introduction*. Springer Science & Business Media, 2007.

[3] P. M. Chaikin, T. C. Lubensky, and T. A. Witten, *Principles of condensed matter physics*. Cambridge university press Cambridge, 1995, vol. 1.

[4] J. W. Goodby, P. J. Collings, T. Kato, C. Tschierske, H. F. Gleeson, and P. Raynes, "Handbook of liquid crystals," 2014.

[5] N. D. Mermin, "The topological theory of defects in ordered media," *Reviews of Modern Physics*, vol. 51, no. 3, p. 591, 1979.

[6] D. Bishop, P. Gammel, D. Huse, and C. Murray, "Magnetic flux-line lattices and vortices in the copper oxide superconductors," *Science*, vol. 255, no. 5041, pp. 165–172, 1992.

[7] V. Ruutu, V. Eltsov, A. Gill, T. Kibble, M. Krusius, Y. G. Makhlin, B. Placais, G. Volovik, and W. Xu, "Vortex formation in neutron-irradiated superfluid 3he as an analogue of cosmological defect formation," *Nature*, vol. 382, no. 6589, p. 334, 1996.

[8] A. Wachowiak, J. Wiebe, M. Bode, O. Pietzsch, M. Morgenstern, and R. Wiesendanger, "Direct observation of internal spin structure of magnetic vortex cores," *Science*, vol. 298, no. 5593, pp. 577–580, 2002.

[9] O. Tchernyshyov and G.-W. Chern, "Fractional vortices and composite domain walls in flat nanomagnets," *Physical review letters*, vol. 95, no. 19, p. 197204, 2005.

[10] S.-B. Choe, Y. Acremann, A. Scholl, A. Bauer, A. Doran, J. Stöhr, and H. A. Padmore, "Vortex core-driven magnetization dynamics," *Science*, vol. 304, no. 5669, pp. 420–422, 2004.

[11] B. Van Heck, M. Burrello, A. Yacoby, and A. Akhmerov, "Topological blockade and measurement of topological charge," *Physical review letters*, vol. 110, no. 8, p. 086 803, 2013.

[12] L. Wang, M. Troyer, and X. Dai, "Topological charge pumping in a one-dimensional optical lattice," *Physical review letters*, vol. 111, no. 2, p. 026 802, 2013.

[13] U. Tkalec, M. Ravnik, S. Čopar, S. Žumer, and I. Muševič, "Reconfigurable knots and links in chiral nematic colloids," *Science*, vol. 333, no. 6038, pp. 62–65, 2011.

[14] B. Senyuk, Q. Liu, S. He, R. D. Kamien, R. B. Kusner, T. C. Lubensky, and I. I. Smalyukh, "Topological colloids," *Nature*, vol. 493, no. 7431, p. 200, 2013.

[15] V. S. R. Jampani, M. Škarabot, M. Ravnik, S. Čopar, S. Žumer, and I. Muševič, "Colloidal entanglement in highly twisted chiral nematic colloids: Twisted loops, hopf links, and trefoil knots," *Physical Review E*, vol. 84, no. 3, p. 031 703, 2011.

[16] I. Muševič and M. Škarabot, "Self-assembly of nematic colloids," *Soft Matter*, vol. 4, no. 2, pp. 195–199, 2008.

[17] I. Muševič, M. Škarabot, U. Tkalec, M. Ravnik, and S. Žumer, "Two-dimensional nematic colloidal crystals self-assembled by topological defects," *Science*, vol. 313, no. 5789, pp. 954–958, 2006.

[18] A. Nych, U. Ognysta, M. Škarabot, M. Ravnik, S. Žumer, and I. Muševič, "Assembly and control of 3d nematic dipolar colloidal crystals," *Nature communications*, vol. 4, p. 1489, 2013.

[19] I. Muševič, M. Škarabot, D. Babič, N. Osterman, I. Poberaj, V. Nazarenko, and A. Nych, "Laser trapping of small colloidal particles in a nematic liquid crystal: Clouds and ghosts," *Physical review letters*, vol. 93, no. 18, p. 187801, 2004.

[20] O. Francescangeli, S. Slussarenko, F. Simoni, D. Andrienko, V. Reshetnyak, and Y. Reznikov, "Light-induced surface sliding of the nematic director in liquid crystals," *Physical review letters*, vol. 82, no. 9, p. 1855, 1999.

[21] M. Nikkhou, M. Škarabot, S. Čopar, M. Ravnik, S. Žumer, and I. Muševič, "Light-controlled topological charge in a nematic liquid crystal," *Nature physics*, vol. 11, no. 2, p. 183, 2015.

[22] R. Snyder, A. Pargellis, P. Graham, and B. Yurke, "Light-transmission study of coarsening in a nematic liquid crystal," *Physical Review A*, vol. 45, no. 4, R2169, 1992.

[23] I. Chuang, N. Turok, and B. Yurke, "Late-time coarsening dynamics in a nematic liquid crystal," *Physical review letters*, vol. 66, no. 19, p. 2472, 1991.

[24] I. Chuang, B. Yurke, A. N. Pargellis, and N. Turok, "Coarsening dynamics in uniaxial nematic liquid crystals," *Physical Review E*, vol. 47, no. 5, p. 3343, 1993.

[25] N. Mermin and T.-L. Ho, "Circulation and angular momentum in the a phase of superfluid helium-3," *Physical Review Letters*, vol. 36, no. 11, p. 594, 1976.

[26] C. N. Weiler, T. W. Neely, D. R. Scherer, A. S. Bradley, M. J. Davis, and B. P. Anderson, "Spontaneous vortices in the formation of bose–einstein condensates," *Nature*, vol. 455, no. 7215, p. 948, 2008.

[27] T. W. Kibble, "Topology of cosmic domains and strings," *Journal of Physics A: Mathematical and General*, vol. 9, no. 8, p. 1387, 1976.

[28] W. H. Zurek, "Cosmological experiments in condensed matter systems," *Physics Reports*, vol. 276, no. 4, pp. 177–221, 1996.

[29] A. Chandran, A. Erez, S. S. Gubser, and S. Sondhi, "Kibble-zurek problem: Universality and the scaling limit," *Physical Review B*, vol. 86, no. 6, p. 064304, 2012.

[30] C. Bahr and H.-S. Kitzerow, *Chirality in liquid crystals*. Springer, 2001.

[31] P. Oswald and P. Pieranski, *Nematic and Cholesteric Liquid Crystals: Concepts and Physical Properties Illustrated by Experiments*. Taylor & Francis Group, 2005.

[32] N. J. Mottram and C. J. Newton, "Introduction to q-tensor theory," *arXiv preprint arXiv:1409.3542*, 2014.

[33] S. Singh, "Phase transitions in liquid crystals," *Physics Reports*, vol. 324, no. 2-4, pp. 107–269, 2000.

[34] M. Ravnik, "Colloidal structures confined to thin nematic layers: Doctoral thesis," PhD thesis, Univerza v Ljubljani, Fakulteta za matematiko in fiziko, 2009.

[35] L. Onsager, "The effects of shape on the interaction of colloidal particles," *Annals of the New York Academy of Sciences*, vol. 51, no. 4, pp. 627–659, 1949.

[36] M. Ravnik and S. Žumer, "Landau–de gennes modelling of nematic liquid crystal colloids," *Liquid Crystals*, vol. 36, no. 10-11, pp. 1201–1214, 2009.

[37] A. Alexe-Ionescu, G. Barbero, and G. Durand, "Temperature dependence of surface orientation of nematic liquid crystals," *Journal de Physique II*, vol. 3, no. 8, pp. 1247–1253, 1993.

[38] G. Crawford, D. W. Allender, and J. Doane, "Surface elastic and molecular-anchoring properties of nematic liquid crystals confined to cylindrical cavities," *Physical Review A*, vol. 45, no. 12, p. 8693, 1992.

[39] G. P. Chen, H. Takezoe, and A. Fukuda, "Determination of ki (i= 1–3) and μj (j= 2–6) in 5cb by observing the angular dependence of rayleigh line spectral widths," *Liquid Crystals*, vol. 5, no. 1, pp. 341–347, 1989.

[40] A. de Lózar, W. Schöpf, I. Rehberg, D. Svenšek, and L. Kramer, "Transformation from walls to disclination lines: Statics and dynamics of the pincement transition," *Physical Review E*, vol. 72, no. 5, p. 051 713, 2005.

[41] B. Jerome, "Surface effects and anchoring in liquid crystals," *Reports on Progress in Physics*, vol. 54, no. 3, p. 391, 1991.

[42] C. F. Bohren and D. R. Huffman, *Absorption and scattering of light by small particles*. John Wiley & Sons, 2008.

[43] T. Scharf, *Polarized light in liquid crystals and polymers*. John Wiley & Sons, 2007.

[44] G. R. Fowles, *Introduction to modern optics*. Courier Corporation, 1989.

[45] J. Li, S. Gauza, and S.-T. Wu, "Temperature effect on liquid crystal refractive indices," *Journal of applied physics*, vol. 96, no. 1, pp. 19–24, 2004.

[46] C. J. F. Böttcher, *Theory of electric polarisation*. Elsevier Publishing Company, 1952.

[47] A. Patani, M. Schlindwein, and Q. Shafi, "Topological charges in field theory," *Journal of Physics A: Mathematical and General*, vol. 9, no. 9, p. 1513, 1976.

[48] E. Brasselet, N. Murazawa, H. Misawa, and S. Juodkazis, "Optical vortices from liquid crystal droplets," *Physical review letters*, vol. 103, no. 10, p. 103 903, 2009.

[49] P. J. Ackerman, Z. Qi, and I. I. Smalyukh, "Optical generation of crystalline, quasicrystalline, and arbitrary arrays of torons in confined cholesteric liquid crystals for patterning of optical vortices in laser beams," *Physical Review E*, vol. 86, no. 2, p. 021 703, 2012.

[50] W. H. Zurek, "Cosmological experiments in superfluid helium?" *Nature*, vol. 317, no. 6037, p. 505, 1985.

[51] G. P. Alexander, B. G.-g. Chen, E. A. Matsumoto, and R. D. Kamien, "Colloquium: Disclination loops, point defects, and all that in nematic liquid crystals," *Reviews of Modern Physics*, vol. 84, no. 2, p. 497, 2012.

[52] M. Kleman and O. D. Lavrentovich, "Topological point defects in nematic liquid crystals," *Philosophical Magazine*, vol. 86, no. 25-26, pp. 4117–4137, 2006.

[53] I. Dierking, *Textures of liquid crystals*. John Wiley & Sons, 2003.

[54] T. Lubensky, D. Pettey, N. Currier, and H. Stark, "Topological defects and interactions in nematic emulsions," *Physical Review E*, vol. 57, no. 1, p. 610, 1998.

[55] S. Čopar and S. Žumer, "Topological and geometric decomposition of nematic textures," *Physical Review E*, vol. 85, no. 3, p. 031 701, 2012.

[56] G. Posnjak, S. Čopar, and I. Muševič, "Hidden topological constellations and polyvalent charges in chiral nematic droplets," *Nature communications*, vol. 8, p. 14 594, 2017.

[57] O. D. Lavrentovich, "Topological defects in dispersed words and worlds around liquid crystals, or liquid crystal drops," *Liquid crystals*, vol. 24, no. 1, pp. 117–126, 1998.

[58] M. Škarabot, M. Ravnik, S. Žumer, U. Tkalec, I. Poberaj, D. Babič, N. Osterman, and I. Muševič, "Interactions of quadrupolar nematic colloids," *Physical Review E*, vol. 77, no. 3, p. 031 705, 2008.

[59] E. Pairam, J. Vallamkondu, V. Koning, B. C. van Zuiden, P. W. Ellis, M. A. Bates, V. Vitelli, and A. Fernandez-Nieves, "Stable nematic droplets with handles," *Proceedings of the National Academy of Sciences*, vol. 110, no. 23, pp. 9295–9300, 2013.

[60] T. Lopez-Leon, V. Koning, K. Devaiah, V. Vitelli, and A. Fernandez-Nieves, "Frustrated nematic order in spherical geometries," *Nature Physics*, vol. 7, no. 5, p. 391, 2011.

[61] A. Martinez, M. Ravnik, B. Lucero, R. Visvanathan, S. Žumer, and I. I. Smalyukh, "Mutually tangled colloidal knots and induced defect loops in nematic fields," *Nature materials*, vol. 13, no. 3, p. 258, 2014.

[62] M. Ravnik, M. Škarabot, S. Žumer, U. Tkalec, I. Poberaj, D. Babič, N. Osterman, and I. Muševič, "Entangled nematic colloidal dimers and wires," *Physical Review Letters*, vol. 99, no. 24, p. 247 801, 2007.

[63] D. Seč, S. Čopar, and S. Žumer, "Topological zoo of free-standing knots in confined chiral nematic fluids," *Nature communications*, vol. 5, p. 3057, 2014.

[64] Z. Bradač, S. Kralj, and S. Žumer, "Molecular dynamics study of the isotropic-nematic quench," *Physical Review E*, vol. 65, no. 2, p. 021 705, 2002.

[65] ——, "Early stage domain coarsening of the isotropic-nematic phase transition," *The Journal of chemical physics*, vol. 135, no. 2, p. 024 506, 2011.

[66] S. Kralj, S. Žumer, and D. W. Allender, "Nematic-isotropic phase transition in a liquid-crystal droplet," *Physical Review A*, vol. 43, no. 6, p. 2943, 1991.

[67] A. D. Pezzutti, L. R. Gomez, M. A. Villar, and D. A. Vega, "Defect formation during a continuous phase transition," *EPL (Europhysics Letters)*, vol. 87, no. 6, p. 66 003, 2009.

[68] P. M. Chesler, A. M. Garcıa-Garcıa, and H. Liu, "Defect formation beyond kibble-zurek mechanism and holography," *Physical Review X*, vol. 5, no. 2, p. 021 015, 2015.

[69] A. Del Campo, T. Kibble, and W. Zurek, "Causality and non-equilibrium second-order phase transitions in inhomogeneous systems," *Journal of Physics: Condensed Matter*, vol. 25, no. 40, p. 404 210, 2013.

[70] A. Del Campo and W. H. Zurek, "Universality of phase transition dynamics: Topological defects from symmetry breaking," *International Journal of Modern Physics A*, vol. 29, no. 08, p. 1 430 018, 2014.

[71] T. Kibble, "Symmetry breaking and defects," in *Patterns of Symmetry Breaking*, Springer, 2003, pp. 3–36.

[72] S. Ulm, J. Roßnagel, G. Jacob, C. Degünther, S. Dawkins, U. Poschinger, R. Nigmatullin, A. Retzker, M. Plenio, F. Schmidt-Kaler, *et al.*, "Observation of the kibble–zurek scaling law for defect formation in ion crystals," *Nature communications*, vol. 4, p. 2290, 2013.

[73] G. Lamporesi, S. Donadello, S. Serafini, F. Dalfovo, and G. Ferrari, "Spontaneous creation of kibble–zurek solitons in a bose–einstein condensate," *Nature Physics*, vol. 9, no. 10, p. 656, 2013.

[74] H. Ghaffari, W. Griffth, P. Benson, K. Xia, and R. P. Young, "Observation of the kibble–zurek mechanism in microscopic acoustic crackling noises," *Scientific reports*, vol. 6, p. 21 210, 2016.

[75] J.-M. Cui, Y.-F. Huang, Z. Wang, D.-Y. Cao, J. Wang, W.-M. Lv, L. Luo, A. Del Campo, Y.-J. Han, C.-F. Li, *et al.*, "Experimental trapped-ion quantum simulation of the kibble-zurek dynamics in momentum space," *Scientific reports*, vol. 6, p. 33 381, 2016.

[76] A. Das, J. Sabbatini, and W. H. Zurek, "Winding up superfluid in a torus via bose einstein condensation," *Scientific reports*, vol. 2, p. 352, 2012.

[77] J. Dziarmaga and W. H. Zurek, "Quench in the 1d bose-hubbard model: Topological defects and excitations from the kosterlitz-thouless phase transition dynamics," *Scientific reports*, vol. 4, p. 5950, 2014.

[78] D.-T. Hoang, B. P. Venkatesh, S. Han, J. Jo, G. Watanabe, and M.-S. Choi, "Scaling law for irreversible entropy production in critical systems," *Scientific reports*, vol. 6, p. 27 603, 2016.

[79] S. Bronnikov and I. Dierking, "Time resolved statistical analysis of liquid crystal nucleus growth from the isotropic melt," *Physical Chemistry Chemical Physics*, vol. 6, no. 8, pp. 1745–1749, 2004.

[80] I. Dierking, "2-dimensional fractally homogeneous distribution of liquid crystalline nuclei in the isotropic melt," *EPL (Europhysics Letters)*, vol. 55, no. 1, p. 40, 2001.

[81] N. Fowler and D. I. Dierking, "Kibble–zurek scaling during defect formation in a nematic liquid crystal," *ChemPhysChem*, vol. 18, no. 7, pp. 812–816, 2017.

[82] I. M. Lifshitz and V. V. Slyozov, "The kinetics of precipitation from supersaturated solid solutions," *Journal of physics and chemistry of solids*, vol. 19, no. 1-2, pp. 35–50, 1961.

[83] B. Yurke, A. Pargellis, T. Kovacs, and D. Huse, "Coarsening dynamics of the xy model," *Physical Review E*, vol. 47, no. 3, p. 1525, 1993.

[84] M. Zapotocky, P. M. Goldbart, and N. Goldenfeld, "Kinetics of phase ordering in uniaxial and biaxial nematic films," *Physical Review E*, vol. 51, no. 2, p. 1216, 1995.

[85] W. E. Ford, H. Hiratsuka, and P. V. Kamat, "Photochemistry of 3,4,9,10-perylenetetracarboxylic dianhydride dyes. 4. spectroscopic and redox properties of oxidized and reduced forms of the bis(2,5-di-tert- butylphenyl)imide derivative," *The Journal of Physical Chemistry*, vol. 93, no. 18, pp. 6692–6696, 1989. DOI: 10.1021/j100355a025.

[86] F. J. Kahn, G. N. Taylor, and H. Schonhorn, "Surface-produced alignment of liquid crystals," *Proceedings of the IEEE*, vol. 61, no. 7, pp. 823–828, 1973.

[87] M. Joshi, R. Pinto, V. R. Rao, and S. Mukherji, "Silanization and antibody immobilization on su-8," *Applied surface science*, vol. 253, no. 6, pp. 3127–3132, 2007.

[88] C. Jones, *Microscopy, optical spectroscopy, and macroscopic techniques*. Springer Science & Business Media, 1994, vol. 22.

[89] P. Török and F.-J. Kao, *Optical imaging and microscopy: techniques and advanced systems*. Springer, 2007, vol. 87.

[90] D. B. Murphy, *Fundamentals of light microscopy and electronic imaging*. John Wiley & Sons, 2002.

[91] O. Lavrentovich, "Fluorescence confocal polarizing microscopy: Three-dimensional imaging of the director," *Pramana*, vol. 61, no. 2, pp. 373–384, 2003.

[92] G. Posnjak, "Topological formations in chiral nematic droplets: Doctoral thesis," PhD thesis, Univerza v Ljubljani, Fakulteta za matematiko in fiziko, 2017.

[93] J. Pawley, *Handbook of biological confocal microscopy*. Springer Science & Business Media, 2010.

[94] G. Posnjak, S. Čopar, and I. Muševič, "Points, skyrmions and torons in chiral nematic droplets," *Scientific reports*, vol. 6, p. 26 361, 2016.

[95] Q. Wu, F. Merchant, and K. Castleman, *Microscope image processing*. Elsevier, 2010.

[96] G. M. van Kempen, L. J. van Vliet, and P. J. Verveer, "Application of image restoration methods for confocal fluorescence microscopy," in *Three-Dimensional Microscopy: Image Acquisition and Processing IV*, International Society for Optics and Photonics, vol. 2984, 1997, pp. 114–125.

[97] R. C. Gonzalez, R. E. Woods, *et al.*, *Digital image processing*. Prentice hall Upper Saddle River, NJ, 2002.

[98] Q. Liu, B. Senyuk, M. Tasinkevych, and I. I. Smalyukh, "Nematic liquid crystal boojums with handles on colloidal handlebodies," *Proceedings of the National Academy of Sciences*, vol. 110, no. 23, pp. 9231–9236, 2013.

[99] M. G. Campbell, M. Tasinkevych, and I. I. Smalyukh, "Topological polymer dispersed liquid crystals with bulk nematic defect lines pinned to handlebody surfaces," *Physical review letters*, vol. 112, no. 19, p. 197 801, 2014.

[100] B. B. Mandelbrot and J. W. Van Ness, "Fractional brownian motions, fractional noises and applications," *SIAM review*, vol. 10, no. 4, pp. 422–437, 1968.

[101] H. E. Stanley, "Application of fractal concepts to polymer statistics and to anomalous transport in randomly porous media," *Journal of Statistical Physics*, vol. 36, no. 5-6, pp. 843–860, 1984.

[102] N. Jouault, P. Vallat, F. Dalmas, S. Said, J. Jestin, and F. Boué, "Well-dispersed fractal aggregates as filler in polymer- silica nanocomposites: Long-range effects in rheology," *Macromolecules*, vol. 42, no. 6, pp. 2031–2040, 2009.

[103] P. Meakin, "Fractal aggregates," *Advances in Colloid and Interface science*, vol. 28, pp. 249–331, 1987.

[104] E. Bullmore and O. Sporns, "The economy of brain network organization," *Nature Reviews Neuroscience*, vol. 13, no. 5, p. 336, 2012.

[105] L. Risser, F. Plouraboué, A. Steyer, P. Cloetens, G. Le Duc, and C. Fonta, "From homogeneous to fractal normal and tumorous microvascular networks in the brain," *Journal of Cerebral Blood Flow & Metabolism*, vol. 27, no. 2, pp. 293–303, 2007.

[106] E. Lieberman Aiden, N. L. Van Berkum, L. Williams, M. Imakaev, T. Ragoczy, A. Telling, I. Amit, B. R. Lajoie, P. J. Sabo, M. O. Dorschner, *et al.*, "Comprehensive mapping of long-range interactions reveals folding principles of the human genome," *science*, vol. 326, no. 5950, pp. 289–293, 2009.

[107] A. L. Goldberger, L. A. Amaral, J. M. Hausdorff, P. C. Ivanov, C.-K. Peng, and H. E. Stanley, "Fractal dynamics in physiology: Alterations with disease and aging," *Proceedings of the national academy of sciences*, vol. 99, no. suppl 1, pp. 2466–2472, 2002.

[108] D. Ma, A. D. Stoica, and X.-L. Wang, "Power-law scaling and fractal nature of medium-range order in metallic glasses," *Nature materials*, vol. 8, no. 1, p. 30, 2009.

[109] B. Yu and J. Li, "Some fractal characters of porous media," *Fractals*, vol. 9, no. 03, pp. 365–372, 2001.

[110] H. Koch, "Sur une courbe continue sans tangente, obtenue par une construction géométrique élémentaire," *Arkiv for Matematik, Astronomi och Fysik*, vol. 1, pp. 681–704, 1904.

[111] S. Hashemi, U. Jagodič, M. Mozaffari, M. Ejtehadi, I. Muševič, and M. Ravnik, "Fractal nematic colloids," *Nature communications*, vol. 8, p. 14026, 2017.

[112] I. I. Smalyukh, S. Shiyanovskii, and O. Lavrentovich, "Three-dimensional imaging of orientational order by fluorescence confocal polarizing microscopy," *Chemical Physics Letters*, vol. 336, no. 1-2, pp. 88–96, 2001.

[113] A. Ryzhkova, U. Jagodič, and I. Muševič, "Nanosecond light source with tunable coherence for fast and low-light microscopy," *Submitted*, 2019.

[114] U. Jagodič, A. Ryzhkova, and I. Muševič, "Localised opto-thermal response of nematic liquid crystal to laser light," *Liquid Crystals*, pp. 1–10, 2018.

[115] V. Fréedericksz and A. Repiewa, "Theoretisches und experimentelles zur frage nach der natur der anisotropen flüssigkeiten," *Zeitschrift für Physik*, vol. 42, no. 7, pp. 532–546, 1927.

[116] P. Oswald, J. Baudry, and S. Pirkl, "Static and dynamic properties of cholesteric fingers in electric field," *Physics Reports*, vol. 337, no. 1-2, pp. 67–96, 2000.

Bibliography

Publications Related to the Thesis

[141] S. Hashemi, U. Jagodič, M. Mozaffari, M. Ejtehadi, I. Muševič, and M. Ravnik, "Fractal nematic colloids," *Nature communications*, vol. 8, p. 14026, 2017.

[142] U. Jagodič, A. Ryzhkova, and I. Muševič, "Localised opto-thermal response of nematic liquid crystal to laser light," *Liquid Crystals*, pp. 1–10, 2018.

[143] A. Ryzhkova, U. Jagodič, and I. Muševič, "Nanosecond light source with tunable coherence for fast and low-light microscopy," *Submitted*, 2019.

Biography

- The author of this thesis Uroš Jagodič was born on the 12th of February 1991 in Celje, Slovenia.
- He finished his Bachelor's degree in Physics in 2012, at the Faculty of Natural Sciences and Mathematics, University in Maribor, Maribor, Slovenia.
- He continued his Master degree in Physics and finished in 2014, at the Faculty of Natural Sciences and Mathematics, University in Maribor, Maribor, Slovenia.
- In 2014 he started his Doctoral degree in the study program Nanosciences and Nanotechnology at the The Jožef Stefan International Postgraduate School, Ljubljana, Slovenia.
- Also in 2014 he was employed as a Young Researcher at the Department of Condensed Matter Physics at the Jožef Stefan Institute, Ljubljana Slovenia, under the supervision of prof. Dr. Igor Muševič.